Functionalization of Cellulose Nanocrystals with Inorganic Nanoparticles

by

Li Chen

A thesis
presented to the University of Waterloo
in fulfillment of the
thesis requirement for the degree of
Doctor of Philosophy
in
Chemical Engineering (Nanotechnology)

Waterloo, Ontario, Canada, 2016

AUTHOR'S DECLARATION

I hereby declare that I am the sole author of this thesis. This is a true copy of the thesis, including any required final revisions, as accepted by my examiners.

I understand that my thesis may be made electronically available to the public.

Abstract

In recent years, cellulose nanocrystals (CNCs) possess attractive features including good mechanical strength, high surface area, low density, crystalline rod-like structure, biocompatibility, biodegradability, and sustainability. In addition, the presence of sulphate ester groups on the surface of CNCs induces colloidal stability through electrostatic repulsion, and the abundant reactive primary hydroxyl groups offer the possibility for further modifications. These inherent properties make CNCs a good supportive substrate for loading inorganic nanoparticles in aqueous media. However, aggregation of CNCs and inorganic nanoparticles are often observed for CNC-inorganic nanohybrids. The aggregation greatly decreases surface area, limits the accessibility of reagents to inorganic nanoparticles, thereby, restricting potential applications. Furthermore, the formation of aggregates can alter the optical, catalytic and chemical characteristics of inorganic nanoparticles. In this study, stable synthetic strategies including physical adsorption, polymer encapsulation, and in-situ deposition were utilized to address the issue of aggregation most commonly observed with these nanoparticles. Fe_3O_4 nanoparticles, Au nanoparticles and CdS quantum dots were loaded onto CNC surface to achieve advanced applications, taking advantage of their attractive magnetic, catalytic and optical properties respectively.

Superparamagnetic Fe_3O_4 nanoparticles have been widely used in numerous applications. We demonstrated the synthesis of Fe_3O_4 nanoparticles through coprecipitation method with further stabilization provided by polyvinylpyrrolidone. The Fe_3O_4 nanoparticles effectively adsorbed onto the surface of CNCs to yield CNC@Fe_3O_4. A silica shell with controllable thickness was then coated onto CNC@Fe_3O_4 to protect from the oxidation of the Fe_3O_4 nanoparticles. Transmission and scanning electron microscopic images confirmed good deposition of Fe_3O_4 nanoparticles on CNCs rods with a uniform silica coating. Thermal gravimetric analysis confirmed that silica coating significantly enhanced the thermal stability of CNCs, where the onset decomposition temperature of CNC@Fe_3O_4@SiO_2 hybrids increased by 60 °C compared to pristine CNCs. Further application of the CNC@Fe_3O_4@SiO_2 was achieved by grafting β-cyclodextrin (β-CD) onto the silica shell. β-CD-modified CNC@Fe_3O_4@SiO_2 nanorods were found to show good adsorption toward two model pharmaceutical residues: procaine hydrochloride and imipramine hydrochloride. The adsorption capacities of the two residual drugs were calculated to be 13.0 ± 0.09 mg/g and 14.8 ± 0.16 mg/g respectively.

Generation 6 poly (amido amine) dendrimer-grafted cellulose nanocrystals (CNC-PAMAM) were obtained via the carbodiimide-mediated amidation method to introduce pH-responsive and fluorescent properties, and metal affinities groups for stabilizing inorganic nanoparticles. The pH-responsive system was investigated and confirmed by zeta potential analyses, UV-vis transmittance data, and interactions between CNC-PAMAM and surfactants were measured by isothermal titration calorimetry. At pH $\leq$ 4, well-dispersed aqueous dispersions were obtained due to the electrostatic repulsion from protonated amine groups on PAMAM. At pH $\geq$ 10, stable aqueous dispersions were attributed to the abundant presence of negatively charged carboxylate and sulphate ester groups on CNCs. In addition, strong blue fluorescent emission was observed and investigated using fluorescent spectrophotometry. Moreover, the fluorescent behaviors of CNC-PAMAM were largely influenced by the formation of aggregates.

Well-dispersed Au nanoparticles (AuNPs) of 2-4 nm were loaded onto CNC-PAMAM by reducing $HAuCl_4$ using $NaBH_4$ with PAMAM playing the role of nanoreactors. The dendrimer-grafted CNC system was also demonstrated to be an effective reducing agent and stabilizer for the synthesis of AuNPs. The impact of temperature, pH values, and CNC-PAMAM concentration on size distribution of AuNPs was studied. A very small size distribution of 10-20 nm was achieved under pH 3.3 at 25 °C with a CNC-PAMAM concentration of 0.008 wt.%. The as-prepared nanocomposites displayed superior catalytic properties with turnover frequencies of up to 5400 h^{-1} towards the reduction of 4-nitrophenol to 4-aminophenol. The enhanced catalytic performance may be attributed to the improved dispersibility and accessibility of AuNPs within the PAMAM dendrimer domain. Thus, we succeeded in demonstrating the versatility of CNC-PAMAM both as an effective nanoreactor and a reducing agent for AuNPs.

Quantum dots (QDs) are attractive in bioimaging application because of their inherent size-tunable emission, flexible excitation wavelength, and good photochemical stability. Particular attention was devoted to the aqueous phase synthesis of QDs that avoids the use of organic solvents and subsequent tedious phase transfer procedures. For the first time, carboxylated CNCs were used as templates to stabilize CdS QDs and CdS@ZnS core-shell QDs in aqueous phase. High colloidal stability was achieved with sufficient negative charge on the CNC surface, and the coordination of Cd^{2+} to carboxylate groups allowed in-situ nucleation and growth of QDs on CNC surface. The influences of CdS/CNC ratio, pH, and ZnS/CdS ratio on colloidal stability and photoluminescence property were also studied. The results showed that products with excellent colloidal stability and the highest

photoluminescence intensity could be obtained at pH 8 with a CdS/CNC weight ratio of 0.19 and a ZnS/CdS molar ratio of 1.5. The as-prepared CNC/CdS@ZnS exhibited long-term colloidal and optical stability. Using biocompatible CNCs as stabilizers, the products have been demonstrated to exhibit low adverse cytotoxicity effects towards HeLa cells, and can serve as promising red-emitting fluorescent bioimaging probes.

Stable colloids are promising building blocks for fabricating functional thin films using the layer-by-layer (LBL) self-assembly method. We report for the first time the use of CdS QD-functionalized CNC colloids for fabricating nanothin films via LBL self-assembly. Both negatively- and positively-charged CNC/QD nanohybrids with high colloidal stability and narrow particle size distribution were synthesized, so electrostatic interaction between the two building blocks can form during the coating process. The controllable LBL coating process was confirmed by SEM images and ellipsometry data. The rigid structure of CNCs leads to nanoporous structured films, and the coated poly(ethylene terephthalate) (PET) substrates display high transmittance (above 70%) over the entire range of visible light and strong hydrophilicity with contact angles around 40. Most significantly, both tunable structural colours from thin-film interference and adjustable photoluminescence colours from embedded QDs were achieved. These coated PET substrates showed good flexibility, and strong stability in both water and ethanol. The modified PET films displayed exciting applications in anti-counterfeiting and security protocols with structural colours from thin-film interference and photoluminescence from QDs.

In conclusion, Fe_3O_4, AuNPs, and CdS QDs were uniformly loaded onto the surface of CNCs through different aqueous synthetic protocols. The well-developed CNC@inorganic nanoparticle systems displayed promising applications as efficient adsorbents for drug removal, catalysts for chemical reduction of 4-nitrophenol, fluorescent emitting bioimaging probes for cancer cells, and structural nanobuilding blocks for thin films.

Acknowledgements

My great appreciations go to my supervisor Prof. Michael Tam. He provided me with unbelievable opportunities, flexibilities and support during my Ph.D program. He believed in me and walked me through English studies and research projects with great patience. He taught me how to use new instruments, encouraged me to try new technologies, methods and analytic techniques, and guided me through many difficulties in various aspects of life. I would like to thank my committee members Prof. Emily Cranston, Prof. Leonardo Simon, Prof. Mike Pope and Prof. Juewen Liu for providing valuable suggestions for my research and my thesis. I would like to thank CelluForce Inc. for providing CNCs for my research and Dr. Richard Berry for offering valuable comments for all my publications.

I am very thankful to my talented labmates who motivated me and provided me with insights in my studies. Patrick Quinlan brightened my life in many ways and helped me with my academic writing and research. Nathan Grishkewich brought great suggestions on the structure of my manuscript on PAMAM-functionalized CNC and provided valuable comments on my thesis. I collaborated with Yibo on the project of CNC-stabilized quantum dots for bioimaging applications, and we had great discussions on the data analysis and manuscript. I would also like to thank Patrick Quinlan, Nathan Grishkewich, Yibo Liu, Dr. Zengqian Shi, Juntao Tang, Nishil Mohammed, Hairong Wang, Debbie Wu, and Fatima Awan for the wonderful chats we had regarding research and life. All my labmates greatly broadened my knowledge on functionalization and applications of CNCs in various fields.

I would like to thank my friends at the University of Waterloo and Beijing University of Chemical Technology for their constant support and help in my research. Dr. Howard Siu constantly supported my search by offering characterization methods for my samples and valuable discussions for my research. Dr. Juewen Liu and Dr. Feng Wang provided facilities and valuable training for evaluating bioimaging applications of CNC-stabilized quantum dots. Without their help, the project would not succeed. Dr. Yibo Dou, Dr. Changming Li, Dr. Shitong Zhang, Wa Gao, and Junyao Zhou offered me prompt help in my research, despite the long distance and time difference between China and Canada.

Last but not the least, I would like to thank my family for their love and support.

Dedication

This thesis is dedicated to my lovely family.

Table of Contents

List of Figures

List of Tables

Chapter 1
Introduction

1.1 Overview

One of nature's remarkable abilities is combining organic and inorganic materials to achieve heightened physical/chemical properties (eg. mechanical strength, durability, stability etc.). These inorganic-organic bionanohybrids have attracted a great deal of attention in both academic research and in industry due to the required improvements in the physical, chemical, biological, and environmental limitations (e.g. aggregation, low thermal stability, toxicity, poor processability, high cost etc.). These bionanohybrids often display enhanced structural or functional properties that possess multifunctional characteristics.[1] As a result, they can be applied to the fabrication of various optical, biomedical, catalytic, and electrochemical devices through bottom-up approaches, which may find application in various industries.[2]

Sustainable biomaterials such as cellulose, starch, chitosan, and poly (lactic acid) are found in abundance in nature, and they are suitable for incorporation into bioinorganic nanocomposites.[3] In addition to their low cost, these biomaterials exhibit excellent biodegradability and biocompatibility. Among these materials, cellulose nanocrystals (CNCs) have aroused a great deal of interest because of their rigid rod-shaped nanostructure, high surface area, good aqueous colloidal stability, favorable surface modification, and excellent mechanical strength.[4] These properties offer higher flexibility when fabricating functional devices through bottom-up approaches. However, CNCs consist of hydrogen-bonded linear chains of β-D-glucopyranose and suffer from limited functional groups. In addition, the grafting chemistry through reactive primary hydroxyl groups on the CNC surface often results in low grafting ratios. Moreover, physical adsorption of chemicals and involvement of organic solvents are common during these reactions, which are problematic for subsequent characterization and evaluation on their applications. Furthermore, similar to other nanoparticles, aggregates, large bundles and networks of CNCs may be formed during the modification processes, although CNCs themselves tend to be well-dispersed in aqueous media.[5] Recently, by taking advantage of the high surface area of CNC, functionalization via the use of inorganic nanoparticles has attracted increasing attention.

Inorganic nanoparticles with sizes between 1 and 100 nm have shown size-dependent magnetic, catalytic, and optical properties, which are significantly different from the bulk samples. Noble metal nanoparticles, metal oxide nanoparticles and quantum dots have aroused substantial interest in both industrial development and academic research. However, inorganic nanoparticles are thermodynamically unstable due to their high surface energy. In surfactant-free chemical reactions, aggregation occurs immediately due to the mutual attraction of the particles through van der Waals forces or chemical bonding as the generation of particles occurs. Aggregation observed either during the production process or post-treatment is a problematic and complex phenomenon for inorganic nanoparticles. Aggregation or agglomeration makes the investigation of nanostructured materials difficult. More importantly, it largely affects their properties and applications.[6] To tackle this problem, two main strategies have been developed. One method is to apply capping agents onto the particle surface to introduce steric or electrostatic repulsion forces, and the second is to adsorb the nanoparticles onto high-surface supporting materials. Unfortunately, some widely used capping agents are cytotoxic and nonbiodegradable,[7–9] and many chemicals fail to provide long-time colloidal stability due to degradation, photolysis or oxidation over time.[10] The majority of supporting materials used are either expensive or they lack metal affinity groups for loading inorganic nanoparticles. More importantly, due to concerns with the environmental and human health, there is increasing interest in using biomaterials as supporting materials for inorganic nanoparticles.

Cellulose nanofibril and their derivatives have been widely applied as green templates for inorganic nanoparticles. With high flexibility and length in microns, cellulose nanofiber/inorganic nanoparticle composites can broaden cellulose nanofibers' applications in industries including paper, membranes, and textiles. However, the large size of cellulose nanofibers limits their applications in fields where nanoscale structure is required. CNCs with adjustable and much shorter length possess excellent colloidal stability, and they are excellent candidates for loading inorganic nanoparticles for applications as nanofillers, bioimaging probes, and nanobuilding blocks. Up to now, many CNC/inorganic nanoparticles hybrids have been developed, however, due to electrostatic interactions between positively charged metal ions and negatively charged CNCs, agglomerated CNC networks of micron sizes are obtained, where colloidal stability, nanostructure and specific surface area of CNCs deteriorated dramatically. Inorganic nanoparticles are often buried within these CNC networks, resulting in the limited accessibility towards active sites on the inorganic nanoparticles. More importantly, the formation of CNC networks may impact the synthetic process of inorganic nanoparticles, leading to poor control over size distribution and physicochemical properties.

By taking advantage of the high surface area and negative surface charge of CNCs, we focused on the development of CNCs/inorganic nanoparticle hybrids with improved particle dispersibility, size control, and colloidal stability; and the exploration of their applications in various fields. Our work would exhibit the following attractive features: (i) metal affinity groups introduced onto CNC surface favor the deposition of inorganic nanoparticle; (ii) strong electrostatic repulsion among CNCs facilitate aqueous colloidal stability of CNC/inorganic nanoparticle systems; (iii) inorganic nanoparticles introduce new functions to the nanoparticle-CNC system and thus expand their usefulness and applications. In this study, iron oxide nanoparticles (Fe_3O_4), noble metal nanoparticles (Au nanoparticles) and quantum dots (CdS) were chosen due to their well-developed facile aqueous synthesis, interesting physiochemical properties, and application prospects. The main challenge was to homogeneously deposit inorganic nanoparticles onto CNC surface, maintaining the nanoscale nature and avoiding the aggregation of both CNCs and inorganic nanoparticles.

1.2 Research objectives

By taking advantage of the beneficial properties of CNCs, the present study will focus on loading functional inorganic nanoparticles without the formation of aggregates of CNCs and inorganic nanoparticles, and to explore the applications of these bioinorganic nanocomposites in water treatment, catalysis, bioimaging and anticounterfeiting applications. In addition, to the best of our knowledge, few attempts have been made in exploiting the combined advantages of introducing metal affinity groups on CNC surface and in controlling the agglomeration of CNCs during the immobilization of inorganic nanoparticles. Without metal affinity groups, free inorganic nanoparticles with broad size control are commonly observed in CNC/inorganic nanoparticle systems. Without further modification, agglomeration of CNCs occurs due to electrostatic attraction between sulphate ester groups on CNC surface and cationic metal ions. More importantly, particle nanostructure is essential for applications in bioimaging and catalysis. While the surface modification of CNCs has been extensively studied, only a few studies have focused on introducing and evaluating metal affinity groups on CNC surface for loading inorganic nanoparticles. Moreover, by maintaining the high colloidal stability, enhanced applications of these bioinorganic nanocomposites have been achieved. To date, no work has been reported on the use of CNC/inorganic nanoparticle composites as building blocks to assemble films, as CNCs agglomerated after the loading of inorganic nanoparticles. Furthermore, by assembling CNC/inorganic nanoparticle composites using bottom-up

layer-by-layer self-assembly method, thin films with more desirable chemical and optical properties could be achieved.

In the present study, surface modification of CNCs through both chemical grafting and coating specifically for further immobilization of inorganic nanoparticles were conducted. One approach is to introduce metal affinity groups (i.e. carboxylate groups and amine groups) onto the CNC surface through covalent bonding, and the other approach is to coat polymers (i.e. poly(diallyldimethylammonium chloride), polyvinylpyrrolidone, and polyethylenimine) onto CNC surface. Fe_3O_4 nanoparticles, Au nanoparticles, and CdS quantum dots were selected and immobilized onto the CNC surface to introduce magnetic, catalytic, and optical properties respectively. With beneficial and advanced properties, it is important to investigate and evaluate the applications of these CNC/inorganic nanoparticle composites in various fields.

Following a comprehensive review of the literature, the objectives for this thesis were formulated:

1. Synthesize and characterize CNC/Fe_3O_4 nanohybrids, and investigate their application in drug removal
2. Synthesize and characterize pH-responsive and fluorescent poly (amidoamine) dendrimer-grafted CNC
3. Develop polyamidoamine dendrimer-grafted CNC/Au nanoparticles as sustainable catalysts
4. Investigate aqueous synthesis of CNC/CdS@ZnS quantum dot nanohybrids and evaluate their application as bioimaging probes for HeLa cells.
5. Fabricate thin films using CNC/CdS quantum dot as building blocks for anti-counterfeiting applications

1.3 Thesis outline

This thesis consists of 8 chapters. The research results are reported in manuscript format from Chapter 3 to Chapter 7. The scope of the chapters is listed as follows: Chapter 1 briefly introduces chemical/physical properties of CNCs and inorganic nanoparticles, and the advantages and importance in developing CNC/inorganic nanoparticle hybrids. The research objectives and outline of the thesis are also included. Chapter 2 introduces CNCs (structure, surface modification, applications), inorganic nanoparticles, and previously developed cellulose nanomaterial/inorganic

hybrids. In this chapter, general introductions of silica coating, *β*-cyclodextrin, and poly (amido amine) dendrimers are also provided; these materials played important roles in our projects. Chapter 3 introduces an improved method for producing CNC/Fe_3O_4 nanohybrids and for protecting the oxidation of Fe_3O_4 by silica coating, and the application of these nanohybrids in drug removal. Chapter 4 reports on the synthesis of poly (amidoamine) dendrimer-grated CNCs and their pH-responsive and fluorescent properties. Chapter 5 investigates the loading and size control of Au nanoparticles using poly (amidoamine) dendrimer-grated CNCs as biosupports and reducing agents. Chapter 6 reports on the aqueous synthesis and stabilization of CdS@ZnS core-shell quantum dot using oxidized-CNCs as templates. The application of CNC/CdS@ZnS as bioimaging probes for HeLa cells was evaluated. Chapter 7 presents the capability of CNC/CdS nanohybrids as nanobuilding blocks in fabricating thin films on various substrates. The optical properties of these films are reported and their application in anti-counterfeiting is demonstrated. Chapter 8 summarizes the key conclusions and major contributions along with recommendations for future studies.

Chapter 2
Literature review

2.1 Introduction

This chapter reviews the literature related to the research performed in this thesis. Firstly, cellulose nanocrystals (CNCs), their properties and applications are discussed. Surface modification of CNC is described with a more detailed focus on TEMPO-mediated oxidation. A review on the aqueous synthesis and colloidal stability of inorganic nanoparticles is presented. Previous published works on the preparation and properties of cellulose nanofiber/inorganic nanoparticle and CNC/inorganic nanoparticle hybrids are described in detail. Finally, brief introductions on silica coating, β-cyclodextrin, and poly(amido amine) dendrimers are also outlined, as these materials played important roles in this research.

2.2 Cellulose nanocrystals

Cellulose is one of the most abundant natural resources in Canada. Products made from cellulose and its derivatives are found extensively in our daily life. Particularly, cellulose nanofibers and CNCs possess attractive features including high mechanical performance, large surface area, favorable chemical modification, sustainability and promising wide applications. Cellulose nanofibers can be produced from wood pulp fiber through the treatment by endoglucanases or acid hydrolysis with the assistance of mechanical shearing.[11] Highly crystalline and individual cellulose nanofibers were also successfully obtained via oxidation of cellulose using 2,2,6,6-tetramethylpiperidine-1-oxyl radical (TEMPO) together with mechanical treatment.[12] Cellulose nanofibers consist of both crystalline and amorphous regions. While crystalline regions offer good mechanical strength for cellulose nanofibers, amorphous regions contribute to flexibility. By further removal of these amorphous regions, pure crystalline parts referred as to CNCs were prepared (Figure 2.1). Compared with cellulose nanofibers, CNCs have a more uniform, rod-like nanostructure with improved mechanical strength.

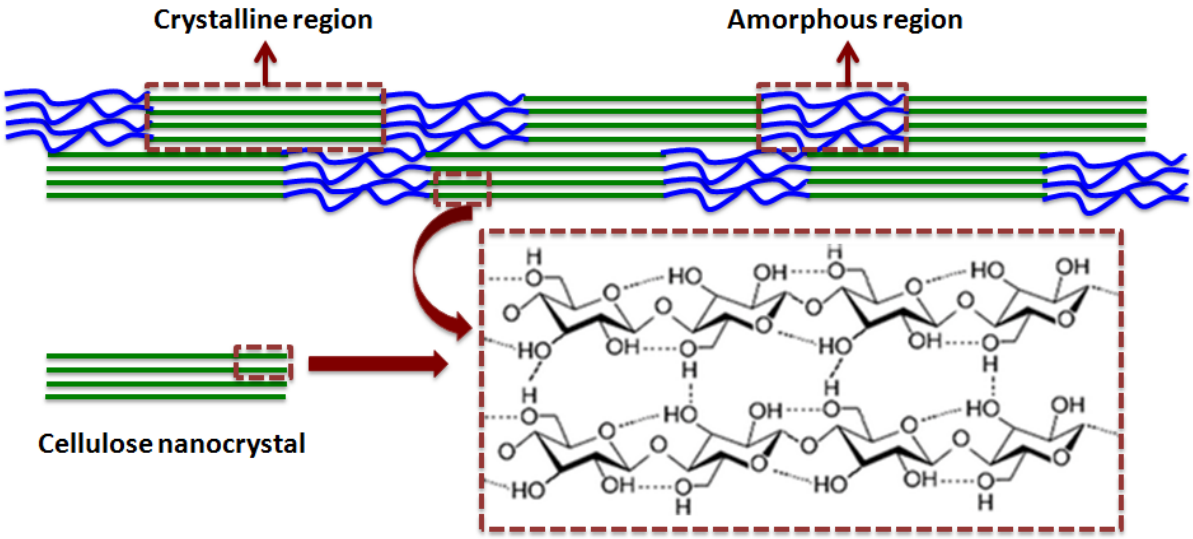

Figure 2.1. Schematic structure of cellulose chains and CNCs.

Sulphuric acid and hydrochloric acid are most commonly used to prepare CNCs.[13–15] Sulphuric acid hydrolysis will introduce an abundance of sulphate ester groups onto the CNC surface, which will induce electrostatic repulsion among CNC particles in aqueous suspension, and will enable the stabilization of CNCs over a wide range of pH values. Hydrochloric acid hydrolysis tends to donate minimal surface charge but will preserve a larger quantity of reactive primary hydroxyl groups that can enhance the grafting ratio of small molecules onto CNCs.[5] Other chemicals including phosphoric acid,[16] hydrobromic acid,[17] 1-butyl-3-methylimidazolium hydrogen sulphate ionic liquid,[18] were also used for the preparation of CNCs.

CNCs consist of hydrogen-bonded linear chains of β-D-glucopyranose bundled together to form a rigid, regular nanoscale material (Figure 2.1). The size and aspect ratio of the CNCs may vary depending on the cellulose source (cotton, tunicate, bacteria, wood pulp etc.).[12] Owing to their nanoscale size and low density, CNCs have a large surface area in the range of 150–250 m^2/g. Remarkable tensile strength (7500 MPa) and high stiffness with a Young's modulus of 100–140 GPa were observed for CNCs.[19] Besides the excellent mechanical properties of CNCs, they also exhibit interesting optical and magnetic properties. In addition, like other rod-like particles, CNCs display liquid crystalline behavior and undergo a self-assembly process to form a chiral nematic phase at high concentrations. These properties have triggered the research on the synthesis of chiral nematic films and mesoporous materials using CNCs as templates.[20] What makes CNCs more attractive is that CNCs are now available in large quantity for demonstration studies.

2.3 Surface modification of cellulose nanocrystals

2.3.1 TEMPO oxidation

To further functionalize CNCs, chemical modifications (including cationization, oxidation, silylation, etc.) of the primary hydroxyl groups of glucose units were reported and they are still being extensively studied. Details of these surface modifications can be found in a recent published review.[4] Here, we introduce one widely applied modification called TEMPO-mediated oxidation, which introduces carboxylate groups onto the CNC surface.

TEMPO oxidation is widely used for the modification of cellulose and its derivatives. The reaction selectively converts C6 primary hydroxyl groups on the surface of cellulose or CNCs to carboxylate groups at an optimum pH value of 10 (Figure 2.2). The conversion is achieved both by oxidized TEMPO and NaBrO/NaClO in the system.[21] One significant role of TEMPO-oxidation is to convert cellulose into individualized cellulose nanofibers together with successive mild disintegration, and the carboxylate content can reach ~1.5 mmol/g.[12] The effect of TEMPO oxidation conditions on the content of carboxylate groups, morphology and crystalline structure was also investigated. The results showed that a long oxidation period (24 h) greatly shortened the fragments.[22] Further details in TEMPO-oxidized cellulose nanofibers were summarized by Akira Isogai and coworkers.[23]

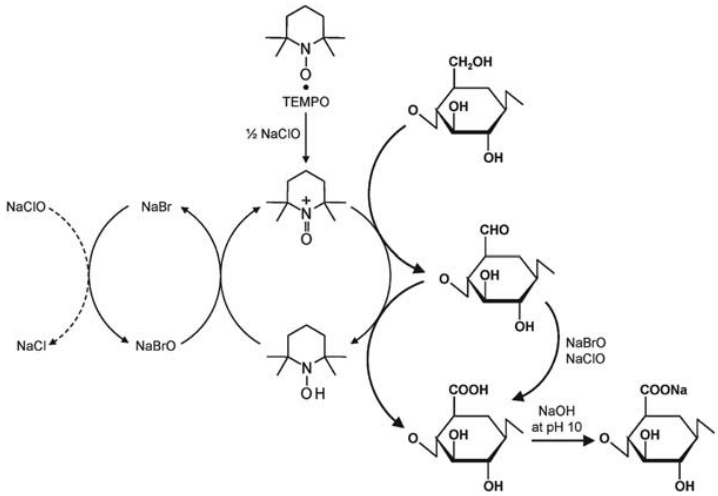

Figure 2.2. TEMPO-oxidation of C6 primary hydroxyl groups to introduce carboxylate groups.[23]

Carboxylated CNCs were synthesized by TEMPO oxidation of hydrochloric acid -hydrolyzed cellulose using the same procedure, and the introduction of carboxylate groups led to better dispersion in aqueous phase.[15] As for CNCs produced by sulphuric acid hydrolysis, the purpose of TEMPO oxidation was to introduce reactive carboxylate and aldehyde groups onto CNC surface, which could then be used for grafting or derivatizing purposes.[24, 25]

2.3.2 Desulphation of CNCs

Similar to TEMPO oxidation, various CNC surface modifications were performed through reactions with primary hydroxyl groups. In most modifications, the quantity of reactive hydroxyl groups on CNC surface affects the grafting ratio of the functional groups. The commercially available CNCs have abundant sulphate ester groups but a reduced amount of primary hydroxyl groups, which largely decrease the grafting ratio of the functional groups. Nevertheless, fully desulphated CNCs or CNCs produced through hydrochloric acid hydrolysis cannot be dispersed well in aqueous media, thereby reducing the surface area and accessibility of reactants, thus hindering their applications. Fortunately, the quantity of primary hydroxyl groups can be adjusted and controlled. One previous work reported the full desulphation of CNCs using solvolytic desulphation and partial desulphation of CNCs through mild acid hydrolysis of sulphuric acid-hydrolyzed CNCs.[26] Although a relatively small amount of aggregation was observed for partially desulphated CNCs due to the reduced repulsive forces, this product was more dispersible in aqueous media than fully desulphated CNCs.

2.4 CNC applications

2.4.1 Nanofillers in polymer matrix

CNCs with superior mechanical properties, nanoscale structure and biocompatibility have served as nanofillers in matrices, such as polycaprolactone-based waterborne polyurethane,[27,28] poly(oxyethylene),[29,30] polyvinyl alcohol,[31] poly(lactic acid),[32] polymethylmethacrylate[33] (Figure 2.3). It is believed that the improvement of the mechanical strength is associated with the formation of hydrogen bonding among CNCs and CNC/polymer matrix, and the improved separation of the soft and hard segments within the polymer matrix.

Films with CNC contents from 0 to 30% in waterborne polyurethane matrix were prepared through physical mixing CNCs and waterborne polyurethane suspensions. With reinforcement from CNCs, dramatic increases in the Young's modulus (from 0.51 to 344 MPa) and tensile strength (from 4.27 to

14.86 MPa) were observed when the content of CNCs was increased from 0 to 30 wt%.[27] Another report by the same group describes the preparation of CNC/waterborne polyurethane composites using *in situ* polymerization, and improved Young's modulus (from 1.7 to 107.4 MPa) and tensile strength (from 4.4 to 9.7 MPa) was observed with increasing CNC content from 0 to 10 wt%.[28] In the composites of CNC/poly(oxyethylene), although the introduction of CNCs led to a decrease in the crystallinity of the matrix, the CNC network within the matrix enhanced the film's stability at temperatures above the melting temperature of the matrix.[29] Enhancement of the elastic modulus was also reported with CNCs serving as nanofillers in polyvinyl alcohol.[31] CNCs with diameters ranging from 8 to 10 nm and lengths between 60 to 120 nm were added to the polymethylmethacrylate matrix, and films with high transparency were achieved due to the small size and good dispersion of CNCs. More importantly, the storage modulus was largely improved compared to pure polymethylmethacrylate sheets.[33] More recently, surfactant-modified CNCs were synthesized to facilitate the dispersion of CNCs in the polylactic acid matrix, and commercial Ag nanoparticles were further added to the matrix. The nanocomposite films maintained good transparency, displayed high tensile Young modulus, and exhibited antibacterial performance towards *Staphylococcus aureus* and *Escherichia coli cells*.[32]

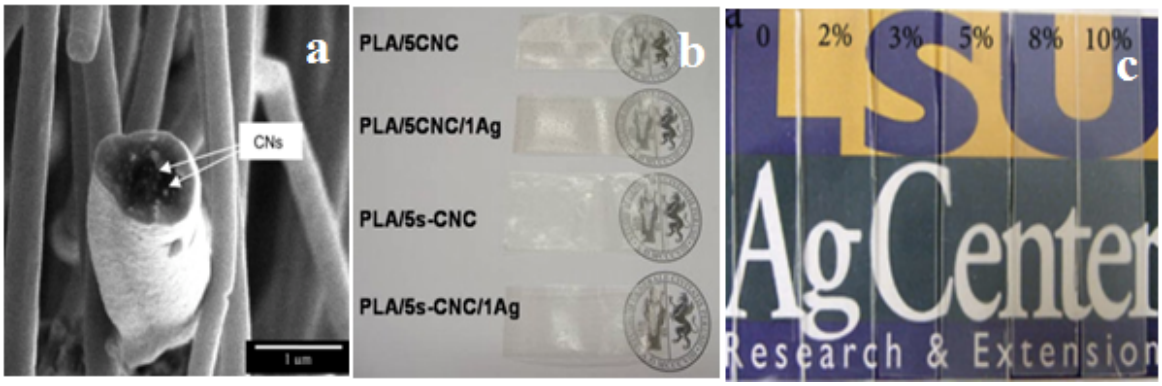

Figure 2.3. CNCs as nanofillers in polyvinyl alcohol (a),[31] poly(lactic acid) (b)[32] and polymethylmethacrylate (c)[33].

2.4.2 Nanobuilding blocks in thin films

CNCs can serve as building blocks for fabricating thin films through layer-by-layer (LBL) assembly on substrates such as silicon wafers, plastic films and quartz glass (Figure 2.4). LBL self-assembly demonstrated many advantages in the preparation of CNC-based thin films. For example, it allows the precise control of film thicknesses; the films prepared often possessed good structure stability against

water over a long period of time; films with high transparency can be obtained due to good dispersion of CNCs, controllable thickness in nanometer scale, and the formation of nanoporous structure. Positively charged polymers such as poly(diallyldimethylammonium chloride),[34] poly(allylamine hydrochloride, PAH),[35,36] chitosan,[37,38] polyethyleneimine (PEI),[39] cationic *β*-chitin nanofibrils,[40] collagen,[41] and xyloglucan[42] have been used as counterparts for CNCs in the LBL deposition process. CNC-based thin films with high mechanical strength, light weight, and even structural colours have been reported, however few applications outside of oxygen barrier,[38] anti-reflection coatings,[39] and enzyme detection[42] have been explored. With the abundance of a variety of nanobuilding blocks available (e.g. graphene oxide, layered double hydroxides nanosheets, noble metal nanoparticles/nanowires, stimuli-responsive organic molecules, etc.), properties, structure, functions, and applications of CNC-based thin films can be tuned and explored.

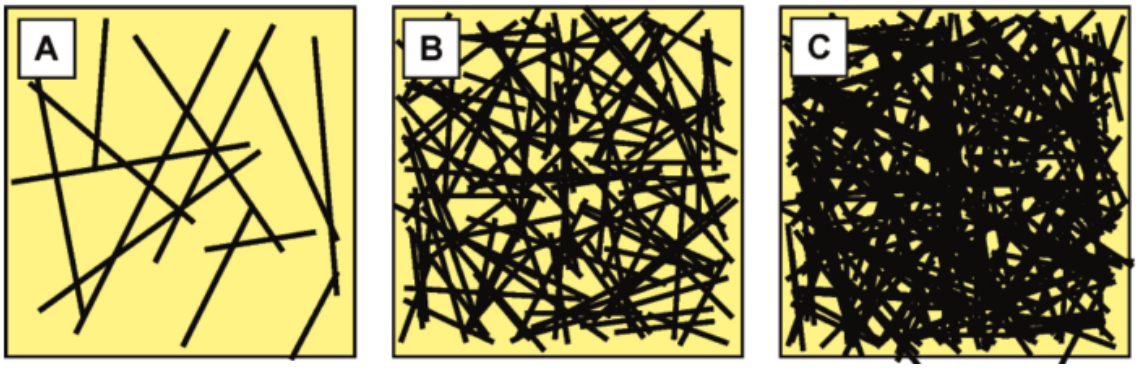

Figure 2.4. Schematic demonstration of fabricating thin films (1 bilayer (A), 12 bilayers (B) and 20 bilayers (C) of PEI/CNC on substrates through LBL assembly.[39]

2.4.3 Biomedical applications

Microcrystalline cellulose and derivatized cellulose (e.g. carboxymethyl cellulose, ethyl cellulose and methyl cellulose) have been widely used in drug-loaded tablets and injectable formulations in pharmaceutical industry.[19] Recently the cytotoxicity of CNCs has been studied using various cell lines. Um and coworkers investigated the cytotoxicity effects of the size and concentration of CNCs against NIH3T3 murine embryo fibroblasts and HCT116 colon adenocarcinoma. Four CNC samples with different lengths ranging from 100 nm to more than 1 micron were prepared through controlled acid hydrolysis. All the samples showed no substantial cytotoxicity with concentrations below 250 μg/mL. At higher concentrations (i.e. 500 μg/mL and 1000 μg/mL), CNCs tend to be cytotoxic due to gelation under high cellular uptake.[43] Catalán and coworkers compared the genotoxic and

immunotoxic effects of CNCs (mean length 135 nm, mean width 7.3 nm) with the microcrystalline cellulose (mean particle size ~50 μm). Both materials showed no genotoxicity in human bronchial epithelial cells under a concentration of 100 μg/mL. When these two materials were exposed for 6 hours in human monocyte-derived macrophages at a dose of 300 μg/mL, microcrystalline cellulose triggered the secretion of pro-inflammatory cytokines tumor necrosis factor α and interleukin 1β, while CNCs did not cause such inflammatory response.[44]

Lately, the interactions of elongated nanoparticles (e.g. carbon nanotubes[45]) or filaments (e.g. filomicelles[46]) with cells and within animals have attracted much attention. These elongated nanomaterials possess advantages in terms of long circulation time, rapid renal clearance and effective urinary excretion.[47] From this perspective, CNCs are good candidates for investigating these interactions with adjustable aspect ratio in the range of 1-100 depending on cellulosic source materials and the conditions of hydrolysis.[15]

Moreover, functionalized CNCs were evaluated for bioimaging applications and drug delivery. Recently, fluorescent-dye-labeled CNCs have been demonstrated as useful markers for bioimaging applications. Luong and co-workers labeled CNCs with negatively charged fluorescein isothiocyanate and positively charged rhodamine B isothiocyanate, and investigated the charge effects on the cellular uptake and cytotoxicity. Their results showed that positively charged fluorescent rhodamine B isothiocyanate-conjugated CNCs did not affect the cell membrane integrity as bioimaging probes, while negatively charged fluorescein isothiocyanate-conjugated CNCs displayed poor cellular uptake and caused cell rupture.[48] Roman and coworkers conjugated both folic acid and fluorescein isothiocyanate onto CNCs, and confirmed the specific folate receptor-mediated cellular uptake of folic acid-conjugated CNCs by human (DBTRG-05MG, H4) and rat (C6) brain tumor cells.[49] Both publications indicated that CNCs have low cytotoxicity and excellent membrane permeability in various cell lines. Notably, the grafting density of these fluorescent dyes can be greatly affected by the charge content or hydroxyl group content on CNC surface. Cranston and coworkers prepared CNC_{sulf} through sulphuric acid hydrolysis, CNC_{desulf} by acid-assisted partial desulphation, and CNC_{HCl} using HCl acid hydrolysis. The three samples possessed sulphur contents of 0.47 wt%, 0.21 wt% and 0 wt% respectively, determined by conductometric titration. The three samples were labeled with 5-(4, 6-dichlorotriazinyl) aminofluorescein under a CNC reaction concentration of 1 wt%, and the results showed that grafting density varied dramatically from 4.5 ± 0.1 nmol/g for CNC_{sulf}, 11.1 ± 0.1

nmol/g for CNC_{desulf}, to 47.5 ± 0.4 for CNC_{HCl}.[5] These results are of great importance as many fluorescent dyes are grafted onto CNC surface through reactions with hydroxyl groups.

Further, CNCs have also been demonstrated to be promising drug carriers. Burt and coworkers confirmed that CNCs with sulphate ester groups were promising materials in binding ionizable drugs, such as tetratcycline and doxorubicin, and that cetyltrimethylammonium bromide/CNC complexes were good candidates in binding hydrophobic drugs, such as docetaxel, paclitaxel, and etoposide. More importantly, significant amounts of drugs were loaded, and fast release of these drugs from CNCs over a 1-day period and controlled release of these hydrophobic drugs from cetyl trimethylammonium bromide/CNC complexes over a 2-day period were observed.[50] Tam and coworkers also reported the grafting of chitosan oligosaccharide on oxidized CNC surface through amide bridges. The as-prepared material displayed a drug loading of 14 wt% towards procaine hydrochloride. A fast release of 85% within 30 min was observed owing to burst release within the first 10 min.[51]

Overall, functionalization of CNCs through chemical reactions with active primary hydroxyl groups is favorable and extensively studied, which would largely expand their applications in biomedical fields.

2.4.4 Self-assembly templates for solid films

Suspensions of CNCs in water self-assemble into a chiral nematic phase, and the corresponding air-dried CNC films can preserve the structure, showing iridescent colours (Figure 2.5). Using the sol-gel method, chiral nematic organization can be retained in SiO_2 and TiO_2. For example, MacLachlan and coworkers reported the preparation of freestanding silica films with chiral nematic organization using CNCs as templates. Briefly, CNC suspension with a weight percentage of 3% and a pH value of 2.4 was mixed with silica precursor (i.e. $Si(OEt)_4$ or $Si(OMe)_4$), where these precursors underwent hydrolysis and condensation to form silica networks. These homogeneous mixtures and the dried films both displayed fingerprint texture, indicating good preservation of the chiral nematic phase. Circular dichroism confirmed the left-handed helical structures of these films. In addition, the peak wavelength reflected by these films can be tuned by adjusting either the average refractive index of films n_{avg} or the helical pitch P based on the following equation (1):

$$\lambda_{max} = n_{avg}P \quad (1)$$

Further, CNCs templates were removed by calcination of the films at a temperature of 540 °C under air, resulting in free-standing silica films with a large amount of mesopores (pore volumes: 0.60–0.25 cm^3 g^{-1}, peak pore diameter: 3.5–4 nm) and strong birefringence. Reflected light from silica films with peak wavelength in the range of 300 nm to 1300 nm was obtained by controlling the quantity of silica precursor added.[20]

Using mesoporous silica films described above as hard templates, self-standing titanium dioxide films with chiral nematic ordering could be further obtained. Typically, $TiCl_4$ solution was first penetrated into the mesopores in silica film, and then the film was heated to 80 °C for half an hour to form TiO_2. Afterwards, TiO_2 within SiO_2 films were crystallized under the calcination at 600 °C. Finally, SiO_2 was etched and removed by 2 M NaOH. The obtained TiO_2 preserved the chiral nematic structure originally from the self-assembly of CNCs and showed similar dimensions as the SiO_2 films. The BET surface area and the pore volume of TiO_2 film were measured to be 234 m^2 g^{-1} and 0.31 cm^3 g^{-1} respectively. The TiO_2 film with abundant pores and high specific surface area may display enhanced performance in dye-sensitized solar cells, photocatalysts for water treatment, gas sensors, and battery applications.[52]

In another work by MacLachlan and coworkers, chiral nematic mesoporous carbon films were prepared using CNCs as templates through a two-step approach. First, CNC/SiO_2 mixture was prepared using the same protocol mentioned above, dried, and pyrolyzed at a temperature of 900 °C under N_2. Afterwards, silica-carbon films were immersed into 2 M NaOH and heated at 90 °C for 4 hours to remove silica. Mesoporous carbon films obtained from CNC/SiO_2 with 65 wt% CNCs showed the highest Brunauer–Emmett–Teller (BET) surface area of 1460 m^2 g^{-1}, total pore volume of 1.22 cm^3 g^{-1}, and a conductivity of 1.3×10^{-2} S cm^{-1} at 25 °C. Moreover, a symmetrical capacitor was made using the mesoporous carbon films with 1 M H_2SO_4 as the electrolyte, triangular galvanostatic charge/discharge profile was obtained, and the specific capacitance was calculated to be 170 F g^{-1} at a current load of 230 mA g^{-1}.[53]

The self-assembled CNC films with attractive optical properties are believed to have promising applications in security papers, tunable reflective filters, and sensors. Mesoporous inorganic materials with photonic crystal properties may be applied in tunable mirrorless lasers. Mesoporous carbon films with high specific area may find applications in catalyst supports, energy-storage devices and adsorption media. However, the fundamental issues regarding helical self-assembly need to be further studied as suggested by Lagerwall.[54]

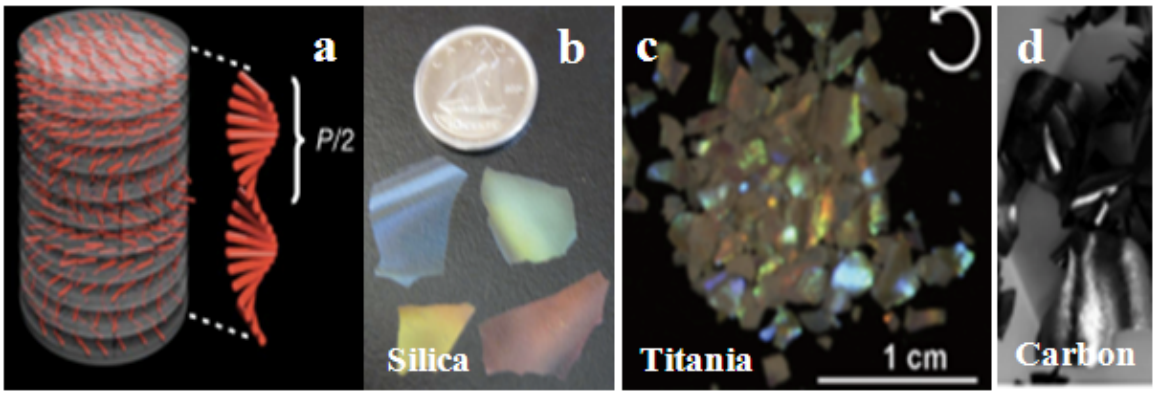

Figure 2.5. Schematic representation the chiral nematic ordering of CNCs (a),[20] and photographs of mesoporous silica (b),[20] mesoporous titania (c),[52] and mesoporous carbon (d)[53] obtained using CNCs as templates.

2.4.5 Pickering emulsifiers

Compared with traditional surfactant stabilized emulsions, Pickering emulsions stabilized by solid colloidal particles have attracted increasing attention due to their advantages in terms of lower toxicity with reduced or no surfactants, better stability with irreversible adsorption, and more controllable viscosity by changing the type or content of the solids. These attractive features have led to promising applications in food industries, pharmaceuticals, and cosmetics.[55] While a wide range of materials can serve as Pickering emulsifiers, CNCs as sustainable and biocompatible nanoparticles can be beneficial in food, pharmaceutical and cosmetics industries..

Both pristine CNCs and functionalized CNCs with uniform rod-shaped nanostructure have been applied to stabilize emulsions. Capron and coworkers reported the stabilization of Pickering emulsions using bacterial CNCs produced from nata de coco through hydrochloric acid hydrolysis (Figure 2.6). Oil in water emulsions with an oil/water ratio of 30/70 was prepared by mixing hexadecane and bacterial CNCs aqueous suspension under sonication. Various concentrations from 0 to 5 g L^{-1} of bacterial CNCs were used to evaluate the capability of bacterial CNCs to stabilize the emulsion. The emulsions with droplet size of around 4 μm showed excellent resistance towards deformation and coalescence even under centrifugation when concentrations of bacterial CNCs were above 2 g L^{-1}. TEM images confirmed the coverage of bacterial cellulose nanocrystals on polystyrene droplets, where bacterial CNCs bent along the bead surface and formed long fibers.[56] The size effect of CNCs on oil in water emulsion stabilization was further investigated by the same group. CNCs

with lengths in the range of 185 nm to 4 μm and aspect ratios ranging from 13 to 160 were prepared through the hydrolysis of cellulose microfibrils. Stable emulsions with similar droplet sizes were obtained using these CNCs in diluted conditions, indicating similar wetting properties and nanocrystal flexibility. However, the length of CNCs greatly impacted the coverage ratios. CNCs with short lengths allowed dense coverage of above 80%, CNCs with long length caused loose coverage and interconnections among droplets.[57]

Another interesting field is to functionalize CNCs with polymers for stimuli responsive Pickering emulsions. Tam and coworkers reported the grafting of poly[2-(dimethylamino)ethyl methacrylate] (PDMAEMA) on CNC surface through free radical polymerization for pH and thermally responsive Pickering emulsions. The PDMAEMA-grafted CNCs displayed reduced surface tensions, compared to CNCs. Oil (i.e. heptane or toluene) in water emulsion with a ratio of 1:4 with pH above 7 showed long-term stability over 4 months. When the pH value was reduced to 3, the emulsion was destabilized, and a stable emulsion could be recovered by raising the pH to 11. In addition, a stable emulsion at pH 11 would destabilize and lead to phase separation when heated at 50 ^{o}C for 5 min. This pH-triggered and thermal-controlled reversible phenomenon would find applications in switchable Pickering emulsion polymerization, fuel production, and oil transport.[58]

More recently, Cranston and coworkers reported the dried and redispersible Pickering emulsions using the combination of CNCs, methylcellulose, and tannic acid (TA). While CNCs could serve as stabilizes for corn oil in water Pickering emulsion, the emulsion broke upon freeze-drying. The mixture of CNCs and methylcellulose could prevent oil-leakage during the freeze-drying process. However, the freeze-dried samples could not be redispersed with the addition of water due to the formation of droplet coalescence. With the addition of tannic acid, complexation between CNCs/methylcellulose and TA occurred, and a dense and insoluble shell around the oil droplets formed. The shell separated oil droplets during the freeze-drying process and assisted the redispersion with the addition of water, and no significant change of the droplet size was observed. The redispersion of the freeze-dried Pickering emulsions with an oil content up to 94%, and the simple procedure without chemical reactions involved could lead to applications of the reported Pickering emulsions in food, cosmetic, and pharmaceutical industries.[59]

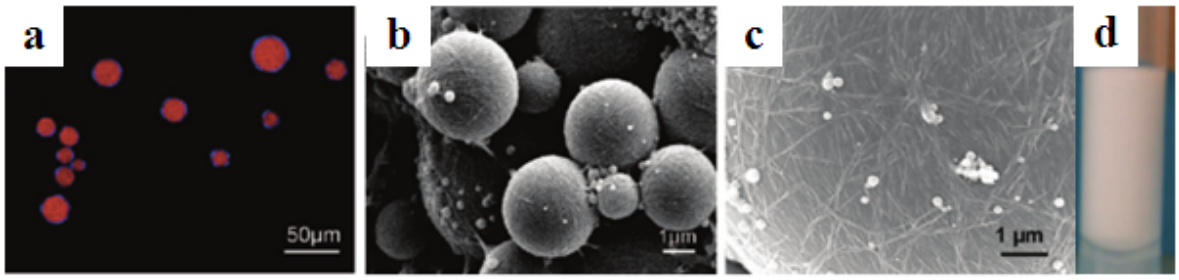

Figure 2.6. Confocal laser scanning micrograph of hexadecane/aqueous droplets stabilized by bacterial cellulose nanofibers (a), scanning electron micrographs of styrene emulsion stabilized by bacterial cellulose nanofibers (b and c), and a digital image of hexadecane/aqueous emulsion stabilized by bacterial cellulose nanofibers (d).[56]

2.4.6 Water treatment

With high specific surface area and abundant negative charge from sulphate ester groups, CNCs are believed to be good dye adsorbents. Tam and coworkers reported the removal of cationic dye - methylene blue using CNCs and carboxylated CNCs as adsorbents, respectively. The adsorption process was exothermically favorable, and a maximum capacity of 118 mg g^{-1} by CNCs was achieved at pH 9. The performance of CNCs is superior to traditional adsorbents such as rice husk kaolin, orange peel, and fly ash. A dramatically increased adsorption capacity of 769 mg g^{-1} was observed using carboxylate CNCs as adsorbents with a COOH concentration of 2.1 mmol g^{-1}. This high adsorption capability is comparable to activated carbons.[60]

While CNC suspension can be directly used to adsorb positively charged dyes, the separation of adsorbents from purified water is usually attained through centrifugation, a process which is both energy intensive and time consuming. To address these challenges, CNC-based films or hydrogel beads were prepared and used to simplify the adsorption/separation process. Mathew and coworkers reported the fabrication of nanoporous membranes using mainly CNCs and chitosan. Chitosan with a concentration of 1 wt% in acetic acid was mixed with CNCs to achieve a final CNC/chitosan ratio of 9/1, and then the mixture was freeze-dried and compacted to form membranes. Afterwards, these membranes were exposed to gluteraldehyde vapours and stabilized through cross-linking. SEM images confirmed the uniform dispersion of CNCs in the chitosan matrices, and BET measurements indicated a surface area of 2.9 m^2 g^{-1} for membranes with an average pore size of 13 nm. These membranes were applied to treat three types of positively charged dyes, and high dye-removal efficiencies of Victoria Blue 2B (98%), Methyl Violet 2B (90%) and Rhodamine 6G (78%) were

achieved with a dye concentration of 1 mg L^{-1}. It was believed that freeze-drying process benefited the formation of individualized CNCs in chitosan matrixes, and that hydrogen bonding and electrostatic interactions were the two driving forces for dye removal.[61]

Another recently published work by Tam and coworkers reported the preparation of CNC-alginate hydrogel beads using $CaCl_2$ as a gelation media. These beads were further loaded in a fixed-bed column to evaluate their adsorption capacity under continuous flow of methylene blue wastewater. The impact of dye concentration, bed depth, column size, dye flow rate, and flow direction was also investigated, and the maximum adsorption capacity towards methylene blue was found to be 255.5 mg g^{-1}.[62]

2.4.7 Other applications

CNC-based composites have been increasingly studied recently. Particularly, the functionalization of CNCs through organic reactions and inorganic nanoparticles immobilization has expanded CNC applications in various fields. Cellulose nanocrystal/inorganic nanoparticle or nanofibril/inorganic nanoparticle composites will be reviewed in detail in the section 2.5.

2.5 Inorganic particles

Materials with a size in the range of 1-100 nm possess properties quite different from those of the bulk. Particularly, many inorganic nanoparticles show attractive magnetic, catalytic and optical properties. Magnetic nanoparticles play an important role in data storage, magnetic resonance imaging contrast agents, magnetic ferrofluids for hyperthermia, targeted drug delivery, and magnetically assisted separation.[63] Noble metal nanoparticles have aroused great interest due to their important roles as catalysts, biomarkers, analytical tools, diagnostics, and therapeutic agents.[64,65] Quantum dots (QDs) show superior optical properties to organic dyes, such as size-tunable absorption and emission, unique flexibilities in excitation and high fluorescence quantum yields. These optical properties would benefit detection and imaging in the life sciences.[66] Further, QDs show promising applications in catalysis and photovoltaic devices.[67] The study on the facile synthesis, stabilization, and regeneration of these inorganic nanoparticles is of great importance.[68] Numerous methods have been developed for the liquid synthesis of inorganic nanoparticles including coprecipitation, sol-gel processing, microemulsion synthesis, and hydrothermal/solvothermal processing.[69] Among these methods, sol-gel processing, microemulsion synthesis, and solvothermal processing involve the use of organic solvents, and hydrothermal/solvothermal processing are usually carried out at high

temperature. While all these methods are extensively applied in achieving various goals (e.g. monodispersity, high crystallinity, shape control, biocompatibility, etc.), coprecipitation has generated a great deal of interest in terms of ease of operation, energy saving process, and green synthesis. Therefore, we focus on the synthesis and size control of inorganic nanoparticles using coprecipitation.

2.5.1 Coprecipitation

Coprecipitation of soluble metal ions from aqueous solutions and subsequent thermal decomposition of these products are among the easiest ways to achieve inorganic nanoparticles. Coprecipitation through chemical reactions is by far the most common method to produce inorganic nanoparticles. During these chemical reductions, several reactions including nucleation, growth, coarsening, and/or agglomeration occur simultaneously. It is difficult to isolate and study each process, which in turn have prevented the in-depth study of these mechanisms. Generally, coprecipitation products with low solubility are formed under supersaturation conditions. Under these conditions, nucleation, Ostwald ripening and aggregation dramatically affect the size, morphology, and properties of the products. Therefore, reaction conditions, such as rate of reactant introduction, stirring speed, and temperature highly influence the size and morphology of inorganic nanoparticles.

Nucleation is greatly influenced by the degree of supersaturation, which is determined by the activities of solutes and solubility product constants. As for the growth process, the majority of coprecipitation reactions are diffusion-limited, where concentration gradients and temperature are key factors in the growth rate. Meanwhile, some growth processes are reported to be reaction-controlled. Ostwald ripening or coarsening is a phenomenon where larger nanoparticles consume smaller ones during growth process. This behavior is caused by the difference in the solubility of nanoparticles. Specifically, the solubility of nanoparticles decreases with increasing particle size. Finally, due to the low solubility of inorganic nanoparticles, aggregation and agglomeration can occur at any step and is inevitable without the existence of stabilizers.[70] To stabilize inorganic nanoparticles produced through coprecipitation reactions, many organic chemicals (e.g. surfactants, polyelectrolytes, amphiphilic polymers, etc.) have been applied to either introduce steric stabilization or electrostatic repulsion.

2.5.2 Synthesis of metal nanoparticles from aqueous solutions

The synthesis of metal nanoparticles by coprecipitation is carried out through the reduction of metal cations, which is illustrated below:

$$M^{n+} + ne^- \longrightarrow M^0 \quad (2)$$

The reducing agents X will go through a corresponding oxidation process as shown below:

$$X^m - ne^- \longrightarrow X^{m-n} \quad (3)$$

The most widely used reducing agents include borohydride ions (BH_4^-), hydrazine hydrate ($N_2H_4 \bullet H_2O$), hydrazine dihydrochloride ($N_2H_4 \bullet 2HCl$), trisodium citrate, ascorbic acid, and H_2. To demonstrate the feasibility of the oxidation-reduction process, here we use borohydride ions as an example. The electrochemical half-reaction for borohydride ions is shown below with standard electrode potential $E°$ of -0.481 V at standard temperature (25 °C) and pressure (100 kPa).

$$B(OH)_3 + 7H^+ + 8e^- \longleftrightarrow BH_4^- + 3H_2O \quad (4)$$

Therefore, any metal with $E°$ more positive than -0.481 V (reference electrode: standard hydrogen electrode) should be possibly reduced by borohydride ions under room temperature with favorable conditions. Particularly, noble metal cations Ag^+ and $AuCl_4^-$ with $E°$ 0.80 and 0.99 respectively can be easily reduced to Ag^0 and Au^0 by borohydride ions. Because of their high $E°$, other weaker reducing agents (e.g. alcohols, ascorbic acid, trisodium citrate) will also work in the synthesis of gold or silver nanoparticles.[71,72]

2.5.3 Synthesis of metal oxide nanoparticles from aqueous solutions

Coprecipitation reactions are also applied in the synthesis of metal oxides or precursors of metal oxides. In some cases, following calcination, annealing or decomposition of hydroxide, carbonate, bicarbonate, or oxalate coprecipitation products are necessary to produce metal oxides. However, these processes usually induce agglomeration when performed at high temperature.[69]

One attractive feature of coprecipitation is to synthesize spinel-structured metal oxides (e.g. Fe_3O_4, $CoFe_2O_4$, $MnFe_2O_4$, etc.) directly at low temperature.[73,74] For example, Fe_3O_4 nanoparticles can be easily synthesized by coprecipitation of an aqueous mixture of Fe^{3+} and Fe^{2+} at a molar ratio of 2:1 by sodium hydroxide or ammonia. The experiment must be conducted in an oxygen-free environment, otherwise the Fe_3O_4 will be oxidized to form $Fe(OH)_3$.[74] Many other factors such as salt, pH, ionic strength, and stirring speed may strongly affect the size and shape of products. As an added precaution, organic or inorganic molecules are usually introduced and coated onto Fe_3O_4 nanoparticle surface to reduce or avoid aggregation.[75]

2.5.4 Synthesis of chalcogenide nanoparticles form aqueous solutions

Chalcogenide nanoparticles are attractive due to the application prospects of quantum dots. The band gap of quantum dots (QDs) is related to their size, specifically, the larger the size, the smaller the band gap. As the band gap determines the optical property of QDs, it is of great importance to control both the size and size distribution during the synthetic process. Significant effort has also been made to prepare monodispersed QDs, and the monodispersity is essential to investigate physical, catalytic or optical properties of QDs. One common method to achieve monodispersed QDs with controllable size is to use metal- and chalcogen-containing covalent compounds (e.g. $Cd(CH_3)_2$ and $[(CH_3)_3Si]_2S$) and organic coordinating solvents (e.g. trioctylphosphine and trioctylphosphine oxide) as the reaction media. These experiments were performed at high temperature (above 200 °C). During the synthesis, the energy barrier created between these organic chalcogenides and metal-covalent chemicals allows the temporal separation of nucleation and crystal growth, which favors the control of the particle size. Meanwhile, these organic coordinating molecules also serve as passivating agents and stabilizers, therefore, monodispersed QDs are obtained. As good dispersions of QDs in aqueous media are required for applications in bioimaging, QDs produced from these methods need to be transferred from organic solvents to water, which can be tedious and problematic.[76,77]

Fortunately, direct aqueous synthesis of QDs (e.g. CdS,[78] CdTe,[79] CdSe,[80] HgTe,[81] and ZnSe[82]) in the presence of stabilizers has been reported. During the synthetic process, instantaneous precipitation occurs when the metal ions mix with chalcogenide ions, but agglomerates with irregular shapes appear. Nevertheless, the particle size can be adjusted using various types of stabilizers, and monodispersity and high quantum efficiency are also achievable through the careful control over the quantity of stabilizers and molar ratios. Other ways including reverse micelle synthesis and in-situ deposition on solid templates are also applied to avoid aggregation.

2.5.5 Aggregation and stability of inorganic nanoparticles

One challenge of synthesizing inorganic nanoparticles is their tendency to form large aggregates instead of well-dispersed nanoparticles due to their high surface energy. Attractive forces (i.e. van der Waals force, hydrogen bonds) can cause inorganic nanoparticles to aggregate.[83] To solve this problem, numerous methods on the protection and passivation of their surfaces have been developed, with some commonly applied approaches including protection from thiols, polymeric matrices, surfactants, polyelectrolytes, etc. Mostly, the aqueous synthesis of inorganic nanoparticles involves various stabilizers, which help to control the nucleation, growth rate, and particle shape. Generally,

these ligand molecules with metal affinity groups are bound to the inorganic nanoparticle surface, introducing repulsive forces (e.g. electrostatic repulsion, steric exclusion, a hydration layer) to stabilize the inorganic nanoparticles. The dispersibility of these inorganic nanoparticles can be largely determined by the solubility of these stabilizers in various solvents. However, many stabilizers undergo dynamic binding and unbinding processes, and the stability they provide for the inorganic nanoparticles may not be strong under changes in their environment. In addition, some ligand molecules suffer from degradation, photolysis or oxidation over time and fail to provide long-term stability. Moreover, pH and salt concentrations may largely affect the charge on the inorganic nanoparticle surface and cause particles to aggregate.[84]

Another simple way to deal with the aggregation problem is to attach or deposit these nanoparticles onto substrates or templates with high surface area. Particularly, the development of green synthesis procedures using environmentally benign solvents accompanied by renewable biostabilizers or biotemplates is attracting increasing interests. It is also believed that abundant carboxylic or sulphonic acid groups can offer longer stability for inorganic nanoparticles and better resistance towards high salt concentrations.[84] Therefore, our goal is to functionalize CNCs to introduce abundant charge and metal affinity groups to stabilize inorganic nanoparticles.

2.6 Cellulose nanofiber@inorganic particle nanocomposites

Cellulose nanofibril were found to be an effective nontoxic biosupport for the in-situ synthesis of inorganic nanoparticles attributing to the high oxygen density.[85] CNCs consisting of the same anhydroglucose units are considered to be promising biotemplates for loading functional inorganic nanoparticles. CNCs can be produced at the industrial scale by acid hydrolysis of pulp fibers. They are attracting increasing interest due to their uniform nanorod shape, good mechanical strength, liquid crystalline character, high specific surface area, biocompatibility, biodegradability, and sustainability. In addition, CNCs that have been functionalized via reactions with abundant primary hydroxyl groups have been applied as efficient adsorbents for water treatment,[86] reinforcing nanofillers within polymers composites,[87] templates for synthesizing chiral nematic mesoporous materials[88] and supporting materials for loading noble metal nanoparticles.[89] Particularly, CNCs acting as natural rigid biotemplates for the loading inorganic nanoparticles are attractive because of their regular nanoscale structure, good colloidal stability in aqueous phase and high surface area. Notebly, “cellulose nanofiber” is used to represent both cellulose nanofibril and cellulose nanocrystal in this chapter.

2.6.1 Cellulose nanofiber@gold nanoparticles

Au nanoparticles (Au NPs) with desirable sizes are synthesized by reduction of Au(III) derivatives, and two most widely applied reducing agents are trisodium citrate and sodium borohydride. To stabilize Au NPs, many chemicals including but not limited to thiols, carboxylate ligands, surfactants, polyelectrolytes have been developed and applied.[90] In addition, Au NPs have been deposited homogenously onto templates such as graphene sheets,[91] carbon nanotubes,[92] TiO_2[93] and silica spheres.[94] Recently, the green synthesis of Au NPs and development of biotemplate@Au nanohybrids have attracted increasing interests. For example, the use of polysaccharides was proven to be a promising reducing and stabilizing agents for Au NPs.[85]

One way of fabricating cellulose/Au NP composites is to use layer-by-layer deposition process, where polyelectrolytes are introduced and coated onto cellulose fibrils to enhance their interactions with Au NPs.[95] Later on, cellulose single nanofibers (CSNFs) with widths of 10-20 nm were prepared by TEMPO oxidation of cellulose fibrils. The oxidation converted the majority of the primary hydroxyl groups into carboxylate groups and introduced sufficient electrostatic repulsion to isolate the individual cellulose fibrils. Au NPs with a size less than 5 nm were deposited onto CSNFs via in-situ reduction of tetrachloroauric acid ($HAuCl_4$) by sodium borohydride ($NaBH_4$) (Figure 2.7a, Figure 2.7b). During the process, the carboxylate groups served as both stabilizers and synthetic sites for Au NPs. Compared with other polymer/Au NP systems, the exposure of Au NPs on the surface of CSNFs greatly increased the accessibility to the reactants and dramatically enhanced the catalytic property.[96] In another work by Qi and co-workers, bacterial cellulose nanofibers were first mixed with poly(ethyleneimine) (PEI). The reduction of $HAuCl_4$ was conducted in situ, with PEI serving as both the reducing and linking agents (Figure 2.7 c). After the immobilization of horseradish peroxidase, the cellulose nanofiber/Au NP composites served as an excellent H_2O_2 biosensor with a detection limit < 1 μM.[97]

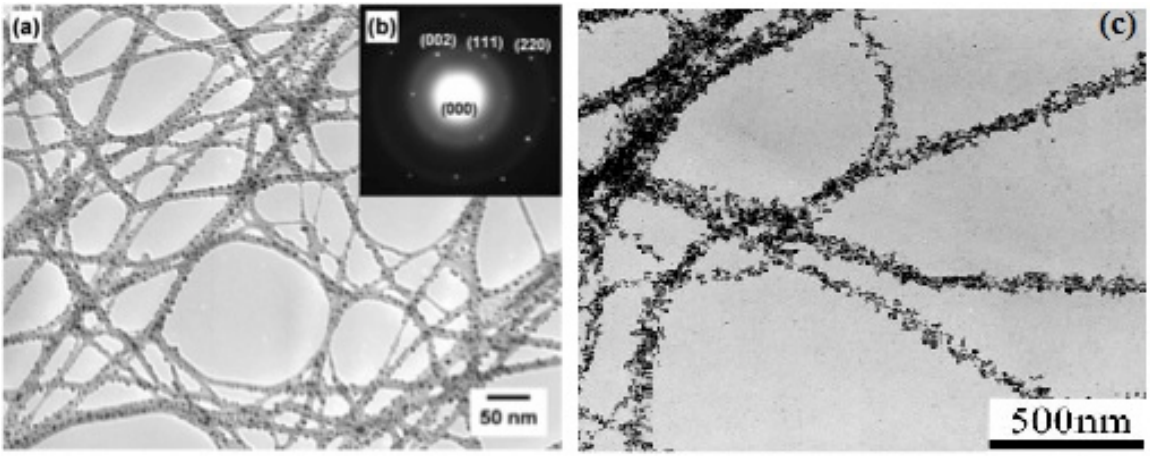

Figure 2.7. TEM image (a) and selected area electron diffraction pattern (b) of CNC@Au NPs;[96] TEM image of bacteria cellulose nanofiber@Au NPs synthesized with the presence of PEI (c).[97]

Later on, carboxylated CNCs were synthesized via a one-step procedure in the presence of ammonium persulphate and served as templates for loading Au NPs. The composite referred to as CNC@PDDA@Au was prepared through three steps: (i) the synthesis of carbonate-stabilized Au NPs; (ii) the coating of poly(diallyldimethyl ammonium chloride) (PDDA) onto CNCs; (iii) the deposition of carbonate-stabilized Au NPs onto PDDA-coated CNCs. In this work, positively charged PDDA attracted negatively charged reactants on the surface of Au NPs and enhanced the catalytic efficiency of Au NPs towards the reduction of 4-nitrophenol to 4-aminophenol. However, the introduction of PDDA caused the formation of CNC aggregates and bundles due to long-range electrostatic interactions (Figure 2.8).[98,99] Phase separation and the formation of large aggregates were also observed when CNCs were employed to stabilize gold-silver alloy NPs. Although the size and aggregation of Au-Ag NPs were well-controlled, the CNCs tended to agglomerate, which would reduce the accessibility to reactants and limit their applications in nanoscale devices (Figure 2.9).[100] Finally, besides CNC/Au NP composites' application as catalysts, they also served as excellent supports for immobilizing enzymes.[101]

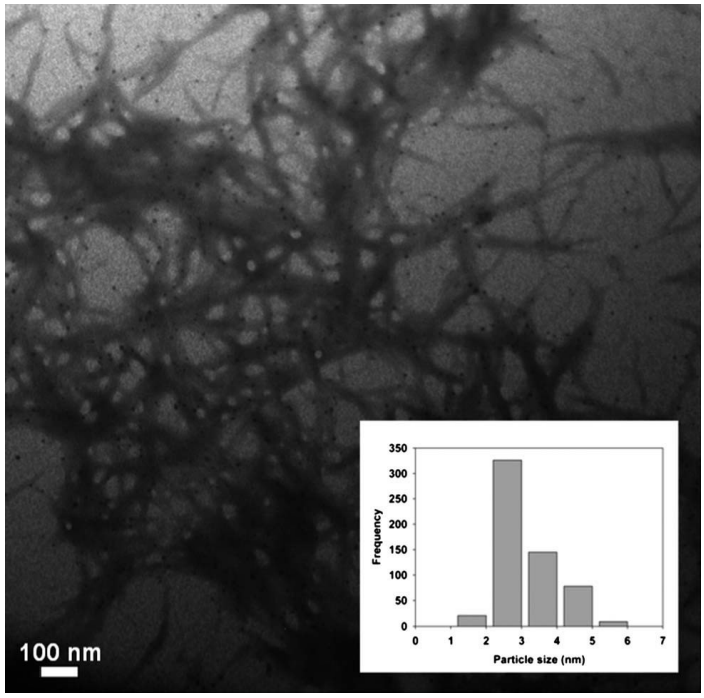

Figure 2.8. TEM image of CNC@PDDA@Au and particle size histogram.[99]

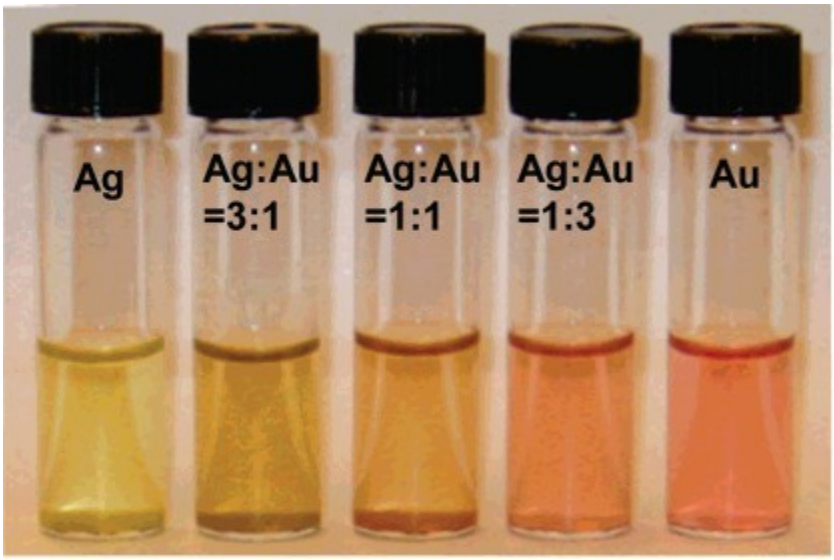

Figure 2.9. Photographs of Au-Ag alloy NPs with various molar ratios on CNCs.[100]

2.6.2 Cellulose nanofiber@silver nanoparticles

Bacterial cellulose/Ag NPs were prepared via an in situ synthesis and were employed as antimicrobial wound dressing due to the moist environment the cellulose provided and the antimicrobial activity

from Ag NPs. This work also demonstrated that a high $NaBH_4$:$AgNO_3$ ratio resulted in small Ag NPs and narrow size distribution.[102] Instead of using $NaBH_4$ as the reducing agent, carboxylated bacterial cellulose/Ag NPs was also synthesized through thermal reduction at a temperature of 100 °C within a short period of 1 hour under atmospheric conditions, the average size of Ag NPs was around 13.1 nm with the degree of dispersion 52.9% (Figure 2.10).[103] Carboxylated CNCs were also used for dispersing Ag NPs and Ag-Pd alloy NPs by in-situ reduction of $AgNO_3$ and $AgNO_3$/$PdCl_2$ using $NaBH_4$. The hydroxyl and carboxyl groups on CNCs prevented the NPs from aggregating. The carboxyl groups also enabled the conjugation of DNA through an amide bridge.[104,105] Carboxylated CNC/Ag NP composites were also used as nanofillers within waterborne polyurethane. The film exhibited enhanced mechanical properties and excellent antimicrobial performance against both *Gram-negative E. coli* and *Gram-positive S. aureus*.[87]

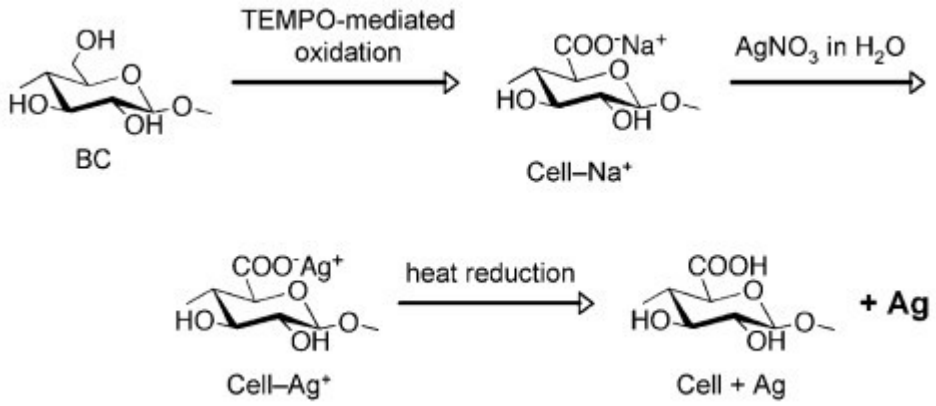

Figure 2.10. Thermal reduction of Ag^+ using bacterial cellulose nanofibers as reducing agents.[103]

In another work, CNCs were treated with $NaIO_4$ in order to introduce aldehyde groups, and Ag NPs were generated on the oxidized CNCs (reducing agent) through the reduction of $AgNO_3$ in 37% NH_4OH at 50 °C (Figure 2.11).[106] Well-dispersed Ag NPs were also prepared through hydrothermal synthesis at 100 °C using CNCs as both the reducing and stabilizing agent. The shape of Ag NPs changed from nanospheres to dendritic nanostructure when the concentration of $AgNO_3$ increased from 0.4 to 250 mM (Figure 2.12). The dendritic Ag NPs demonstrated improved antibacterial performance towards *Escherichia coli* and *Staphylococcus aureus* compared with Ag nanospheres.[107]

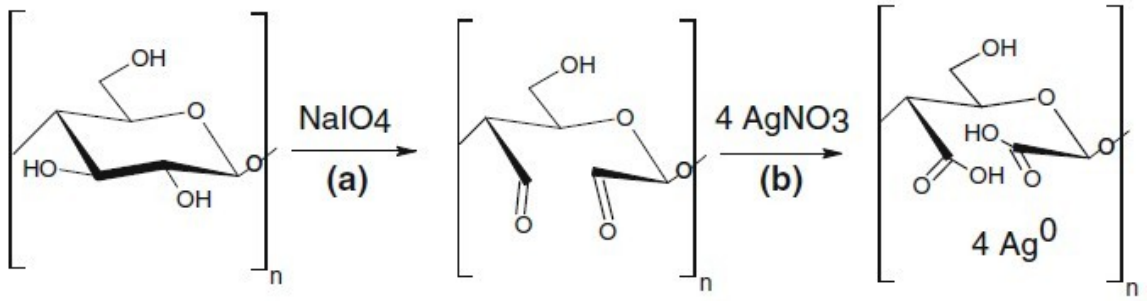

Figure 2.11. Periodate oxidation of CNCs (a) and reduction of $AgNO_3$.[106]

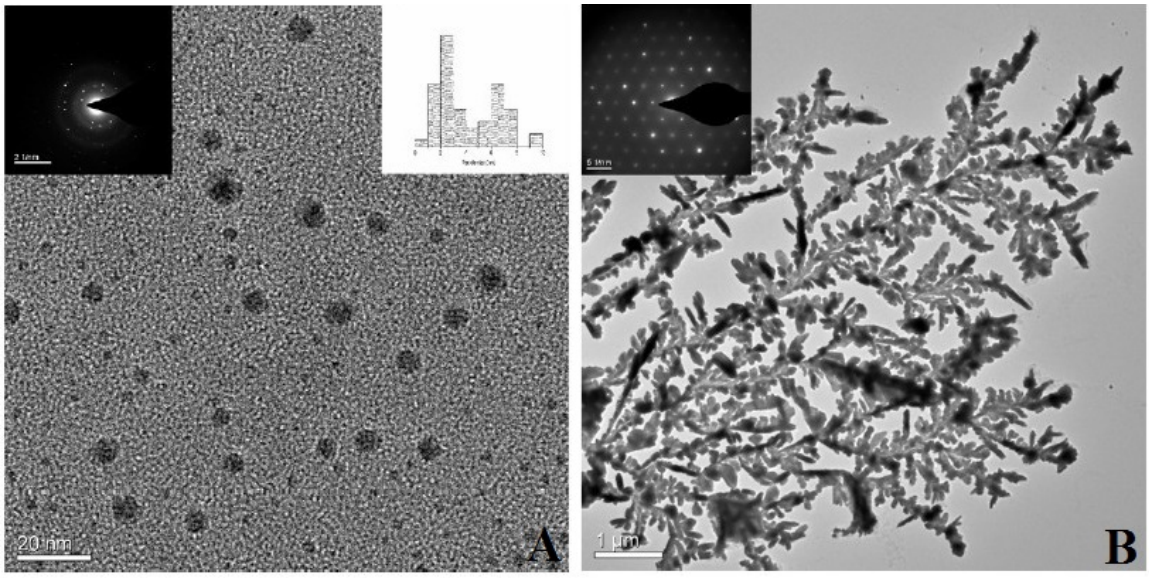

Figure 2.12. TEM images of Ag NPs prepared with 0.4 mM $AgNO_3$ (A) and 250 mM $AgNO_3$ (B).[107]

2.6.3 Cellulose nanofiber@platinum nanoparticles

The synthesis of cellulose nanofiber@Pt NPs has also been reported by several groups due to the promising applications of Pt NPs as catalysts. Carboxylated CNCs served as a reducing agent for H_2PtCl_6 to produce Pt NPs at a temperature of 80 °C for 24 h. The size of Pt NPs was insensitive to the reactant concentrations and was around ~ 2 nm in diameter.[108] In another work, cellulose nanowhisker/Pt NP nanocomposites were prepared with the assistance of supercritical carbon dioxide. The reduction of H_2PtCl_6 by cellulose nanowhiskers occurred only in the presence of supercritical carbon dioxide, and fast formation of Pt NPs in less than 1 min was observed at 80 °C and 100 bar.[109] This work demonstrated that cellulose nanofibers were effective reducing agents for H_2PtCl_6 under relatively high temperatures.

2.6.4 Cellulose nanofiber@palladium nanoparticles

CNC/Pd nanocomposites were prepared through two steps: the formation of CNC/$PdCl_2$ mixture and the reduction of Pd^{2+} under H_2 pressure (Figure 2.13). The Pd NPs were well dispersed on CNCs and limited aggregation of CNCs was observed. However, free Pd NPs possibly produced in the process leads to Pd loss. The product showed good catalytic performance for the hydrogenation of phenol and Heck coupling reaction.[110]

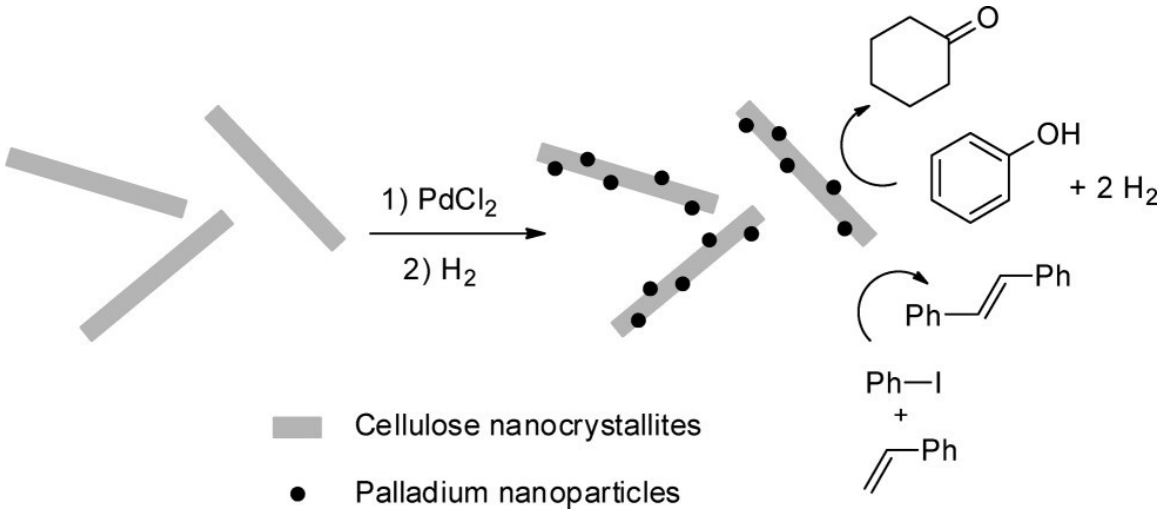

Figure 2.13. Synthesis of CNC@Pd and its roles as catalysts for hydrogenation of phenol and Heck coupling of styrene and iodobenzene.[110]

2.6.5 Cellulose nanofiber@selenium nanoparticles

Se NPs were also prepared and stabilized using CNCs as a reducing and structure-directing agent under hydrothermal synthesis at an optimal temperature range of 120-180 °C. The size of the Se NPs was controllable and increased from 10 nm at 120 °C to 20 nm at 160 °C. As for the stability of CNCs, the diffraction peaks of CNCs remained evident for the CNC@Se composite obtained at 160 °C, however, the formation of aggregates and deterioration of CNC morphology were observed.[111] Further study on developing controllable synthesis of CNC/Se hybrids under mild conditions is still necessary.

2.6.6 Cellulose nanofiber@magnetic nanoparticles

Magnetic nanomaterials have been widely used in separation processes, biomedicine and data storage. However, the formation of nanoparticle aggregates, especially at high concentrations, is a common problem due to magnetic dipolar forces. Previous work indicated that the incorporation of Fe_3O_4 NPs, $CoFe_2O_4$ NPs or Ni NPs into a cellulose matrix could largely reduce aggregation. Cellulose nanofibrils as green and renewable biotemplates were investigated for supporting magnetic nanoparticles. Non-agglomerated $CoFe_2O_4$ ferromagnetic NPs with a size of 40-120 nm were precipitated onto freeze-dried bacterial cellulose nanofibril aerogels (Figure 2.14). High inorganic content up to ~95% was achieved. The magnetic aerogel also showed excellent flexibility, lightweight and high porosity (up to 98%).[112]

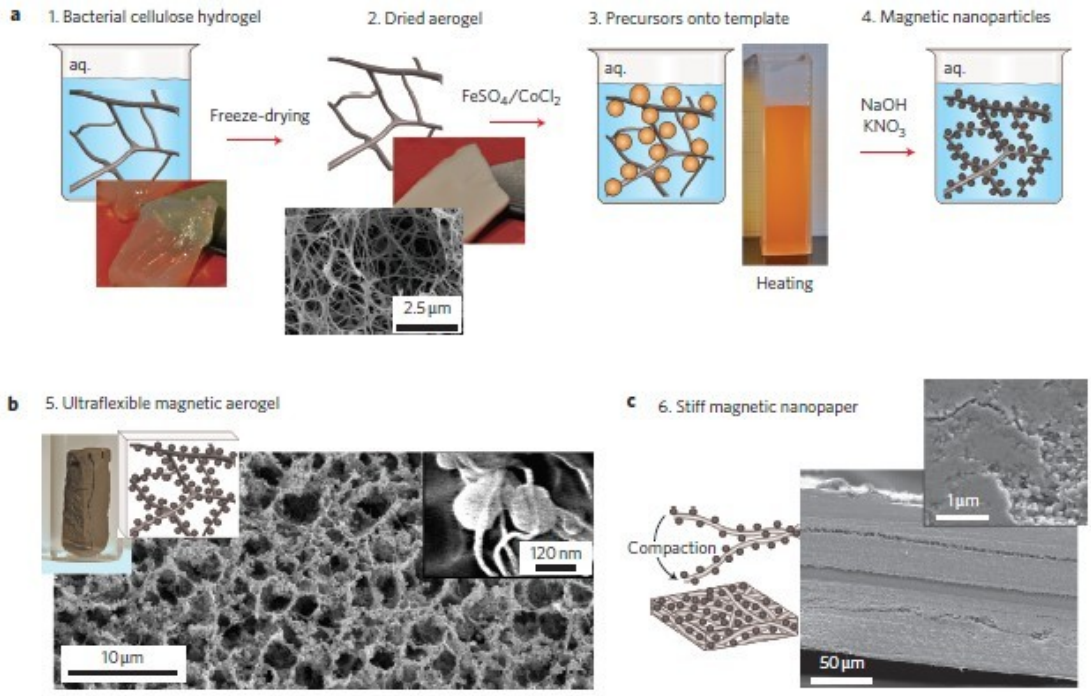

Figure 2.14. Schematic showing the preparation of a magnetic aerogel (a). SEM image of a 98% porous freeze-dried magnetic nanogel (b). SEM image of a dried magnetic paper made by stacking an aqueous magnetic hydrogel (c).[112]

Magnetic antimicrobial nanocomposites were also prepared by combining bacterial cellulose with both Fe_3O_4 NPs and Ag NPs. Fe_3O_4 NPs were first loaded onto bacterial cellulose through *in situ* precipitation, and then a polydopamine shell was coated onto cellulose/Fe_3O_4, and Ag NPs were

finally deposited onto the surface of polydopamine, taking advantage of the reducing capability of polydopamine. By introducing Fe_3O_4 NPs, the purification during synthesis and the recycling during the antimicrobial test were greatly simplified in the presence of an external magnetic field.[113]

Compared with cellulose nanofiber@magenetic NPs systems, limited study has been conducted on CNC/magnetic NP hybrids. This is due to the fact that well-dispersed CNC aqueous suspensions undergo phase separation once Fe^{2+}, Fe^{3+}, and other metal cations are introduced. The electrostatic interactions between sulphate ester groups and metal cations cause random, severe and irreversible aggregations of CNCs. This occurs even more when large quantities of metal cations are added to obtain high inorganic content. While this aggregation problem changes the nanoscale nature of CNCs and thus hinders the applications CNC/magnetic NP hybrids as nanodevices, this does not affect their applications in magnetic assisted separation processes.

CNC@Fe_3O_4 nanocomposites were obtained through in situ coprecipitation of Fe^{2+} and Fe^{3+} by ammonium hydroxide, and Au NPs were later embedded for the immobilization of papain. Although Fe_3O_4 NPs and Au NPs were well-dispersed on the CNC surface, the aggregation and crosslinking of CNCs occurred due to electrostatic attraction and caused the formation of a micron-sized network (Figure 2.15). Despite the aggregation, the nanocomposite showed a significantly high loading of papain.[114]

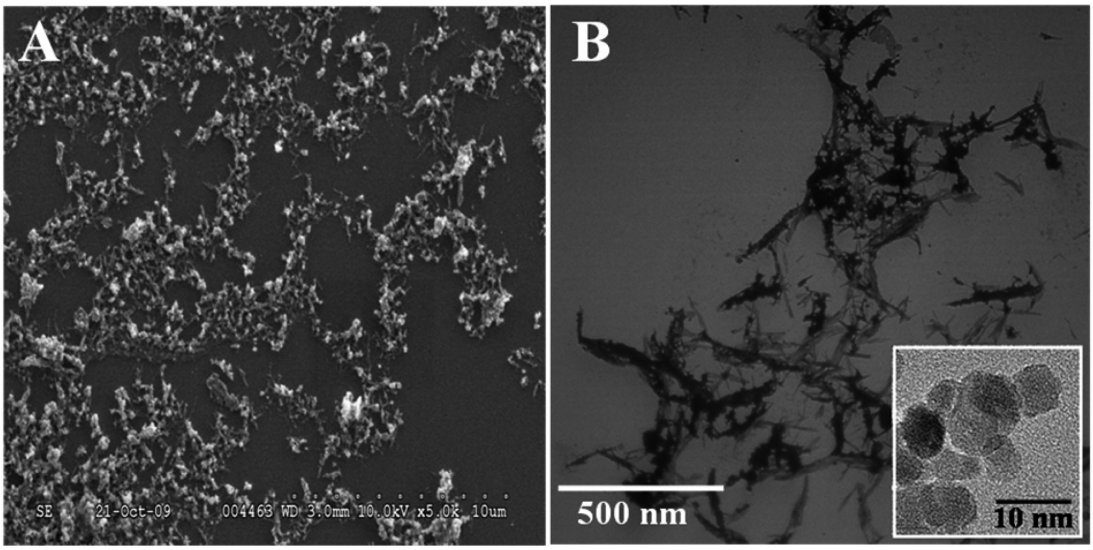

Figure 2.15. (A) SEM micrographs of CNC/Fe_3O_4 and (B) LVTEM image of CNC/Fe_3O_4/Au. Inset shows the HRTEM contrast and size difference between Au NPs (3−7 nm) and Fe_3O_4 NPs (10−20 nm).[114]

Finally, Ni NPs were deposited homogenously onto carbonized CNCs by in-situ reduction of Ni^{2+} under N_2 at a temperature above 400 °C. During the carbonization of CNCs, electrons were released and used for the reduction of Ni^{2+}. The proposed mechanism is shown in equation (5) and (6). This process can also be applied for the deposition and dispersion of other transition metal NPs on carbonized CNCs.[115]

$$[C_6H_{10}O_5]n \longrightarrow n[CO_2] + 5nC + nH^+ + ne^- \quad (5)$$

$$Ni^{2+} + 2e^- \longrightarrow Ni \quad (6)$$

2.6.7 Cellulose nanofiber@CdS quantum dots

CdS quantum dots (QDs) have attracted great interests due to their easy synthesis, excellent water photosplitting property, visible light induced photodegradation of dyes and adjustable optical properties. However, the applications are greatly limited due to the aggregation or precipitation of CdS NPs. Among abundant substrates, cellulose[116] and cellulose nanofibril[117] were found to be a promising biotemplate for the synthesis and stabilization of CdS QDs. Cellulose nanofibers@CdS nanocomposite films were usually prepared by in situ adsorption of Cd^{2+} and the following introduction of S^{2-}. In addition to good photocatalytic performance, the regeneration process was greatly simplified by depositing CdS QDs onto cellulose films.

2.7 Silica coating

2.7.1 Advantages of silica coating

Silica coating has been applied in various systems due to its simple processability, optical transparency, chemical inertness, excellent thermal stability, biocompatibility and synthetic versatility. Silica coating can assist in addressing some limitations of nanomaterials (e.g. ease of aggregation, low thermal stability, high chemical reactivity and toxicity) with no or little influence on the properties of the nanomaterials. Silica coating also shows a multitude of attractive features, such as good chemical robustness and chemical inertness, high optical transparency, well-developed surface modification, tunable mesoporous structure and biocompatibility. In addition, silica has no chemical reactions with most nanoparticles and shows no effect on their reactivity. Silica layers can also provide a chemically inert surface for nanoparticles and thus protects the nanoparticles inside silica shells.[118]

2.7.2 Silica coating by modified Stöber method

Silica coating by modified Stöber Method is a sol-gel process and was first used to synthesize silica spheres using ammonia as a catalyst for tetraethyl orthosilicate hydrolysis. Later on, the Stöber Method was modified to coat nanomaterials in order to obtain a core-shell structure. The modified Stöber Method can be divided into two steps: hydrolysis of metal alkoxides to produce hydroxyl groups and polycondensation of hydroxyl groups to form Si-O network. The general scheme is shown in Figure 2.16.[119]

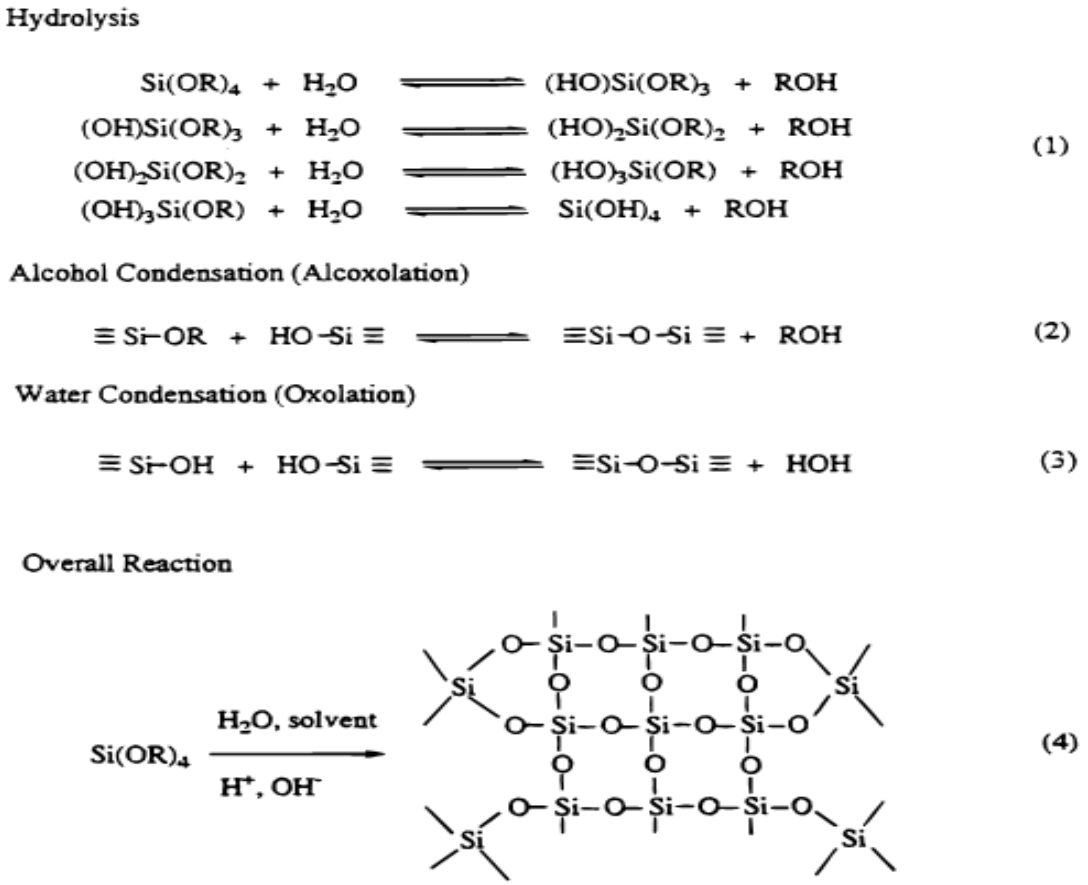

Figure 2.16. The general scheme of the sol-gel silica coating process.[119]

In practical experiments, silica coating by the modified Stöber Method is difficult to control due to the following reasons: (1) too many species exist in the reaction solution; (2) hydrolysis and polycondensation occur simultaneously; (3) too many factors affect the reaction rate; (4) the order of the polycondensation varies with time. However, it is well-known that H^+ increases the rate of hydrolysis, while OH^- increases the rate of condensation. Therefore, a linear structure is obtained

under acidic conditions; while highly crosslinked branched polymers are formed under basic conditions. Therefore, silica coating is usually conducted in basic conditions.[120] Due to these complexities, silica coating on nanomaterials can be influenced by several factors, such as solvents, water/alcohol volume ratio, the amount of catalysts, the amounts of precursor and reaction time. Optimum conditions for silica coating often vary from one system to another.[121,122]

Another challenge of silica coating is the adhesion of silica-coated nanocomposites with one another. This phenomenon, caused by the strong hydrogen bonding between the silica-coated nanoparticles and the covalent bonds formed during the sol-gel process, exists when the concentration of nanoparticles is high. Several ways to solve this problem are to: (i) introduce very low concentrated solution of nanoparticles; (ii) add positive or negative charges to increase electrostatic repulsion; (iii) apply water-in-oil microemulsion synthesis during which surfactants and organic solvents can help separate the nanoparticles. However, avoiding such adhesion using these methods will largely decrease productivity.

There are many surfaces that can be directly coated with silica without any treatment due to the strong affinity between these surfaces and silica, such as clay minerals, hematite, zirconia, titania, iron oxide, etc. However, the majority of surfaces can only be coated with silica after pretreatment with other chemicals (e.g. stabilizers, surfactants and silane coupling agents). Ligands are commonly used to minimize core-shell interfacial tension, which improves the coating process.[123] The most widely applied ligands are summarised in a recent review.[118] Among these ligands, polyvinylpyrrolidone (PVP) is considered to be a widely applicable ligand for silica coating on both inorganic and organic particles with different shapes and charges on their surfaces.[124]

2.7.3 Further modification and applications

In order to be used in various applications, further modification of the silica shell is necessary. Silane precursors with different functional groups (e.g. —SH, —NH_2, —Cl) can react with the silanol groups on the surface of silica shell to tailor the charge and functionality (Figure 2.17). In addition, due to high chemical reactivity of these functional groups, various functional groups can be further grafted on silica surface.[125,126]

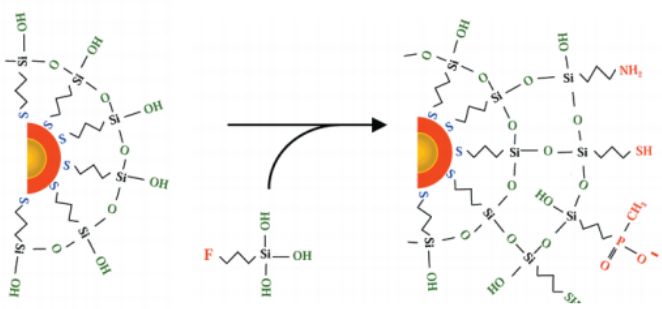

Figure 2.17. Silanization method for introduction of functional groups.[125]

Silica coated organic or inorganic materials have been applied in various fields due to favorable surface chemistry. Here, several examples are chosen to demonstrate the enhanced or improved applications of nanoparticles coated with a silica shell. It is well-known that CdSe QDs suffer from poor dispersibility, toxicity, and aggregation, which greatly limit their applications. Nevertheless, silica coated CdSe QDs demonstrate high luminescence, narrow size distribution, good photostability, low toxicity, and no aggregation, compared to organically coated QDs. These features allow the application of silica-coated QDs in bioimaging, drug delivery, and light-emitting devices.[125,127,128] Fe_3O_4@silica core–shell nanoporous particles were prepared and pH-sensitive amides were further modified on the silica surface. The hybrids obtained were used to load and release the anti-cancer drug doxorubicin at different pHs, which showed their potential applications in pH-triggered drug delivery.[129] Silica-coated nanoparticles are considered to be good systems for high-temperature reactions. Pt/SiO_2 showed high catalytic activity for ethylene hydrogenation and CO oxidation, and enabled the study of high-temperature CO oxidation.[130] In addition, silica coatings can protect NPs against aggregation and sintering. Because of these advantages, Pd nanoparticles captured inside a mesoporous silica shell served as efficient nanoreactors and showed high activity and stable performance towards Suzuki cross-coupling reactions.[131]

2.8 Cyclodextrins

2.8.1 Structure and physicochemical properties

Cyclodextrins (CDs) are cyclic oligosaccharides with 6-13 α-(1,4) linked glucopyranose subunits. The most well-known and widely studied CD are α-CD, β-CD and γ-CD with 6, 7 and 8 subunits respectively (Figure 2.18).[132] In CDs, secondary hydroxyl groups at C2 and C3 are situated at the edge of the secondary face and primary hydroxyl groups at C6 are located at the edge of primary face,

leading to hydrophilic exterior that enhances the solubility of CDs in water. The apolar C3, hydrogen at C5 and ether-like oxygen are located at the interior of the torus, resulting in a hydrophobic cavity and capability of encapsulating hydrophobic molecules. Notably, the diameter of the cavity on the secondary face side is larger than that on the primary face side, due to the decrease of the effective diameter resulting from the free rotation of primary hydroxyl groups at C6.[133]

α-CD, *β*-CD and *γ*-CD, as well as their derivatives, are produced in industry and commercially available. The characteristics of *α*-, *β*-, and *γ*-CDs are quite different from one another and are summarized in Table 2. 1. In the *β*-CD molecule, hydroxyl groups at C2 can form hydrogen bonds with these at C3, forming a complete rigid belt structure. The formation of intramolecular hydrogen bond is believed to be the cause of the low water solubility of *β*-CD. Compared with *β*-CD, *α*- and *γ*-CDs are much more soluble in water. In the *α*-CD molecule, one glucopyranose subunit is distorted, and an incomplete region of hydrogen bonds is formed. In the *γ*-CD molecule, the structure is flexible, thus *γ*-CD is the most soluble. Among these three CDs, *β*-CD is most widely used partly due to its lowest price.[134]

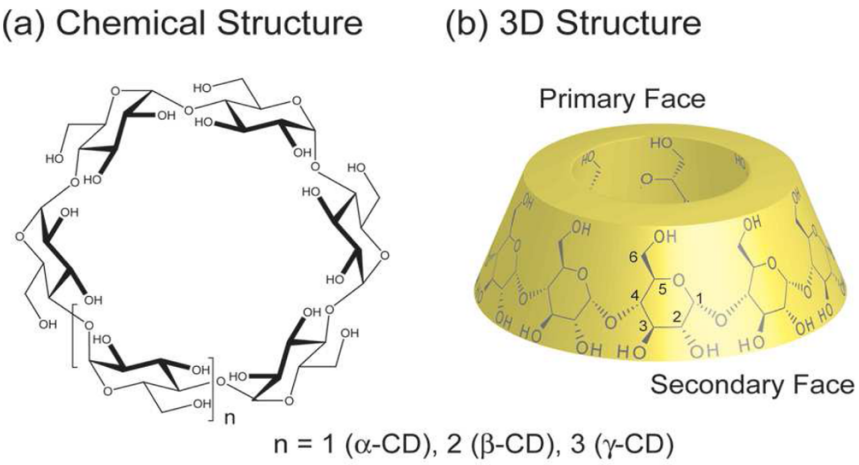

Figure 2.18. Structures of cyclodextrins (CDs).[132]

Table 2.1. Characteristics of α-, β-, and γ-CDs.[134]

Properties	α-CD	β-CD	γ-CD
Number of glucopyranose units	6	7	8
Molecular weight (g/mol)	972	1135	1297
Solubility in water at 25 °C (g/100 mL)	14.5	1.85	23.2
Cavity diameter (Å)	4.7-5.3	6.0-6.5	7.5-8.3
Outer diameter (Å)	14.6 ± 0.4	15.4 ± 0.4	17.5 ± 0.4
Height of torus (Å)	7.9 ± 0.1	7.9 ± 0.1	7.9 ± 0.1
Cavity volume (Å^3)	174	262	427

The most notable and attractive feature of CDs is their capability in hosting hydrophobic molecules within its cavity to form host-guest complexes through supermolecular chemistry. In an aqueous solution of CDs, water molecules occupy the apolar cavity of CDs, and energetically unfavorable polar-apolar interactions exist. With the introduction of less polar molecules, the water molecules within the cavity can be easily replaced (Figure 2.19). Most frequently, the host/guest ratio is 1:1, although more complicated complexes (e.g. host/guest ratio of 2:1, 1:2, 2:2) and higher order equilibria have also been reported. The formation of host-guest complex is a dynamic equilibrium, and a complex stability constant is often calculated to demonstrate the equilibrium. Take the 1:1 host/guest formation in Figure 2.19 as an example, the complex stability constant is defined to be [complex]/([CD][p-Xylene], where [complex], [CD] and [p-Xylene] are the concentrations of complex, CD and p-Xylene respectively.[134] The complexation process can be greatly affected by factors including solution dynamics, temperature, and solvents.

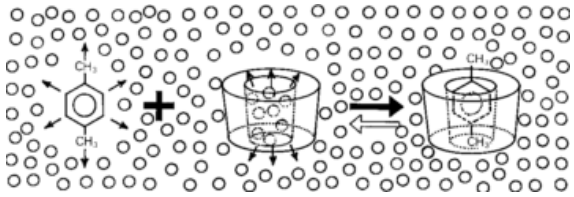

Figure 2.19. Schematic representation of the CD/ *p*-Xylene host/guest complex formation; water molecules are represented by small circles.[134]

2.8.2 Applications of *β*-CD

β-CD displays capability in hosting various molecules in its hydrophobic cavity. During the inclusion, the physicochemical property change of guest molecules (e.g. shift of UV spectra; shift or intensity change of fluorescence spectra; enhanced aqueous solubility; decreased volatility, sublimation and diffusion) is often observed. With these attractive features, *β*-CD molecules are widely used in pharmaceuticals, food, and cosmetics. In pharmaceuticals, many poorly soluble hydrophobic molecules can be entrapped in *β*-CD molecules, and an increased solubility of these drugs in aqueous phase can be achieved. *β*-CD molecules can also decrease the bitterness and malodours of drugs, and stabilize active compounds. In food industry, *β*-CD molecules are employed to protect flavor through complexation with volatile natural and artificial flavors. In cosmetics, *β*-CD molecules are mainly used in the volatility suppression and controlled release of fragrances.

Other attractive applications of *β*-CD in chemical sensors and environmental protection have also been explored. Ogoshi and Harada summarized the "turn-off" and "turn-on" fluorescent chemical sensors based on CD derivatives.[132] Recently, due to increasing concern on pharmaceutical residues in drinking water, *β*-CD has been applied in the encapsulation of hydrophobic drugs. Nagy and coworkers evaluated the efficiency of *β*-CD bead polymer as a sorbent in removal of pharmaceuticals, hormones, and industrial additives. Two model systems (i.e. filtration and fluidization), and different filter systems combining *β*-CD bead polymer with various sorbents (i.e. commercial filter and activated carbon) were applied and evaluated. Their results confirmed that *β*-CD bead polymer was essential in the effective and selective removal of bisphenol-A. *β*-CD bead polymer also showed high efficiency (> 85%) in the removal of estrogenic compounds including 17*β*-estradiol, ethinylestradiol, and estriol in fluidization experiment.[135] Záray and coworkers studied the application of *β*-CD polymer bead-containing nanofilters towards the removal of ibuprofen using total organic carbon analyzer. The adsorption capacity of *β*-CD polymer beads was 16.0 μmol/g, whereas a loss of adsorption capacity was observed for nanofilters where *β*-CD polymer beads embedded in ultrahigh molecular weight polyethylene. The highest adsorption capacity of 4.5 μmol/g was achieved with the lowest nanofilter thickness of 1.5 mm and a content of 40 wt. % *β*-CD polymer beads. In addition, the adsorption capacity of nanofilters was enhanced by using inorganic additives (e.g. NaCl, NH_4HCO_3), and the nnofilters can be generated with ethanol.[136]

In addition, *β*-CD molecules were also grafted onto inorganic nanoparticle surface and trapped in inorganic particles for adsorptive removal of drugs. Kurapati and Raichur prepared *β*-CD/$CaCO_3$

porous microparticles through the coprecipitation of Ca^{2+}- β-CD complex and CO_3^{2-}. With the addition of β-CD, the crystal growth of $CaCO_3$ was affected, porous structure was formed and β-CD molecules were trapped and distributed homogeneously in a $CaCO_3$ matrix. Afterwards, four PAH/PSS layers were coated onto the β-CD/$CaCO_3$ porous microparticle surface, and then $CaCO_3$ as sacrificial templates was dissolved by adding ethylenediaminetetraacetic acid. The as-prepared capsules with abundant β-CD in the interior showed efficient encapsulation of hydrophobic fluorescent dye and could serve as potential hydrophobic carriers.[137] Uddin and coworkers reported the preparation of β-CD grafted superparamagnetic nanoparticles for adsorptive removal of pharmaceutically active compounds (i.e. naproxen and carbamazepine) and endocrine disrupting compounds (i.e. bisphenol A) (Figure 2.20). The effect of pH values on the adsorption efficiency was studied, and neutral pharmaceuticals were more likely to be removed by forming β-CD/drug host/guest associations due to favourable hydrophobic interactions. Adsorption kinetics confirmed the fast formation of associations at the initial stage, and equilibrium adsorption occurred in the first 40 min for bisphenol A, 60 min for naproxen, and 120 min for carbamazepine. The difference in adsorption rate was possibly due to the different sizes of the three molecules. Further, the β-CD grafted superparamagnetic nanoparticles were regenerated using ethanol, where efficient desorption of the three drugs (> 75%) happened. The regenerated nanoparticles were reused for two more adsorption–desorption cycles, and no reduction in adsorption capacity towards the three drugs was found.[138]

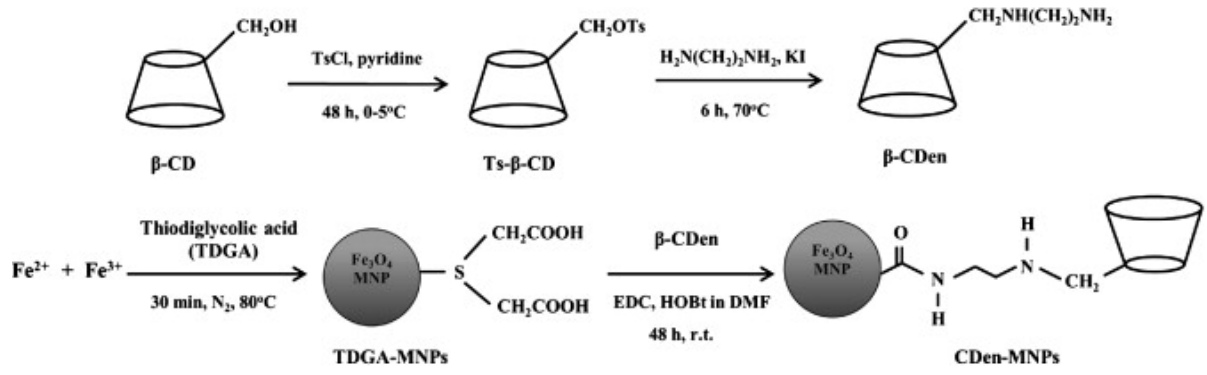

Figure 2.20. Schematic illustration of the preparation of the β-CD grafted superparamagnetic nanoparticles.[138]

2.9 Poly(amidoamine) (PAMAM) dendrimers

2.9.1 Structure and physicochemical properties

Dendritic structure is universally seen in biological systems. Trees with dendritic branches above ground and roots beneath ground are good examples (Figure 2.21).[139] Dendritic architecture also appears in human anatomy (e.g. lungs, liver) and in cerebral neurons. These ubiquitous dendritic patterns are believed to offer maximum interfaces and optimum performance advantages (e.g. energy extraction and distribution; information storage and retrieval).[140]

PAMAM dendrimers are the first synthesized, characterized and commercialized dendrimer family, and they are also the most extensively studied dendrimers. Two major strategies have been developed for dendrimer synthesis. One is the divergent method, where branches originate from a core site. The other one is the convergent method, where branches are synthesized first and then reacted with a core to form dendrimers (Figure 2.22). The divergent method has been used for synthesizing PAMAM dendrimers using an ethylenediamine core by researchers and industrial producers worldwide.[140]

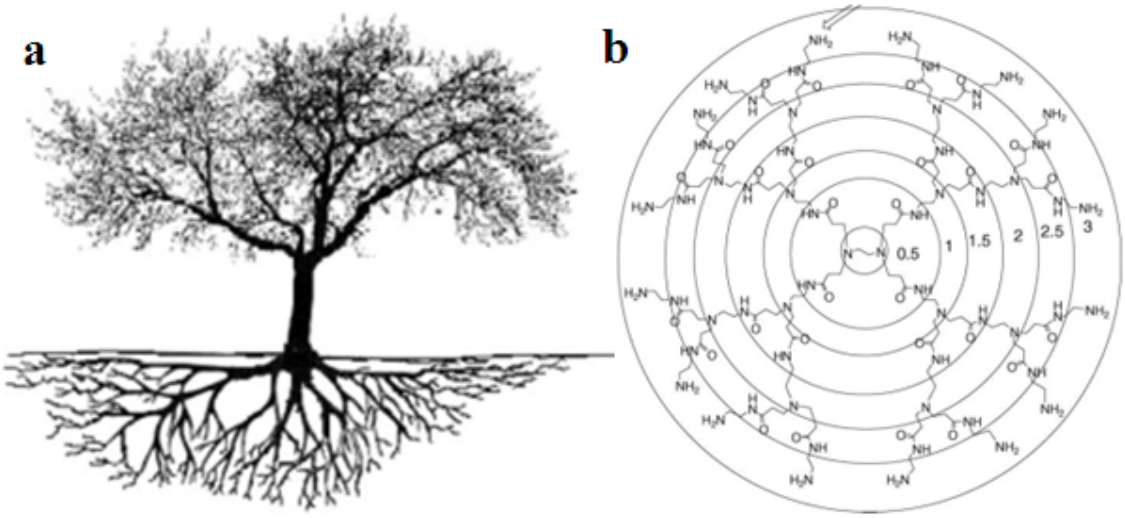

Figure 2.21. PAMAM dendrimers with generation of shell depiction.[139]

PAMAM dendrimers are a complete family. Generation (G) and end group are important terms or abbreviations in describing PAMAM dendrimers. The numbers in Figure 2.21 are PAMAM dendrimer generation numbers. End groups describe the surface groups or terminal groups. The end groups of half-generation PAMAM dendrimers (e.g. G0.5, G1.5, G2.5) are usually carboxylate groups, whereas these of full generation dendrimers are amine groups (Figure 2.21). Notably,

hydroxyl groups can also serve as terminal groups for PAMAM dendrimers. As an example, a 5th generation PAMAM dendrimer with hydroxyl groups as terminal groups is abbreviated to G5 hydroxyl-terminated PAMAM dendrimer or G5 PAMAM-OH.[139]

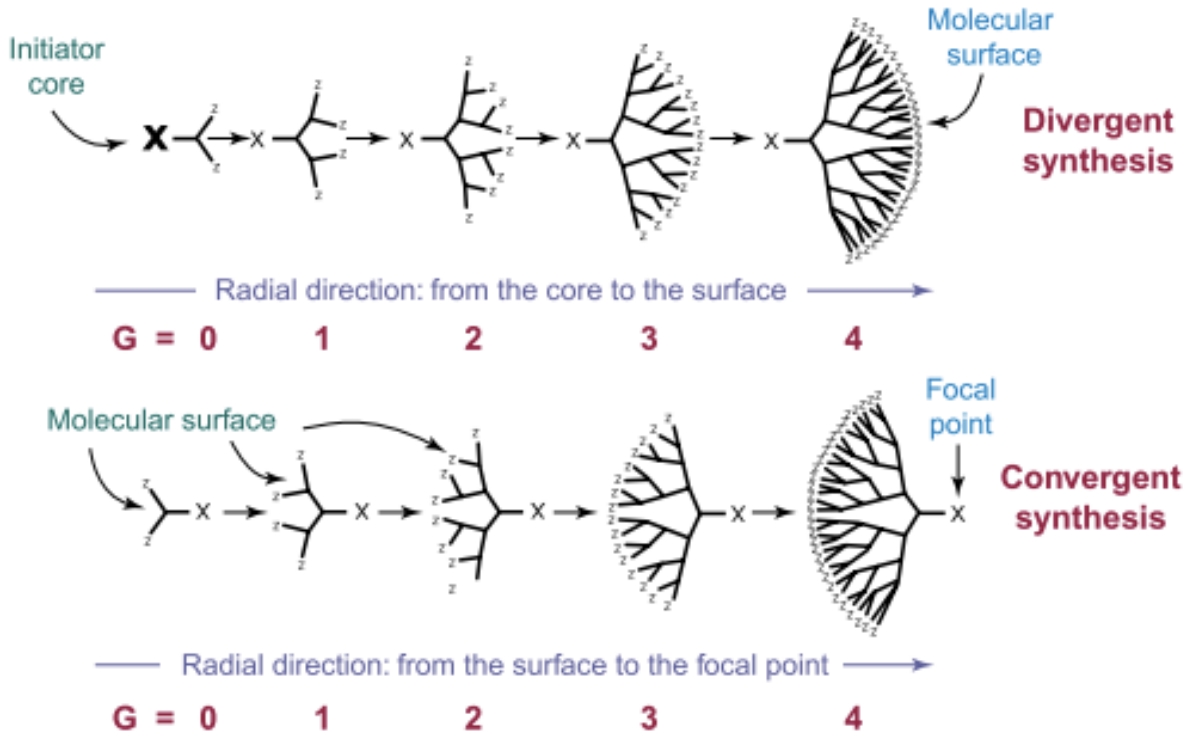

Figure 2.22. Divergent and convergent synthetic methods for constructing dendritic macromolecules.[140]

With a well-controlled synthetic process, the size, molecular weight, and structure of each generation PAMAM dendrimers are well defined. The diameter of PAMAM dendrimers increases linearly with the increase in generation, and the number of terminal groups increases exponentially from G0 to G10. Geometrically closed structures are formed due to congestion by abundant terminal groups on PAMAM dendrimers up to a certain high generation, while nanopores appear in the interior due to relatively low-density packing (Figure 2.23).[141] In addition, PAMAM dendrimers are often referred to as "artificial proteins" due to their mimicry of globular protein (i.e. dimensions and electrophoretic property), and as "'unimolecular micelles" due to similar topologies and surface groups.[140]

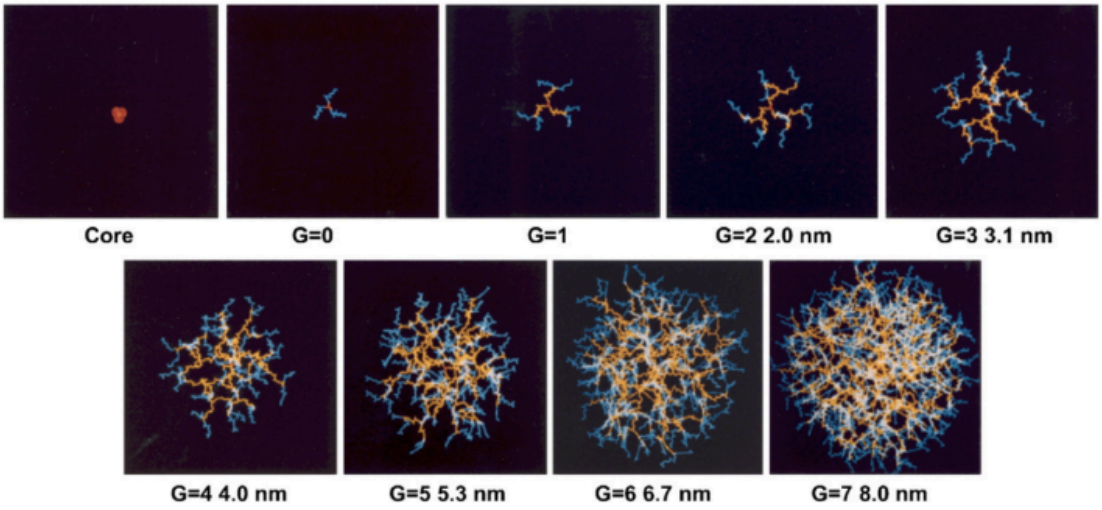

Figure 2.23. Graphical presentation of core and various full generation PAMAM dendrimers (G0-G7), showing the linear increase in diameter.[141]

2.9.1.1 Conformational change

Based on their chemical structure, high generation PAMAM dendrimers possess abundant tertiary amine groups in the interior, and functional groups on the surface. The protonation/deprotonation process of these two amino groups occurs at different pH ranges permitting one to tune their pH-responsive property. Baker and coworkers analyzed the structural variations of PAMAM dendrimers (G2-G6) under different pH values using molecular dynamics (MD) simulations without explicit water. The results showed that PAMAM dendrimers have globular and compact structure at pH ≥ 10, a bulky dense interior at neutral pH due to significant branch back-folding, and a highly ordered extended open structure at pH ≤ 4 with a hollow interior (Figure 2.24). Notably, the protonation of tertiary amine groups stops branch back-folding at pH ≤ 4, forming an open structure with protonated primary amine groups on the periphery of the dendrimer.[142] Goddard and coworkers investigated the conformational change of PAMAM dendrimers (G5-G6) using MD simulations under different pH values in explicit solvent. G5 PAMAM dendrimer underwent swelling by 33% in the presence of solvent, compared to the situation of no solvent, and its radius of gyration changed from 21 Å at pH 10 to 22 Å at pH 7 to 25 Å at pH 4. The results confirmed the formation of an open structure of G5 PAMAM dendrimer at pH 4 with ~6 water/tertiary amine penetrated into the dendrimer, but a denser interior at pH 7 with only ~3 water/tertiary amine penetrated into the dendrimer. Differently, branch back-folding was observed at all pH values in this work.[143]

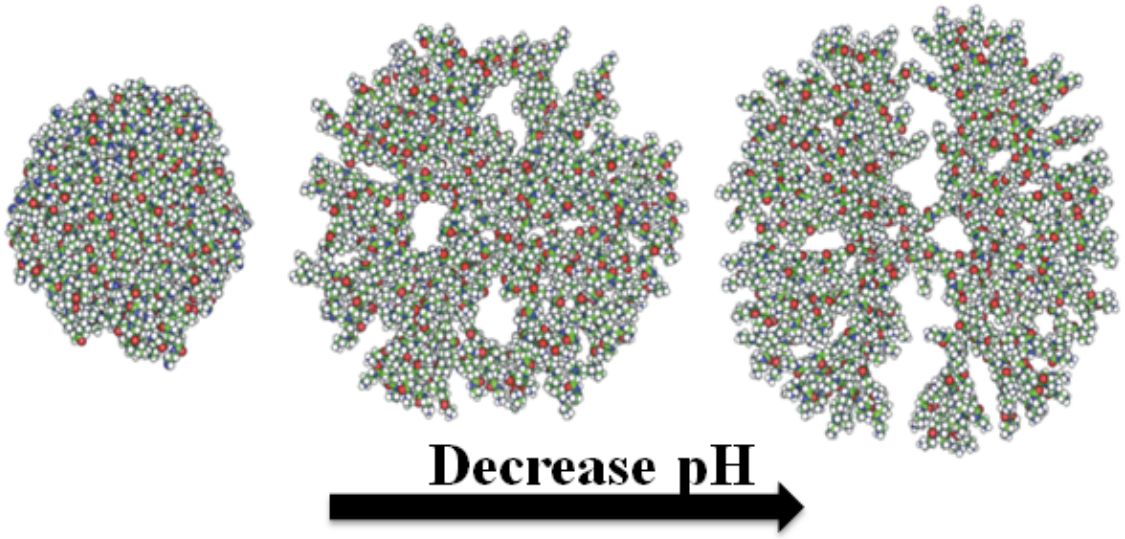

Figure 2.24. Conformation of G6 PAMAM dendrimer upon changing pH values. (a) at pH ≥ 10 (no amine groups are protonated), (b) at pH = 7 (only primary amines are protonated), and (c) at pH ≤ 4 (both tertiary and primary amine groups are protonated).[142]

Welch and Muthukumar demonstrated the conformation change of dendrimers under different ionic strength of the solvent using Monte Carlo simulations. They found that dendrimers exhibited a reversible transition between a "dense core" under high ionic strength and a "dense shell" under low ionic strength in aqueous solutions (Figure 2.25).[144]

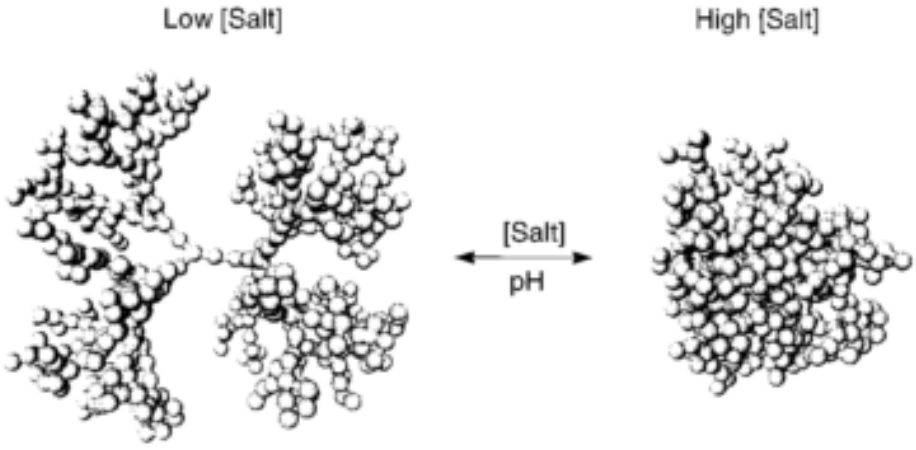

Figure 2.25. Three-dimensional conformation of dendrimers upon changing ionic strength.[144]

2.9.1.2 Intrinsic Fluorescence

No functional groups from PAMAM dendrimers are considered to be able to emit fluorescence, however, many researchers have observed strong blue fluorescence emission from PAMAM dendrimers. Larson and Tucker studied the intrinsic fluorescence of carboxylate-terminated PAMAM dendrimers (G2.5, G3.5, G4.5, G5.5 and G7.5) using two techniques (i.e. excitation-emission matrices and lifetimes). Their results showed that all samples had a similar excitation maximum wavelength of 380 nm and an emission peak of 440 nm. An increasing trend of fluorescence intensity over increasing generations was observed. PAMAM dendrimers exhibited two lifetimes, which tended to get longer with increasing generations due to a more protected microenvironment. The authors attributed the fluorescence to an n-π^* transition from the amido groups.[145]

Later on, a research group from Japan further investigated on the fluorescence of PAMAM dendrimers. Wang and Imae observed strong blue fluorescence from all amine-, hydroxyl- and carboxylate-terminated PAMAM dendrimers. In addition, G2 and G4 amine-terminated PAMAM dendrimers showed quite different fluorescent spectra. Moreover, significant increase of fluorescence intensity was found for G4 amine-terminated PAMAM dendrimer upon the decrease of pH values.[146] Imae and coworkers later found that both low pH and high temperature were able to enhance their fluorescence intensity, and that the formation of a fluorescence-emitting moiety was related to the protonation of tertiary amine groups in PAMAM dendrimers.[147] Chu and Imae demonstrated blue fluorescence from oxygen-doped triethylamine with similar tertiary amine group as PAMAM dendrimers, and concluded that fluorescence property of PAMAM dendrimers originates from the interior tertiary amino-branching sites. They also believed that oxygen molecules played an important role in forming complexes (i.e. peroxyl radical or exciplex) and thus inducing the fluorescence property. In addition, the fluorescence intensity of PAMAM dendrimers was enhanced when tertiary amine groups located densely in the interior.[148] Recently, the intrinsic fluorescence from PAMAM dendrimers was used by the same group to monitor the cellular uptake and flow cytometry during the study of gene delivery and transfection toward rat C6 glioma cell lines.[149]

2.9.2 Applications of PAMAM dendrimers

Taking advantage of their well-defined structure, controllable surface charge, favorable surface modification and encapsulation capacity, PAMAM dendrimers have been showing promising applications in biomedical and catalytic fields. The extensive applications of PAMAM dendrimers in

the biomedical field (e.g. drug delivery, gene transfection, bioimaging, biosensing, photodynamic therapy, photothermal therapy) can be found in recently published reviews.[141,150]

2.9.2.1 Encapsulation of inorganic nanoparticles

PAMAM dendrimer-encapsulated inorganic nanoparticles with well-controlled diameter in the range of 1 nm to 5 nm and good stability have aroused great interest. There are many advantages in using PAMAM dendrimers as host materials for inorganic nanoparticles. PAMAM dendrimers with uniform composition and structure guarantee the reproducibility of inorganic nanoparticles with certain sizes. In most cases, these monodispersed inorganic nanoparticles are encapsulated in the interior of dendrimers, where no aggregates/agglomerates are formed. More importantly, the surface of these inorganic nanoparticles are often not passivated due to steric effects within dendrimers and demonstrate increased catalytic performance. Finally, the surface groups, solubility, and accessibility of PAMAM dendrimer-encapsulated inorganic nanoparticles can be tailored through the favorable surface modification. The general synthetic procedure of PAMAM dendrimer-encapsulated inorganic nanoparticles involves the complexation of metal cations within the dendrimers and the following reduction of metal cations using $NaBH_4$ (Figure 2.26). A wide range of inorganic nanoparticles (e.g. Au, Pt, Ag, Pd, CdS) has been prepared using PAMAM dendrimers as host materials. In addition, bimetallic nanoparticles (e.g. Ag/Cu, Pd/Cu, Pt/Cu, Pt/Pd) and trimetallics can be prepared by coprecipitation of multiple metal cations at one time or by reduction of different metal cations step by step.[151]

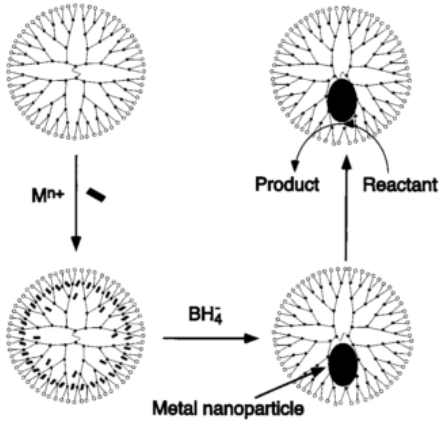

Figure 2.26. Schematic synthetic procedure of PAMAM dendrimer-encapsulated inorganic nanoparticles.[151]

The simple preparation of PAMAM dendrimer-encapsulated Au nanoparticles with high monodispersity and diameters of 1.3 ± 0.3 and 1.6 ± 0.3 nm was reported by Crooks and coworkers. The narrow size distribution was attributed to "magic number" ratios of [$HAuCl_4$]/[dendrimer] (i.e. 55 and 140), where energetically favorable Au structures could be formed. The methods used were highly reproducible, and no post-synthetic purification was required.[152] Amis and coworkers studied the formation of Au nanoclusters using PAMAM dendrimers with generations from 2 to 10. G2-G4 PAMAM dendrimers served as colloid stabilizers for gold nanoparticles, where several dendrimers gathered around each nanoparticle. G6-G9 PAMAM dendrimers encapsulated one gold nanoparticle per dendrimer molecule. Each G10 PAMAM dendrimer hosted multiple gold nanoparticles. The successful encapsulation of gold nanoparticles by PAMAM dendrimers was confirmed by TEM images, where PAMAM dendrimers were stained with phosphotungstic acid.[153]

The small size and narrow size distribution of other nanoparticles was also observed using PAMAM dendrimers as host materials. Cu nanoclusters with a diameter of less than 1.8 nm were prepared in the presence of G4 and G6 hydroxyl-terminated PAMAM dendrimers under careful control of Cu^{2+} loading. However, larger Cu nanoparticles with a diameter of 9 ± 4 nm were observed when excess Cu^{2+} were added. Moreover, the primary amine groups tended to adsorb Cu^{2+} and led to the formation of large Cu nanoparticles.[154] Pt and Pd nanoparticles with diameters in the range of 1.2-1.6 and 1.6-2.0 nm were also obtained using PAMAM dendrimers (G3, G4, G5) as templates. These nanoparticles showed good performance towards the catalytic reduction of 4-nitrophenol.[155] Lemon and Crooks reported the size control of CdS QDs using different generation hydroxyl-terminated PAMAM dendrimers (i.e. G4, G6, G8), where the increasing size of CdS QDs upon increasing generation was easily seen and confirmed by the red shift of size-tunable fluorescence emission spectra. The average diameter of CdS QDs was 1.3 nm for G4, 1.8 nm for G6, and 2.3 nm for G8 hydroxyl-terminated PAMAM dendrimers.[156]

Together with the attractive features of inorganic nanoparticles, it is believed that PAMAM dendrimer-encapsulated inorganic nanoparticles would play important roles in the fields of catalysis, biotechnology, medicine, photonics, etc.

2.9.2.2 Stabilization of inorganic nanoparticles

PAMAM dendrimers can also serve as stabilizers for inorganic nanoparticles. Amis and coworkers reported that low generation PAMAM dendrimers (G2-G4) served as colloid stabilizers rather than encapsulation agents for gold nanoparticles, probably due to their small size.[153] Chen and coworkers

demonstrated the dual applications of poly(ethylene glycol) grafted PAMAM dendrimers in the stabilization of Fe_3O_4 nanoparticles and the encapsulation of doxorubicin (DOX) (Figure 2.27). Their results showed that all PAMAM dendrimers with different generations (i.e. G3, G5, G6) successfully stabilized Fe_3O_4 nanoparticles, and that G6 PAMAM dendrimers exhibited the highest efficiency towards the loading of DOX at pH 7.4 and controlled release of DOX at pH 5. More importantly, no significant adverse effect on cellular proliferation and morphology was found by using poly(ethylene glycol) grafted PAMAM dendrimers as stabilizers and drug carriers.[157] With favorable surface modification and multifunctionality, PAMAM dendrimers could serve as colloid stabilizers for a wide range of inorganic nanoparticles and achieve advanced applications in various fields.

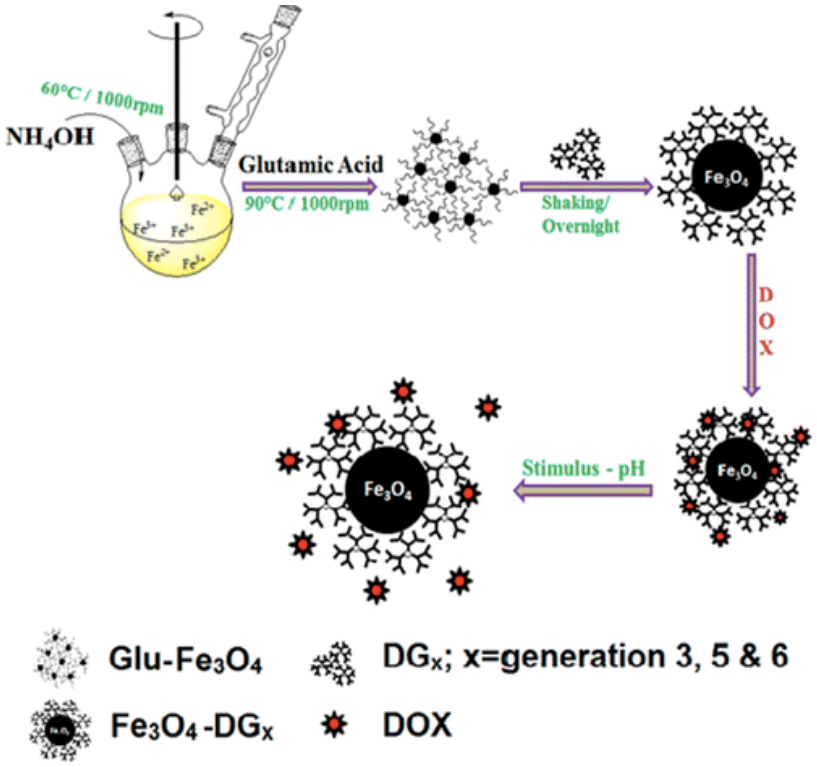

Figure 2.27. Schematic representation of PAMAM dendrimers' applications in the stabilization of Fe_3O_4 nanoparticles and the encapsulation of DOX.[157]

2.10 Summary

In this chapter, a background on CNCs, their functionalization and applications are presented. Inorganic nanoparticles and previous reported cellulose nanofiber/inorganic nanoparticle nanohybrids have been reviewed. The broadened applications of CNC/inorganic nanoparticle nanohybrids and

challenges from particle aggregation trigger the desire to develop new methodologies for controlling particle dispersion, particle size distribution, and aqueous colloidal stability. Therefore, our goal is to apply well-studied functional materials (i.e. silica, *β*-CD, PAMAM dendrimer) to assist the immobilization of inorganic nanoparticles, and the stabilization and applications of CNC/inorganic nanoparticle nanohybrids. More importantly, these functional materials introduce attractive features, enhancing applications of CNC/inorganic nanoparticle nanohybrids in various fields.

Chapter 3*

Synthesis of *β*-cyclodextrin modified cellulose nanocrystal (CNC)@Fe_3O_4@SiO_2 superparamagnetic nanorods

This study reports on the synthesis of *β*-cyclodextrin modified CNC@Fe_3O_4@SiO_2 superparamagnetic nanorods for the removal of two model compounds, procaine hydrochloride and imipramine hydrochloride. During the synthetic process, sustainable natural materials and low-cost chemicals were used, and mild reaction conditions were adopted. TEM and SEM images indicated good dispersion of Fe_3O_4 nanoparticles with uniform silica coating on CNCs. The thickness of the silica coating was controlled by manipulating the amounts of precursor solution used. TGA data confirmed that the silica coating significantly enhanced the thermal stability of CNCs. The onset decomposition temperature of CNC@Fe_3O_4@SiO_2 hybrids increased by 60 °C, compared to pure CNCs. XRD, EDS and FT-IR analyses confirmed the structure of CNC@Fe_3O_4@SiO_2 and the successful grafting of *β*-cyclodextrin. The CNC@Fe_3O_4@SiO_2@*β*-CD hybrids displayed good adsorption towards the model pharmaceutical residues: procaine hydrochloride and imipramine hydrochloride.

3.1 Introduction

Pharmaceutical residues in aquatic environment have been attracting increasing attention worldwide due to their long term potential risk to ecosystems and human health.[158,159] Effluent discharge from pharmaceutical manufacturing facilities is considered one of the major sources of contaminants in the environment.[160] In addition, toxic contaminants from manufacturing operations (e.g. chemical plants) and human activities (e.g. using detergents, shampoos, pesticides and fertilizers) continue to accumulate in our water systems, both at the surface (e.g. rivers and reservoirs), and underground (e.g. aquifers). While many approaches have been developed to eliminate these pollutants, such as electrochemical oxidation, photoelectrocatalysis, and nonthermal plasma,[161] physical adsorption is considered an attractive solution due to its low cost and simple process design.[162] As a rapid and effective technique, magnetic separation can be used to remove various types of organic

*This chapter is adapted from a paper "L. Chen, R. M. Berry and K. C. Tam. Synthesis of *β*-cyclodextrin-modified cellulose nanocrystals (CNCs)@Fe_3O_4@SiO_2 superparamagnetic nanorods. *ACS Sustainable Chem. Eng.*, 2014, 2, 951-958".

contaminants.[163] To achieve this, an effective protocol in fabricating magnetic nanoparticles that are suitable for the removal of pharmaceutical contaminants is required.

Superparamagnetic iron oxide nanoparticles have been widely used in numerous applications, such as magnetic resonance imaging contrast agents,[164] magnetic ferrofluids for hyperthermia,[165] targeted drug delivery,[166] and magnetically assisted separation.[167] However, aggregation and oxidation of iron oxide nanoparticles, in a water and oxygen environment significantly reduce their superparamagnetic properties. Although coating the particles with a nonreactive shell as an oxygen barrier is common, it suffers from several shortcomings, but most notably the reduction in the magnetic properties of iron nanoparticles. Recently, there are several reported studies on the use of controlled silica coating, where the superparamagnetic property of the nanoparticle is preserved.[168] However, silica-coated magnetic nanoparticles tend to aggregate into irregular or non-uniform shapes making the synthesis a significant challenge.[169]

Hybrid inorganic–organic nanocomposite materials are of practical interest due to their multifunctionality, processability, and potential large-scale production.[170,171] CNCs are attracting increasing interest due to their uniform nanorod shape, good mechanical strength, liquid crystalline character, high specific surface area, biocompatibility, biodegradability, and sustainability.[172,173] In addition, they can be produced at an industrial scale by acid hydrolysis of pulp fibers. CNCs consist of hydrogen bonded linear chains of β-D-glucopyranose bundled together to form nanorods with a diameter of 10-20 nm and a length of 200-400 nm.[174] The negative charge and hydroxyl groups on the surface of CNCs make them good template materials for noble metal nanoparticles (e.g. Au,[175] Ag,[106] Pd[176]). However, there is currently limited study on the preparation of iron oxide nanoparticles on the surface of CNCs.

Recently, silica-CNCs composites have aroused great interest and were applied to obtain chiral nematic mesoporous carbons,[53] mesoporous TiO_2[52] and carbon needles,[177] where silica served as frameworks and robust nanoreactors respectively. Here, we have chosen CNCs and silica as supporting template and coating materials respectively for iron oxide nanoparticles, and we propose strategies to address the issues relating to aggregation and oxidation of the magnetic nanorods. The proposed system would exhibit the following attractive features: (1) CNCs and silica are abundant, and they are environmentally-friendly and biocompatible; (2) silica coating is controllable and can enhance the thermal stability of CNCs; (3) silica can further be modified due to the abundance of hydroxyl groups.

β-cyclodextrin (*β*-CD) has been extensively investigated in the pharmaceutical industry,[178] as food additives,[179] and for water treatment,[180] due to its special structure, biocompatibility and low cost. Here, we grafted *β*-CD onto the surface of CNC@Fe_3O_4@SiO_2 hybrids and explored their application in the adsorption of two model organic compounds, procaine hydrochloride and imipramine hydrochloride.

3.2 Experimental design

3.2.1 Materials.

CNCs were supplied by CelluForce Inc. Ammonia and ethanol were purchased from Fisher Scientific. Aqueous solution of poly (diallydimethylammonium chloride) (20% PDDA, MW: 100,000–200,000), polyvinylpyrrolidone (PVP, MW: 10,000), *β*-cyclodextrin, NaOH, $NaHCO_3$, toluene, cyanuric chloride were purchased from Sigma Aldrich. Tetraethyl orthosilicate (98%) and 3-aminopropyl-triethoxysilane (99%) were purchased from Acros Organics. All the chemicals were used without further purification. Purified water from a Milli-Q Millipore system (>18 MΩ cm) was used in preparing the sample solutions.

3.2.2 Methods.

The preparation of CNC@Fe_3O_4@SiO_2@*β*-CD comprises of six steps as shown in Figure 3.1. Details on the synthesis of CNC@Fe_3O_4@SiO_2 hybrids with different thicknesses of silica shell are summarized in Table 3.1.

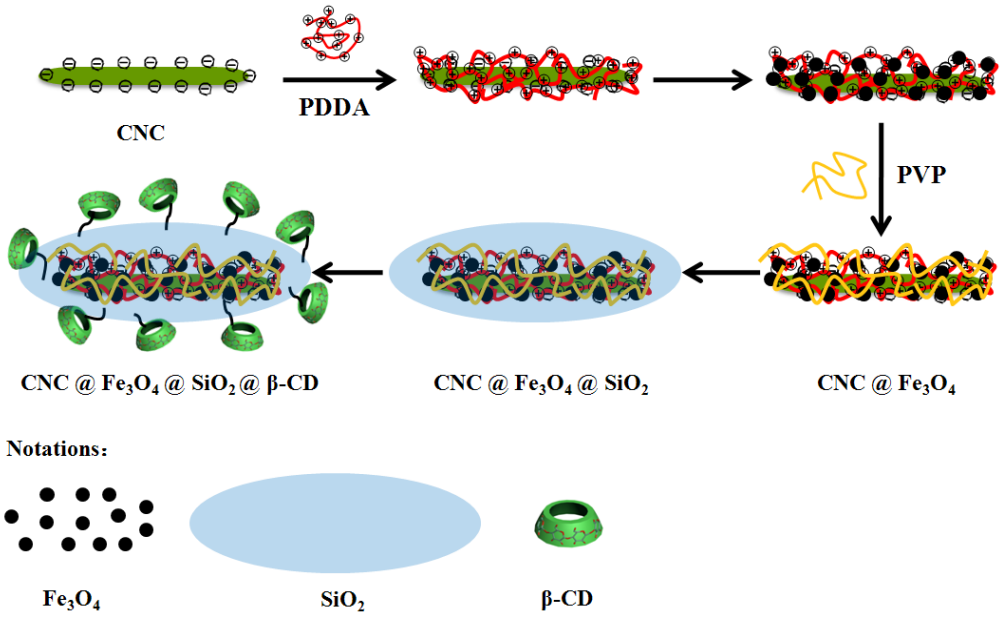

Figure 3.1. Schematic representation for the synthesis of CNC@Fe_3O_4@SiO_2@*β*-CD. CNC: cellulose nanocrystal; PDDA: poly (diallydimethylammonium chloride); PVP: polyvinylpyrrolidone; *β*-CD: *β*-cyclodextrin.

Table 3.1. Summary of notation and component quantities used to synthesize CNC@Fe_3O_4@SiO_2 hybrids with controllable thicknesses of silica coating.

Nanocomposites	CNC (g)	PDDA (mL)	Fe_3O_4 (g)	PVP (g)	TEOS (*μ*L)
CNC@Fe_3O_4	0.15	0.5	0.02	0.15	0
CNC@Fe_3O_4@SiO_2-50	0.15	0.5	0.02	0.15	50
CNC@Fe_3O_4@SiO_2-100	0.15	0.5	0.02	0.15	100
CNC@Fe_3O_4@SiO_2-150	0.15	0.5	0.02	0.15	150
CNC@Fe_3O_4@SiO_2-200	0.15	0.5	0.02	0.15	200

3.2.2.1 Synthesis of Fe_3O_4 nanoparticles

Fe_3O_4 nanoparticles were synthesised by co-precipitation of Fe^{2+} and Fe^{3+} cations as previously reported.[181] The co-precipitation overall reaction is described by the chemical reaction scheme:[75]

$Fe^{2+} + 2Fe^{3+} + 8OH^- \longrightarrow Fe_3O_4 + 4H_2O$

In a typical procedure, 0.24 g $Fe(NO_3)_3 \cdot 9H_2O$ and 0.08 g $FeSO_4 \cdot 7H_2O$ were dissolved in 15 mL water, then 10 mL 1 N HCl was added. The homogeneous solution obtained was added dropwise into 100 mL 1.5 M NaOH solution under vigorous stirring in the presence of a nitrogen blanket. Then, 1.0 g PVP 10 was added; the adsorbed PVP enhanced the stability of the Fe_3O_4 nanoparticles through steric repulsive forces. The precipitate was washed 4 times using a high gradient magnetic separator (HGMS), and the particles were redispersed in deoxygenated ethanol.

3.2.2.2 Synthesis of CNC@Fe_3O_4

As PDDA and PVP have been widely used in the fabrication of various types of nanoparticles,[182,183] they were used here in the synthesis CNC@Fe_3O_4. CNCs with diameter 10-20 nm and length 200-400 nm were used without further treatment (Figure 3.2A). To immobilize Fe_3O_4 onto CNCs, 0.15 g CNCs were first dispersed in 100 mL of a water solution containing 0.5 mL PDDA. The solution suspension was stirred on a magnetic stirrer and incubated for 16 h to obtain PDDA modified CNCs. Then, 0.02 g Fe_3O_4 nanoparticles were added and the suspension was stirred for another 4h after which 0.15 g PVP 10 was added. After 16h, PVP capped CNC@Fe_3O_4 was recovered via centrifugation at 4000 rpm for 15 minutes. The TEM of CNC@Fe_3O_4 confirmed the successful synthesis of a well-dispersed iron oxide nanoparticle/CNC system (Figure 3.2B).

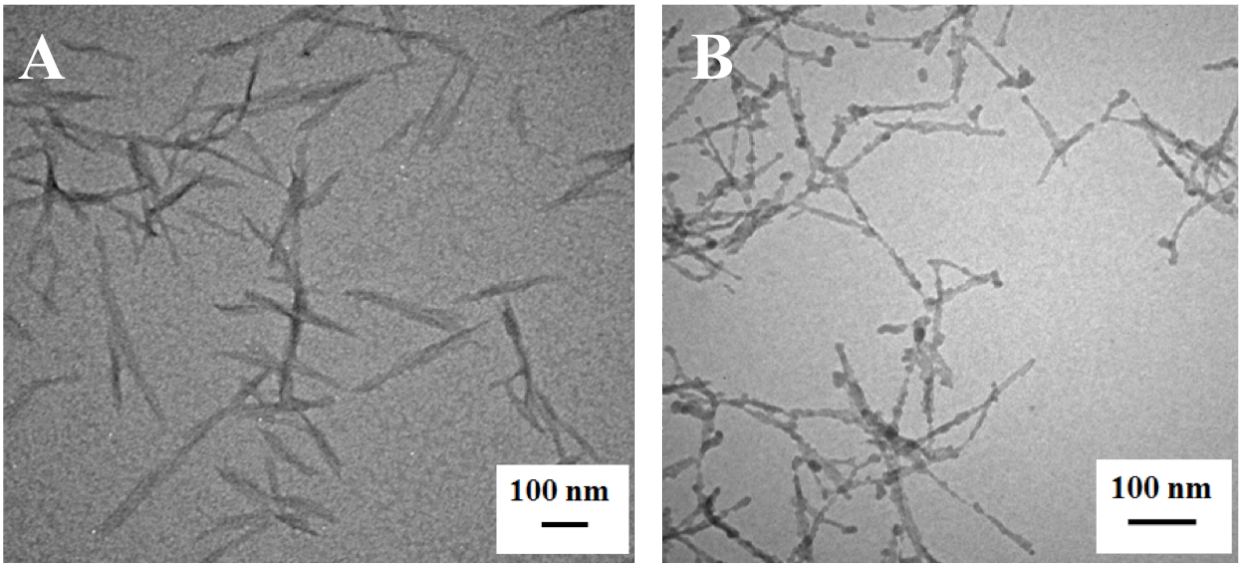

Figure 3.2. TEM images for CNCs (A) and CNC@Fe_3O_4 (B).

3.2.2.3 Synthesis of CNC@Fe_3O_4@SiO_2

The precipitates obtained previously were redispersed in ethanol/H_2O (80 mL/20 mL) solution, and then 10 mL of dilute ammonia solution (4.2% in ethanol) and various amounts of TEOS were added (Table 3.1). The reaction mixture was allowed to react at room temperature under continuous stirring for 20 h. The product was separated and purified by decantation, and freeze-dried.

3.2.2.4 Synthesis of Monochlorotriazine-*β*-CD (MCT-*β*-CD)

MCT-*β*-CD was synthesized according to previously reported method.[184,185] In a typical procedure, 5.5 g cyanuric chloride was dispersed into 30 mL cold water with the help of emulsifier and stirring. 12 mL 5 mol·L^{-1} sodium hydroxide was added dropwise. The mixture was allowed to react at 0 °C until a pH of around 8, and then 11.35 g *β*-CD solution was introduced. The system was kept at 10 °C overnight. The clear solution obtained was precipitated using acetone, desalted by DMF, precipitated again by acetone. The precipitation was dried in a vacuum oven at 40 °C. The structure of MCT-*β*-CD is shown in Figure 15. FT-IR spectrum of MCT-*β*-CD confirmed the coexistence of bands from *β*-CD (1158 and 1028 cm^{-1}) and cyanuric chloride (1579 and 1464 cm^{-1}) (Figure 3.3). ESI-MS analyses demonstrated that the synthesized MCT-*β*-CD is a mixture of mono-, di- and tri-substituted *β*-CD (Figure 3.4).

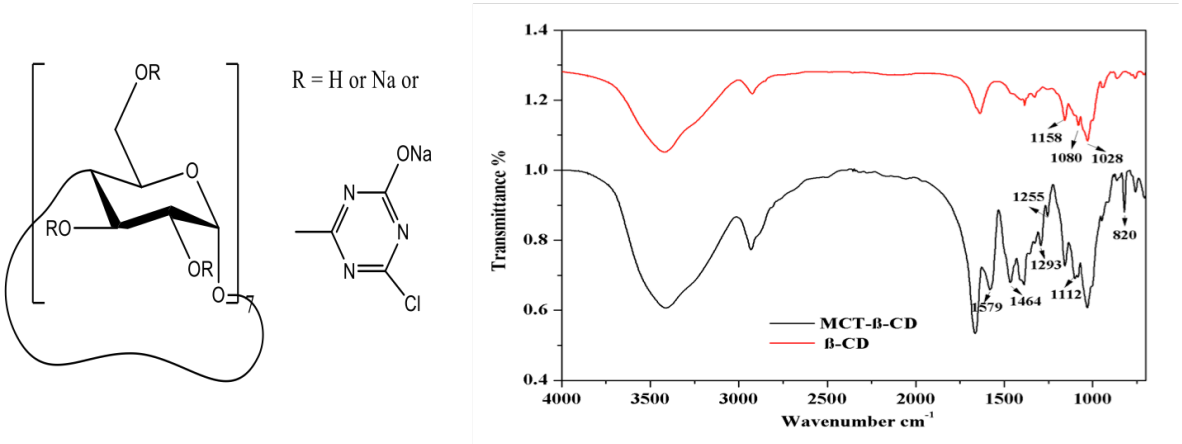

Figure 3.3. Chemical structure of MCT-*β*-CD and FT-IR spectra of *β*-CD and MCT-*β*-CD.

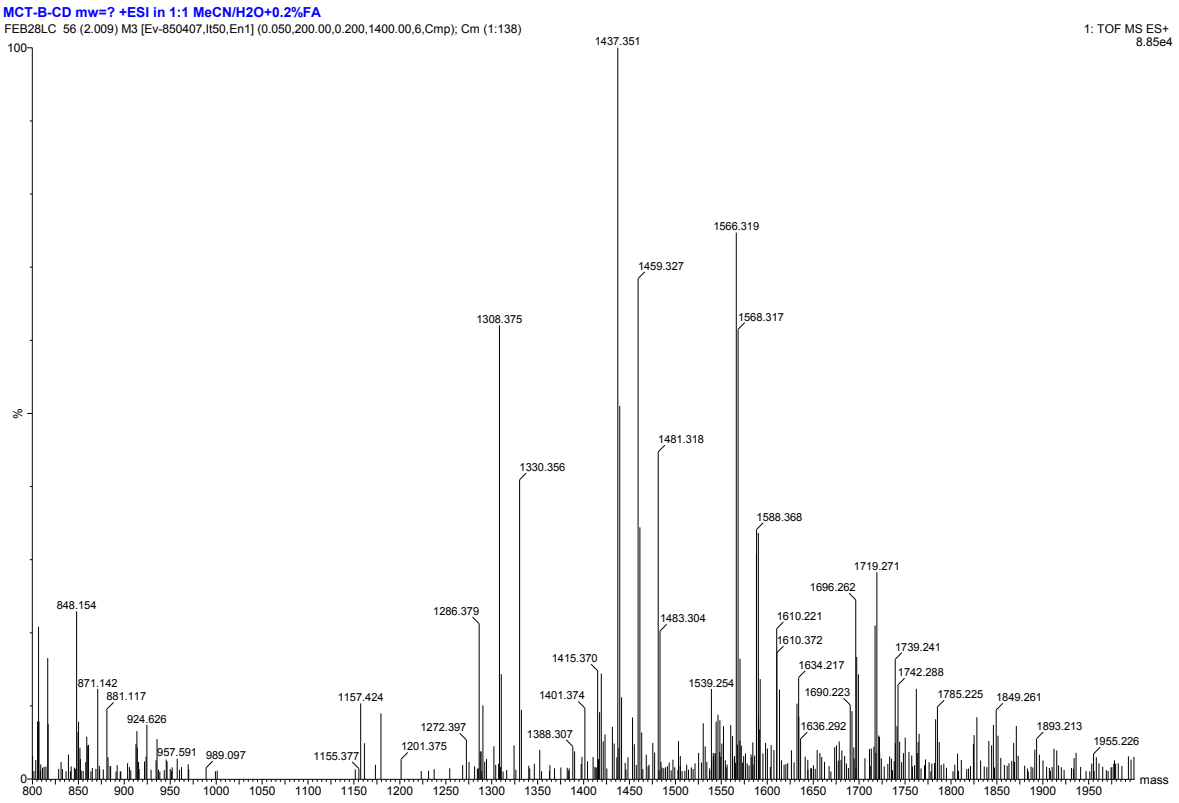

Figure 3.4. ESI-MS spectra of MCT-*β*-CD.

3.2.2.5 Synthesis of CNC@Fe_3O_4@SiO_2@*β*-CD

MCT-*β*-CD was then used to graft onto the CNC@Fe_3O_4@SiO_2 hybrid nanostructures. First, the silica shell was functionalized with primary amines, which was then reacted with MCT-*β*-CD. Typically, 150 mg CNC@Fe_3O_4@SiO_2-100 was dispersed in a solution of 50 mL toluene and 150 µL 3-aminopropyltrimethoxysilane (APTEOS). The solution was kept at 80 ^oC and stirred under nitrogen for 2 h. The aminated CNC@Fe_3O_4@SiO_2-100 was thoroughly washed, purified by decantation and then freeze-dried. Then, 150 mg aminated CNC@Fe_3O_4@SiO_2-100 was dissolved in 50 mL water containing 300 mg MCT-*β*-CD, and a saturated solution of $NaHCO_3$ was introduced into the solution to maintain a pH of 8. After 24 hours, the product was washed, separated by decantation and freeze-dried.

3.2.2.6 Depollution procedure

Adsorption tests were carried out in 20 mL beakers. In each beaker, 10 mL of an aqueous solution containing 23.6 ppm procaine hydrochloride and 10 mg of CNC@Fe_3O_4@SiO_2-100@*β*-CD or

CNC@Fe_3O_4@SiO_2-100 as adsorbents were thoroughly mixed. The mixture was stirred for 5 min before passing through the HGMS at a flow rate of 0.25 mL/s. The magnetic field of 1.0 T was applied for the separation process. The magnetic nanoparticles were retained in the HGMS, while unbound organic compounds in the form of a clear solution were collected and measured by UV-vis spectroscopy. After the measurement, the magnetic nanoparticles and the clear solution were carefully recovered and mixed again. This process was repeated 5 times until no further reduction in the absorbance was observed.

3.2.3 Characterization.

The morphology of CNC@Fe_3O_4@SiO_2 hybrids were evaluated using transmission electron microscopy (TEM). The features of CNC@Fe_3O_4@SiO_2 were observed using a scanning electron microscope (SEM ZEISS) with energy dispersive spectroscopy (SEM-EDS) under an accelerating voltage of 20 kV. X-ray diffraction (XRD) patterns were recorded by a Rigaku XRD-6000 diffractometer, using Cu Kα radiation (λ=0.154 nm) at 40 kV, 30 mA. Fourier-transform infrared (FT-IR) spectroscopy was used to study the chemical composition of CNC@Fe_3O_4@SiO_2 nanocomposites. The magnetic property of the samples was characterized with Lake Shore 7410 vibrating sample magnetometer. Mass spectrometer (Q-TOF Ultima Global, Waters, the University of Waterloo Mass Spectrometry Facility) was applied to confirm the synthesis of MCT-β-CD. A high gradient magnetic separator (HGMS) (Frantz Isodynamic Magnetic Separator-ModelL-1, Frantz Inc.) was used to recover the magnetic nanoparticles in the study on the removal of model organic compounds. The UV–vis spectra were obtained using a Shimadzu U-3000 spectrophotometer.

3.3 Results and discussion

3.3.1 Morphology study

The CNC@Fe_3O_4@SiO_2 containing various silica coatings of varying thickness were obtained by controlling the amounts of TEOS added during the coating process (Table 3.1). The morphology and architecture of CNC@Fe_3O_4@SiO_2 were investigated using TEM and SEM. The TEM images confirmed the homogeneous dispersion of Fe_3O_4 nanoparticles on the surface of CNC and the uniform silica coating on the CNC@Fe_3O_4 hybrid nanostructure. Because of the contrast between the various components, a distinct core-shell structure was observed for the CNC@Fe_3O_4@SiO_2 hybrid systems. When the amounts of TEOS added was increased from 50 µL (Figure 3.5A) to 200 µL (Figure 3.5D), the thickness of silica coating increased correspondingly. Shell thicknesses for samples A to D were

determined to be 5.9, 8.0, 10.9 and 14.1 nm respectively. In addition, no obvious aggregation of CNCs and Fe_3O_4 nanoparticles was observed. However, due to excess of TEOS, small amounts of spherical silica spheres were evident as indicated in Figure 3.5C and Figure 3.5D. It was previously reported that thin silica coatings obtained via the Stöber method was not homogeneous and could be unstable, where the coating could be redissolved when the nanoparticles were stored in an aqueous solution for a prolong period of time.[186] From this study, the optimum sample CNC@Fe_3O_4@SiO_2-100 was selected for further characterization and for subsequent grafting of β-CD.

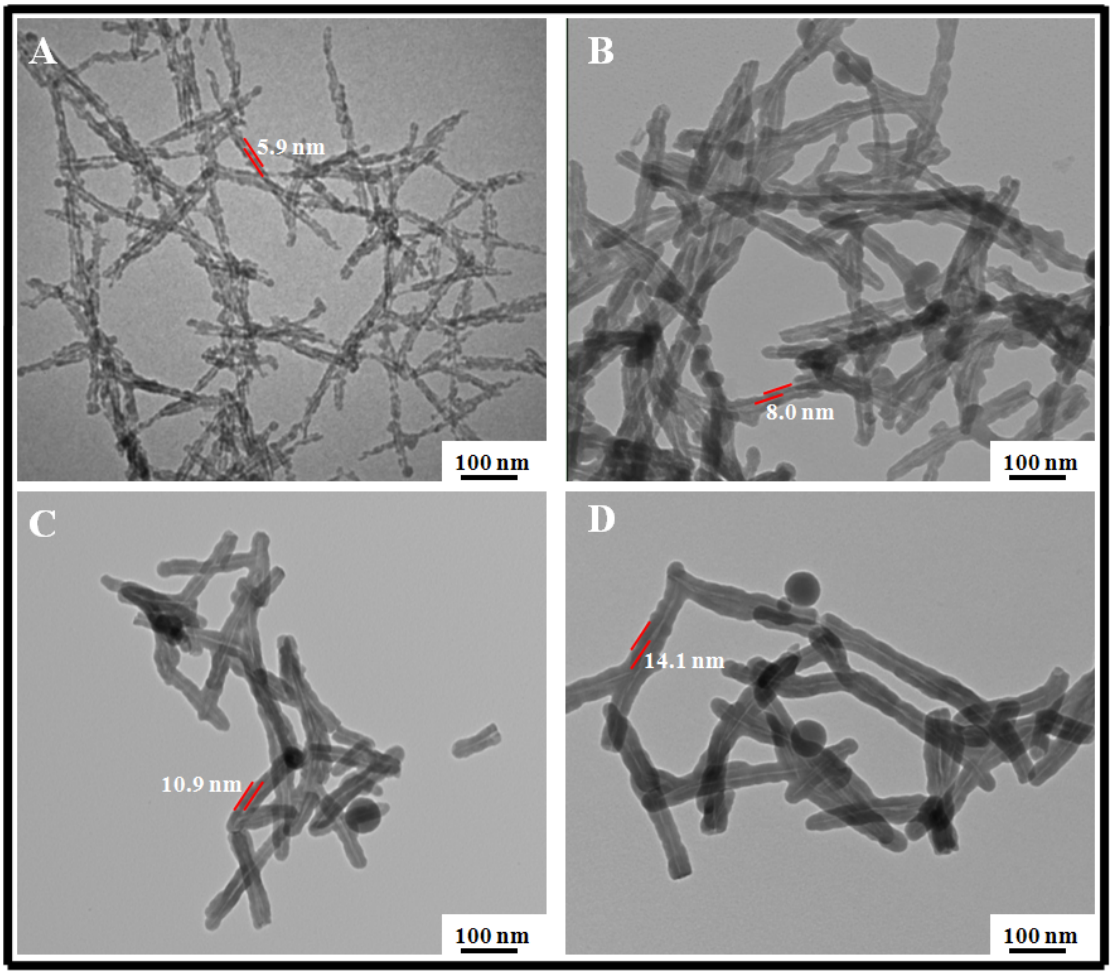

Figure 3.5. TEM images of CNC@Fe_3O_4@SiO_2-50 (A), CNC@Fe_3O_4@SiO_2-100 (B), CNC@Fe_3O_4@SiO_2-150 (C), CNC@Fe_3O_4@SiO_2-200 (D).

The top-view SEM images of CNC@Fe_3O_4@SiO_2 exhibited uniform rod-like structure (Figure 3.6A and Figure 3.6B). Meanwhile, CNC@Fe_3O_4@SiO_2 nanocomposites did not contain any large

aggregates (Figure 3.6C) in contrast to Fe_3O_4 nanoparticles where larger aggregates were evident (Figure 3.7). To further confirm the structure of CNC@Fe_3O_4@SiO_2 nanocomposites, SEM and EDX was used to measure the atomic species present in CNC@Fe_3O_4@SiO_2-100 (Figure 3.6 D), and the elements C, O, Si and Fe were detected. Based on EDX analysis, SiO_2/Fe_3O_4 molar ratio for CNC@Fe_3O_4@ SiO_2-100 was calculated to be 8.22.

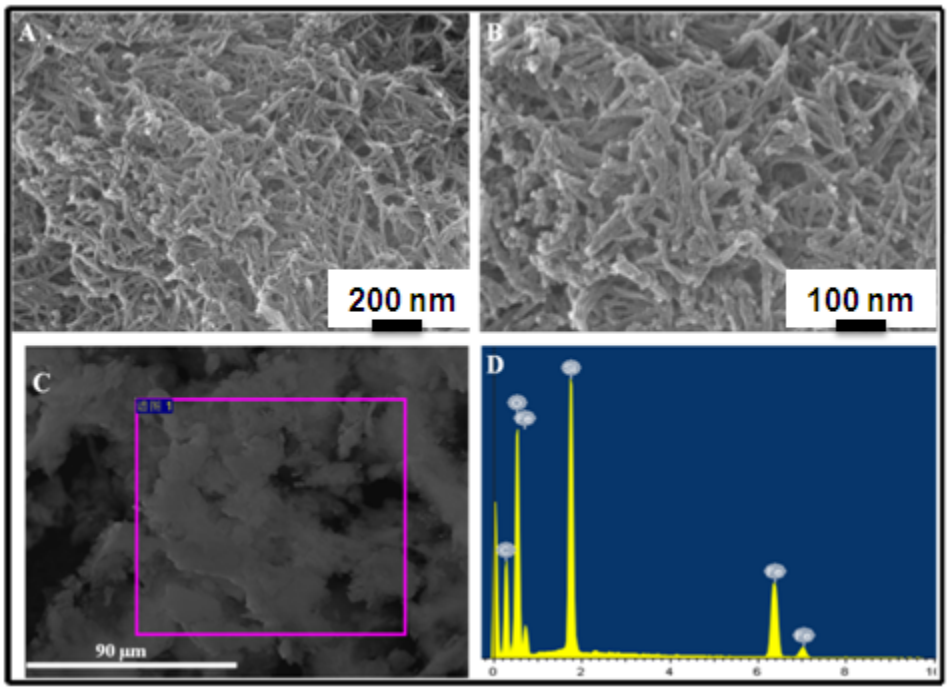

Figure 3.6. SEM images for the CNC@Fe_3O_4@SiO_2-100: low magnification (A); high magnification (B). SEM image (C) and corresponding EDX data (D) for the CNC@Fe_3O_4@SiO_2-100.

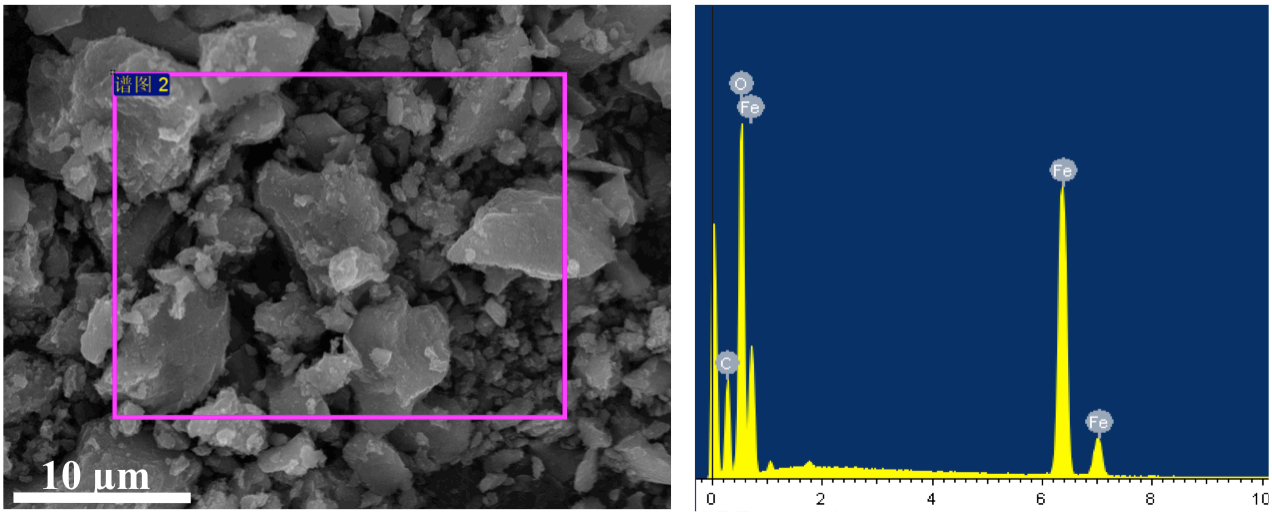

Figure 3.7. SEM image and EDX analysis for Fe_3O_4 nanoparticles.

3.3.2 Chemical structure characterization

The influence of varying the amounts of TEOS on the CNC@Fe_3O_4@SiO_2 hybrids was analyzed by FT-IR (Figure 3.8). Compared to CNCs, new absorbance bands at 789 cm^{-1} and 450 cm^{-1} corresponding to the symmetric stretching vibrations and the bending mode of Si-O-Si was detected. The band centered at 960 cm^{-1} is due to Si-O in-plane stretching vibrations of silanol groups. The bands in the range of 1200-1000 cm^{-1} assigned to Si-O covalent bond vibrations further confirmed the formation of a dense silica network.[187] In addition, the characteristic band at 620 cm^{-1} attributed to the asymmetric stretching vibration of Fe-O appeared in the FTIR spectra of CNC@Fe_3O_4@SiO_2 hybrids. Further, CNCs displayed distinct peaks at 2907 cm^{-1} and 2855 cm^{-1} that are assigned to C-H asymmetric and symmetric stretching vibrations, while CNC@Fe_3O_4@SiO_2 hybrids showed small peaks in these wavenumbers[188] due to non-hydrolyzed alkoxy groups on the silica surface.[28] In general, the absorbance bands of silica became sharper and more obvious with increasing amounts of TEOS added to the reaction mixtures, while the bands of CNCs decreased or disappeared. These trends confirmed the existence of Fe_3O_4 and the increasing thicknesses of silica shell from A to D.

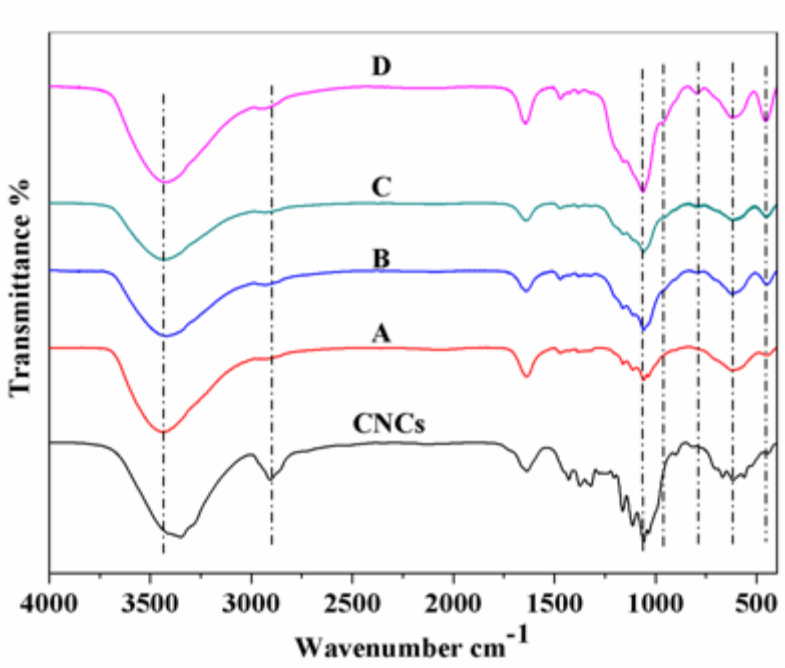

Figure 3.8. FT-IR spectra of CNCs, CNC@Fe_3O_4@SiO_2-50 (A), CNC@Fe_3O_4@SiO_2-100 (B), CNC@Fe_3O_4@SiO_2-150 (C), CNC@Fe_3O_4@SiO_2-200 (D).

To further confirm the formation of the silica-coated CNC@Fe_3O_4 core-shell structure, XRD was employed to examine the crystal structure of the samples (Figure 3.9). The Fe_3O_4 nanoparticles exhibited well resolved peaks at 30.0°, 35.4°, 43.2°, 57.0°and 62.7° which are attributed to (220), (311), (400), (422), (511) and (440) reflections of Fe_3O_4.[189] For CNC@Fe_3O_4@SiO_2 hybrids, new broad reflection profiles centered at 22.5° should be ascribed to the amorphous silica.[190] The data showed that CNC@Fe_3O_4@SiO_2 hybrids possessed diffraction peaks of Fe_3O_4 nanoparticles and amorphous SiO_2. CNCs are crystalline, and the XRD pattern of CNCs exhibits diffractions at 15.2°, 23.0° and 34.8° (Figure 3.10). However, there are no obvious diffraction peaks from CNCs in the hybrids, which is probably due to the considerable difference in the atomic scattering factors.[191] In addition, liquid ammonia used as catalyst for silica coating at 25 °C may have altered the crystalline structure of CNCs,[192] which further reduced the diffraction pattern of the CNCs. Together with the results from TEM and SEM, we could conclude that Fe_3O_4 nanoparticles were encapsulated within the silica shells.

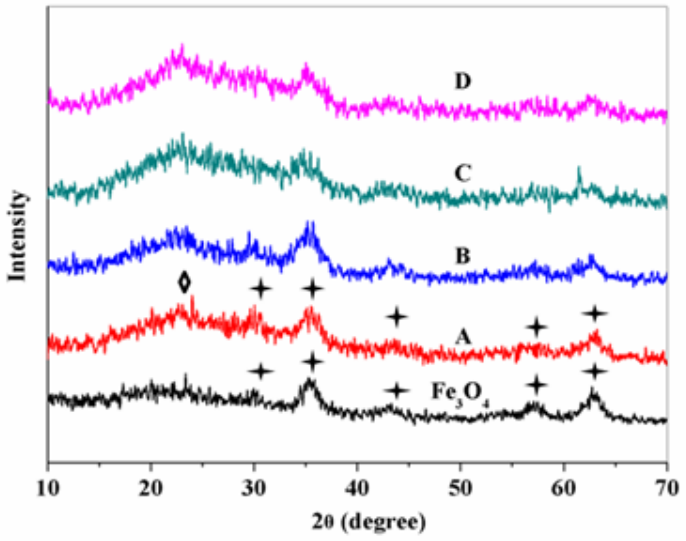

Figure 3.9. XRD patterns of Fe_3O_4 nanoparticles, CNC@Fe_3O_4@SiO_2-50 (A), CNC@ Fe_3O_4@SiO_2-100 (B), CNC@Fe_3O_4@SiO_2-150 (C), CNC@Fe_3O_4@SiO_2-200 (D). Diffractions peaks from SiO_2 (diamond) and Fe_3O_4 (star) are labeled.

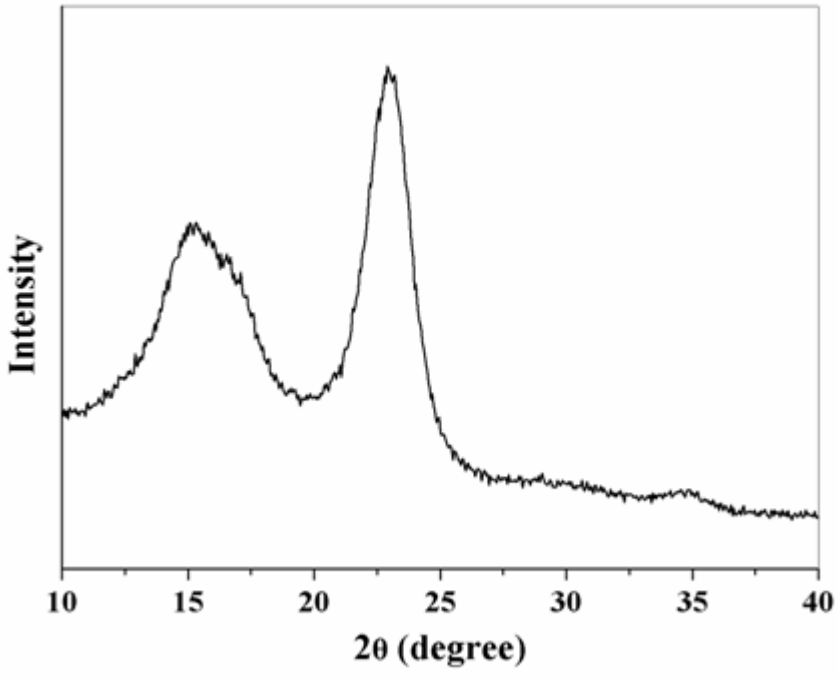

Figure 3.10. XRD pattern of CNCs.

3.3.3 Magnetic property

The magnetic properties of CNC@Fe_3O_4@SiO_2 hybrids with different silica shell thicknesses were studied with a vibrating sample magnetometer at 300 K (Figure 3.11). The hysteresis loops revealed that both the Fe_3O_4 and CNC@Fe_3O_4@SiO_2 hybrids displayed low coercivity with no obvious hysteresis confirming the superparamagnetism of the hybrid systems. Due to the superparamagnetic property, the CNC@Fe_3O_4@SiO_2 hybrids exhibited fast response to an external magnetic field and quickly redispersed under slight shaking once the magnetic field was removed (Figure 3.11). The reversible process is an advantage in many applications. With increasing amounts of TEOS, the magnetization value of CNC@Fe_3O_4@SiO_2 hybrids decreased from 14.0, 10.3, 7.0 to 5.0 emu/g, which further confirmed the increasing thicknesses of the silica coating on CNC@Fe_3O_4.

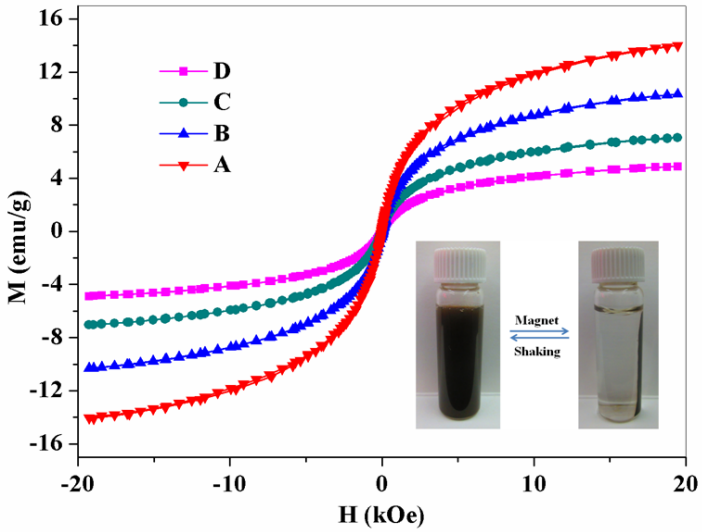

Figure 3.11. Room-temperature (300 K) magnetic hysteresis loops of CNC@Fe_3O_4@SiO_2-50 (A), CNC@Fe_3O_4@SiO_2-100 (B), CNC@Fe_3O_4@SiO_2-150 (C), CNC@Fe_3O_4@SiO_2-200 (D).

3.3.4 Thermal stability

The thermal stability of CNCs and CNC@Fe_3O_4@SiO_2 hybrids was measured by thermogravimetric analysis (TGA) under N_2 at a heating rate of 10 °C/min. The TGA plot in Figure 3.12 demonstrates that CNC started to decompose at 260 °C resulting in a weight loss of 56%. As for the CNC@Fe_3O_4@SiO_2 systems, the weight loss between room temperature to 320 °C was due to the absorbed water and dehydroxylation on the surface and interior of the silica.[193] The thermal onset for

the decomposition of CNC@Fe_3O_4@SiO_2 hybrids was shifted from 260 to 320 °C, indicating that silica coating served as a thermal barrier[194] and thus greatly enhanced the thermal stability of CNCs.

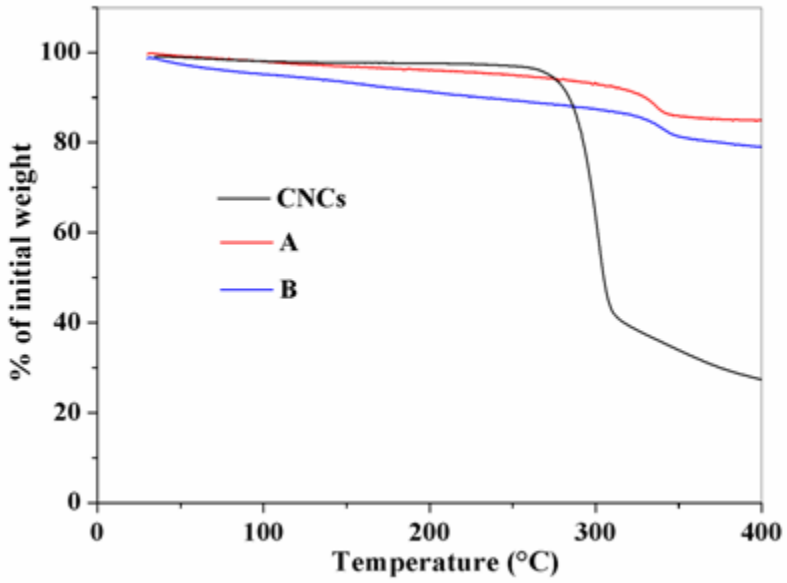

Figure 3.12. TGA patterns of CNCs, CNC@Fe_3O_4@SiO_2-50 (A), and CNC@Fe_3O_4@SiO_2-100 (B).

3.3.5 Drug removal

In this section, CNC@Fe_3O_4@SiO_2-100 was chosen as the optimum hybrid for further modification with MCT-*β*-CD to produce the CNC@Fe_3O_4@SiO_2-100@*β*-CD system for drug removal. The FTIR spectrum of *β*-CD revealed three typical peaks at 1157, 1080 and 1031 cm^{-1}.[195] Compared with the spectrum of *β*-CD, the FTIR spectrum of MCT-*β*-CD displayed a new peak at 1112 cm^{-1}, which corresponded to the C–O–C stretching vibration. Other new bands at 1579 cm^{-1}, 1464 cm^{-1}, 1293 cm^{-1}, 1255 cm^{-1}, 820 cm^{-1} can be assigned to the triazinyl ring (Figure 3.3).[196,197] As for the FT-IR of the synthesized CNC@Fe_3O_4@SiO_2-100@*β*-CD nanocomposites (Figure 3.13), the sharp peaks at 706 cm^{-1} and 757 cm^{-1}, assigned to the stretching vibration υ(C-Cl),[198] disappeared in the grafted products, confirming the reaction between MCT-*β*-CD and modified CNC@Fe_3O_4@SiO_2. C-H asymmetric and symmetric stretching vibrations appeared at 2918 and 2850 cm^{-1} which can be attributed to the carbon chain between the silica surface and *β*-CD. In addition, the vibrations of the triazinyl ring (1465 cm^{-1}), Fe-O (620 cm^{-1}), Si-O (1110 cm^{-1}) were observed. These results confirmed that *β*-CD was successfully grafted on the surface of CNC@Fe_3O_4@SiO_2-100.

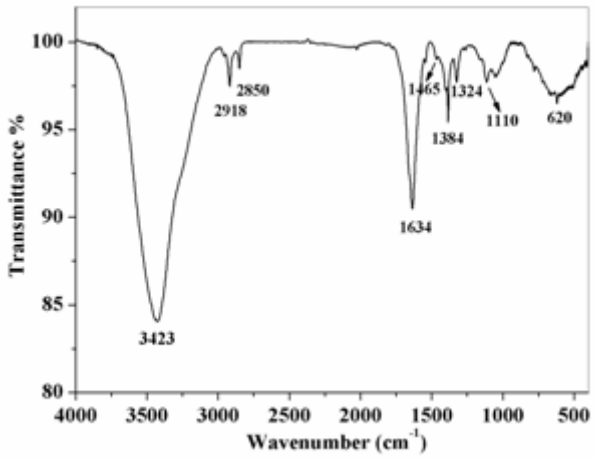

Figure 3.13. FT-IR of β-CD modified CNC@Fe_3O_4@SiO_2-100.

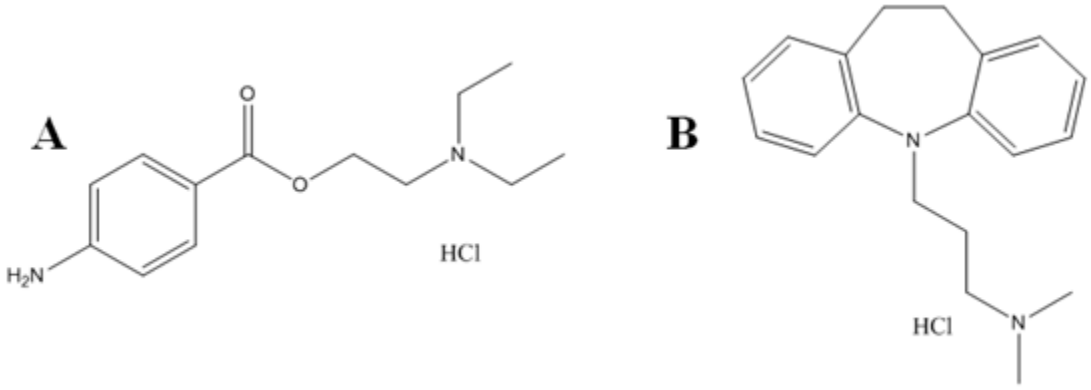

Figure 3.14. Chemical structure of procaine hydrochloride (A) and imipramine hydrochloride (B).

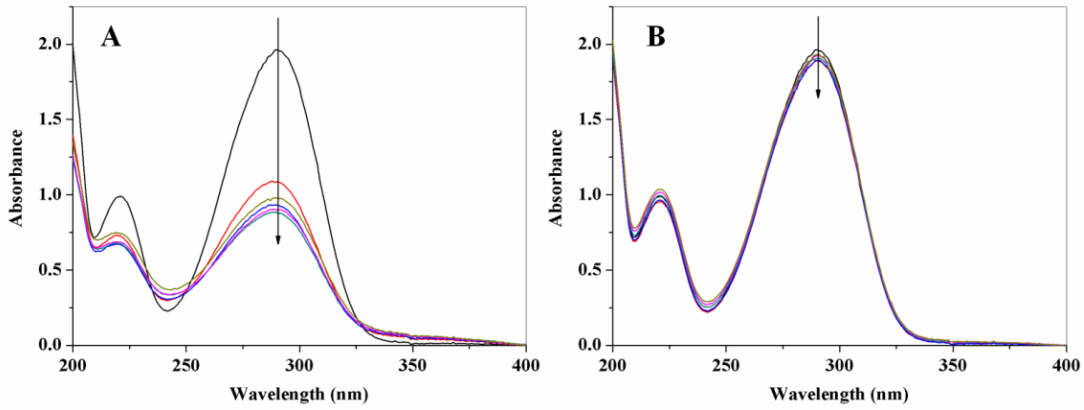

Figure 3.15. UV-vis of the upper clear Procaine solution in 10 mg CNC@Fe_3O_4@SiO_2-100@*β*-CD (A) and in 10 mg CNC@Fe_3O_4@SiO_2-100 (B) with different adsorption times.

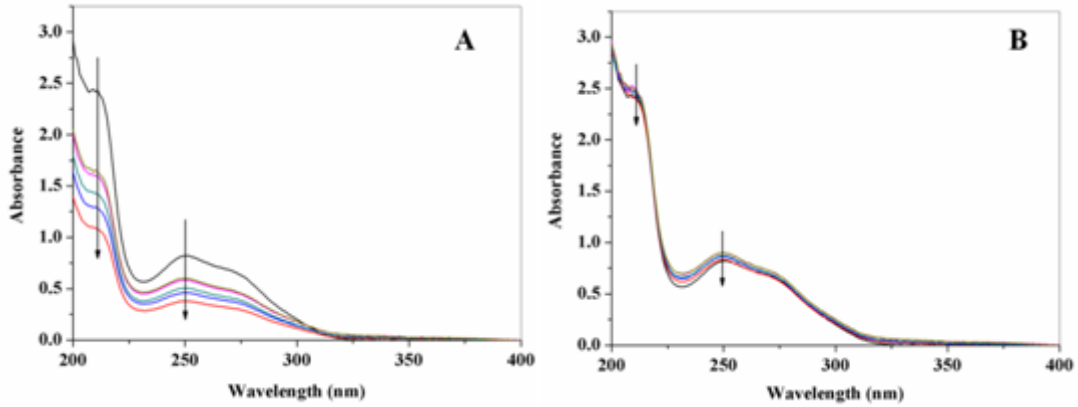

Figure 3.16. UV-vis of the upper clear imipramine solution in 10 mg CNC @ Fe_3O_4 @ SiO_2-100 @ *β*-CD (A) and in 10 mg CNC @ Fe_3O_4 @ SiO_2-100 (B) with different adsorption time.

The behaviour of CNC@Fe_3O_4@SiO_2-100@*β*-CD in removing model organic compounds (Figure 3.14) was investigated by UV-vis spectroscopy. In order to study the adsorption process, a control CNC@Fe_3O_4@SiO_2-100 was also tested under similar conditions. Typically, the adsorption tests were carried out in 20 mL beakers. In each beaker, 10 mL of an aqueous solution containing 23.6 ppm procaine hydrochloride and 10 mg of CNC@Fe_3O_4@SiO_2-100@*β*-CD or CNC@Fe_3O_4@SiO_2-100 as adsorbents were added. The mixed solution was stirred for 5 min, and then the samples were passed through the HGMS, where the magnetic nanoparticles were retained in the HGMS and unbound organic compounds in the form of a clear solution were recovered. The concentration of the supernatant in the filtered solution was monitored by UV-vis spectroscopy. This

adsorption/separation process was repeated several times until the value of the absorbance approached a stable value. The UV-vis data indicate there is no obvious change of absorbance of the supernatant for the procaine hydrochloride solution in the 10 mg CNC@Fe_3O_4@SiO_2-100 sample, while fast adsorption of procaine hydrochloride by CNC@Fe_3O_4@SiO_2-100@*β*-CD was observed (Figure 3.15). These results further confirmed the successful synthesis of CNC@Fe_3O_4@SiO_2-100@*β*-CD. The adsorption capacity was determined to be 13.0 ± 0.09 mg/g. Similar phenomenon was also observed for removal of imipramine hydrochloride with adsorption capacity of 14.8 ± 0.16 mg/g (Figure 3.16). The final concentrations for procaine hydrochloride and imipramine hydrochloride were 10.6 ppm and 11.1 ppm respectively. Compared with conventional membrane separations which generally suffer from fouling, poor permeate quality and low flux enhancement,[199] the magnetic separation shows several advantages including rapid process (short residence time & fast kinetics), simple clean-up, and easy recovery of adsorbents. In addition, the flow rate of the mixture of polluted water and magnetic particles can be easily adjusted and increased using various diameter tubes.

3.4 Conclusions

A *β*-CD modified CNC@Fe_3O_4@SiO_2-100 inorganic-organic hybrid was successfully prepared. The TEM, SEM-EDX, XRD and FT-IR confirmed its core-shell structure. The structural morphology studies indicated that there is no obvious aggregation of Fe_3O_4 on the CNCs and the thicknesses of silica could be controlled by varying the amounts of TEOS. The TGA spectra revealed that silica coating could significantly enhance the thermal stability of CNCs, where the onset decomposition temperature was increased by 60 ^{o}C. Furthermore, the as-prepared CNC@Fe_3O_4@SiO_2-100@*β*-CD hybrid displayed good magnetic property and effective adsorption characteristic towards two model organic compounds. Therefore, the CNC@Fe_3O_4@SiO_2-100@*β*-CD inorganic-organic hybrid can be potentially applied for the removal of pharmaceutical residues. Finally, the procedure reported here can be extended to prepare other inorganic-organic nanocomposites using CNCs as the template material.

Chapter 4*

Synthesis of pH-responsive and fluorescent poly (amidoamine) dendrimer-grafted cellulose nanocrystals

Poly (amidoamine) (PAMAM) dendrimers have found promising applications in biomedicine and in the encapsulation of inorganic nanoparticles. G6 PAMAM dendrimer-grafted cellulose nanocrystals (CNC-PAMAM) were prepared via carbodiimide-mediated amidation process and they displayed pH-responsive and fluorescent characteristics as confirmed by zeta potential, transmittance and isothermal titration calorimetry (ITC). Stable aqueous dispersions of CNC-PAMAM were obtained at pH $\leq$ 4 and pH $\geq$ 10, driven by electrostatic repulsion from positive charge and negative charge respectively. However, large aggregates were formed at pH values from 5 to 9 due to electrostatic attraction. In addition, strong blue fluorescent emission was observed, and the fluorescent behaviour of CNC-PAMAM was influenced by the formation of aggregates. The pH-responsive and fluorescent properties of CNC-PAMAM may be suitable for their applications in pH-responsive nanodevices, fluorescent-based pH sensors, optical markers, and nanoreactors for the encapsulation of inorganic nanoparticles.

4.1 Introduction

Poly (amidoamine) (PAMAM) dendrimers have attracted increasing attention due to their well-defined unique dendritic architecture, controllable size, mimicry of globular proteins, encapsulation capability, favorable surface modification, and commercial availability.[139,141] PAMAM (full generation) contains an abundant amount of primary amines on the surface as well as tertiary amines in the interior. The protonation/deprotonation process of these two amino groups occurs at different pH permitting one to tune their pH-responsive property.[142] Specifically, PAMAM structures are extensively stretched yielding a highly ordered open structure at pH $\leq$ 4, while they are globular and compressed at pH $\geq$ 10.[143,200] This pH-responsive property enables their use as macromolecular vectors for drugs[140,201] and nanoreactors for encapsulating inorganic nanoparticles.[151] In addition, intrinsic fluorescence from carboxylate-,[145] amine-,[146] and hydroxy-terminated[202] PAMAM dendrimers have been reported, which leads to their potential use in fluorescent-based detection and diagnostics.

*This chapter is adapted from a paper "L. Chen, W. Cao, N. Grishkewich, R. M. Berry and K. C. Tam. Synthesis and characterization of pH-responsive and fluorescent poly (amidoamine) dendrimer-grafted cellulose nanocrystals. *J. Colloid Interface Sci.*, 2015, 450, 101-108".

For example, intrinsic fluorescent PAMAM dendrimers were recently applied as both gene carriers and a nanoprobes for monitoring the delivery of nucleic acids.[149]

PAMAM dendrimers have been anchored onto various templates and substrates, such as on multi-walled carbon nanotubes,[203] iron oxide nanoparticles,[204] silica nanoparticles,[205] silica support,[206] and indium tin oxide electrodes[207] for use in both biomedical and catalytic applications. Here we report on the functionalization of one excellent biotemplate-cellulose nanocrystals (CNCs) with PAMAM dendrimers. CNCs continue to attract an increasing amount of attentions due to their high mechanical strength, rigidity, high specific area, biocompatibility, biodegradability, sustainability and commercial availability.[4] In addition, the abundant reactive primary hydroxyl groups at the surface of CNCs allow for chemical modification that extended their applications in new fields. These attractive features have greatly improved the performance of CNCs as efficient adsorbents for water treatment,[86] reinforcing nanofillers in polymers nanocomposites,[87] templates for fabricating chiral nematic mesoporous films,[88] supporting materials for loading noble metal nanoparticles,[110] building blocks for layer-by-layer assembly,[34] drug delivery vectors,[49] as well as bioimaging probes.[48] Particularly, surface modifications of CNCs to impart reversible pH-responsive behaviour and/or fluorescent emission character have received some attention. While pH responsive CNCs demonstrated facial control over flocculation[208] and hydrogel formation,[209] several fluorescently labelled CNCs showed promise in the fields of optical labelling[5] and bioimaging.[48,210] Further, dual fluorescent labelling of CNCs reported by Nielsen and co-workers showed pH dependent fluorescent response as well as their potential use as pH nanosensors.[211]

In this study, intrinsic fluorescent G6 PAMAM dendrimers were grafted onto the surface of CNCs via amide bonds. The obtained product referred to as CNC-PAMAM not only shows pH responsive properties and fluorescent emission but also adds the encapsulation capability of PAMAM dendrimers. In addition, the pH-responsive property of CNC-PAMAM caused by the pH dependent protonation/deprotonation and stretch-compress properties of PAMAM display interesting characteristics and may assist in the regeneration process for practical applications. Moreover, investigation on the surface charge of CNC-PAMAM was conducted by examining the interactions between CNC-PAMAM and surfactants (sodium dodecyl sulphate and hexadecyltrimethylammonium bromide) at different pH values. The results obtained from the interactions provide important information critical for the application of CNC-PAMAM in pharmaceutical industry, as cosmetic additives and as catalyst carriers. This pH-responsive property, encapsulation capability and

fluorescent emission of CNC-PAMAM would find promising applications in the fields of pH-responsive separation, optical imaging, antimicrobial, nanotemplates and biomedicine.

4.2 Experimental section

4.2.1 Materials

Generation 6.0 poly (amidoamine) dendrimers (5 wt. % solution in methanol) (G6-PAMAM), N-hydroxysuccinimide (NHS), sodium bromide, sodium dodecyl sulphate (SDS), MES hydrate, Sodium hypochlorite (NaClO, available chlorine, 10-15%), N-(3-dimethylaminopropyl)-N'-ethyl-carbodiimide hydrochloride (EDC) and hexadecyltrimethylammonium bromide (CTAB) were purchased from Sigma-Aldrich and used without further purification. CNCs were supplied by CelluForce Inc. Deionized water from a Milli-Q Millipore system (>18 MΩ cm) was used in the sample preparation.

4.2.2 Methods

The synthetic process of CNC-PAMAM is shown in Figure 4.1. It includes the oxidation of CNCs and the grafting of PAMAM dendrimers onto CNCs.

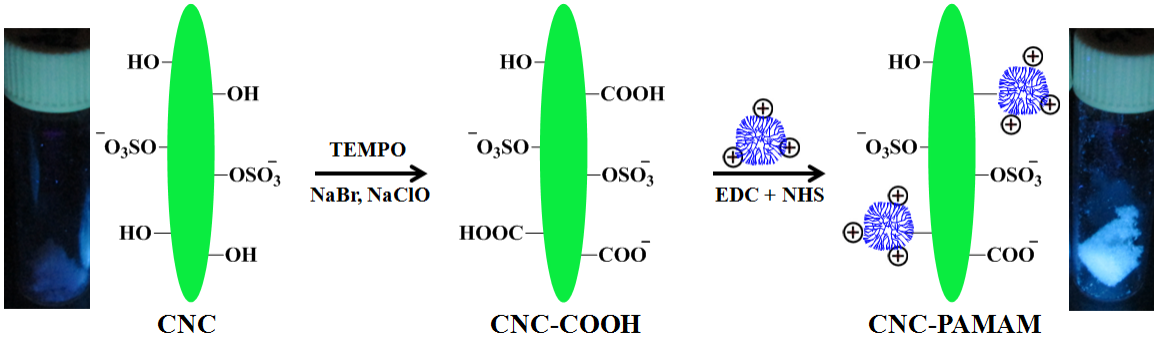

Figure 4.1. Schematic representation for the synthesis of CNC-PAMAM.

4.2.2.1 TEMPO mediated oxidation of cellulose nanocrystals

Grafting of PAMAM via an amide bond requires the primary hydroxyl groups of CNCs to be converted into carboxyl groups. 5 g CNCs were added to 375 mL water with 0.0125 g TEMPO and 0.125 g NaBr, and sonicated for 15 min using a Branson 1510 sonicator to form a stable, homogeneous suspension. 50 mL NaClO was slowly added to the CNC suspension, and the pH value was maintained at 10.5 throughout the reaction. After stirring for 4 h, 5 mL

ethanol was added to quench the oxidation. The suspension containing oxidized CNCs (CNC-COOH) was dialyzed in deionized water for 72 h to remove excess reactants, and then freeze-dried.

4.2.2.2 Grafting reaction of G6-PAMAM onto CNC-COOH

The grafting reaction of G6-PAMAM onto the surface of CNC-COOH was carried out using the carbodiimide-mediated amidation method reported by Sehgal and Vijay.[212] 50.0 mg freeze-dried CNC-COOH was homogeneously dispersed in 50mL of the MES buffer (25 mM, pH 6.5) via sonication for 10 min. Afterwards, 100 mg EDC and 100 mg NHS were added slowly to the mixture under sonication. The mixture was reacted under stirring for 2 h and was then added drop-wise to 10 mL diluted G6 PAMAM dendrimers aqueous solution (containing 500 μL 5 wt. % G6 PAMAM in methanol) under sonicating condition. The final mixture was allowed to react for 24 h. The product was purified by dialysis and ultrafiltration.

4.2.3 Characterization

Fourier-transform infrared (FT-IR) spectroscopy was employed to study the chemical composition of freeze-dried CNCs, CNC-COOH and CNC-PAMAM. KBr pellets containing these samples were analysed using a Bruker Tensor 27 spectrometer with resolution of 4 cm^{-1}. The morphologies of these samples were examined using a Philip CM 10 transmission electron microscope (TEM) under an accelerating voltage of 60 kV. Approximately 10 μL of a 0.01 wt% sample were sprayed onto carbon-coated copper grids, dried and placed in the vacuum chamber of the TEM. The interaction between CNC-PAMAM and SDS/CTAB was studied using a Microcal VP- isothermal titration calorimeter. Control experiments were carried out by titrating surfactants into water under same conditions. Typically, ~ 282 μL of titrant (SDS or CTAB) was injected at different volume increments into a 1.4551 ml CNC-PAMAM (0.04 wt%) solution or water. Zeta potential values were measured using a Malvern Zetasizer nano ZS instrument. The concentrations and pH values of samples were well controlled and adjusted using a Metrohm 809 Titrando autotitrator, where titrants (0.1 M HCl or 0.1 M NaOH) were introduced at a flow rate of 0.1 mL/min. All samples were sonicated for 5 min and kept still for 30 min prior to testing. Transmittance values at 600 nm were recorded using a Cary 100 Bio UV-visible spectrophotometer. The reported values are an average of 6 measurements, and error bars represent the standard deviation. Fluorescent emission spectra were recorded on a Varian Cary

Eclipse fluorescent spectrophotometer with excitation wavelength of 370 nm and an emission range from 400 nm to 600 nm.

4.3 Results and discussion

4.3.1 CNC-PAMAM characterization

In order to investigate the morphology, CNC-COOH (0.01 wt. %, pH 7) and CNC-PAMAM (0.01 wt. %, pH 3) dispersions were sprayed onto copper grids and then characterized by TEM (Figure 4.2). CNC-COOH displayed a regular rod-shaped structure, and CNC-PAMAM possessed no obvious morphology difference or cross-linking aggregation, indicating the synthetic process was well controlled.

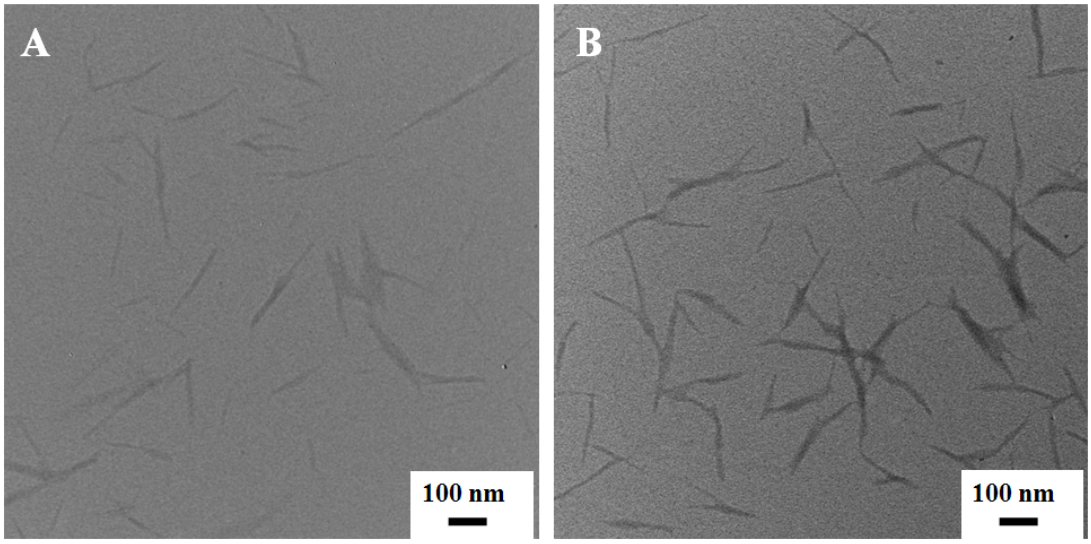

Figure 4.2. TEM images of CNC-COOH (A) and CNC-PAMAM (B).

FT-IR spectroscopy is widely applied in structural characterization. The FT-IR spectra of CNCs, CNC-COOH and CNC-PAMAM are shown in Figure 30. The spectrum of CNCs (Figure 4.3a) showed the O-H stretching vibration at 3350 cm^{-1}, bending vibrations of C-H at 2906 cm^{-1} and glucose ring bands between 1040 and 1160 cm^{-1}.[51] CNC-COOH (Figure 4.3b) exhibited a new peak at 1724 cm^{-1}, which was attributed to the carbonyl stretching vibration from the abundance of carboxyl groups added through the oxidation of the CNCs.[101] As for CNC-PAMAM (Figure 4.3c), two new peaks appeared at 1652 and 1540 cm^{-1}, corresponding to the stretching mode of amide-I and amide-II respectively.[213] In addition, the C=O stretching of CNC-PAMAM shifted to 1710 cm^{-1} and appeared

as a shoulder, which indicated the consumption of carboxyl groups during the grafting of PAMAM dendrimers. Moreover, CNC-COOH and CNC-PAMAM exhibited similar absorption peaks to CNCs below 1500 cm^{-1}, indicating the retention of the CNC framework.

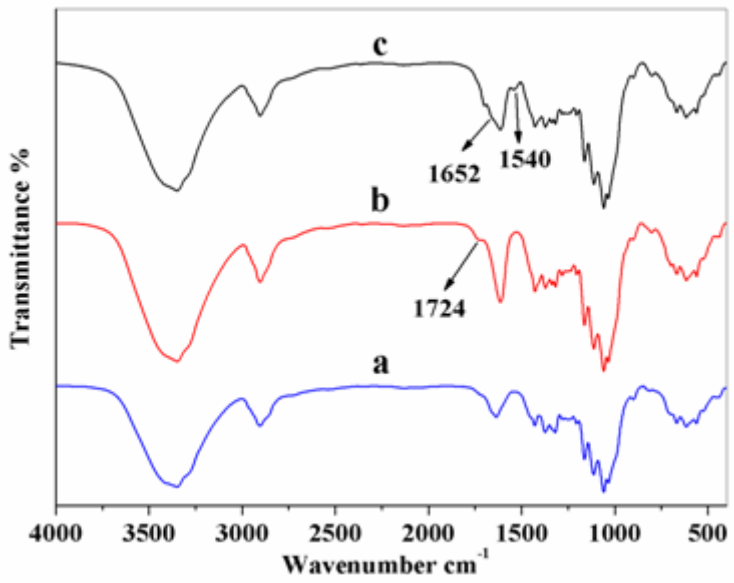

Figure 4.3. FT-IR spectra of CNCs (a), CNC-COOH (b) and CNC-PAMAM (c).

Elemental analysis was conducted to monitor the changes in the elemental composition, and the results are summarized in Table 4.1. The weight percentage of carbon decreased from 41.120% in CNCs to 39.320% in CNC-COOH, which resulted from the increased oxygen content during the oxidation process. The content of carboxyl groups was further evaluated using a Metrohm 809 autotitrator. Briefly, 50 mL of CNC-COOH (0.1 wt%) was prepared, and the pH value of the suspension was adjusted to ~ 3.5 by adding HCl (0.1 M). Afterwards, the suspension was titrated to pH ~ 10 using NaOH (0.035 M) under stirring. Measurements of pH and conductivity were simultaneously obtained throughout the titration, using respective probes on the autotitrator (Figure 4.4). Change in conductivity with increasing volume of NaOH was used to determine the amount of functional groups, and the concentration of carboxyl groups (pKa = 5.1) was calculated to be ~ 1.05 mmol/g.[214] PAMAM dendrimers were then grafted onto CNC-COOH via amide bridges, and the obtained CNC-PAMAM exhibited 8.890% N indicating the presence of PAMAM dendrimers.

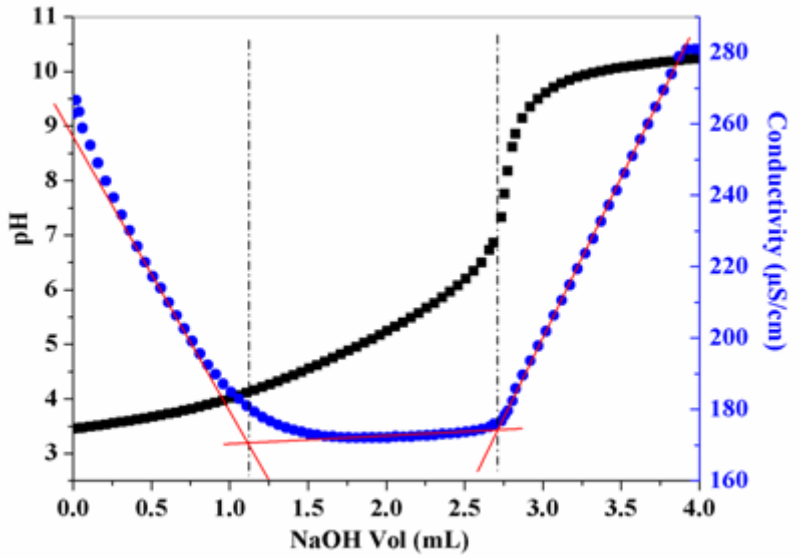

Figure 4.4. Simultaneous conductometric-potentiometric titration curve of CNC-COOH.

Table 4.1. Elemental weight compositions of CNCs, CNC-COOH and CNC-PAMAM

	N [%]	C [%]	H [%]	S [%]
CNCs	0	41.120	5.616	0.699
CNC-COOH	0	39.320	5.081	0.679
CNC-PAMAM	8.890	42.710	6.364	0.434

4.3.2 pH-responsive property of CNC-PAMAM

To analyze the pH-responsive property of CNC-PAMAM, 0.027 wt. % solutions at different pH values were prepared. Figure 4.5A shows the digital image of these solutions. At pH $\leq$ 4 and pH $\geq$ 10, CNC-PAMAM dispersions were translucent, while large aggregates and phase separation were observed at pH values ranging from 5 to 9. The Zeta potential of these same samples (0.027 wt. %) were measured in order to study surface charge of CNC-PAMAM at various pH values (Figure 4.5B). At pH 3, the zeta potential was highly positive with a value of + 42.2 mV, owing to the protonation of amine groups on dendrimers and carboxylate groups on the surface of CNCs. At pH 11, the zeta potential value decreased to be - 36.5 mV, which was caused by the sulphate ester groups as well as the unreacted carboxylate groups at

CNC surface. It is believed that PAMMA dendrimers were deprotonated and compressed at pH 11, which in turn enhanced the exposure of these negative charges. As for the systems with pH values from 5 to 9, the suspensions of CNC-PAMAM were not stable as evident from Figure 4.4A. This may be due to the electrostatic interactions between the coexisting positive charges on PAMAM dendrimers and negative charges from the modified CNCs. The high transmittance values (average data of 6 measurements) of the CNC-PAMAM dispersions (0.027 wt. %) at 600 nm at pH 3 and pH 11 further confirmed the pH responsive behaviour of CNC-PAMAM (Figure 4.5C). Furthermore, this pH dependent dispersibility is reversible.

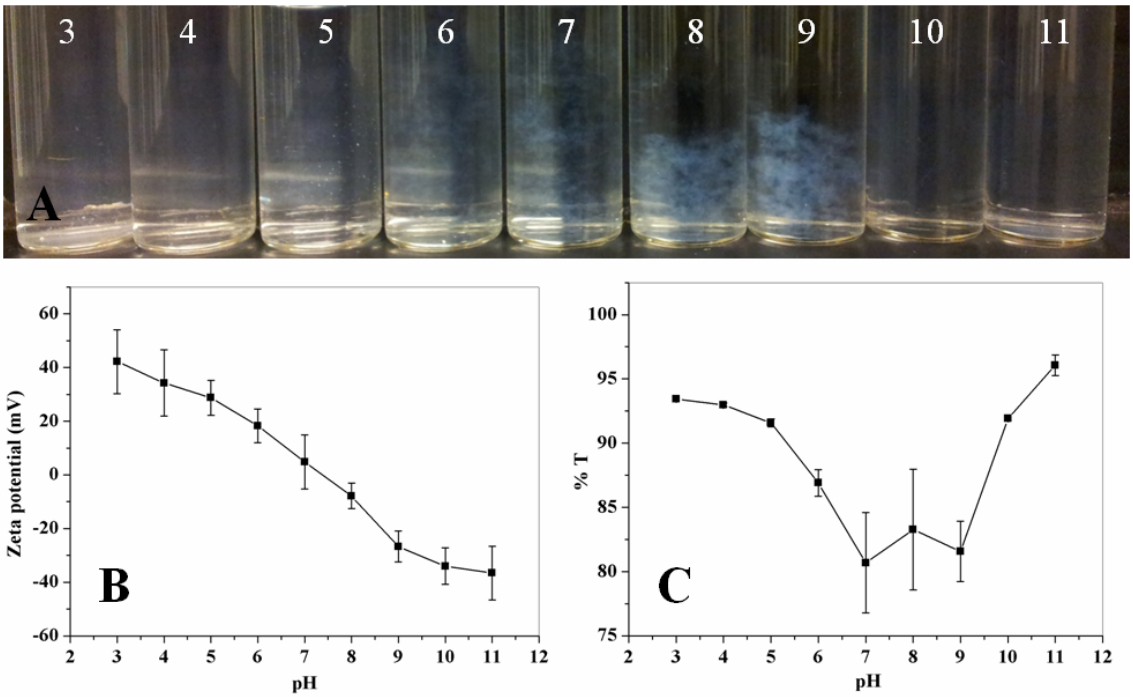

Figure 4.5. Digital image (A), zeta potential values (B) and transmittance at 600 nm (C) of CNC-PAMAM at different pH values.

4.3.3 pH dependent interactions between CNC-PAMAM and surfactants

Following the pH dependant stability tests in an aqueous medium, experiments were conducted to investigate the interactions between CNC-PAMAM and anionic (SDS)/cationic (CTAB) surfactants, that are relevant for the applications of CNC-PAMAM in pharmaceutical and cosmetic industries. SDS (100 mM at 25 °C) and CTAB (10 mM at 28 °C) were titrated into CNC-PAMAM (0.04 wt. %) aqueous dispersion under various pH values, and the interactions were measured by ITC, UV-vis

transmittance and zeta potential. To facilitate the analysis, SDS (100 mM at 25 °C) and CTAB (10 mM at 28 °C) were also titrated into water as a control.

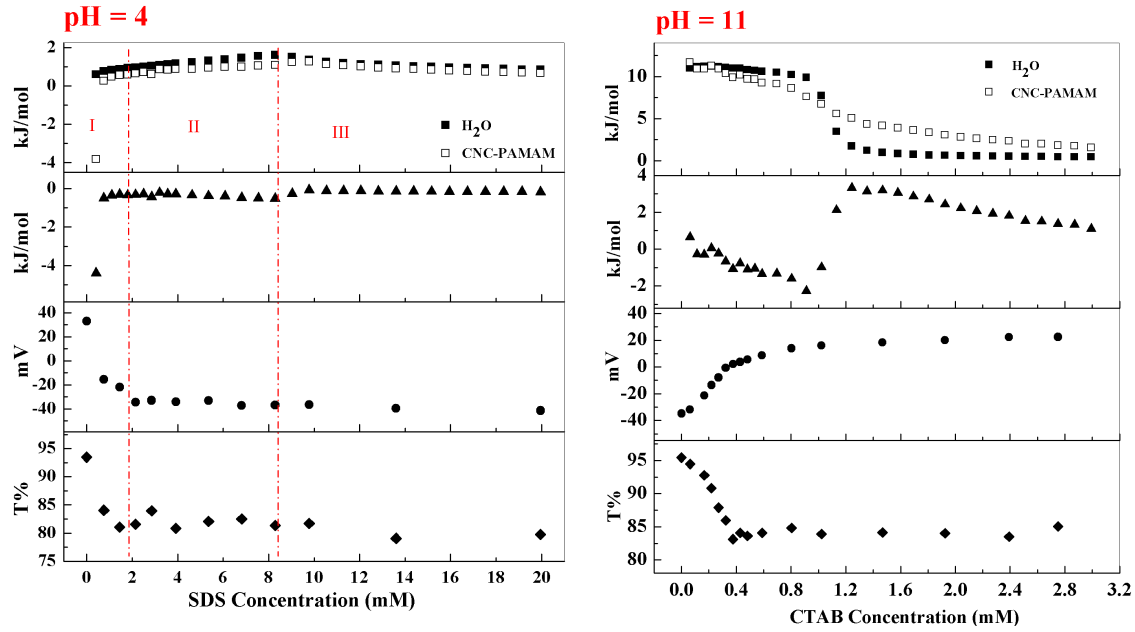

Figure 4.6. The interaction between SDS and CNC-PAMAM studied at pH 4 by isothermal titration calorimetry, zeta potential and transmittance at 600 nm (graph on the left). The interaction between CTAB and CNC-PAMAM studied at pH 11 by isothermal titration calorimetry, zeta potential and transmittance at 600 nm (graph on the right).

The interactions between SDS and CNC-PAMAM at pH 4 are shown in Figure 4.6, where three stages of interaction were observed. In the first stage, SDS molecules were bound to CNC-PAMAM via electrostatic interaction producing a negative zeta potential and a corresponding reduction in the transmittance from 94 % to 81 % caused by the formation of large aggregates. In the second stage, more SDS molecules were attracted to CNC-PAMAM due to the hydrophobic interaction between the SDS molecules. Finally, free micelles formed at the third stage with increasing amounts of SDS.

At pH 7 (Figure 4.7), in the first stage, reduced amounts of SDS were bound to the CNC-PAMAM due to significantly reduced positive charge with a zeta potential value of ~ 10 mV. With the increase in SDS concentration to 1.8 mM, the zeta potential value of the mixture dropped to - 28 mV and the transmittance declined from 84 % to 81 %. With further titration of SDS, a slight drop in the zeta potential and increase in the transmittance were observed, which was probably due to formation of micelles on the CNC-PAMAM surface. For the titration of SDS conducted at pH 9 (Figure 4.7), no

significant interactions were detected, and no obvious change in zeta potential values and transmittance were observed. These results are probably due to the largely exposed negative charge of CNC-PAMAM surface and the deprotonation of amine groups.

To further confirm the surface charge, the interactions between CNC-PAMAM and CTAB at pH 11 were verified (Figure 4.6). Based on the data from ITC, zeta potential and transmittance at 600 nm, the interactions can be divided into two stages. Below 0.4 mM CTAB, strong electrostatic and hydrophobic interaction were observed with the zeta potential value shifting from - 36 mV to around 0 mV, and transmittance values decreasing from 96 % to 82 %. Upon the further titration of CTAB, more CTAB molecules assembled around the CNC-PAMAM to minimize the exposed hydrophobic domains, and the zeta potential gradually increased to + 23 mV. Similarly, no significant interactions were seen when CTAB was titrated into CNC-PAMAM dendrimers at pH 4 (Figure 4.8) and pH 7 (Figure 4.8) due to the protonation of the dendrimers. These interactions carried out at different pH values further confirmed the pH responsive property of CNC-PAMAM.

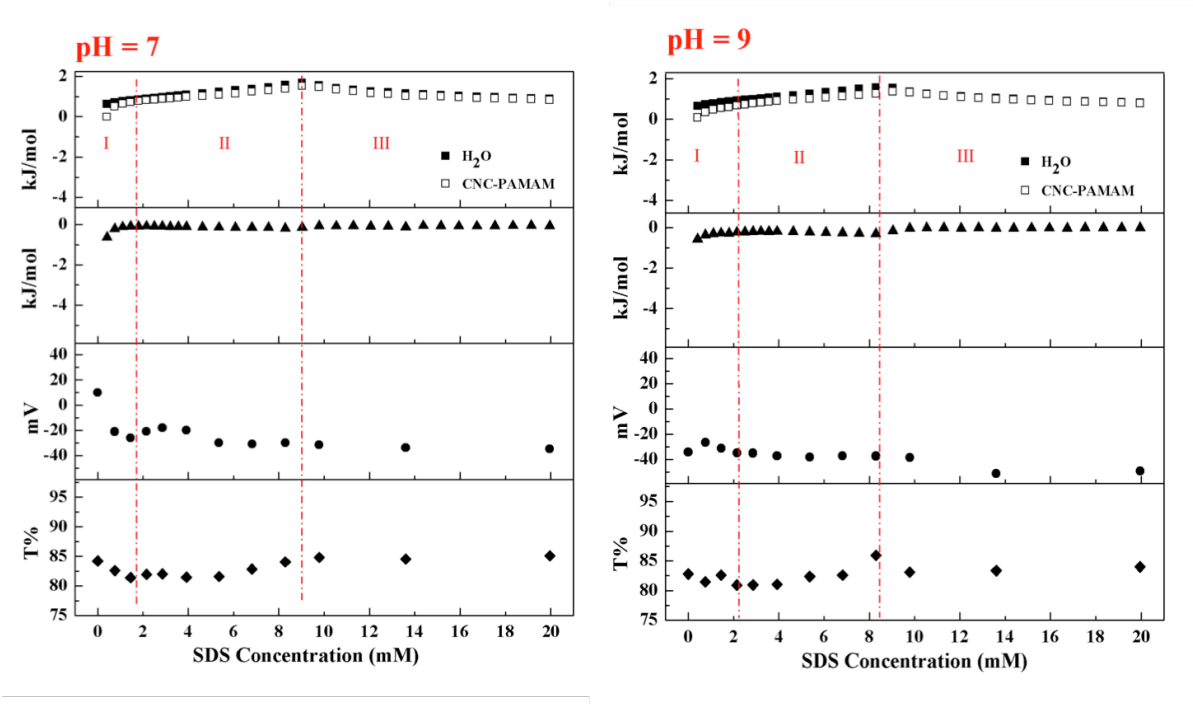

Figure 4.7. The interaction between SDS and CNC-PAMAM studied at pH 7 and pH 9 by isothermal titration calorimetry, zeta potential and transmittance at 600 nm.

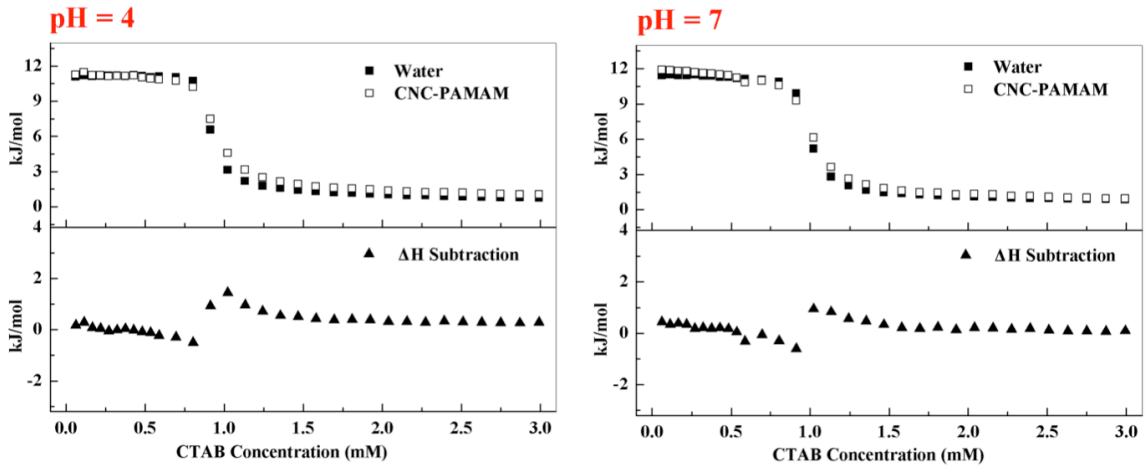

Figure 4.8. The interaction between CTAB and CNC-PAMAM studied at pH 4 and pH 7 by isothermal titration calorimetry.

4.3.4 CNC-COOH, CNC-PAMAM, and CNC-COOH + PAMAM fluorescent emission studies

In addition to pH responsive behaviour, CNC-PAMAM exhibited blue fluorescent emission under 365 nm UV light due to the intrinsic fluorescent property of PAMAM dendrimers. The fluorescent emission of PAMAM dendrimers is puzzling and surprising, as conventional fluorophores are not present while fluorescence quenchers are abundant. Some works reported that the intrinsic fluorescent emission of PAMAM dendrimers originates from the interior tertiary amino-branching sites[148] and may result from n-π* transition from the amido groups.[145] Further, several factors were found to play important roles in the fluorescent emission from PAMAM dendrimers, which include luminescent-moiety generation by oxidation, rigidity of dendrimer backbone, hydrogen-bonding ability, and the fractal aggregation in PAMAM dendrimers.[147,202,215,216]

Based on the pH responsive property of CNC-PAMAM observed in the previous section and previous work on PAMAM dendrimers, pH responsive and fluorescent behaviours of CNC-PAMAM are illustrated in Figure 4.9. Blue fluorescent emissions were observed for CNC-PAMAM aqueous dispersions at all three pH values (3.0, 6.5 and 11.0). Phase separation was only observed at pH 6.5, and brighter emission was achieved at pH 3.0 than that at pH 11.0.

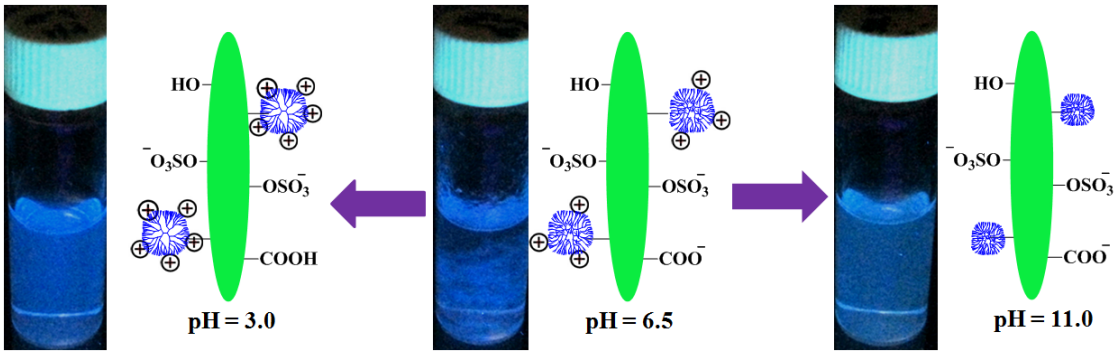

Figure 4.9. Schematic representation of the pH responsive and fluorescent behaviours of CNC-PAMAM at different pH values.

To further study the fluorescent performance of CNC-PAMAM, 0.08 wt. % of CNC-PAMAM aqueous dispersions at several pH values were prepared and measured. The excitation spectrum of CNC-PAMAM at pH 3.0 is shown in Figure 4.10, with 370 nm (λ_{max}) being chosen as the excitation wavelength. The 0.08 wt. % CNC-COOH suspension at pH 6.5 was evaluated first, but no fluorescent emission was detected (Figure 4.11A spectrum "a", digital image "a"). However, for CNC-PAMAM, bright blue emissions were observed at different pH values as revealed by the inset digital image in Figure 4.11A. Spectra of CNC-PAMAM showed three emission peaks at 429, 448 and 478 nm. When the pH was increased from 3.0 to 6.5, the peaks at 448 and 478 nm decreased, while no significant change was observed for the peak at 429 nm. The emission intensity of CNC-PAMAM dropped at pH 11.0, which was in agreement with the previous work.[151] These spectra for CNC-PAMAM at pH 11.0 and pH 3.0 were different from the spectrum at pH 6.5, indicating the formation of large aggregates affected the fluorescent behaviour.

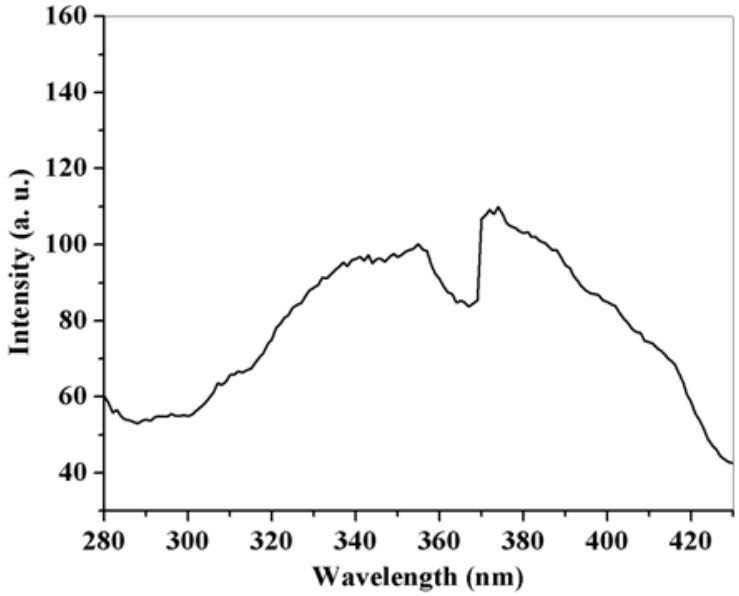

Figure 4.10. Excitation spectrum of CNC-PAMAM.

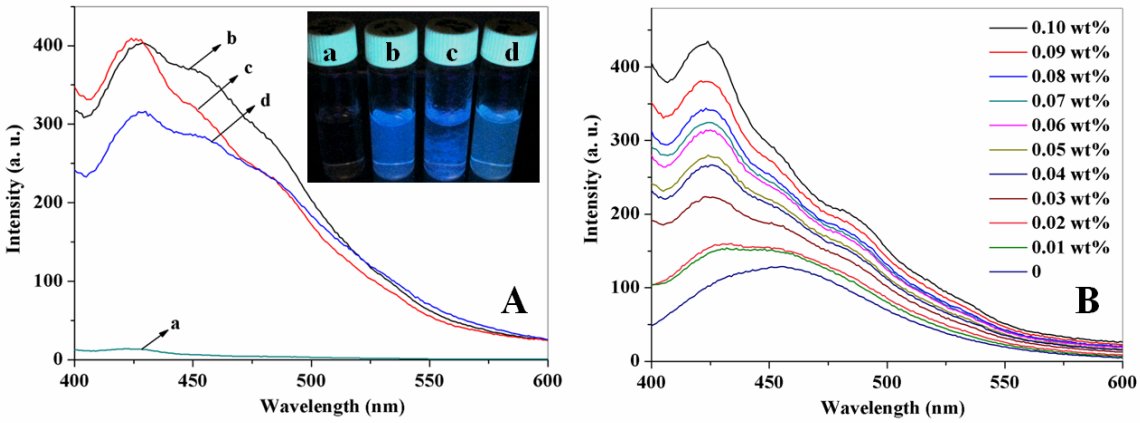

Figure 4.11. Fluorescent emission spectra (A) of CNC-COOH at pH 6.5 (a) and CNC-PAMAM at pH 3.0 (b), pH 6.5 (c) and pH 11.0 (d); fluorescent emission spectra (B) of 0.033 wt. % G6 PAMAM dendrimers (the concentration for synthesizing CNC-PAMAM) with different concentrations of CNC-COOH at pH 3.0.

Meanwhile, physical mixtures of G6 PAMAM dendrimers with CNC-COOH at pH 3.0 were measured using fluorescence spectrophotometry. The data in Figure 4.11B showed that emission intensity of G6 PAMAM dendrimers at around 430 nm increased dramatically after the addition of

CNC-COOH, probably due to light scattering of the aggregates formed. In addition, the observed spectra gradually changed and finally conformed to the spectrum observed for CNC-PAMAM aggregates at pH 6.5 (Figure 4.11A spectrum "c"). While aggregates were formed and phase separation was observed when CNC-COOH was mixed with G6 PAMAM dendrimer suspensions at pH 3.0, CNC-PAMAM was well dispersed at the same pH value. These results further confirmed the covalent grafting of G6 PAMAM dendrimers on CNCs rather than adsorption onto their surface.

4.3.5 Fluorescent emission of CNC-PAMAM/surfactant complexes

Fluorescent emission intensity of CNC-PAMAM/surfactant mixtures at different pH values was further studied. At pH 3.0, aggregates were formed with increasing SDS concentration due to strong electrostatic interactions, and emission intensity of the mixture increased due to enhanced scattering (Figure 4.12A). However, no obvious aggregation and fluorescent emission change was observed when CTAB was added into CNC-PAMAM at pH 3.0, and the negligible decrease of intensity was due to the slightly diluted CNC-PAMAM dispersion (Figure 4.12B). This result indicated that the aggregation level could be effectively evaluated from the fluorescent emission intensity. Similar phenomenon was seen for CNC-PAMAM dispersions at pH 11.0. Negligible emission change was evident after the addition of SDS (Figure 4.12C), while aggregates were formed when CTAB was introduced, which resulted in the increase of fluorescent emission intensity (Figure 4.12D). In addition, the peak at 429 nm gradually shifted to 424 nm. It was also found that when the concentration of SDS reached 0.96 mM at pH 3.0 (Figure 4.12A) and CTAB 0.72 mM at pH 11.0 (Figure 4.12D), no further increase of emission intensity was observed, implying that further increasing the surfactant concentration did not contribute the aggregation level. Furthermore, the final aggregates shared similar spectra with the spectrum of CNC-PAMMA aggregates at pH 6.5 (Figure 4.11A, c), demonstrating the effect of aggregation.

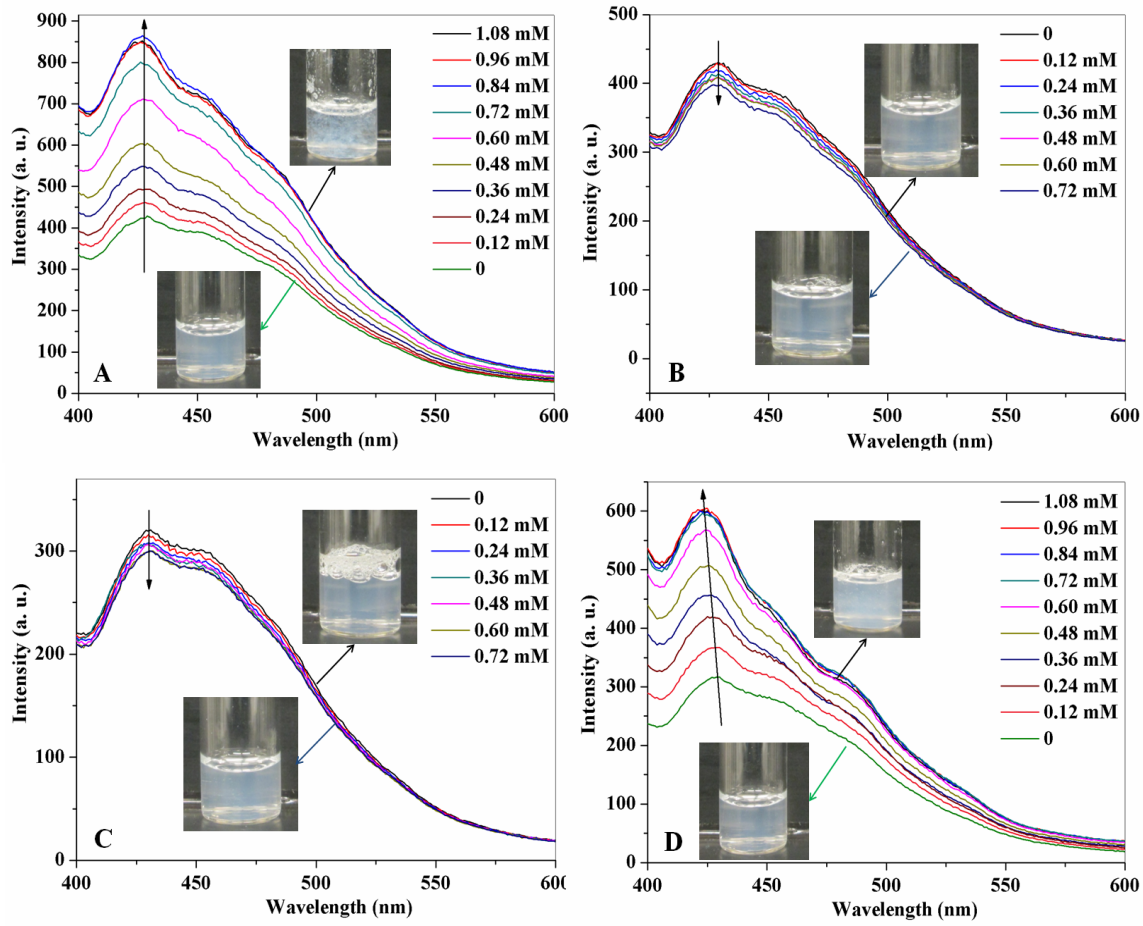

Figure 4.12. Fluorescent emission of 0.08 wt% CNC-PAMAM with increasing concentration of SDS (A) and CTAB (B) at pH 3.0, and SDS (C) and CTAB (D) at pH 11.0.

Based on the results above, we confirmed the fluorescent emission of CNC-PAMAM and the effect of aggregation on the emission intensity. The increase of emission intensity was probably due to scattering from the aggregates formed, and this property can be applied to evaluate the aggregation level.

4.4 Conclusions

G6 PAMAM dendrimer-grafted CNCs (CNC-PAMAM) were successfully prepared. The results of ITC, zeta potential and transmittance measurements demonstrated that CNC-PAMAM showed pH-responsive behaviour. Stable dispersions of CNC-PAMAM were achieved at highly acidic (pH $\leq$ 4) or basic aqueous (pH $\geq$ 10) conditions. Although no obvious crosslinking was observed, large

aggregates or bundles were observed at pH values from 5 to 9 due to insufficient electrostatic repulsion. The pH-responsive performance of CNC-PAMAM was further studied through interactions with SDS and CTAB. These interactions also confirmed the pH dependent surface charge changes of CNC-PAMAM. Moreover, CNC-PAMAM demonstrated strong blue fluorescent emission, and its fluorescent behaviours were largely influenced by the formation of aggregates. Fluorescent intensity may also be applied for the rapid determination of aggregation level. The pH responsive and fluorescent CNC-PAMAM may have potential applications in pH responsive nanodevices, fluorescence-based sensing, and catalytic field as nanoreactors.

Chapter 5*

Sustainable catalysts from gold-loaded polyamidoamine dendrimer-cellulose nanocrystals

Generation 6 polyamidoamine (G6 PAMAM) dendrimer-grafted cellulose nanocrystals (CNCs) (CNC-PAMAM) were synthesized and employed as supports for gold nanoparticles. The successful grafting of PAMAM dendrimers was first confirmed by conductometric-potentiometric titration and pH-dependent zeta potential analyses. Gold nanoparticles with diameters of approximately 2 to 4 nm were synthesized with the PAMAM dendrimers playing the role of nanoreactors and $NaBH_4$ as the reducing agent. More importantly, gold nanoparticles were successfully prepared at pH 3.3 with the PAMAM dendrimers playing the functional role of reducing agent. The effects of CNC-PAMAM concentration and temperature on resulting size of the gold nanoparticles were studied. The gold nanoparticles immobilized on CNC-PAMAM displayed superior catalytic properties towards the reduction of 4-nitrophenol to 4-aminophenol. The enhanced catalytic behavior may be attributed to the improved dispersibility and accessibility of gold nanoparticles within the PAMAM dendrimer network. This work has demonstrated the versatility of CNC-PAMAM both as an effective nanoreactor and reducing agent.

5.1 Introduction

Gold nanoparticles have been employed in a myriad of applications, including bioimaging, biomedicine, chemical sensing and drug delivery.[217] They have also been explored as green catalysts for a variety of chemical reactions, including the oxidation of CO to CO_2, aerobic oxidation of alcohols, C-C coupling reactions and reduction reactions via transfer hydrogenation.[218] As has been observed with other nanoparticle catalysts, gold nanoparticles have a propensity to aggregate in solution, which hinders their performance and ultimately limit their application. In an effort to stabilize gold nanoparticles in solution, complexation with a range of compounds including, but not limited to, thiols, carboxylate ligands, surfactants and polyelectrolytes have been investigated.[90] However, many of these stabilizers are restricted by their low stability, potential toxicity, poor biocompatability or limited biodegradability.[219] Another method under investigation to prevent

*This chapter is adapted from a paper "L. Chen, W. Cao, P. J. Quinlan, R. M. Berry and K. C. Tam. Sustainable catalysts from gold loaded polyamidoamine dendrimer-cellulose nanocrystals. *ACS Sustainable Chem. Eng.*, 2015, 3, 978-985".

aggregation is the homogenous deposition of gold nanoparticles onto a template material, such as graphene sheets,[91] carbon nanotubes,[92] TiO_2[93] and SiO_2 spheres.[94] However, most of the template materials explored thus far lack sufficient functional groups with a metal affinity, such as $–NH_2$, –SiH and –SH, to effectively stabilize and disperse gold nanoparticles.[220]

Recently, CNCs have been explored as renewable biotemplates due to their uniform shape, stability in aqueous suspension, good mechanical strength, high specific surface area, biocompatibility and biodegradability.[19] These attractive features make CNCs promising supports for inorganic nanoparticles, such as Au,[175,221] Ag,[106] Ag-Au alloy,[100] Pd,[89,176] Pt,[108] Se,[111] Fe_3O_4,[114] and our work in Chapter 3. However, generating uniformly dispersed nanoparticle-containing CNCs with well-controlled size and structure remains a challenge. Moreover, the electrostatic attraction that exists between metal ions in solution and sulphate ester moieties present on the surface of CNCs can induce severe irreversible aggregation and phase separation.[100] Since aggregation makes the catalyst surface less accessible to reactants, it reduces the performance of the catalyst system. To circumvent these undesirable characteristics, it is necessary to modify the CNC surface with metal-affinity groups and develop new strategies to minimize particle aggregation.

In this study, poly(amidoamine) (PAMAM) dendrimers were covalently grafted onto the surface of oxidized CNCs (CNC-COOH) via amide bonds. PAMAM dendrimers have a well-defined three-dimensional hyper-branched structure, with primary and tertiary amine groups present at the dendrimer surface and core, respectively. The dissociation properties of these two types of amine groups impart attractive pH-responsive structural changes to the dendrimer.[142,200] Under acidic conditions in aqueous media, the cavities within the PAMAM dendrimers are ideal nanoreactors for producing and hosting inorganic nanoparticles, such as Au,[152,222] Ag,[155] Pt,[223] and Pd[224]. The well-defined structure and size of the cavities yield a narrow size distribution for loaded nanoparticles and the electrostatic and steric repulsions minimize aggregation of the nanoparticles. In contrast to capping agents, each inorganic nanoparticle is stabilized by one dendrimer, imparting high structural stability. The surface of these inorganic nanoparticles is often unpassivated and fully accessible during the catalytic process,[151] which enhances the catalytic performance.[225]

Compounds with abundant amino groups have been applied as metal binding groups,[226] stabilizers[227] and reducing agents[97] for the preparation of inorganic nanoparticles. Their ability to reduce metal ions facilitates the synthesis of inorganic nanoparticles via a simple and green synthetic process. In this work, a CNC-PAMAM hybrid, with abundant metal-binding NH_2 groups, was used as

a support and reducing agent for the incorporation of gold nanoparticles within the dendrimer core. Gold nanoparticles were prepared using sodium borohydride and PAMAM dendrimers as reducing agents. The effects of CNC-PAMAM concentration and temperature on the size of the resulting gold nanoparticles were studied. All CNC-PAMAM-Au systems were stable and dispersible in acidic aqueous solution. The catalytic activity of the two systems was evaluated by the reduction of 4-nitrophenol (4-NP) to 4-aminophenol (4-AP). An added benefit of complexing gold nanoparticles with CNC-PAMAM is that it allowed for direct observation of the complex under TEM, which can also be used to confirm the successful grafting of the PAMAM dendrimer on the CNC surface. Finally, the pH-responsive property of CNC-PAMAM may simplify the separation process and the recycling of the catalysts.

5.2 Experimental section

5.2.1 Materials

Generation 6.0 poly(amidoamine) dendrimers (G6-PAMAM, 5% w/w solution in methanol), sodium hypochlorite (NaClO, 10-15% available chlorine), *N*-hydroxysuccinimide (NHS, 98%), sodium bromide (NaBr, ≥99.0%), gold(III) chloride trihydrate ($HAuCl_4$, ≥99.9%), 2-(*N*-Morpholino)ethanesulfonic acid hydrate (MES buffer, ≥99.5%), *N*-(3-dimethylaminopropyl)-*N'*-ethyl-carbodiimide hydrochloride (EDC, ≥98.0% AT), sodium borohydride ($NaBH_4$, ≥98.0%) and 4-nitrophenol (4-NP, ≥99.5%) were purchased from Sigma-Aldrich and used without further modification. CNCs were supplied by CelluForce, Inc. Purified water was obtained from a Millipore Milli-Q water purification system and was used in preparing all sample solutions.

5.2.2 Methods

5.2.2.1 TEMPO mediated oxidation of CNCs

Oxidized CNCs (CNC-COOH) were prepared according to the method described in a previous report.[22] Typically, 5 g CNCs were dispersed in 375 mL water under sonication. A 10 mL aqueous solution containing 0.0125 g TEMPO and 0.125 g NaBr was then added, followed by the addition of 50 mL NaClO (10-15% w/w). Upon the introduction of NaClO, the dispersion became cloudy, and light yellowish. Sodium hydroxide (0.1 M) was used to maintain a pH value of 10.5 throughout the reaction. After reacting for 4 h, 5 mL ethanol was added to terminate the oxidation and hydrochloride

acid (0.1 M) was used to adjust the pH to 7. The reaction product was purified by dialysis and freeze-dried.

5.2.2.2 G6-PAMAM grafting onto CNCs

The carbodiimide-mediated amidation reaction[212] was used for grafting. CNC-PAMAM was prepared using the previous procedure reported in Chapter 4. 50 mg CNC-COOH was dispersed into MES buffer (pH 6.5, 25 mM) with sonication. Then, 100 mg EDC and 100 mg NHS were introduced into the dispersion, and the mixture was sonicated for 10 min, followed by stirring for 2 h. Next, the mixture was added dropwise to a flask containing 500 µL 5% w/w G6 PAMAM dendrimer in 10 mL water. The reaction was stirred for 24 h, and the CNC-PAMAM product was purified by dialysis and ultrafiltration.

5.2.2.3 Synthesis of CNC-PAMAM-Au using PAMAM as nanoreactors

The pH of a 10 mL 0.008% w/w CNC-PAMAM solution was adjusted to pH 3.3 and stirred for 30 min. 100 µL 5 mM $HAuCl_4$ was then added and the mixture was stirred for 1 h to allow for the adsorption of $AuCl_4^-$ onto CNC-PAMAM. 100 µL 0.05 M $NaBH_4$ was added under vigorous stirring and the initially colourless solution immediately became light brown. The reaction was continued for another 20 min and purified by dialysis (Figure 5.1).

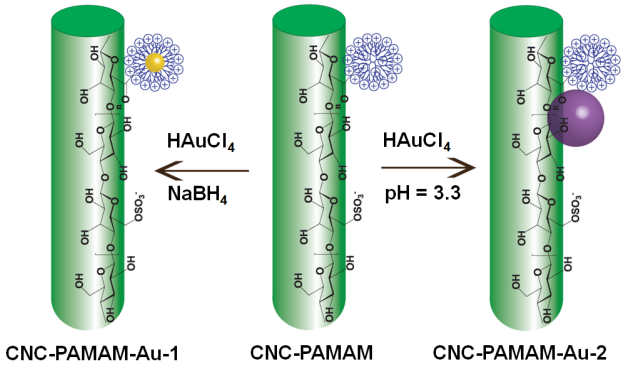

Figure 5.1. Schematic illustration of the CNC-PAMAM-Au synthetic process. The blue spheres represent PAMAM dendrimers, while the yellow and purple spheres signify small and large gold nanoparticles, respectively.

5.2.2.4 Synthesis of CNC-PAMAM-Au using CNC-PAMAM as reducing agents

100 µL 5 mM $HAuCl_4$ was added to 10 mL CNC-PAMAM aqueous solutions of varying concentration with a same pH value of 3.3. The mixtures were stirred for a designated period of time at a given temperature (Scheme 1). By the end of the reactions, the initially colourless solution had turned red. Details on the synthesis of CNC-PAMAM-Au nanohybrids are summarized in Table 5.1.

Table 5.1. Summary of notation and component quantities used to synthesize CNC-PAMAM-Au.

Nanohybrids	CNC-PAMAM (w/w)	$HAuCl_4$ (5 mM)	Reducing agent	T	Time
CNC-PAMAM-Au-1	0.008%	100 µL	$NaBH_4$	25 °C	2 h
CNC-PAMAM-Au-2	0.040%	100 µL	CNC-PAMAM	25 °C	24 h
CNC-PAMAM-Au-3	0.020%	100 µL	CNC-PAMAM	25 °C	24 h
CNC-PAMAM-Au-4	0.008%	100 µL	CNC-PAMAM	25 °C	24 h
CNC-PAMAM-Au-5	0.008%	100 µL	CNC-PAMAM	50 °C	1 h
CNC-PAMAM-Au-6	0.008%	100 µL	CNC-PAMAM	75 °C	0.5 h

5.2.2.5 Evaluation of catalytic performance

A 2.5 mL solution containing 0.10 mM 4-NP and 40 mM $NaBH_4$ was prepared. Then 50 µL 0.009% w/w CNC-PAMAM-Au (Au content: 2.5 nmol) was added to the mixture. The reaction was carried out at room temperature in a quartz cuvette and monitored via UV-vis spectrophotometry.

5.2.3 Characterization

The morphologies of CNCs, CNC-COOH, CNC-PAMAM and CNC-PAMAM-Au were evaluated using a Philip CM 10 transmission electron microscope (TEM) under an accelerating voltage of 60 kV. TEM samples were prepared by spraying 10 µL of a 0.01% w/w dispersion onto a carbon-coated copper grid and drying. The concentrations of functional groups were determined through conductometric-potentiometric titration using a Metrohm 809 Titrando autotitrator. The zeta potential and size distribution of CNCs, CNC-COOH and the CNC-PAMAM system were measured using a Malvern Nano-ZS90 Zetasizer. The pH of the solutions were adjusted using the autotitrator. Titrant solutions (0.1 M HCl or 0.1 M NaOH) were introduced at a flow rate of 0.1 mL/min. Successive UV-

vis absorption spectra were obtained using a Shimadzu U-3000 spectrophotometer with a specified scanning interval of 1 min.

5.3 Results and discussion

5.3.1 Characterization of CNCs, CNC-COOH, and CNC-PAMAM

Conductometric-potentiometric titration has been widely applied to determine the amount of weak acid in cellulose-based systems.[51,228] In a typical procedure, a 0.03% w/w sample dispersion was prepared and the pH was adjusted to ~ 3 by adding 0.1 M HCl, followed by titration using 0.01 M NaOH and simultaneous measurements of solution conductivity and pH. The concentrations of specific functional groups were determined from the quantity of NaOH required to reach the equivalence points. The titration curve of CNCs is shown in Figure 5.2A. One equivalence point (EP), attributed to the neutralization of excess H^+ from HCl, was observed. In Figure 5.2B, the titration curve of CNC-COOH exhibits two EPs, with the first indicating the neutralization of free H^+ and the second signifying the complete dissociation of carboxyl groups. The three regions from left to right correspond to strong acid neutralization, weak acid neutralization and the addition of excess base. From the amounts of NaOH titrated in the second stage, the carboxylate content on CNC-COOH was calculated to be approximately 1.05 mmol/g. Figures 5.2C and 5.2D display the three EPs observed for CNC-PAMAM. The second and third EPs indicate the complete dissociation of carboxyl and amino groups, respectively. The carboxyl and amino content were evaluated to be approximately 0.85 and 1.20 mmol/g, respectively. The titration details are summarized in Table 5.2.

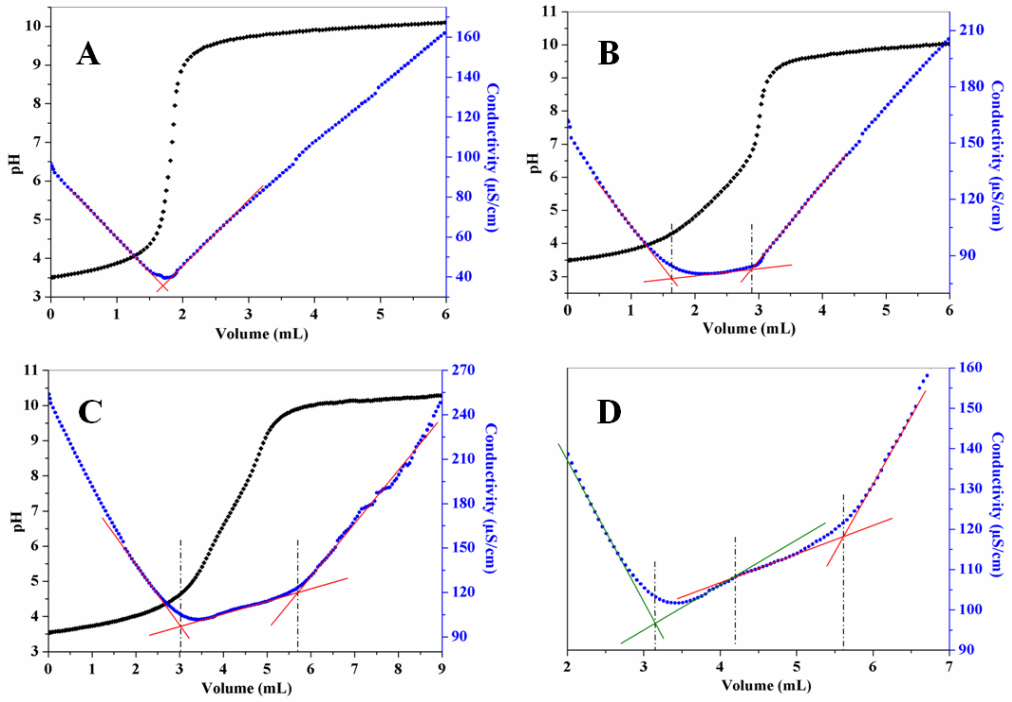

Figure 5.2. Simultaneous conductometric-potentiometric titration curves of 0.03% w/w CNCs (A), CNC-COOH (B), CNC-PAMAM (C and D).

Table 5.2. The calculated concentrations of carboxyl and amine groups on CNCs, CNC-COOH, and CNC-PAMAM.

Sample	Carboxyl groups (mmol/g)	Amino groups (mmol/g)
CNCs	0	0
CNC-COOH	1.05	0
CNC-PAMAM	0.85	1.20

Zeta potential is commonly used to measure the electrostatic potential of nanoparticles at the electrical double layer. Since both CNC-COOHs and PAMAM dendrimers possess pH-dependent functional groups, it is important to analyze and understand the effect of pH on the surface charge of CNC-PAMAM. The pH-dependent zeta potential of CNC-PAMAM is shown in Figure 5.3A. At pH 3, the surface of CNC-PAMAM was highly cationic, with a zeta potential value of + 52 mV.

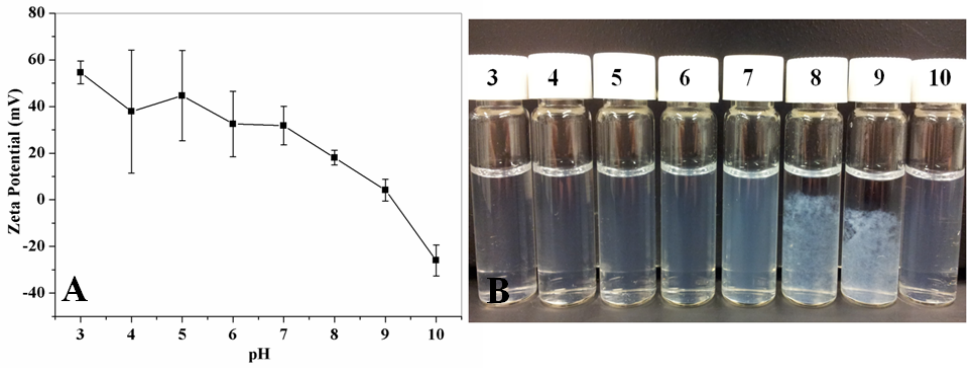

Figure 5.3. pH-dependent zeta potential (A) and corresponding optical photographs (B) of 0.08% w/w CNC-PAMAM solutions.

The observed positive charge is a result of the protonation of amine groups on the surface grafted PAMAM dendrimers. Increasing the pH resulted in a reduction in the zeta potential of CNC-PAMAM due to the deprotonation of carboxyl groups present on the CNC surface. The highly positive zeta potential values observed for pH ≤ 7 suggest a high PAMAM grafting density. Further increase in the pH resulted in the complete deprotonation of amino groups, as illustrated by the corresponding reduction in zeta potential. This resulted in particle instability and formation of precipitates as depicted in Figure 5.3B. As the pH approached 10, the zeta potential of CNC-PAMAM decreased to -30 mV due to the exposure of unreacted carboxylate and sulphate ester groups on the CNC surface. The pH dependent behavior of CNC-PAMAM offers chemical and physical properties that may be valuable for applications ranging from pharmaceutical delivery to Pickering emulsification.

Dynamic light scattering (DLS) was used to measure the size distributions of CNCs, CNC-COOH and CNC-PAMAM (Figure 5.4). CNC-COOH was slightly smaller than the unmodified CNC, which may be attributed to the improved dispersibility of CNC-COOH and the slight degradation of CNC during the alkaline oxidation process. PAMAM grafting on the surface of CNC-COOH, however, yielded particles twice the size of unmodified CNC, as well as a small number of aggregates with a size of 1 to 2 μm. The presence of micron-sized particles suggested the existence of CNC crosslinking via the amine groups present on the PAMAM dendrimers. To further investigate the presence of crosslinking and the overall morphology of the particles, TEM images were taken for both CNC-COOH (Figure 5.5A) and CNC-PAMAM (Figure 5.5B). Figure 5.5A shows well-dispersed CNC-COOH particles, with lengths ranging from 200 to 400 nm. Meanwhile, nanorod bundles were

observed in Figure 5.5B, supporting the hypothesis that some degree of crosslinking exists between CNC-PAMAM particles. Although crosslinking could not be completely avoided during the synthesis process, the PAMAM grafting reaction was still well controlled, and stable dispersions of CNC-PAMAM in water were achievable under acidic and alkaline conditions.

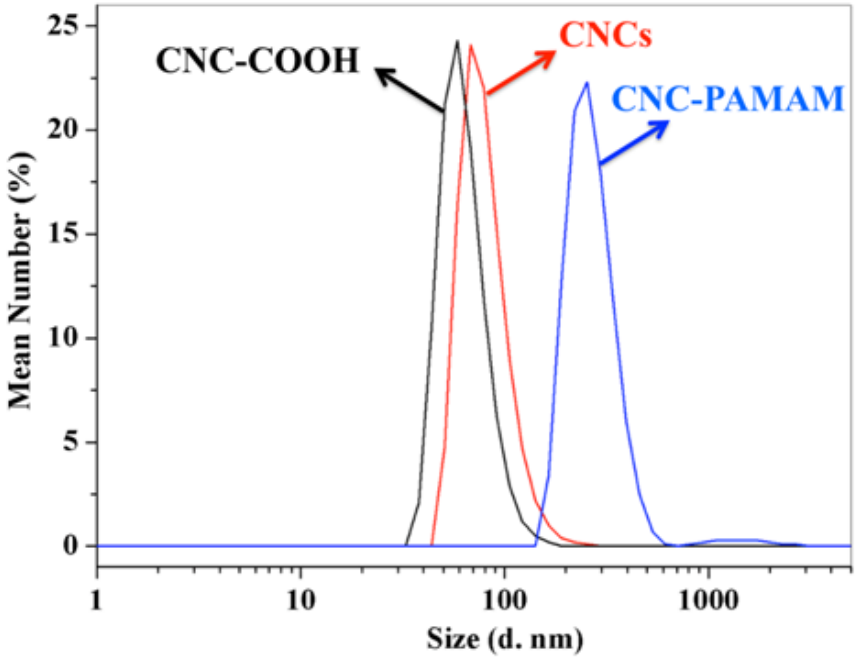

Figure 5.4. Size distribution of CNCs, CNC-COOH at pH 6.5 and CNC-PAMAM at pH 3.5.

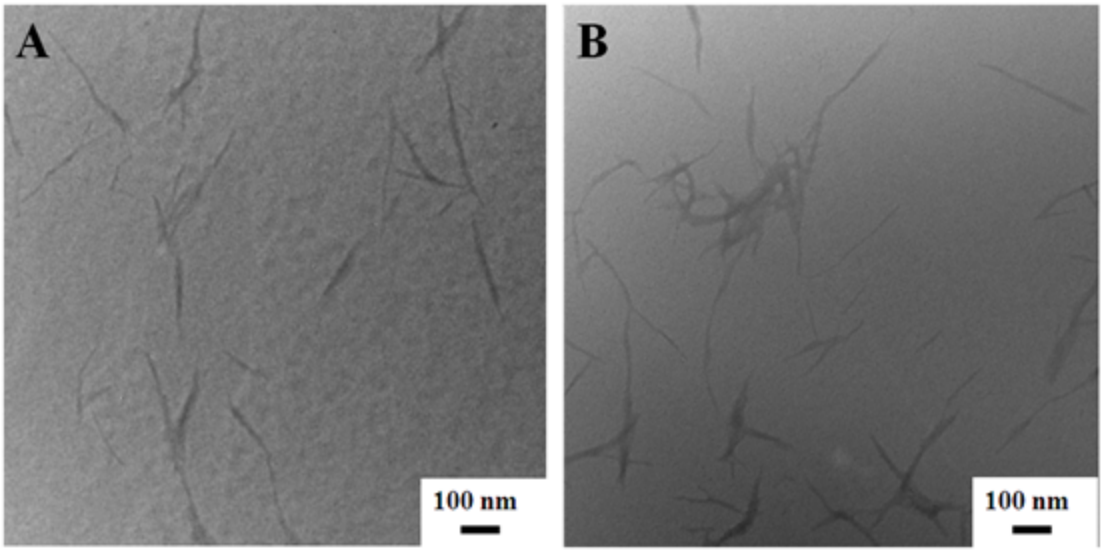

Figure 5.5. TEM images of CNC-COOH (A) and CNC-PAMAM (B).

5.3.2 TEM analyses of Au nanoparticles encapsulated in PAMAM

Due to their small size, it is often difficult to observe dendrimers under TEM. One way to facilitate the direct observation is to encapsulate metal particles within the dendrimer network.[229] In this study, gold nanoparticles were not only used to provide additional functionality to CNC-PAMAM, but also to confirm the successful grafting of PAMAM on CNC. CNC-PAMAM-Au-1 was prepared using $NaBH_4$ as the reducing agent (Table 5.1). Figure 5.6A shows the well-dispersed gold nanoparticles of the order of 2 to 4 nm on CNC-PAMAM, which confirmed the successful grafting of PAMAM dendrimers on CNC.

5.3.3 TEM analyses of Au nanoparticles synthesized using CNC-PAMAM as reducing agents

In a recent study, it was suggested that polymers rich in amine functionality may serve as effective reducing agents for the synthesis of gold nanoparticles.[97] To investigate the efficacy of CNC-PAMAM as both a nanoreactor and reducing agent, gold nanoparticles were prepared on the surface of CNC-PAMAM in the absence of $NaBH_4$ over a range of pH values. Figure 5.7 shows the successful reduction of $AuCl_4^-$ by CNC-PAMAM (0.008% w/w) under mild acidic conditions (pH 3.3 and 4.6). The production of gold nanoparticles caused the solution to turn into a red dispersion. No colour change was observed under neutral and basic conditions (pH $\geq$ 6.2), indicating that the protonated amine groups played an important role in the reduction of $AuCl_4^-$ to Au^0. Large CNC-

PAMAM aggregates were observed for pH ≥ 4.6 due to electrostatic attraction between protonated amine groups and $AuCl_4^-$. However, the sufficiently high positive surface charge of CNC-PAMAM at pH 3.3 allowed for the solution to remain stable. Therefore, all subsequent synthesis reactions were maintained at pH 3.3.

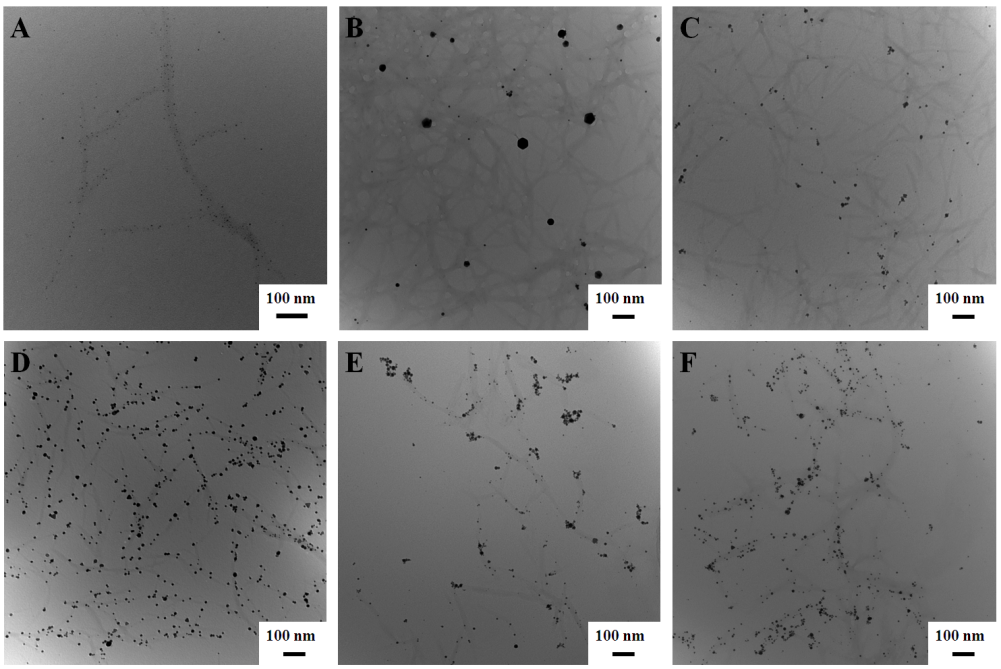

Figure 5.6. TEM images of CNC-PAMAM-Au-1 (A), CNC-PAMAM-Au-2 (B), CNC-PAMAM-Au-3 (C), CNC-PAMAM-Au-4 (D), CNC-PAMAM-Au-5 (E), and CNC-PAMAM-Au-6 (F).

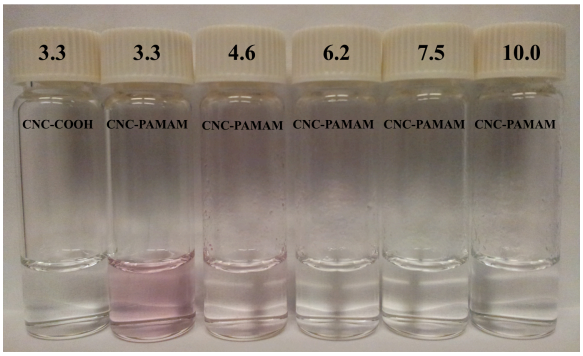

Figure 5.7. Optical photograph of CNC-COOH and CNC-PAMAM solutions after the introduction of $AuCl_4^-$.

To study the effect of CNC-PAMAM concentration on the size of the resulting gold nanoparticles, three concentrations (0.040%, 0.020% and 0.008% w/w) were applied for the reduction of $HAuCl_4$ at 25 °C. TEM images were taken to study the morphologies of the resulting CNC-PAMAM hybrids (CNC-PAMAM-Au-2, CNC-PAMAM-Au-3 and CNC-PAMAM-Au-4, respectively). The TEM image of CNC-PAMAM-Au-2 showed gold nanoparticles with diameters in the range of approximate 10 to 50 nm (Figure 5.6B). Meanwhile, the TEM images of CNC-PAMAM-Au-3 (Figure 5.6C) and CNC-PAMAM-Au-4 (Figure 5.6D) displayed gold nanoparticles with diameters limited to less than 20 nm. Further, the particle size distributions were greatly narrowed by decreasing the concentration of CNC-PAMAM. These results indicate that a high concentration of CNC-PAMAM results in rapid $HAuCl_4$ reduction and nanoparticle growth, yielding a broad size distribution of gold nanoparticles bound to CNC-PAMAM. Therefore, enhanced control over the uniformity of the gold nanoparticle size may be achieved by using a less concentrated CNC-PAMAM reaction system.

To evaluate the effect of temperature on the size of the gold nanoparticles, CNC-PAMAM (0.008% w/w) was also used to reduce $HAuCl_4$ at 50 °C for 1 h (CNC-PAMAM-Au-5) and 75 °C for 0.5 h (CNC-PAMAM-Au-6). The reaction time was significantly shortened due to the increased reaction rate at higher temperatures. Using a low CNC-PAMAM concentration (0.008% w/w), no large gold nanoparticles were observed for either sample. However, minor aggregation of the particles was observed, broadening the overall particle size distributions. Upon comparing CNC-PAMAM-Au-5 (Figure 5.6E) with CNC-PAMAM-Au-6 (Figure 5.6F), the latter was observed to show a slight increase in the size of the particles, which may result from the rapid reduction and particle growth rate at the elevated temperature.

The effect of concentration and temperature on gold nanoparticle size were further confirmed by TEM images of CNC-PAMAM-Au nanohybrids synthesized with different concentrations of CNC-PAMAM at 75 °C. The TEM images showed the aggregates and increased size of gold nanoparticles with 0.020% (Figure 5.8A) and 0.040% CNC-PAMAM (Figure 5.8B). Therefore, good dispersion and narrow size distribution of gold nanoparticles are more likely to be achieved with low concentration of CNC-PAMAM at moderate temperature, when PAMAM serves as the reducing agent. However, particle-size distributions are much narrower for products obtained using $NaBH_4$ as the reducing agent. Generally, no large CNC-PAMAM aggregates were observed for all products, and the attachment of gold nanoparticles on the CNC surfaces were seen, confirming the successful grafting of G6 PAMAM dendrimers on CNCs. With their abundant positive surface charge at pH 3.3,

all CNC-PAMAM-Au hybrid systems were very stable, with no observable precipitates forming within a one-month period.

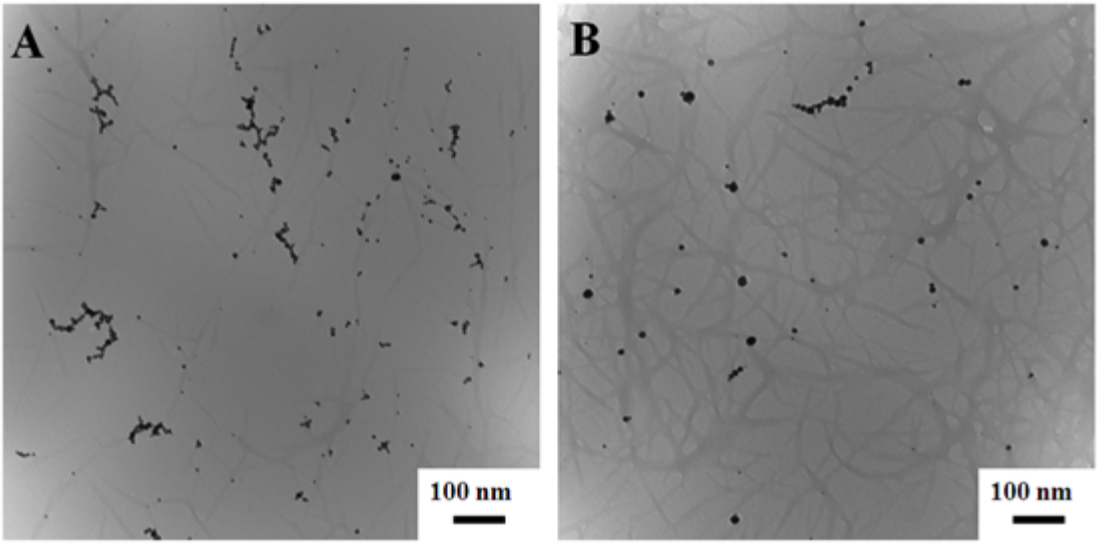

Figure 5.8. TEM images of CNC-PAMAM-Au synthesized under 0.020% (A) and 0.040% (B) CNC-PAMAM at 75 °C.

5.3.4 UV-vis spectra of CNC-PAMAM-Au nanohybrids

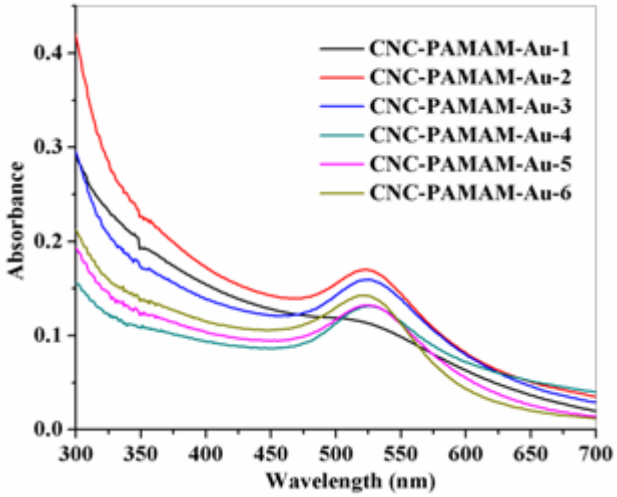

Figure 5.9. UV–vis absorption spectra of CNC-PAMAM-Au nanohybrids.

UV-vis absorption spectra of CNC-PAMAM-Au nanohybrids were measured from 300 to 700 nm (Figure 5.9). These absorption peaks result from localized surface plasmon oscillation and are

characteristic for small gold nanoparticles.[230] CNC-PAMAM-Au-1 possessed a light pinkish colour and a weak, broad absorption peak centered at approximately 510 nm. The CNC-PAMAM-Au nanohybrids produced in the absence of $NaBH_4$, on the other hand, exhibited a rich red wine colour and a strong absorption peak at approximately 525 nm. Compared with CNC-PAMAM-Au-1, the observed red shift indicates an increase in the size of the gold nanoparticles, which agrees with the TEM micrographs.

5.3.5 Catalytic activity of CNC-PAMAM-Au nanohybrids

To evaluate the catalytic activity of gold nanoparticles loaded on CNC-PAMAM, the reduction of 4-NP to 4-AP in the presence of excess $NaBH_4$ and CNC-PAMAM-Au was tested. The corresponding rates of reaction were calculated using the pseudo-first-order kinetic model, where the reduction process was monitored by UV-vis spectrophotometry. Figure 5.10 shows that, in the absence of a catalyst, no reduction of 4-NP occurred. However, when CNC-PAMAM-Au was introduced to the system, the absorbance peak ascribed to 4-NP at 400 nm decreased as a function of time, while a new peak assigned to 4-AP at 290 nm appeared. The catalytic reduction was complete within 270 s for CNC-PAMAM-Au-1 (Figure 5.11A) and 510 s for CNC-PAMAM-Au-4 (Figure 5.11C). Linear correlations between $\ln (A_t / A_0)$ (A_t and A_0 represent the absorbance values of 4-NP at 400 nm at designated time t and t = 0, respectively) and the kinetic parameters were obtained (Figure 5.11B and Figure 5.11D). The pseudo-first-order rate constant *k* was 1.5×10^{-2} s^{-1} and 7.2×10^{-3} s^{-1} for CNC-PAMAM-Au-1 and CNC-PAMAM-Au-4, respectively. These results indicated that the smaller gold nanoparticles present on the surface of CNC-PAMAM-Au-1 displayed a more efficient catalytic performance. The improved efficiency is attributed to their larger specific surface area, which provided more accessible area for the reduction reaction to occur.[231] The activity factor κ, which is a ratio of the rate constant *k* over the total catalyst mass, was calculated in order to compare the present results with those of previously reported studies. κ was estimated to be 3333 and 1600 $s^{-1}g^{-1}$ for CNC-PAMAM-Au-1 and CNC-PAMAM-Au-4, respectively. In comparison with a recently reported Au/graphene catalyst ($\kappa = 31.7$ $s^{-1}g^{-1}$),[232] the environmentally friendly and sustainable catalysts described here offer two orders of magnitude improvement. The turnover frequency (TOF), which represents the number of moles of 4-NP reacted per mole Au per hour, was evaluated for each system and found to be 1.7×10^5 and 8.8×10^4 h^{-1}.

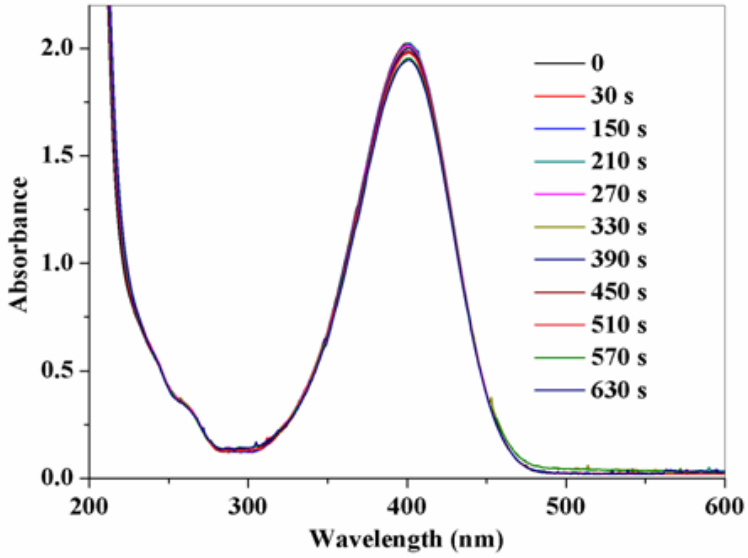

Figure 5.10. Successive UV-vis absorption spectra of the reduction of 4-nitrophenol by $NaBH_4$ in the absence of catalysts.

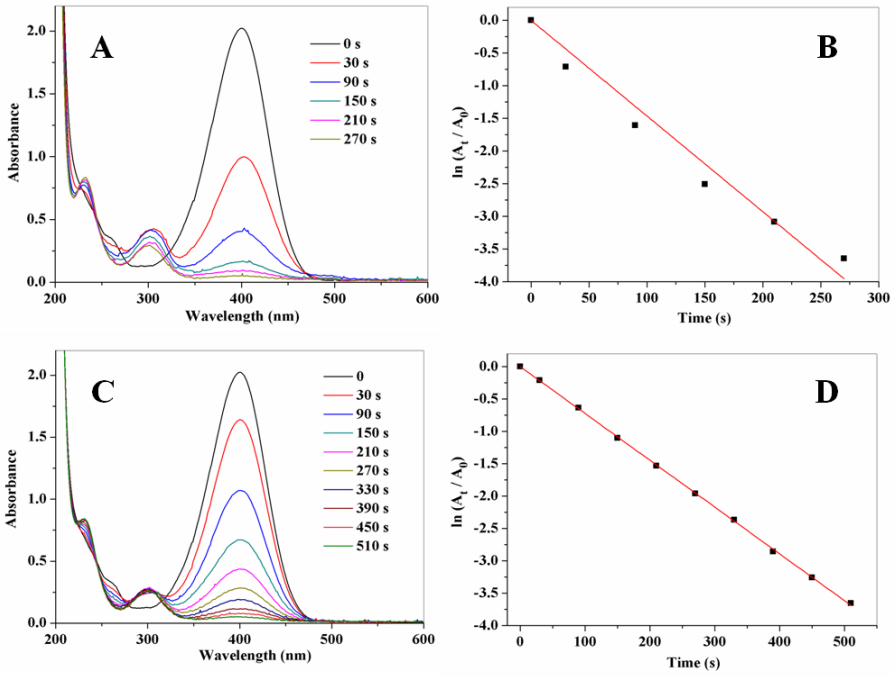

Figure 5.11. Successive UV-vis absorption spectra of the reduction of 4-NP by $NaBH_4$ in the presence of CNC-PAMAM-Au-1 (A) and CNC-PAMAM-Au-4 (C); and the corresponding logarithm of the absorbance at 400 nm as a function of time (B and D).

The catalytic performances of the other CNC-PAMAM-Au nanohybrids were evaluated under same conditions and the results are summarized in Table 5.3. The successive UV-vis absorption spectra and the corresponding logarithm of the absorbance at 400 nm as a function of time are shown in Figure 5.12 for CNC-PAMAM-Au-2 and CNC-PAMAM-Au-3 (effect of CNC-PAMAM concentration) and Figure 5.13 for CNC-PAMAM-Au-5 and CNC-PAMAM-Au-6 (effect of temperature). The results showed that CNC-PAMAM-Au-2 exhibited the lowest catalytic activity, likely a result of the large size of the gold nanoparticles. Other products using CNC-PAMAM dendrimers as the reducing agent for gold nanoparticles displayed good catalytic behavior. No significant trends were observed in their catalytic performance. In general, these results confirmed the relatively high catalytic efficiency of the CNC-PAMAM-Au systems, which may be attributed to well-dispersed, easily accessible, and unpassivated gold nanoparticles present on CNC-PAMAM.

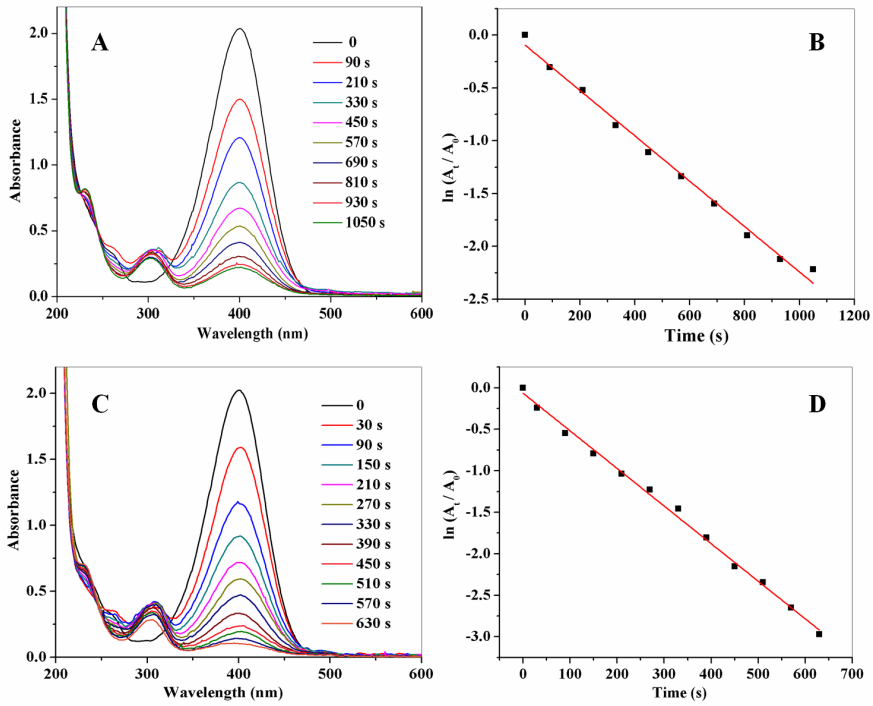

Figure 5.12. Successive UV-vis absorption spectra of the reduction of 4-NP by $NaBH_4$ in the presence of CNC-PAMAM-Au-2 (A) and CNC-PAMAM-Au-3 (C); and the corresponding logarithm of the absorbance at 400 nm as a function of time (B and D).

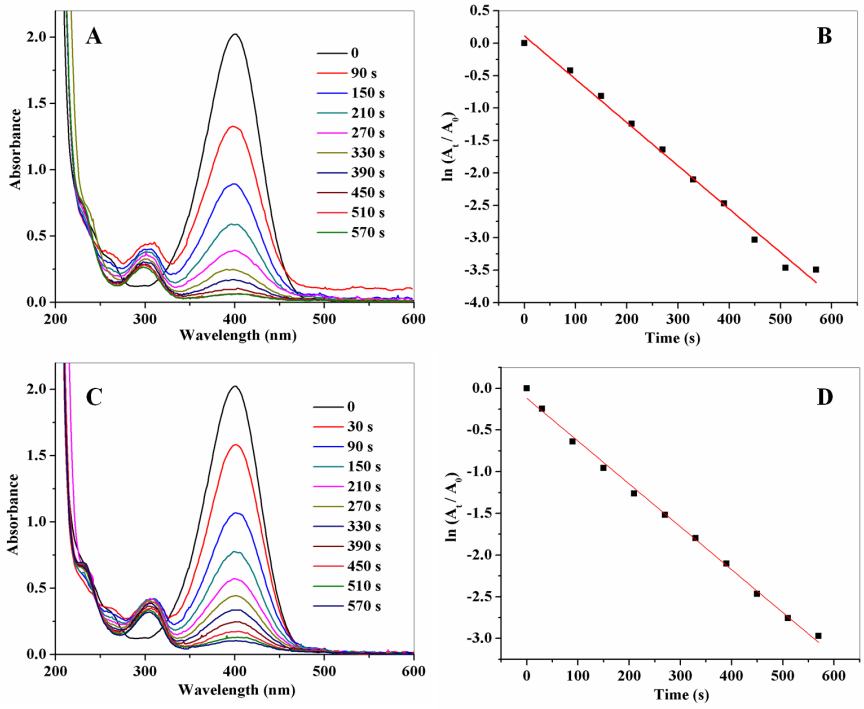

Figure 5.13. Successive UV-vis absorption spectra of the reduction of 4-NP by $NaBH_4$ in the presence of CNC-PAMAM-Au-5 (A) and CNC-PAMAM-Au-6 (C); and the corresponding logarithm of the absorbance at 400 nm as a function of time (B and D).

Table 5.3. Catalytic performance of six products obtained.

Sample	Au nanoparticle diameter (nm)	Pseudo-first-order rate constant k (s^{-1})	Activity factor $\varkappa$ ($s^{-1}g^{-1}$)	Turnover frequency TOF (h^{-1})
CNC-PAMAM-Au-1	2 – 4	0.015	3333	5400
CNC-PAMAM-Au-2	10 – 50	2.2×10^{-3}	489	792
CNC-PAMAM-Au-3	10 – 20	4.5×10^{-3}	1000	1620
CNC-PAMAM-Au-4	10 – 20	7.2×10^{-3}	1600	2590
CNC-PAMAM-Au-5	10 – 25	6.7×10^{-3}	1489	2410

CNC-PAMAM-Au-6	10 – 25	5.1×10^{-3}	1133	1840

5.3.6 Recyclability of CNC-PAMAM-Au nanohybrids as catalysts

It is often valuable to recover and reuse noble metal nanoparticle catalysts. By taking advantage of the pH-responsive characteristics of these new nanostructure systems, the catalysts could be readily recovered by adjusting the pH to neutral, inducing particle aggregation. The aggregated nanocatalysts could then be recovered via filtration, washed and recycled for at least 3 cycles (Figure 5.14). This recyclability of the CNC-PAMAM-Au is particularly relevant to their application in large-scale operations.

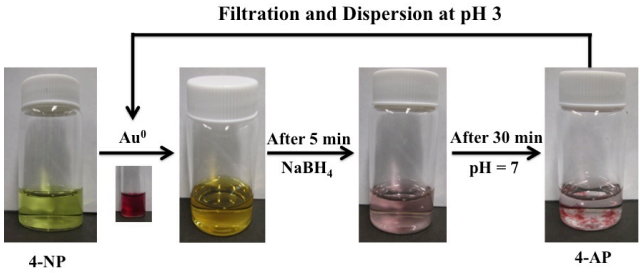

Figure 5.14. Schematic illustration demonstrating the recyclability of the CNC-PAMAM-Au catalytic process.

5.4 Conclusions

PAMAM dendrimers were successfully grafted onto oxidized CNCs using carbodiimide-mediated amidation reaction. FTIR and pH-dependent zeta potential values confirmed the presence of PAMAM dendrimers on the CNC surface. The size of the CNC-PAMAM hybrid, as determined by DLS, was greater than that of CNC and CNC-COOH. The TEM image of CNC-PAMAM showed that the characteristic rod-like CNC structure was preserved, confirming that the grafting reaction was well controlled. Gold nanoparticles of different sizes were formed on the CNC-PAMAM hybrid using $NaBH_4$ or PAMAM dendrimers as reducing agents. The use of $NaBH_4$ resulted in homogeneously dispersed gold nanoparticles (CNC-PAMAM-Au-1) with size 2 ~ 4 nm in diameter. The size distributions of gold nanoparticles were much broader for products obtained using PAMAM dendrimers as the reducing agent. The effects of CNC-PAMAM concentration and temperature on gold nanoparticle size were investigated. No significant difference was observed for their catalytic activities, with the exception of CNC-PAMAM-Au-2, which exhibited the lowest catalytic activity

due to the large size and low specific surface area of the bound gold nanoparticles. CNC-PAMAM-Au-1 and CNC-PAMAM-Au-4 systems displayed good catalytic properties towards reducing 4-NP to 4-AP, with rate constants of 1.5×10^{-2} s^{-1} and 7.2×10^{-3} s^{-1}, respectively. In addition, simple separation and recovery was achieved by adjusting the pH of the system, causing the catalyst particles to phase separate out of solution. Based on the well-studied encapsulation of inorganic nanoparticles within PAMAM dendrimers, other functional inorganic nanoparticle complexes can be further explored.

Chapter 6*

Aqueous synthesis and biostabilization of CdS@ZnS quantum dots for bioimaging applications

Bionanohybrids, combining biocompatible natural polymers with inorganic materials, have aroused interest because of their structural, functional, and environmental advantages. In this work, we report on the stabilization of CdS@ZnS core-shell quantum dots (QDs) using carboxylated cellulose nanocrytals (CNCs) as nanocarrieers in aqueous phase. The high colloidal stability was achieved with sufficient negative charge on CNC surface and the coordination of Cd^{2+} to carboxylate groups. This coordination allows the in-situ nucleation and growth of QDs on CNC surface. The influences of QD to CNC ratio, pH and ZnS coating on colloidal stability and photoluminescence property of CNC/QD nanohybirds were also studied. The results showed that products obtained at pH 8 with a CdS to CNC weight ratio of 0.19 and a ZnS/CdS molar ratio of 1.5 possessed excellent colloidal stability and highest photoluminescence intensity. By anchoring QDs on rigid bionanotemplates, CNC/CdS@ZnS exhibited long-term colloidal and optical stability. Using biocompatible CNC as nanocarriers, the products have been demonstrated to exhibit low cytotoxicity towards HeLa cells and can serve as promising red-emitting fluorescent bioimaging probes.

6.1 Introduction

ZnS-coated core-shell quantum dots (QDs) have attracted a great deal of attention in bioimaging because of their superior properties, such as size-tuneable emission, flexible excitation wavelength, good photochemical stability, and low toxicity.[66,233]. Particular attention has been paid to aqueous phase synthesis of QDs, which avoids the use of organic solvents and subsequent tedious phase transfer procedures.[234,235] One common strategy to obtain well-dispersed QDs in aqueous solution is the utilization of capping agents, physically or chemically attached, to stabilize QDs and reduce aggregation/agglomeration by providing steric or electrostatic repulsion.[10,236] Unfortunately, some widely used capping agents (e.g. mercaptoacetic acid and cetyltrimethyl ammonium bromide) are cytotoxic and nonbiodegradable,[7–9] and many chemicals fail to provide long-time colloidal stability due to degradation, photolysis or oxidation over time (e.g. mercaptoundecanoic acid).[10] These issues

*This chapter is adapted from a paper "L. Chen, Y. Liu, C. Lai, R. M. Berry and K. C. Tam. Aqueous synthesis and biostabilization of CdS@ZnS quantum dots for bioimaging applications. *Materials Research Express*. **2015**, 2(10), 105401".

greatly hamper their biological applications. Another method under investigation to prevent aggregation is the homogeneous deposition of QDs onto carriers with high specific surface area, such as carbon nanotubes[237] and mesoporous silica spheres.[238] These carriers do not only reduce the aggregation of QDs, but also allow the preparation of multifunctional systems by introducing other functional organic groups or inorganic nanoparticles.

Recently, bionanohybrids, combining biocompatible natural polymers with inorganic materials, have aroused considerable interest because of their structural, functional, environmental advantages and enhanced chemical/physical properties.[3] CNCs derived from renewable plant sources possess attractive features such as good aqueous colloidal stability, regular rod-shaped nanostructure, high specific surface area (150–250 m^2/g), high tensile strength (7500 MPa), high stiffness (Young's modulus of 100–140 GPa), low density (1.6 g/cm^3), favourable chemical functionalization, biocompatibility, biodegradability, sustainability, and low cost.[19,172] With these advantages, CNCs have been widely used as reinforcing nanofillers in polymer matrices,[27,239] building blocks or templates in chiral-nematic self-ordering films.[20,240] Recently, CNCs have also been applied as bionanotemplates for various inorganic nanoparticles by our group (e.g. Fe_3O_4 (Chapter 3), Au (Chapter 5), Ag[219]) and others (e.g. Pd,[89,176] Pt,[108] Au,[99,221] Ag,[106] and Ag−Au alloy[100]). Inspired by these works, CNCs functionalized with metal affinity groups are proposed to be promising templates for QDs that possess attractive optical properties.

CNC-supported QDs (CNC/QDs) would find promising applications as optical markers and in biomedical fields. Recently, fluorescent-dye-labelled CNCs have been demonstrated to be useful markers for bioimaging applications. Luong and co-workers illustrated the promising application of positively charged fluorescent rhodamine B isothiocyanate-conjugated CNCs as bioimaging probes.[48] Recent report by Roman and coworkers confirmed the specific folate receptor-mediated cellular uptake of folic acid-conjugated CNCs through fluorescent labels grafted on CNCs.[49] Both publications indicated that CNCs have low cytotoxicity and excellent membrane permeability in various cell lines. However, considering concerns on the low grafting ratio, diffusion of physically adsorbed dyes, and CNC aggregation during dye grafting,[5] photoluminescent QDs stabilized by CNCs may serve as an attractive alternative for bioimaging applications. In addition, the interactions of elongated nanoparticles or filaments (e.g. carbon nanotubes[45] and filomicelles[46]) with cells and within animals have attracted great attention lately. Elongated nanoparticles or filaments showed advantages in terms of long circulation time, rapid renal clearance and effective urinary excretion.[47]

Further assessment of carbon nanotube on cell division, cell survival, cell communication, tissue, and organ formation was conducted in living developing drosophila embryos. The intra- and extracellular accumulation of carbon nanotube did not show interference with cellular divisions and the overall embryonic development.[241] In this perspective, with adjustable aspect ratio in the range of 1-100 depending on cellulosic source materials and the conditions of hydrolysis,[15] CNCs would be good models to investigate these interactions, and CNC/QD allow the direct observation of cellular uptake under fluorescent microscopy.[49] While carbon nanotube and microcrystalline cellulose tend to stimulate inflammatory response, nanosized CNCs are neither genotoxic nor immunotoxic.[43,44,241] Moreover, cellulosed-based materials have demonstrated high biocompatibility with connective tissue formation and long-term stability.[242] Further, functionalization of CNCs through chemical reactions with active primary hydroxyl groups is favorable and well studied, which would largely expand their applications in biomedical fields. Finally, considering the increasing concerns on pharmaceutical substances and nanoparticles in the aquatic environment, our systems also offer a green method by using nontoxic and biodegradable cellulose nanocrystals as stabilizers.

In this work, we report a one-pot facile synthesis of CNC/CdS@ZnS nanohybrids and their application in the in vitro bioimaging of HeLa cells. The sample preparation is illustrated in Figure 6.1. According to previous works, metal carboxylate could serve as specific nucleation sites for the growth of QDs.[243] Therefore, carboxylated CNCs were first synthesized through TEMPO-oxidation process and used as biotemplates for QDs. The loading of QDs involves the metal coordination to carboxylate groups on CNCs and the following in situ growth of CdS QDs. Subsequently, a ZnS shell was coated onto the surface of CdS QDs, playing a dual function in both reducing the toxicity and enhancing the emission intensity. Long-term colloidal stability of these nanohybrids could be achieved through the electrostatic repulsion provided by carboxylated CNCs. The facile synthetic process is highly reproducible. Using biomaterial as stabilizers, the developed CNC/QDs bionanohybrids would have low cytotoxicity and could be directly applied as effective bioimaging probes. In comparison with capping agent- or synthetic polymer-stabilized QD systems, such a nanoparticle-stabilized QD system would exhibit following attractive features: (1) long-term stability could be achieved as QDs are anchored onto CNC surface rather than being stabilized by multiple molecules, thus molecule diffusion is eliminated in our system; (2) in situ aqueous synthetic method offers scalability; (3) highly stable freeze-dried products allow easy storage and transportation due to easy redispersion under sonication.

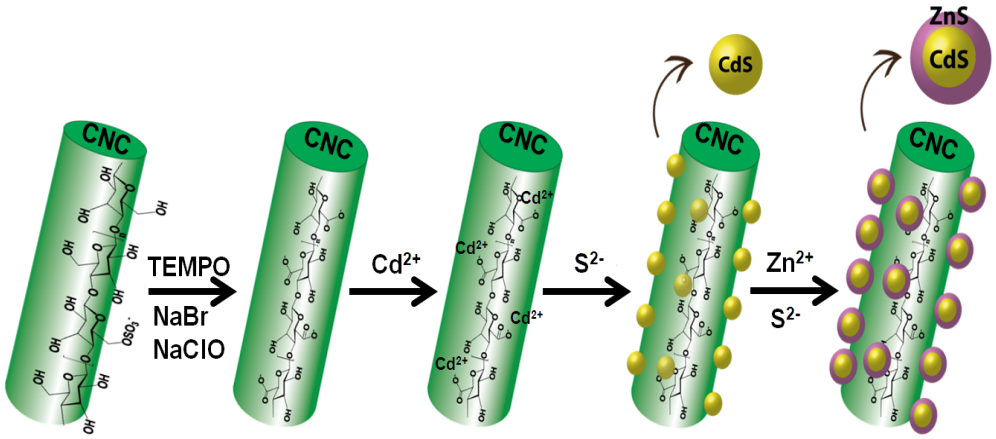

Figure 6.1. Schematic illustration of the synthetic procedure for CNC/CdS@ZnS.

6.2 Experimental

6.2.1 Materials

CNCs were supplied by CelluForce, Inc. Sodium hypochlorite (available chlorine, 10-15%), 2,2,6,6-tetramethylpiperidine-1-oxyl-4-yl (TEMPO), sodium bromide, cadmium chloride, sodium sulphide, zinc nitrate hexahydrate, sodium hydroxide, sodium dodecyl sulphate (SDS), dimethylformamide (DMF), Triton X-100 and 3-(4,5-dimethylthiazol-2-yl)-2,5-diphenyltetrazolium bromide (MTT) were obtained from Sigma-Aldrich Co (St Louis, MO). Alexa Fluor 488 phalloidin were from Life Technologies. The HeLa cell line was purchased from the American Type Culture Collection (ATCC, MD, USA). All the cell culture related chemicals including medium, sera, and antibiotics were purchased from Fisher Scientific Inc. Milli-Q water was used to prepare all the buffers and solution. All other reagents and solvents were of analytical grade and used as received.

6.2.2 Characterization

The UV-Vis absorption spectra were recorded using a Cary 100 Bio UV-Vis spectrophotometer. CNC/CdS and CNC/CdS@ZnS samples for photoluminescence (PL) characterization share the same concentration of CdS QDs. PL spectra were recorded on a Varian Cary Eclipse fluorescent spectrophotometer with an excitation wavelength of 410 nm and an emission range from 500 nm to 780 nm. The Zeta potential was measured using a Zetasizer Nano 90, Malvern at 25 °C. CNC/CdS and CNC/CdS@ZnS samples with a carboxylated CNC concentration of 0.03 wt. % were used for the above tests. TEM characterization was conducted using a Philips CM10 transmission electron

microscope under an accelerating voltage of 60 kV. Around 10 μL of each sample with a carboxylated CNC concentration of 0.03 wt. % was sprayed onto carbon-coated copper grids and dried at room temperature before being observed under TEM. CNC/CdS and CNC/CdS@ZnS (ZnS/CdS = 1.5: 1) samples are purified through dialysis and then freeze dried before being tested under XRD. XRD patterns were recorded by a Rigaku XRD-6000 diffractometer, using Cu Kα radiation (λ = 0.154 nm) at 40 kV, 30 mA. Cell viability of CNC/CdS and CNC/CdS@ZnS treated HeLa cells after a 72-hour incubation period was measured using the tetrazolium-based colourimetric assay (MTT assay). The absorbance at 570 nm was measured by a SpectraMax M3 microplate reader. Confocal fluorescence micrographs were taken using a laser scanning confocal fluorescence microscope (LSM510Meta, CarlZeiss Inc., Thornwood, NY).

6.2.3 Synthesis of CNC/CdS@ZnS

Carboxylated CNCs with a concentration of carboxylate groups of approximately 1.05 mmol/g were produced. The synthesis and characterization protocols of carboxylated CNCs were available in Chapter 4. The as-prepared carboxylated CNCs displayed regular rod-like structure with a size of 10-20 nm in diameter and 200-400 nm in length (Figure 6.2). CNC/CdS nanohybrids were prepared through direct coprecipitation of Cd^{2+} and S^{2-} ions in an aqueous carboxylated CNC suspension at 50 °C. Typically, 15 mg carboxylated CNCs were dispersed in 50 mL water, and the pH value of the dispersion was adjusted to 8 before the introduction of 1 mL 0.02 M Cd^{2+} ions. The mixture was sonicated for 15 mins and stirred for 4 hr under N_2 at 50 °C to allow the formation of carboxylated CNC-Cd^{2+} complex. Then, 1 mL 0.02 M S^{2-} was added to the above solution at a rate of 0.1 mL/min, and CdS QDs was produced instantly. The coating of ZnS was achieved by simultaneously adding various amounts of 0.02 M Zn^{2+} and 0.02 M S^{2-} ions to the CNC/CdS suspension at the rate of 0.1 mL/min.

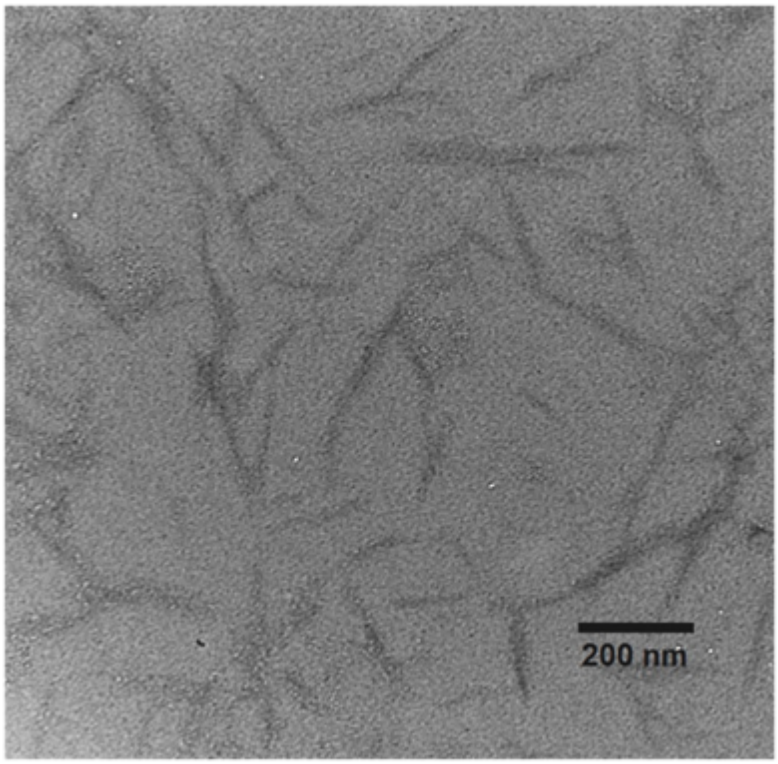

Figure 6.2. TEM image of carboxylated CNCs.

6.2.4 Colloidal and photoluminescent stability test

CNC/CdS and CNC/CdS@ZnS samples were stored at room temperature under an oxygen free environment for a period of 2 months without any sonication or stirring. Then digital images were taken to show the colloidal stability. The fluorescent emission spectra were measured for the same CNC/CdS@ZnS sample with Zn/Cd ratio 1.5: 1 every other week for 2 months.

6.2.5 Cell growth inhibition assay

Cell growth inhibition and the cellular uptake described in the next section were carried out according to one reported procedure.[244] HeLa cells were seeded in 96-well plates with approximate 5,000 cells per well in 100 μL of DMEM/F12 medium and incubated at 37 °C for 24 hours. Afterwards, 100 μL culture medium with various concentrations of CNC/CdS and CNC/CdS@ZnS were prepared and applied to replace the cell medium in each well. Three parallel samples were carried out for each concentration to guarantee the accuracy of data. These cells were incubated for another 72 hours at 37 °C, and then 25 μL freshly prepared MTT solution (5 mg/mL in PBS) was added to each well to achieve a final volume of 125 μL and a final MTT concentration of 1 mg/mL. The 96-well plates

were then placed in the incubator for another 2 hr before the addition of 100 μL extraction buffer (20% SDS in 50% DMF, pH 4.7) to each well. Another 4-hour incubation was allowed before the measurement of absorbance at 570 nm. Cell viability was normalized to that of HeLa cells incubated in the normal cell media, and error bars represent the standard deviation of three parallel samples conducted at each concentration.

6.2.6 Cellular uptake using confocal fluorescence microscopy

HeLa cells were seeded onto 14 mm coverslips with approximate 50,000 cells per well in 24-well plates and incubated for 24 hours at 37 °C. Afterwards, the cells were incubated with CNC/CdS@ZnS at a concentration of 5.80 μg/mL CdS QDs for another 4 hours. Then, the cells in each well were washed with 200 μL ice-cold PBS for three times and then fixed with fresh 4% paraformaldehyde for 10 minutes at room temperature. Alexa Fluor 488 phalloidin was then introduced to stain cell actin. The coverslips were finally placed on one drop of anti-fade mounting media on glass slides to decrease photobleaching of the fluorescent dye. In vitro confocal microscopy images were taken, and the intracellular localization of CNC/CdS@ZnS was visualized using a laser scanning confocal fluorescence microscope.

6.3 Results and Discussion

6.3.1 Impact of CdS/CNC weight ratios on colloidal stability and photoluminescence

It is often observed that large aggregates form when positively charged metal ions are introduced to negatively charged CNC suspension due to electrostatic attractions. The formation of aggregation changes the nanoscale nature and limits their applications. To avoid severe aggregation, products with different CdS to CNC weight ratios (0.29, 0.19, 0.096 and 0.058) were prepared. For CdS to CNC with a ratio of 0.29, phase separation was seen during the reaction, and no PL was observed. However, clear dispersions were achieved for products with lower CdS loading, and red emission was seen under 365 nm UV light. The good dispersion may be attributed to low loading ratio of CdS and excessive negative charges from both carboxylate groups and sulphate ester groups on CNC surface. Interestingly, the different loading ratio of CdS does not affect the emission wavelength, while the PL intensity increases along with the increase of CdS to CNC ratio from 0.058 to 0.19 (Figure 6.3). Therefore, feeding ratio of CdS to CNC was kept at 0.19 in the following sections.

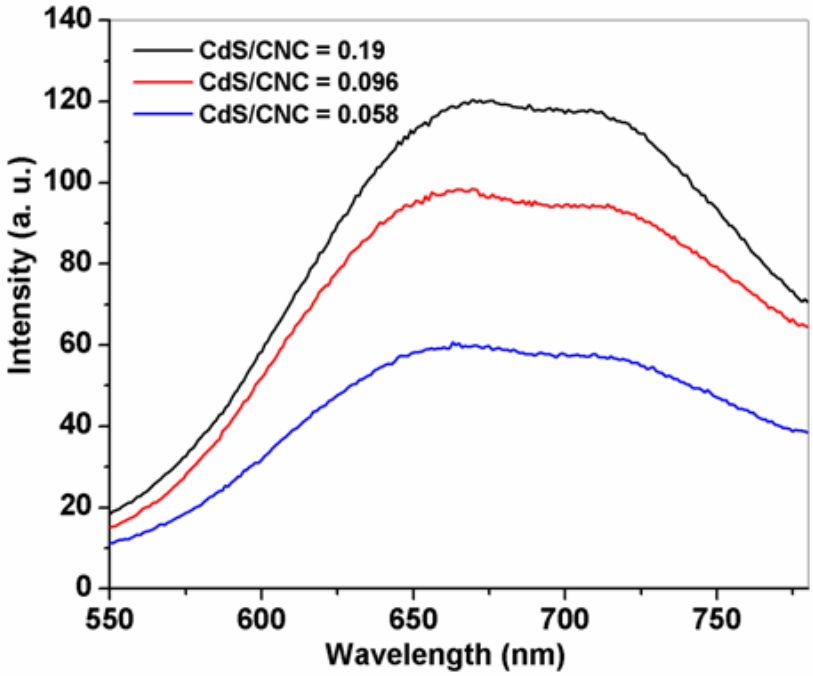

Figure 6.3. PL spectra of CNC/CdS bionanohybrids produced at pH 5 with various CdS to CNC feeding ratio.

6.3.2 Impact of pH and ZnS coating on colloidal stability and photoluminescence

The influence of pH and ZnS coating on CNC/QD PL intensity was studied. The effect of pH was first evaluated, as the nucleation and the growth of CdS QDs during coprecipitation and the stability of carboxylated CNCs strongly depend on pH. The PL intensity of the CNC/CdS hybrid excited at 410 nm increased as pH increased from 5 to 8, a slight decrease of PL intensity was observed for CNC/CdS prepared at pH 9, and a large decline was seen for that synthesized under pH 10 (Figure 6.4a). The effect of pH on PL was further confirmed from digital images taken under 365 nm UV light (Figure 6.4b). The results are in good agreement with previously published work [245]. It shows that the decrease of PL intensity at pH < 8 occurs because of the increase in the solubility of CdS QDs, while the decrease at pH > 8 is due to the formation of hydrated products. Thus, a pH of 8 is maintained to achieve the most efficient PL for aqueous synthesis of CdS QDs. In addition, Zeta potential measurement (Figure 6.5) and transmission electron microscopy (TEM) (Figure 6.6) were used to elucidate the pH effect on the colloidal stability and the morphology of CNC/CdS bionanohybrids. At pH 5, a zeta potential value of –21.7 ± 8.34 mV for CNC/CdS was detected, and

phase separation was observed within a period of 2 weeks due to the protonation of carboxylate groups on CNCs. TEM image of CNC/CdS obtained at pH 5 (Figure 6.6a) showed the cross-linking of CNCs and large CdS particles, which provided further evidence for the poor colloidal stability and reduced PL intensity. The zeta potential of products prepared under pH 6.5 and pH 8 are –50.5 ± 6.8 mV and –45.7 ± 10.3 mV respectively, suggesting high colloidal stability. TEM image (Figure 6.7a) confirmed the uniform dispersion of CdS QDs on CNC surface without forming any QD aggregation and CNC network, indicating that carboxylated CNCs served as good supporting templates and stabilizers for CdS QDs. However, carboxylated CNCs underwent hydrolysis at pH above 9,[51] which led to an increased zeta potential of –21.7 ± 9.3 mV at pH 9 and –23.1 ± 10.2 mV at pH 10. In the TEM images of CNC/CdS synthesized at pH 9 (Figure 6.6b) and 10 (Figure 6.6c), appearance of hydrated products and free CdS aggregates were observed, resulting in decreased colloidal stability and PL intensity. Therefore, pH 8 is optimum for achieving CNC/CdS bionanohybrids with uniform CdS distribution on CNC surface, high colloidal stability and good PL intensity. All products in the following sections are prepared under pH 8.

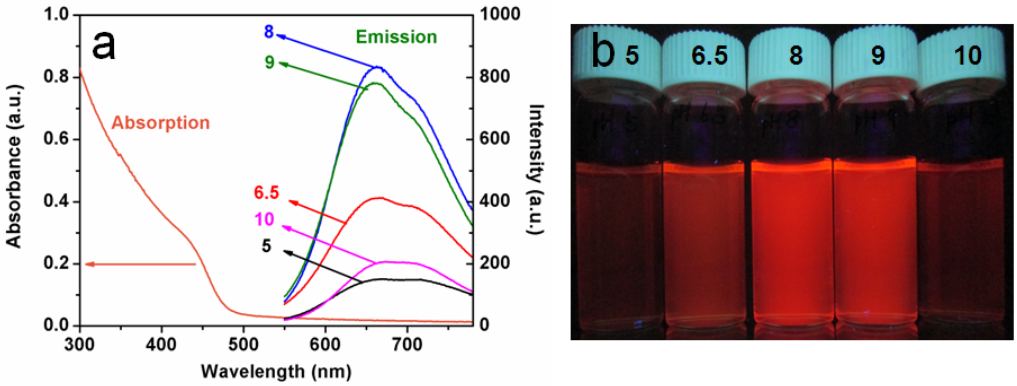

Figure 6.4. PL spectra of (a) CNC/CdS obtained at different pHs and (b) digital image under UV.

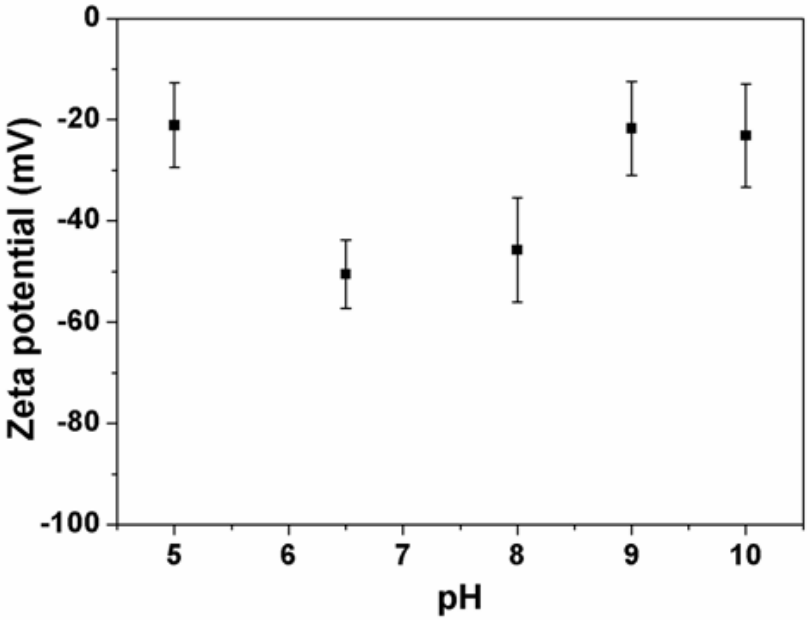

Figure 6.5. Zeta potential of CNC/CdS bionanohybrids produced at various pH values.

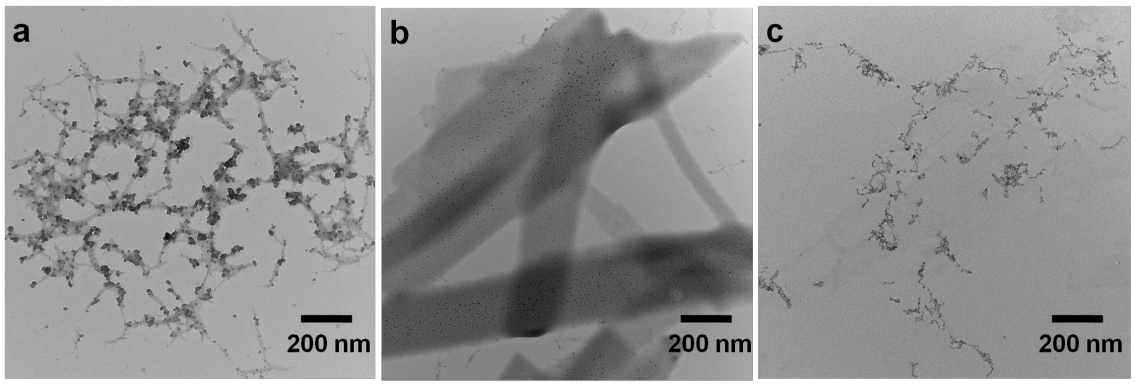

Figure 6.6. TEM images of CNC/CdS obtained under different pHs (a) 5, (b) 9 and (c) 10.

In a control experiment, precipitates formed immediately when the reaction was conducted in the absence of carboxylated CNCs. TEM image (figure 6.7b) confirmed the formation of CdS aggregates, and no PL was observed under UV light. These results indicate the essential role of carboxylated CNCs as stabilizers.

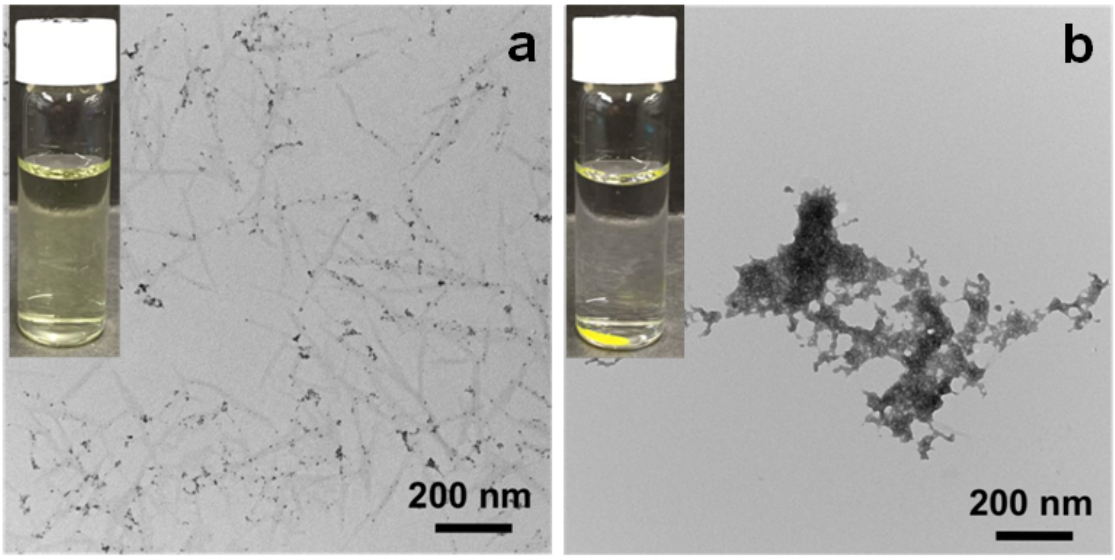

Figure 6.7. TEM images and digital images of (a) CNC/CdS and (b) CdS prepared without carboxylated CNCs.

Dynamic light scattering (DLS) was often applied to evaluate aggregation level and colloidal stability. The size distributions of carboxylated CNC and CNC/CdS QDs based on number are shown in Figure 6.8. Both samples displayed narrow size distribution. No aggregates were seen from the data, indicating the well-controlled synthetic process and well-maintained nanoscale nature of CNC/CdS QDs.

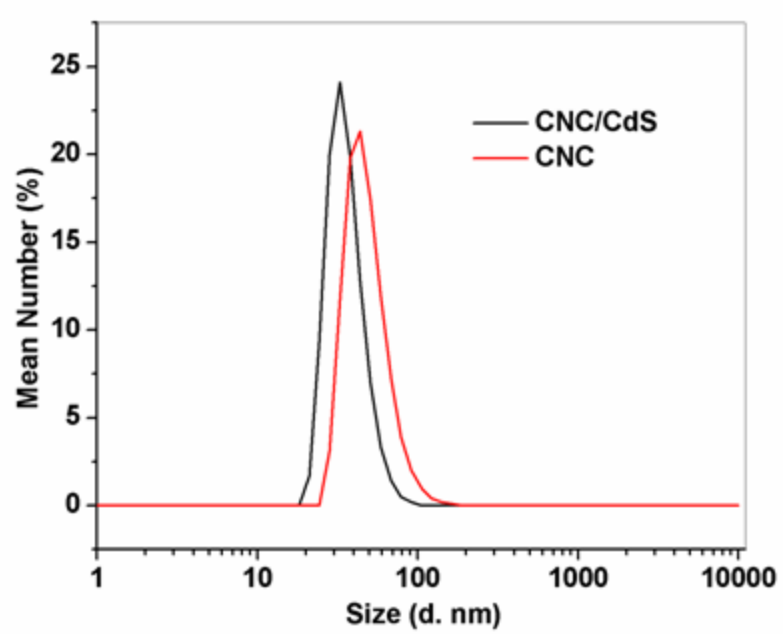

Figure 6.8. Size distribution of oxidized CNC and CNC/CdS nanohybrid measured using a Malvern Nano-ZS90 Zetasizer.

In order to reduce the oxidative degradation and cytotoxicity of CdS caused by the dissociation of Cd^{2+} over time, a ZnS shell was further used to passivate CdS surface. Moreover, ZnS coated CdS QDs are reported to show more efficient PL, as ZnS shells tend to reduce nanoradiative recombination.[246] Therefore, products with ZnS/CdS molar ratios of 0.5: 1, 1: 1, 1.5: 1, and 2: 1 were prepared at pH 8 to determine the optimum condition. Transparent light yellow dispersions with no precipitates were obtained in all cases. Emission spectra (Figure 6.9a) of these samples indicate that PL intensity increased dramatically after the coating of ZnS on CdS, and that PL intensity was the highest for the product with a ZnS/CdS ratio of 1.5: 1. In addition, a blue shift of peaks from 664 nm for CNC/CdS to 644 nm for CNC/CdS@ZnS (ZnS/CdS = 1.5: 1) was evident. The enhancement of PL and the blue shift are associated with interband connection between the CdS core and the ZnS shell,[246] confirming the successful coating of ZnS on CdS surface. The digital image (Figure 6.9b) showed clearly the PL enhancement and the emission colour change from red to orange. However, the PL intensity decreased when the ZnS/CdS ratio was increased to 2: 1, which can be attributed to the incoherent growth of and the formation of defects in the ZnS shell.[247] Therefore, CNC/CdS@ZnS (ZnS/CdS = 1.5: 1) was chosen for further analysis and bioimaging applications.

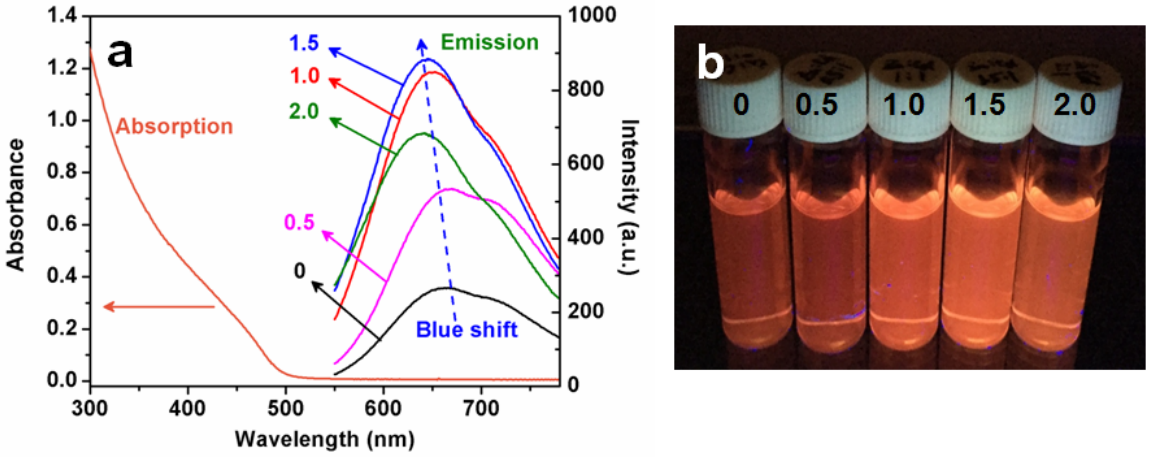

Figure 6.9. (a) PL spectra of CNC/QDs with different ZnS to CdS ratios and (b) digital image of CNC/CdS@ZnS QDs with different ZnS to CdS ratios under UV Lamp.

6.3.3 Crystal structure, morphology, and stability of CNC/CdS@ZnS hybrid

X-ray diffraction (XRD) was applied to examine the crystal structures of CNC/CdS and CNC/CdS@ZnS (ZnS/CdS = 1.5: 1). Both samples displayed the diffraction peaks of CNCs and QDs (Figure 6.10). The well-resolved peaks at 16.1°, 21.7° and 34.2° are attributed to (110), (200), and (004) planes of cellulose crystal structure.[248] The diffraction peaks at 26.2°, 43.7°, and 51.7° are ascribed to (111), (220) and (311) reflections of CdS QDs, indicating a cubic zinc blend crystalline structure of CdS QDs.[249] In addition, the average grain size of the synthesized CdS QDs was estimated to be 3.6 nm using the Scherrer equation: $D = k\lambda/\beta_D \cos\theta$, where D is the average diameter of crystalline domains, λ is the wavelength of the radiation (0.154 nm), k is a constant equal to 0.9, β_D is the peak width at half-maximum intensity in radians and θ is the peak position.[250] With ZnS shell, the peak widths are slightly narrower due to the larger particle size, and the diffraction peaks for CdS@ZnS shifted towards higher 2θ degree, suggesting the successful coating process.[251] Similar changes have also been observed for other core-shell nanomaterials.[250,252,253]

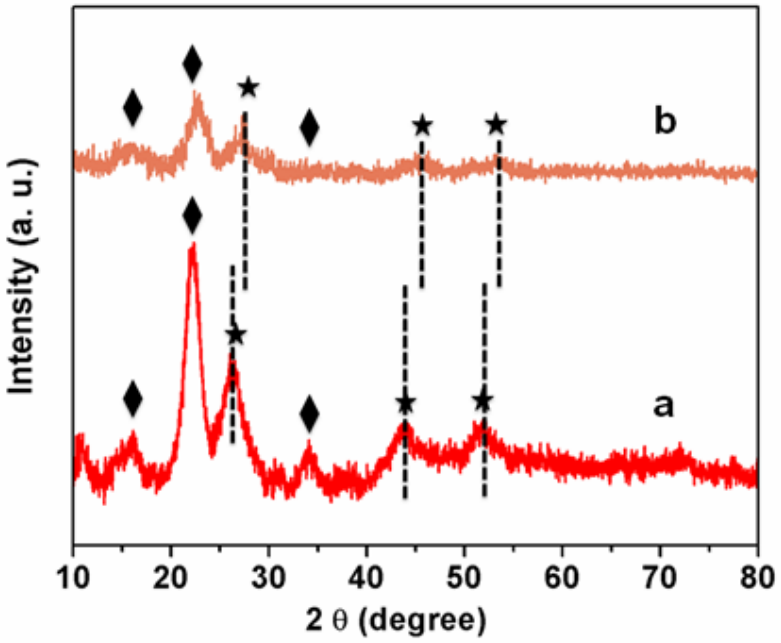

Figure 6.10. XRD patterns of (a) CNC/CdS and (b) CNC/CdS@ZnS. Diffractions peaks from CNCs (diamond) and QDs (star).

TEM images were taken to study the morphologies of CNC/CdS@ZnS prepared at pH 8. With the high contrast between organic CNCs and inorganic QDs, well dispersed CdS@ZnS QDs were only seen on CNC surface. Neither free CdS@ZnS QDs nor CNC aggregates were observed (Figure 6.11). The zeta potential of CNC/CdS@ZnS with values of approximate -40 mV showed no obvious change with the increasing ZnS/CdS ratios (Figure 6.12). No precipitates were formed for CNC/CdS@ZnS over 2 months in an oxygen free environment, and no obvious decrease of PL intensity was detected, indicating the high colloidal and optical stability (Figure 6.13).

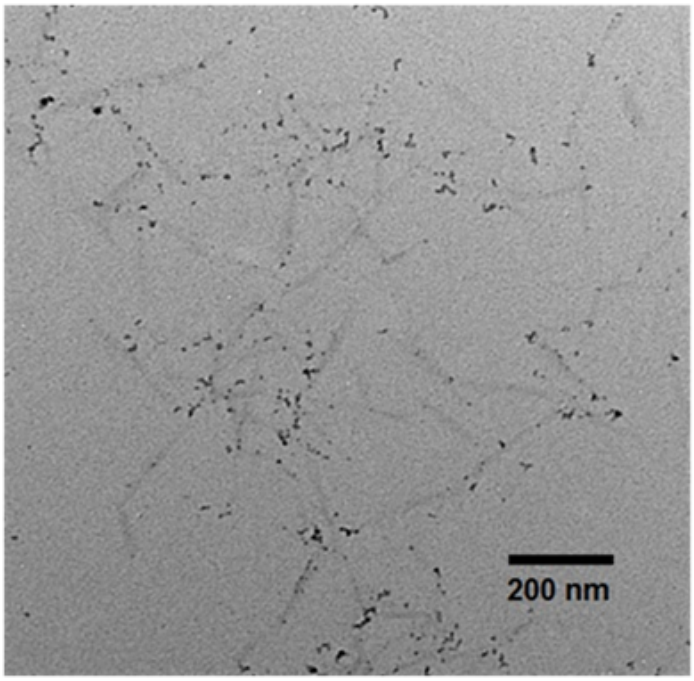

Figure 6.11. TEM image of CNC/CdS@ZnS with a ZnS to CdS ratio of 1.5.

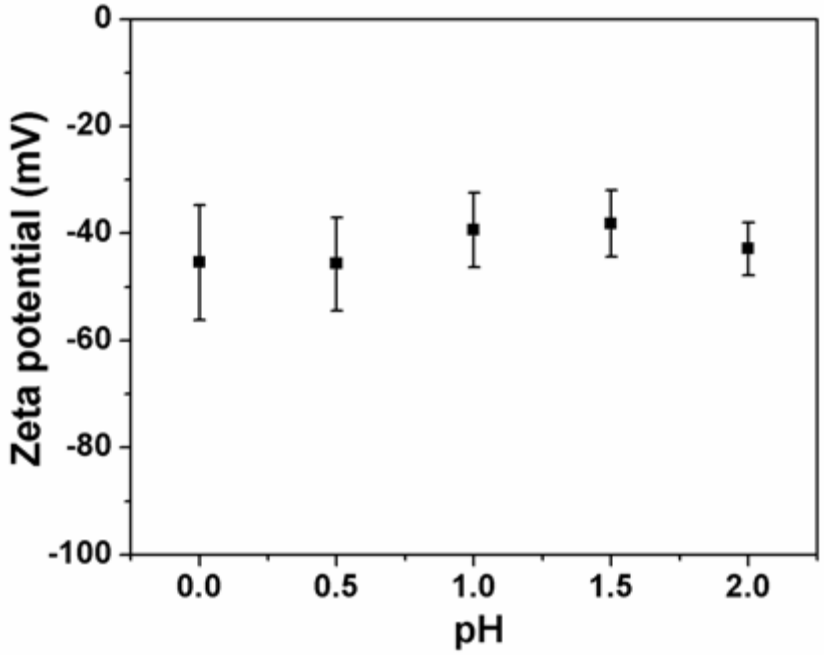

Figure 6.12. Zeta potential of CNC/CdS@ZnS bionanohybrids with various ZnS to CdS ratios.

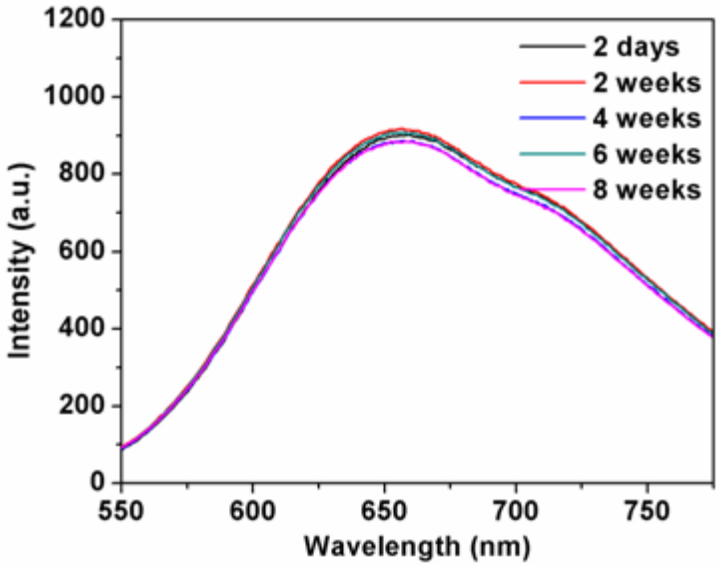

Figure 6.13. PL spectra of CNC/CdS@ZnS taken every other week over a period of two months.

6.3.4 Cytotoxicity of CNC/QD hybrids

With attractive optical properties from QDs, CNC/CdS@ZnS could be a promising candidate for biomedical applications. Therefore, we further evaluated the cytotoxicity of CNC/CdS@ZnS, and HeLa cells were chosen for the present study due to their broad applications in cell studies. MTT assay has been widely employed to study the metabolic activity of cells to evaluate the cytotoxicity of QDs and other materials. The cell viability of CNC/CdS and CNC/CdS@ZnS (ZnS/CdS = 1.5: 1) treated HeLa cells over a 72-hour incubation period is presented in Figure 6.14, and the results are based on the concentrations of CdS QDs. Both CNC/CdS and CNC/CdS@ZnS showed no obvious drop in cell viability with concentrations below 5.80 μg/mL, which can be attributed to the stability of the QDs and the biocompatibility of CNCs. The slight increase of cell viability under mild concentrations of QDs was due to the proliferation. At a CdS concentration of 11.6 μg/mL where CNC concentration reaches 60 μg/mL, cell viability slightly dropped to around 80% for both systems, indicating low cytotoxicity but inhibition of the cell growth under high-dose treatment. The CNC/CdS@ZnS bionanohybrids show less cytotoxicity than a majority of cadmium-based QD systems stabilized by organic capping agents.[254] Further, the improvement of cell viability was seen for CNC/CdS@ZnS, indicating the protection from ZnS shell.

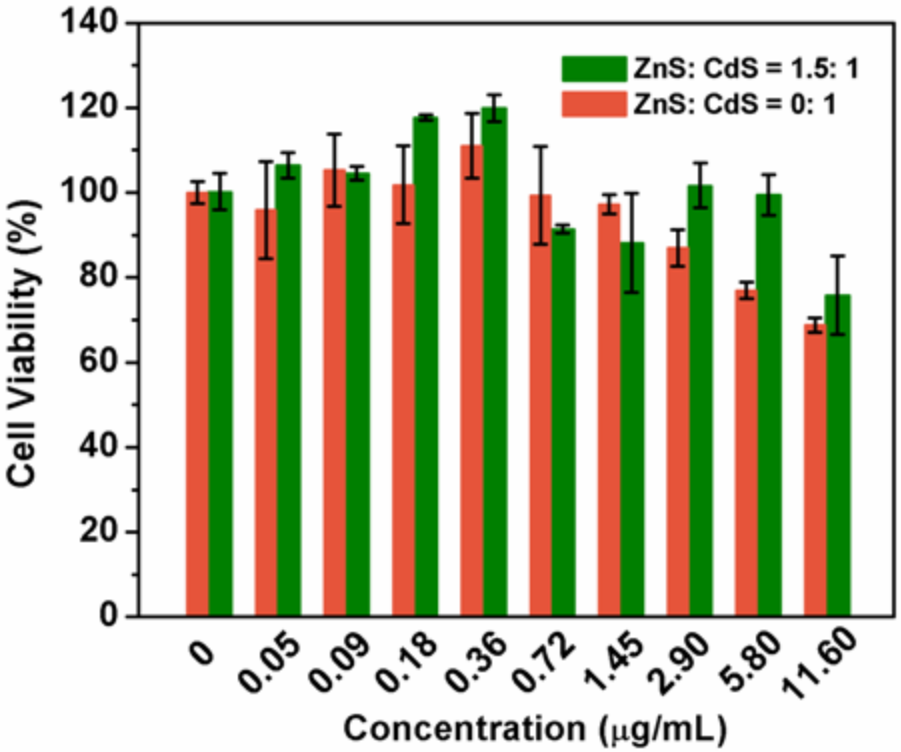

Figure 6.14. Cell viability of CNC/CdS and CNC/CdS@ZnS treated HeLa cells after a 72-hour incubation period measured using the MTT assay. Concentration was based on CdS QDs, and error bars represent standard deviations (n = 3).

6.3.5 Bioimaging applications CNC/CdS@ZnS hybrids

With low cytotoxicity, CNC/CdS@ZnS bionanohybrids are furthered evaluated for bioimaging applications. Cellular uptake of CNC/CdS@ZnS by HeLa cells was examined using confocal fluorescent microscopy. Cytoskeleton actin of HeLa cells was selectively stained green using Alexa Fluor 488 phalloidin (Figure 6.15a). The excitation wavelength of 4', 6-diamidino-2-phenylindole for staining nuclei is 405 nm using confocal fluorescence microscopy, which can also excite CdS@ZnS QDs. Therefore, HeLa cell nuclei were not stained during the sample preparation for bioimaging test. The empty areas within HeLa cells represent the cell nuclei. The intense red PL from CNC/CdS@ZnS (Figure 6.15b) was observed, indicating a high level of cellular uptake. The images also revealed that CNC/CdS@ZnS bionanohybrids were mostly in cytoplasmic area, as minimal red emission was seen in the cell nucleus (Figure 6.15c). Red emission from CNC/CdS@ZnS bionanohybrids appeared mostly in regions of high curvature in Figure 6.14b, which are due to the

locations of CNC/CdS@ZnS bionanohybrids in areas of cytoplasm near the cell nuclei. Another image (Figure 6.16) with more HeLa cells further confirmed the accumulation of CNC/CdS@ZnS bionanohybrids in cytoplasmic area. The location of CNC/CdS@ZnS in cytoplasmic area with much weaker signals in the cell nucleus region is consistent with previous works on bioimaging applications using carbon nanotubes,[241] organic fluorescent nanorods,[255] and gold nanorods.[256] The results demonstrate the effective cellular uptake of CNC/CdS@ZnS, which may lead to potential bioapplications of CNC/CdS@ZnS.

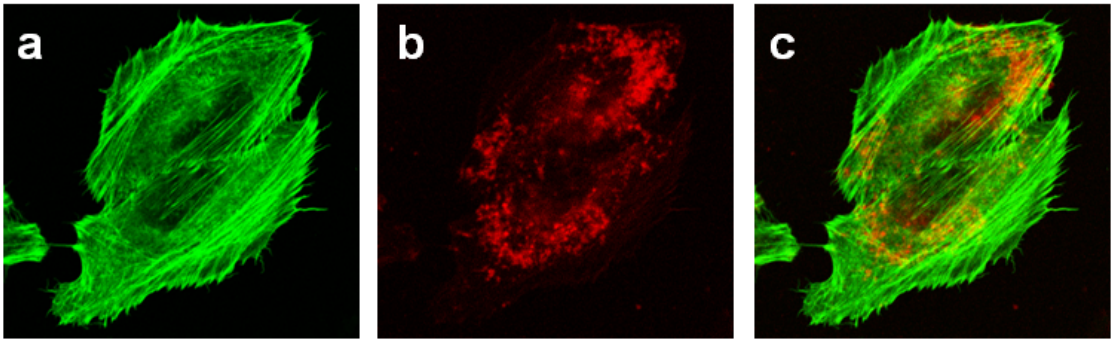

Figure 6.15. Confocal fluorescence micrographs of HeLa cells incubated with CNC/CdS@ZnS (ZnS: CdS = 1.5: 1) at 37 °C for 4 h. The cytoskeleton actin in a and c is stained in green, and the red PL in b and c is from CNC/CdS@ZnS.

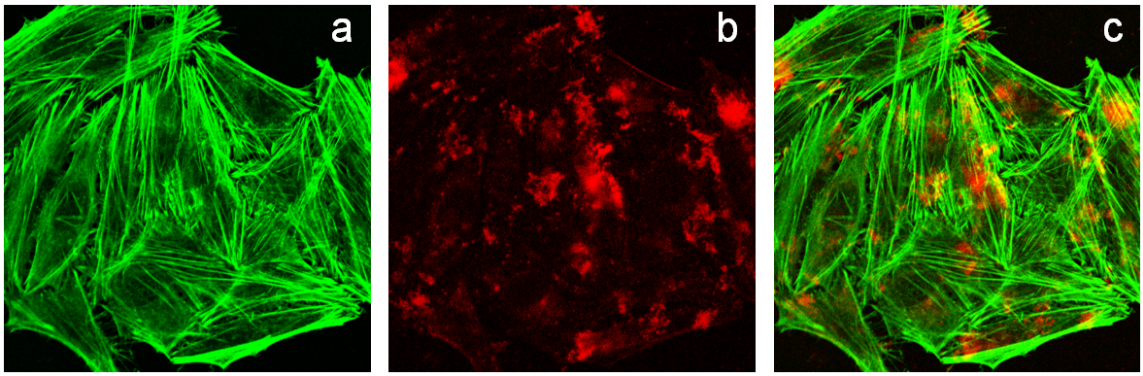

Figure 6.16. Confocal fluorescence micrographs of HeLa cells incubated with CNC/CdS@ZnS (ZnS: CdS = 1.5: 1) at 37 °C for 4 h. The cytoskeleton actin in a and c is stained in green, and the red PL in b and c is from CNC/CdS@ZnS.

6.4 Conclusions

Biostabilized CdS@ZnS QDs were produced through a one-pot reaction in aqueous phase, where carboxylated CNCs served as bionanocarriers. The synthetic method reported here is simple, inexpensive, highly reproducible and scalable. Products obtained at pH 8 with a CdS to CNC weight ratio of 0.19 and a ZnS/CdS ratio of 1.5: 1 exhibited the highest PL intensity and lowest cytotoxicity. Excellent colloidal stability of our products over 2 months and low cytotoxicity were confirmed. CNC/CdS@ZnS bionanohybrids were successfully taken up by HeLa cells, demonstrating their potential applications as bioimaging probes. More generally, the abundant carboxylate groups on this form of CNCs allow further conjugation with drugs, targeting agents and other functional molecules, which may greatly expand their applications in biomedical fields. Furthermore, other optical films or sensors could also be achieved by integrating CNC-stabilized CdS@ZnS into polymer matrices or onto substrates through various bottom-up approaches.

Chapter 7*

Use of CdS quantum dot-functionalized cellulose nanocrystal films for anti-counterfeiting applications

Structural colours and photoluminescence have been widely used for anti-counterfeiting and security applications. In this work, we report for the first time the use of CdS quantum dot (QD)-functionalized CNCs as building blocks for fabricating nanothin films via layer-by-layer (LBL) self-assembly for anti-counterfeiting applications. Both negatively- and positively-charged CNC/QD nanohybrids with high colloidal stability and narrow particle size distribution were prepared. The controllable LBL coating process was characterized through SEM images and ellipsometry data. The rigid structure of CNCs leads to nanoporous structured films on poly(ethylene terephthalate) (PET) substrates with high transmittance (above 70%) over the entire range of visible light, and also result in strong hydrophilicity (contact angles around 40). Most significantly, both tunable structral colours from thin film interference and adjustable emssion colours from embedded QDs can be achieved. Nanothin film coated PET substrates show good flexibility, and strong stability in both water and ethanol. The modified PET films displays exciting applications in anti-counterfeiting with structural colours from thin-film interference and photoluminescence from QDs.

7.1 Introduction

Anti-counterfeiting organizations are in a constant and growing technological arms race to protect the security of goods for consumers and manufacturers.[257] Counterfeit currency, pharmaceuticals, and products in the food industry all lead to severe economic problems and health risks that universally affect consumers.[258,259] For example, according to Currency Counterfeiting Statistics issued by the Royal Canadian Mounted Police, in 2014 alone, over $2.4M worth of counterfeit Canadian banknotes were passed, and only about 18% of counterfeit banknotes were seized.[260] As for pharmaceuticals, it is widely accepted that up to 10% of medicines globally are counterfeit.[261] As such it is of great importance to develop highly scalable and innovative anti-counterfeiting technologies. Traditional

*This chapter is adapted from a paper "L. Chen, C. Lai, R. Marchewka, R. M. Berry and K.C. Tam, Use of CdS quantum dot-functionalized cellulose nanocrystal films for anti-counterfeiting applications. *Nanoscale,* **2016**, 8, 13288-13296".

anti-counterfeiting technologies include watermarks, holograms, security inks, fluorescent inks and colourimetric labels.

While these are inexpensive to manufacture and largely operate on a primary level, allowing consumers to check authenticity, they can be more easily counterfeit without extremely careful examination. Recently developed technologies such as molecular coding, radio frequency identification and laser coding add secondary and tertiary levels of protection.[262] These secondary and tertiary systems are very difficult to counterfeit, however they require expensive equipment to determine their authenticity. Among these systems, multilayer security label techniques have attracted great attention by combining a simple colourimetric system for consumer identification and an additional covert identification authenticated by select instruments, offering significantly enhanced protection.[263] Particularly, colourimetric and fluorometric approaches have attracted a great deal of attention for anti-counterfeiting purposes.[258] In this work, we report a novel thin-film system, which combines structural colours from thin-film interference for colourimetric identification, with photoluminescence from QDs for additional authentication.

Many creatures in nature, such as butterflies and peacocks, display unique and brilliant colours known as 'structural colours'. These colours result from the interaction of light with periodic nanostructures on the surfaces of their wings and feathers.[264] Artificial structural colours have attracted a great deal of attention in anti-counterfeiting applications, display devices, and even liquid sensors.[265] Particularly, for anti-counterfeiting applications, the iridescence of structural colours is of great importance, as it cannot be mimicked using organic dyes.[266] Structural colours are also more durable than organic dyes, and do not suffer from photobleaching over time.

Techniques such as layer-by-layer (LBL) deposition, lithography, and electrochemical etching, have all been applied to create artificial structural colours. Among these techniques, LBL assembly has attracted great attention, owing to its simple manipulation, versatility in choosing building blocks and substrates, and nanoscale control over film thickness and architecture. These films display good structural stability towards heat, solvents and sonication,[267] which is essential for their practical application. Moreover, LBL self-assembly of various building blocks (e.g. graphene nanosheets, metal hydroxide nanosheets, inorganic nanoparticles, fluorescent molecules, polymers, etc.) has been proven to provide enhanced performance of nanothin films in energy storage,[268] gas-barrier packaging,[269] and photo catalysis.[270] With this in mind, LBL self-assembly was chosen in this work to fabricate robust nanothin films for anti-counterfeiting applications.

For many years, cellulose-related products have been incorporated in a huge number of consumer products, and they continue to play important roles in our daily lives. Recently, the discovery and commercial production of CNCs has triggered the development of new products by manipulating this material at the nanoscale level. Compared to other nanosized building blocks, CNCs demonstrate a unique combination of different properties, including very low density, high mechanical strength, uniform nanoscale nature, a wide range of aspect ratios (from 1 to more than 100), abundant negative surface charges from sulphate ester groups, and reactive primary hydroxyl groups. Furthermore, CNCs are readily produced from natural resources such as wood pulp, are commercially available, and are also very low-cost to manufacture.[172] These features make CNCs highly attractive options for developing functional thin films.

Pristine CNCs have served as building blocks for preparation of nanothin films using LBL deposition. The abundant sulphate ester groups on the pristine CNC surface provide a negative charge, and positively charged polymers such as poly(diallyldimethylammonium chloride),[34] poly(allylamine hydrochloride, PAH),[35,36] chitosan,[37,38] polyethyleneimine (PEI),[39] cationic β-chitin nanofibrils,[40] collagen,[41] and xyloglucan[42] can be used as counterparts for the LBL deposition process. Cellulose based thin films with high mechanical strength, light weight, and even structural colours have been reported, however few applications outside of oxygen barriers,[38] anti-reflection coatings,[39] and enzyme sensors[42] have been explored.

In order for these films to find practical applications in other areas such as packaging, sensing, and anti-counterfeiting, it is of significant importance to functionalize CNCs in order to add unique properties. Functionalization of CNCs with organic compounds through chemical reactions with reactive primary hydroxyl groups has been shown to provide unique properties, however, many of these reaction processes suffer from low grafting ratios.[5] Functionalization of CNCs with inorganic nanoparticles (noble metal nanoparticles,[99,108,176] Fe_3O_4 (Chapter 3), alloys,[100] etc.) is still under development. Unfortunately, aggregation of nanoparticles and deterioration of dispersions are commonly observed during immobilization of inorganic nanoparticles, hindering the applications of inorganic nanoparticle-CNCs as nanofillers and nanobuliding blocks. To our best knowledge, inorganic nanoparticle functionalized CNCs have not been reported as building blocks for LBL self-assembled films.

In this paper, we report the fabrication of nanothin films using QD-functionalized CNCs via LBL self-assembly. Thin films fabricated on silicon substrates using LBL deposition of CNCs and PAH have been found to exhibit iridescent colours resulting from thin film interference. These colours can be easily tailored simply by adjusting the layer thickness.[36] Meanwhile, fluorescence from dyes,[271,272] upconversion nanoparticles[273–275] and quantum dots[276,277] have been widely used in anti-counterfeiting. QDs were selected in this work because of their superior optical properties for introducing additional authentication. While capping agent-stabilized QDs can be applied as individual nanobuilding blocks, the fabrication process can be time consuming, tedious and expensive. To simplify the experimental procedure, QDs were anchored onto the surface of CNCs in aqueous solution to produce CNC/QDs. Careful synthetic procedures were applied to achieve highly stable dispersions. Both negatively- and positively-charged CNC/QDs were prepared, and were then alternatively self-assembled on various substrates to form nanothin films. Iridescent colours from thin film interference provide a method for colourimetric security, and the embedded QDs offer a secondary UV-emission based security layer. Furthermore, by making negatively-charged CNC/QDs with red emission QDs, and positively-charged CNC/QDs with green emission QDs, we have shown many different emission colours can be achieved in the overall film by carefully adjusting the concentrations of the two building blocks. Combining these aspects, we report a novel, widely applicable, and highly affordable multilayer security film for anti-counterfeiting applications.

7.2 Experimental section

7.2.1 Materials

Sodium hypochlorite (NaClO, 10-15% available chlorine), sodium bromide (NaBr, ≥99.0%), 2, 2, 6, 6-tetramethylpiperidine-1-oxyl (TEMPO), cadmium chloride, sodium sulphide, sodium hydroxide, polyethyleneimine (PEI), sodium hydroxide, hydrochloric acid, polyvinyl alcohol (PVA), and poly(sodium 4-styrenesulfonate) (PSS) were purchased from Sigma-Aldrich and used without further modification. CNCs were supplied by CelluForce, Inc., and were produced through sulphuric acid hydrolysis of wood pulp, resulting in regular rod-like structure with a diameter of 10-20 nm and a length of 200-400 nm. Purified water was obtained from a Millipore Milli-Q water purification system and was used in preparing all sample solutions.

7.2.2 Methods

7.2.2.1 Synthesis of CNC-COOH and partially desulphated CNCs (pdsCNCs)

CNC-COOH was prepared using TEMPO-mediated oxidation.[22] The synthesis and characterization are available in Chapter 4. Partially desulphated CNCs were produced according to a previously published work.[26] In a typical procedure, CNCs (0.5 g) were dispersed in water (250 mL), and HCl (0.5 M) was added to achieve a final acid concentration of 0.025 M. Afterwards, the dispersion was heated to 80 °C and kept under stirring for 24 h. The reaction was terminated by immersing the reaction flask into an ice bath, and the partially desulphated CNCs were purified using a 12,000-14,000 molecular weight cut-off dialysis membrane and subsequently freeze-dried.

7.2.2.2 Synthesis of CNC-COOH@CdS nanohybrids

CNC-COOH/CdS nanohybrids were prepared through direct co-precipitation of Cd^{2+} and S^{2-} ions in an aqueous carboxylated CNC suspension at 50 °C. Typically, carboxylated CNCs (15 mg) were dispersed in water (50 mL) under sonication for 15 minutes. The pH value of the dispersion was adjusted to 8 before introducing Cd^{2+} ions (1 mL, 0.02 M). The mixture was sonicated for another 15 minutes and then stirred for 4 hours under N_2 at 50 °C to allow the formation of carboxylated CNC-Cd^{2+} complexes. Then, S^{2-} (1 mL, 0.02 M) was added to the above solution at a rate of 0.1 mL/min, and CdS QDs were produced instantly.

7.2.2.3 Synthesis of pdsCNC-PEI@CdS nanohybrids

15 mg pdsCNCs were mixed with 50 mL water, and then 1 mL 2 wt. % PEI was added. The mixture was sonicated for 30 min until a homogenous suspension was obtained, and further stirred for 1 hour to form PEI-coated pdsCNCs (pdsCNC-PEI*)*. Then 1 mL of 0.02 M Cd^{2+} was introduced, and the mixture was stirred for 4 hours to allow the formation of NH_2-Cd^{2+} complexes. 1 mL of 0.02 M S^{2-} was added to form CdS QDs. The obtained pdsCNC-PEI@CdS was directly used without any purification.

7.2.2.4 Preparation of $(pdsCNC\text{-}PEI@CdS/CNC\text{-}COOH@CdS)_n$ thin films on various substrates

Silicon wafers were immersed in fresh piranha solution (H_2SO_4: H_2O_2 (30%) = 3:1, v/v) (warning: piranha solution is very corrosive and must be treated with extreme care) for 30 minutes, followed by rinsing in deionized water and drying under N_2 flow before being used. Polyethylene terephthalate

(PET) substrates were washed using water and ethanol, and then dried. (CNC-COOH@CdS/pdsCNC-PEI@CdS)$_n$ thin films were coated onto these substrates through LBL self-assembly. In this experiment, CNC-COOH@CdS is negatively charged, and pdsCNC-PEI@CdS is positively charged. Therefore, these two CNC/QD systems are perfect counterparts to fabricate thin films through electrostatic LBL deposition. PVA with a final concentration of 0.1 wt. % was added to pdsCNC-PEI@CdS, which acts as a binder inside the thin films. Substrates were first dipped into pdsCNC-PEI@CdS suspension for 10 min, rinsed using water, and then dried using N_2. The same procedure was repeated many times, immersing substrates alternatively in both CNC/QD suspensions to achieve (pdsCNC-PEI@CdS/CNC-COOH@CdS)$_n$ multilayer thin films.

7.2.3 Characterization

Elemental analysis of CNCs, CNC-COOH and pdsCNC was performed using an elemental analyzer (Vario Micro cube, Elementar Americas, Inc.) to study the atomic composition of these materials. Three parallel measurements were conducted for each sample, and the average data is reported. The UV-Vis absorption spectra of CNC/QDs were recorded using a Cary 100 Bio UV-Vis spectrophotometer (Varian). Emission spectra of CNC-COOH@CdS, pdsCNC-PEI@CdS and modified PET films were recorded on a Varian Cary Eclipse fluorescent spectrophotometer. X-ray diffraction (XRD) patterns were recorded by a Rigaku XRD-6000 diffractometer, using Cu Kα radiation (λ = 0.154 nm) at 40 kV and 30 mA. Zeta potential measurements of CNC-COOH@CdS and pdsCNC-PEI@CdS were conducted using a Malvern Zetasizer Nano 90 at 25 °C. The reported zeta potential data is an average of 13 tests, and includes standard deviations. A Malvern Zetasizer Nano ZS 90 dynamic light scattering system (25 °C; laser wavelength 633 nm; scattering angle 90°) was used to evaluate the aggregation levels of CNC-COOH@CdS and pdsCNC-PEI@CdS by taking 3 parallel measurements for each sample. All thermogravimetric analysis (TGA) tests were conducted using a high-resolution instrument (Mettler/Toledo, SDA851e) under a steady flow of N_2 with a temperature range of 30-700 °C at a constant heating rate of 10 °C min^{-1}. The morphology of thin films was investigated using a scanning electron microscope (SEM ZEISS) with an acceleration voltage of 20 kV. Energy dispersive X-ray spectroscopy (EDX) was used to identify atomic species present in CNC/QDs. The morphologies of CNC/QDs were evaluated using a Philip CM 10 transmission electron microscope (TEM) under an acceleration voltage of 60 kV. The reflectivity measurements for nanofilms on silicon wafers were conducted using a UV-2501 PC Spectrophotometer (Shimadzu). A Horiba Jobin Yvon MM-16 Spectroscopic Ellipsometer was used

to measure the film thickness of the CNC@QD layers on a silicon wafer. The ellipsometer was set to 633 nm at a fixed angle of 70° off-normal. Water contact angle measurements were carried out by placing 3 water droplets of 5 μL on different spots of both raw and modified PET substrates, and the contact angle was determined by analyzing the images of water droplets using MATLAB code. The orientation of nanorods was also studied using a polarized optical microscope.

7.3 Results and Discussion

7.3.1 Characterization of CNC-COOH and pdsCNC

To successfully prepare positively- and negatively- charged CNC/QD systems, CNCs underwent TEMPO-oxidation to form CNC-COOH and partial desulphation to prepare pdsCNC. The TEMPO-assisted oxidation introduces carboxyl groups onto the CNC surface. These carboxyl groups are vital for loading QDs on CNCs by forming carboxyl-Cd^{2+} complexes. This results in negatively charged CNC-COOH@CdS with abundant carboxyl groups and sulphate ester groups. To obtain pdsCNC-PEI@CdS, partial desulphation is required to obtain a uniform coating of PEI on the CNC surface. Without partial desulphation, agglomeration and phase separation happens immediately when adding PEI into the CNC dispersion, due to strong electrostatic attractions. Reducing the number of sulphate ester groups is required to prevent agglomeration, however a slight negative charge is still required to assist the coating of PEI on the CNC surface. The PEI coating provides positive charges around the CNC surface, providing a good counterpart for LBL deposition.

Table 7.1. Elemental weight compositions of CNCs, CNC-COOH and pdsCNCs

Sample	N [%]	C [%]	H [%]	S [%]
CNCs	0	41.1	5.6	0.7
CNC-COOH	0	39.3	5.1	0.7
pdsCNCs	0	40.9	5.0	0.4

To confirm the oxidation and partial desulphation of CNCs, elemental weight compositions (nitrogen, carbon, hydrogen, sulphur) of CNCs, CNC-COOH and pdsCNCs were obtained (Table 7.1). The weight percentage of carbon decreased from 41.1% to 39.3% after oxidation mainly due to the increase of oxygen content. The pdsCNCs show a large decrease in sulphur content of 0.4 %, indicating the successful partial removal of sulphate ester groups.

7.3.2 Morphology and optical property of CNC-COOH@CdS and pdsCNC-PEI@CdS

Stable CNC-COOH@CdS and pdsCNC-PEI@CdS aqueous dispersions were then prepared. No obvious precipitants were observed over a 6-month period for dispersions stored in a 4 °C fridge. The high colloidal stability can be attributed to the low density of CNCs (1.6 g cm^{-3}) and sufficient electrostatic repulsion among nanoparticles. TEM images were taken to analyze the morphology of the system. Figure 7.1A shows the nanorod structure of CNC-COOH and the well-dispersed CdS QDs (around 4 nm in diameter) on the CNC surface. Figure 7.1B displays the morphology of pdsCNC-PEI@CdS, where the diameter of the nanorods increases dramatically due to the PEI coating, when compared to CNC-COOH@CdS. CdS QDs with a decreased size of approximate 2 nm in diameter were seen within the PEI shell on pdsCNC. The reduced size of CdS QDs may be attributed to abundant amine groups on branched PEI that serve as nucleation sites for synthesizing CdS QDs.[278,279]

The optical properties of CNC-COOH@CdS (Figure 7.1C) and pdsCNC-PEI@CdS (Figure 7.1D) were further studied using UV-vis spectroscopy and fluorescence spectroscopy. CNC-COOH@CdS shows an absorption peak at 410 nm, which was subsequently used as the excitation wavelength for florescence spectroscopy. A broad emission peak in the range of 550-780 nm was obtained for CNC-COOH@CdS, which suggests a red emission colour (Figure 7.1A, inset). For pdsCNC-PEI@CdS, blue shifts in both the absorption and emission spectrum were observed due to the decrease in size of the CdS QDs. An emission peak centered at 480 nm was seen with an excitation wavelength of 365 nm, indicating green-white emission (Figure 7.1B, inset). The sizes of CdS QDs were estimated to be 4.0 nm for CNC-COOH@CdS and 2.1 nm for pdsCNC-PEI@CdS based on their UV-vis spectra,[280] which are consistent with the TEM images.

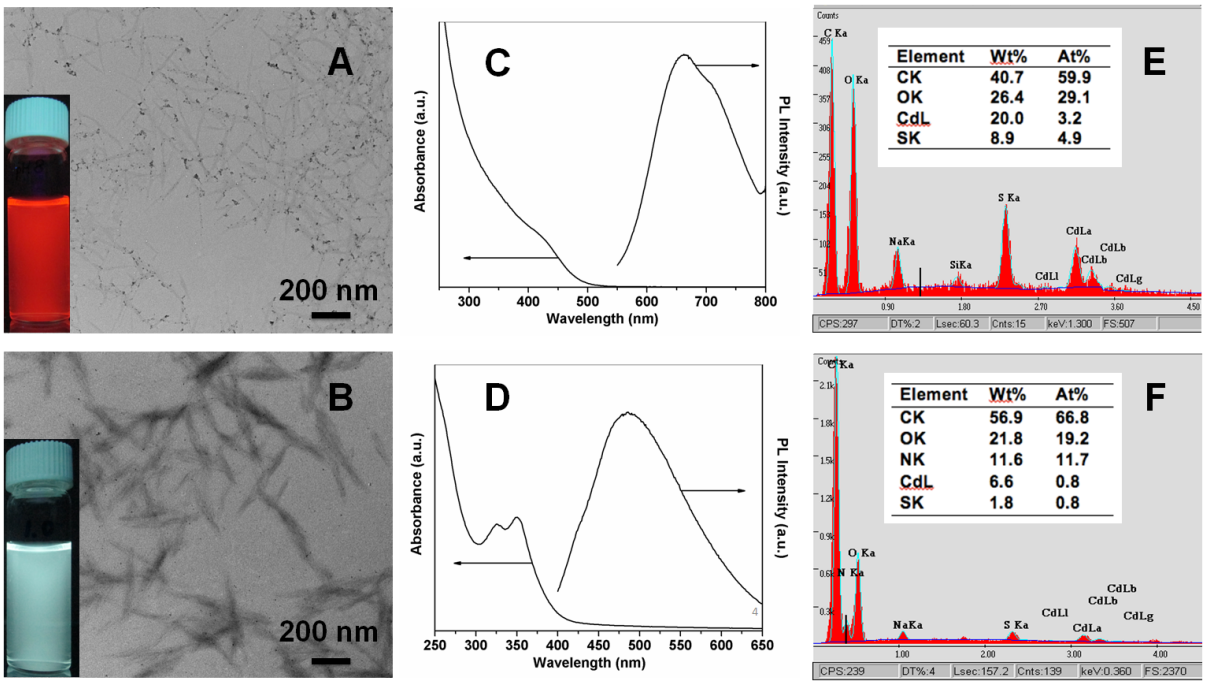

Figure 7.1. TEM image (A), optical properties (C) and EDX data (E) of CNC-COOH@CdS; TEM image (B), optical properties (D) and EDX data (F) of pdsCNC-PEI@CdS.

7.3.3 Crystal structure and atomic species of CNC-COOH@CdS and pdsCNC-PEI@CdS

XRD and EDX measurements were used to study the crystal structure and the atomic species present in these CNC/QD systems. XRD data for CNC-COOH@CdS and pdsCNC-PEI@CdS exhibited the diffraction peaks of CNCs at 14.7, 22.4, and 34.0 corresponding to (110), (200), and (004) planes,[248] and those of CdS QDs at 26.1, 43.4 and 51.5 assigned to (111), (220) and (311) planes (Figure 7.2).[249] These results suggest a good retention of CNC crystal structure under mild reaction conditions, and confirm a cubic zinc blend crystalline structure of CdS QDs. EDX data for CNC-COOH@CdS showed the presence of C, O, S and Cd (Figure 7.1E). EDX data for pdsCNC-PEI@CdS showed the presence of C, O, S, Cd, and N (Figure 7.1F).

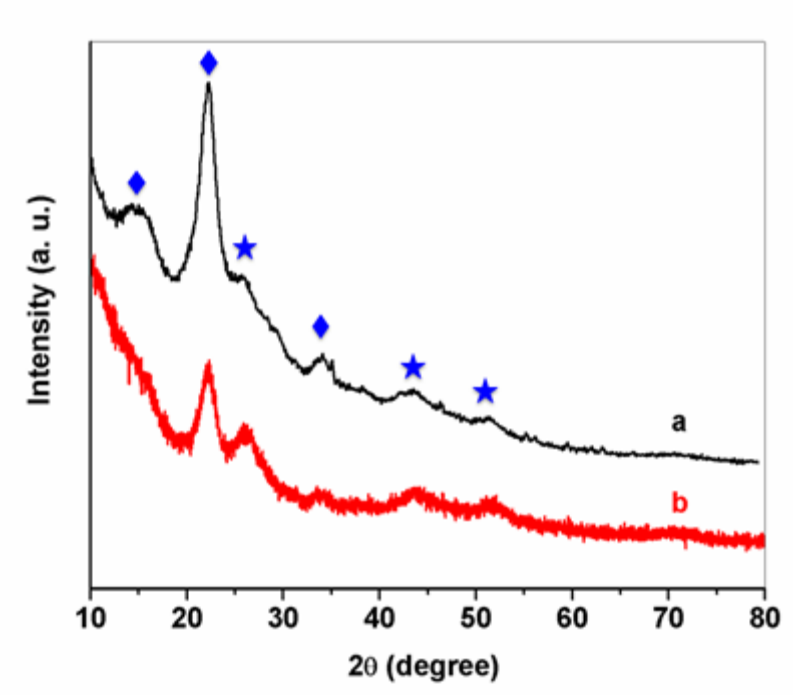

Figure 7.2. XRD patterns of CNC-COOH@CdS (a) and pdsCNC-PEI@CdS (b). Diffraction peaks from CNCs (diamonds) and QDs (stars) are also labelled.

7.3.4 Thermal degradation behaviors of CNCs and CNC@QD systems

The thermal degradation behaviors of CNCs and CNC@QD systems were investigated using TGA (Figure 7.3). The thermal stability of CNCs after functionalization was displayed, and the weight percentages of residues were used to analyze the content of CdS QDs. CNCs showed a sharp weight loss of 59% starting from 260 °C to 312 °C. CNC-COOH@CdS started to decompose at a lower temperature of 208 °C and over a broader temperature range due to the introduction of carboxyl groups onto the CNC surface during TEMPO oxidation.[281] pdsCNC-PEI@CdS began to lose weight at 96 °C due to the decomposition of PEI, followed by the weight loss from the decomposition of pdsCNCs. The amounts of CdS and char residues from CNC-COOH@CdS and pdsCNC-PEI@CdS were much higher than the quantity of char residue from CNCs at temperature at 700 °C, indicating the existence of CdS QDs. These results together with the TEM images, EDX analysis and emission spectra confirm the successful synthesis of CNC-COOH@CdS and pdsCNC-PEI@CdS.

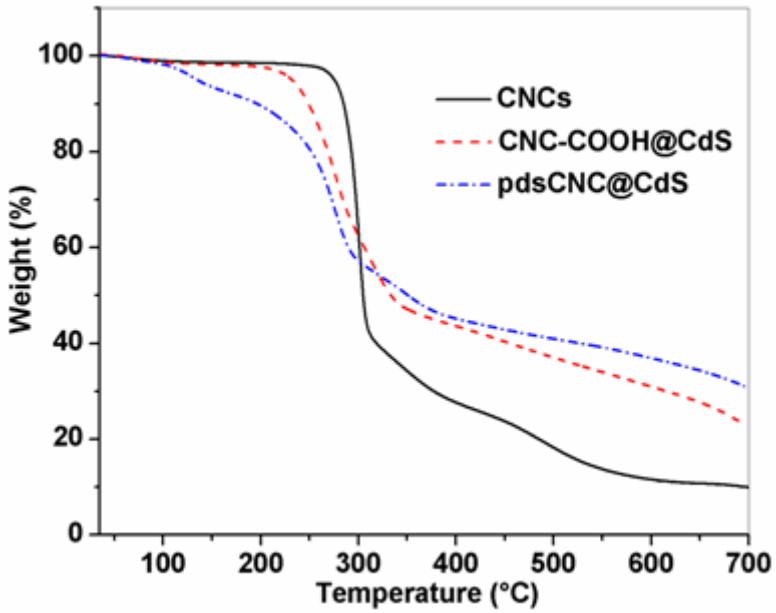

Figure 7.3. TGA patterns of CNCs, CNC-COOH@CdS and pdsCNC-PEI@CdS.

7.3.5 Colloidal stability of CNC-COOH@CdS and pdsCNC-PEI@CdS

To fabricate nanothin films, colloidal stability of building blocks is essential. As pdsCNC-PEI@CdS and CNC-COOH@CdS are neither core-shell structure nor spherical structure, zeta potential and dynamic light scattering were mainly used to demonstrate the good colloidal stability of pdsCNC-PEI@CdS and CNC-COOH@CdS.[89,219] With abundant sulphate ester groups and carboxylate groups, CNC-COOH@CdS at pH 8 showed a zeta potential of - 45.7 ± 10.3 mV. As for pdsCNC-PEI@CdS, a zeta potential of + 31.9 ± 4.2 mV was measured due to abundant amine groups. The DLS data shows an increase in size for pdsCNC-PEI@CdS, further confirming the PEI coating. Both CNC-COOH@CdS and pdsCNC-PEI@CdS display narrow size distributions with no large agglomerates (Figure 7.4). These results indicate high stability and good dispersion of both CNC/QD systems, supporting their use as building blocks for fabricating nanothin films.

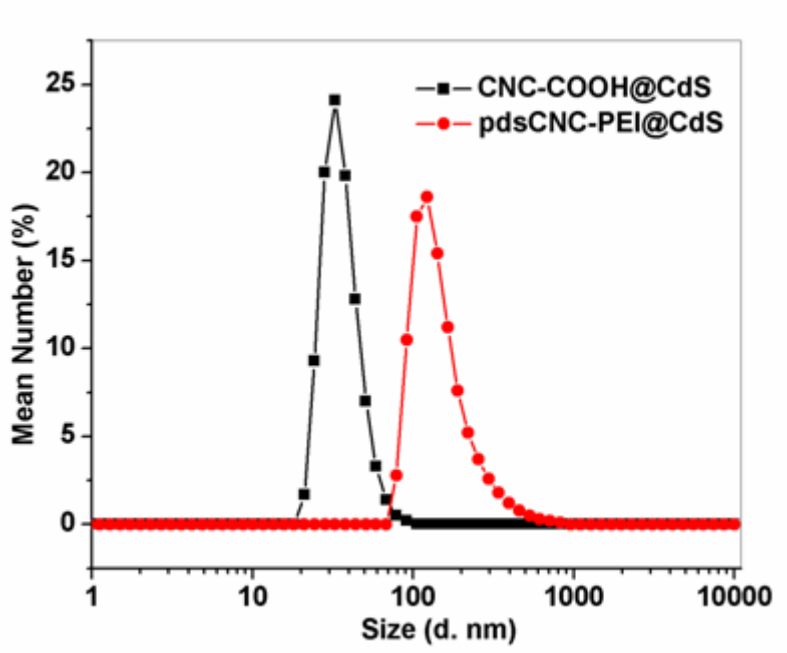

Figure 7.4. Size distributions of CNC-COOH@CdS and pdsCNC-PEI@CdS measured using a Malvern Nano ZS90 Zetasizer DLS system.

7.3.6 Characterization of thin films on silicon wafers

7.3.6.1 Controllable film thicknesses

Thin films fabricated on silicon substrates using LBL deposition of CNCs and PAH have been shown to exhibit iridescent colours resulting from thin film interference. These colours can be easily tailored simply by adjusting the layer thickness.[36] Previous work has shown that iridescent colours are only observed for films made using spin-coated LBL deposition; no structural colours were observed for solution dipped LBL films. Spin-coated LBL deposition resulted in films that were 7 times thicker than solution-dipped LBL deposition. While good colourimetric identification can be obtained from spin-coated films thanks to the observable iridescence, the loss of transparency due to heavy light scattering from thick films may hinder photoluminescence from QDs. Further, good transparency is highly desirable in anti-counterfeiting products. Therefore, we attempted to obtain thin films with high transparency using the LBL solution-dipping method. Taking advantage of the atomically flat surface of silicon wafers, the $(CNC\text{-}COOH@CdS/pdsCNC\text{-}PEI@CdS)_n$ multilayer thin films were first deposited onto silicon wafers to study the relationship between film thickness and the number of layers deposited. Side-view SEM images revealed a linear increase of film thickness with an increase

of layers from 10 to 30, indicating a well-controlled fabrication process (Figure 7.5A). The average thickness is estimated to be about 5.1 nm per CNC-COOH@CdS/pdsCNC-PEI@CdS layer. The enlarged SEM image for $(CNC\text{-}COOH@CdS/pdsCNC\text{-}PEI@CdS)_{30}$ displays the distinct nanorod structure and the dense packing structure of CNCs, further proving the successful coating of CNC/QD on the substrates (Figure 7.5B).

Ellipsometry measures the change in polarization of elliptically polarized light reflecting from sample surfaces and collects the changes in the ellipsometric angles (Ψ and Δ).[282] With these two parameters and the refractive index of the material, film thicknesses can be deduced. In this work, this technique was also used to further confirm the controllable fabrication process. An average refractive index of 1.52 for nanothin films was applied during the measurement, based on previously reported CNC films.[36,283,284] Film thicknesses were obtained from the ellipsometer using DeltaPsi 2 analyzing software and are summarized in Table 7.2. Reported values are an average of 3 measurements at different locations on each film. These data are in good agreement with the film thicknesses measured by SEM.

Table 7.2. Film thicknesses measured using ellipsometry.

Layers	Average film thickness [nm]	Standard deviation [nm]
10	50	5
20	118	1
30	185	6

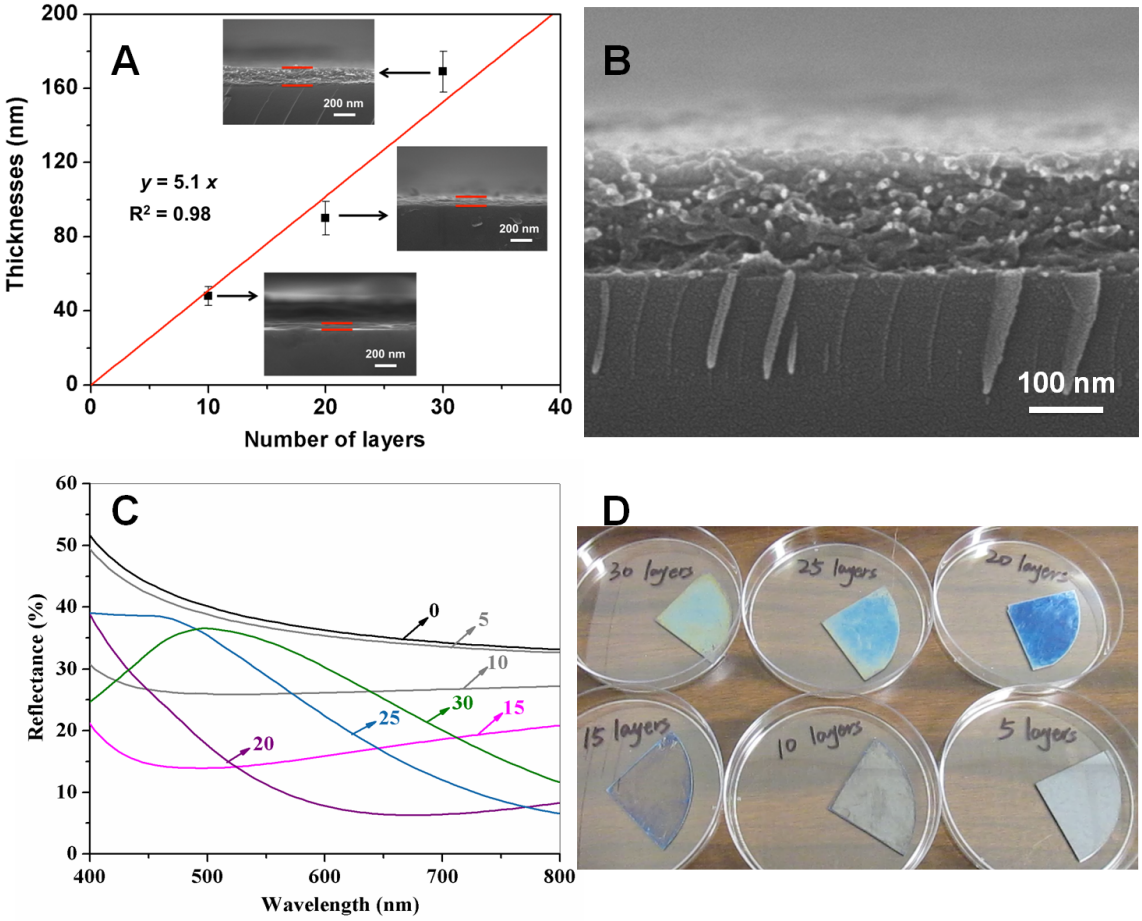

Figure 7.5. (A) Side-view SEM images for CNC/QD coatings with layer numbers n = 10, 20 and 30 on silicon wafers. (B) Enlarged side-view image of CNC/QD coating with n = 30. (C) Reflectance spectra of modified silicon wafers with increasing layers of CNC/QD coatings. (D) Digital image of (CNC-COOH@CdS/pdsCNC-PEI@CdS)n (n = 5-30) modified silicon wafers.

7.3.6.2 Structure colours from thin film interference

Reflectance spectra of these modified films were obtained to study the colour changes over different CNC-COOH@CdS/pdsCNC-PEI@CdS layers (Figure 7.5C). Coated silicon substrates exhibited different structural colours with increasing numbers of layers of CNC-COOH@CdS/pdsCNC-PEI@CdS coatings (Figure 7.5D). $(CNC\text{-}COOH@CdS/pdsCNC\text{-}PEI@CdS)_5$ showed high reflectance (above 35%) towards all visible light, similar to pure silicon wafers. When the number of layers increased to 10, the coated silicon wafer showed reduced reflectance due to the anti-reflectance property of cellulose films. After reaching 15 layers, the reflectance further decreased to 20% with

slightly more reflected light in the 600-800 nm range, resulting in a yellow-red colour of the film. For (CNC-COOH@CdS/pdsCNC-PEI@CdS)$_{20}$, the film reflected more blue light, resulting in a blue colour of the film. With further increases of *n* to 25 and 30, a red shift of reflectance spectra was observed, and film colour changed from blue (*n* = 20) to green (*n* = 30).

7.3.7 Characterization of thin films on PET substrates

7.3.7.1 Surface morphology

Next we coated the same (CNC-COOH@CdS/pdsCNC-PEI@CdS)$_n$ onto PET substrates, as the high transparency of PET would be beneficial for observing both photoluminescence from the QDs and the structural colours from thin film interference. LBL self-assembly occurred on both sides of the PET substrates, and the number *n* represents film layers only on one side of the PET substrates. The same sample preparation procedure from the silicon substrate coating was applied, and the morphologies of these nanothin films on PET substrates were studied using SEM (Figure 7.6). Low-magnification SEM images of (CNC-COOH@CdS/pdsCNC-PEI@CdS)$_{30}$ (Figure 7.7A) showed a uniform coating of the final film, and this was further confirmed using a fluorescence microscope. Fluorescence microscopy also revealed a homogenous red emission from the QDs (Figure 7.7B). Porous film structure was also observed for all (CNC-COOH@CdS/pdsCNC-PEI@CdS)$_n$ coatings. For (CNC-COOH@CdS/pdsCNC-PEI@CdS)$_5$, both CNC-COOH@CdS and pdsCNC-PEI@CdS nanorods were observed (Figure 7.6). The formation of pores was attributed to parallel packing of rigid CNC nanocolloids on the substrates. As the number of coating layers increased (from 5 to 30), a gradual decrease in pore number and pore size was observed with more nanorods piling up and filling holes. The observed pores have a diameter of several nanometers up to 170 nm. The low-layer films predominantly consist of large pores, and the high-layer films are distinguished by small pores. A similar decrease in pore size with an increase in layers was reported using cellulose nanowires with length in the micron range as building blocks for thin films.[39]

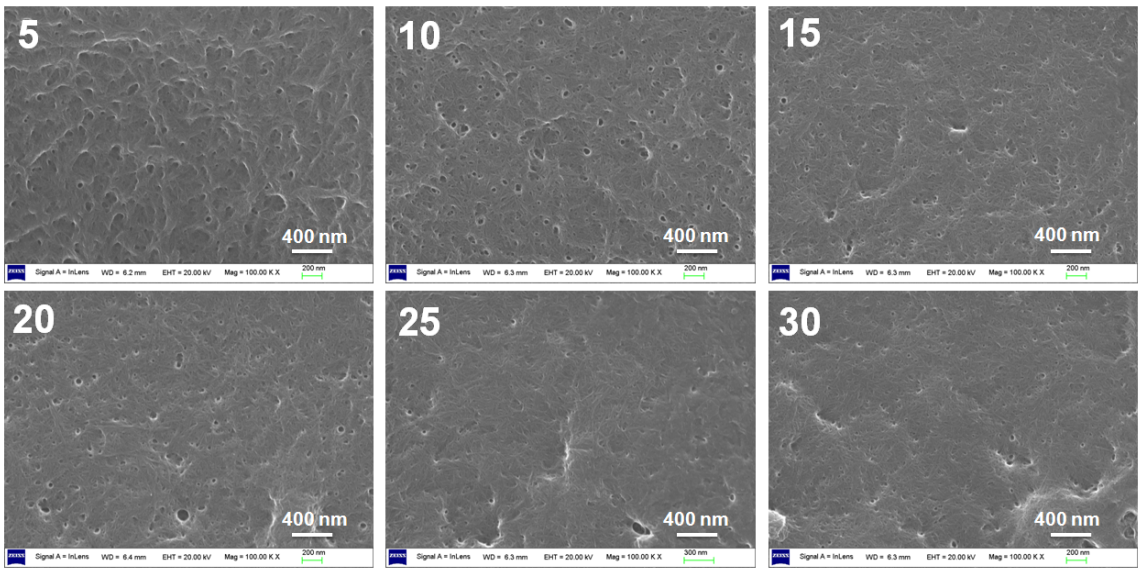

Figure 7.6. Top-view SEM images of $(CNC\text{-}COOH@CdS/pdsCNC\text{-}PEI@CdS)_n$ nanothin films on PET substrates.

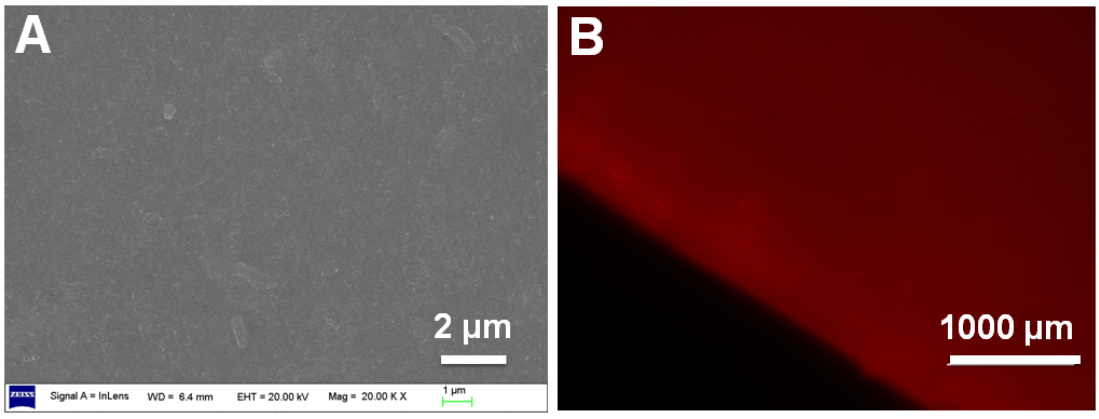

Figure 7.7. Top view SEM image (A) and fluorescence microscope image (B) of $(CNC\text{-}COOH@CdS/pdsCNC\text{-}PEI@CdS)_{30}$ modified PET substrate.

7.3.7.2 Hydrophilicity

It is important to note that nanopores within films tend to decrease the refractive index, resulting in antireflection coatings.[39] In addition, three-dimensional nanopores can also lead to increased hydrophilicity of the resulting films. Previous work reported the preparation of superhydrophilic coatings by creating a highly porous film structure using hydrophilic building blocks.[285] These superhydrophilic films have promising applications in antifogging products. In this work, we

observed antireflection behaviour when the layers increase from 0 to 15. With larger layers, thin-film interference suppresses the effect of antireflection performance (Figure 7.8A). To investigate the influence of coatings on hydrophilicity, the water contact angles of these modified PET films were measured using a water droplet of 5 μL as an indicator. Bare PET substrates display a contact angle of 93.0°, while (CNC-COOH@CdS/pdsCNC-PEI@CdS)$_n$ coated substrates showed dramatically decreased contact angles in the range of 33.7° ~ 43.8°. The decrease of contact angle is likely due to a combination of the hydrophilic building blocks used and the nanoporous structure of the films.

7.3.7.3 Transparency

The transparency of modified PET films was studied using UV-vis transmittance measurements (Figure 7.8B). Raw PET substrate displayed high transmittance over 90% in the visible light range. With increasing layers of coatings, the transmittance of films decreases gradually at around 420 nm along with the increase of layers from 5 to 30. This is due to the increasing absorption from CNC-COOH@CdS as the layers increase. The overall slight decrease of transmittance in the visible range with layers can be attributed to increasing light scattering as coatings become thick. This further confirms the successful coating on PET substrates. All modified films displayed high transparency over 70% in the visible region of the spectrum. The two rigid CNC-based building blocks were observed to play essential roles in achieving high transparency of films owing to the formation of porous structure. In a control experiment, PET film first modified with (CNC-COOH@CdS/pdsCNC-PEI@CdS)$_{25}$ and then (PSS/pdsCNC-PEI@CdS)$_5$ on the top resulted in a sharp decrease in transmittance and a lack of thin film interference(Figure 7.9), which may be caused by the dense packing of PSS and pdsCNC-PEI@CdS as indicated in previous works.[34,286] Moreover, all modified PET substrates show obvious oscillations referred to as Fabry-Perot fringes. This phenomenon is caused by the interference of transmitted light and partially reflected light at film-air / film-PET interfaces, and films with Fabry-Perot fringes may be used in selective sensor for chemical vapours and gases.[287] The inserted image shows the high visible transparency of (CNC-COOH@CdS/pdsCNC-PEI@CdS)$_{30}$ (Figure 7.8B, inset a). The film colour turned to green when aligned with the inverted image of an indoor white-light lamp, demonstrating its structural colour from thin film interference (Figure 7.8B, inset b).

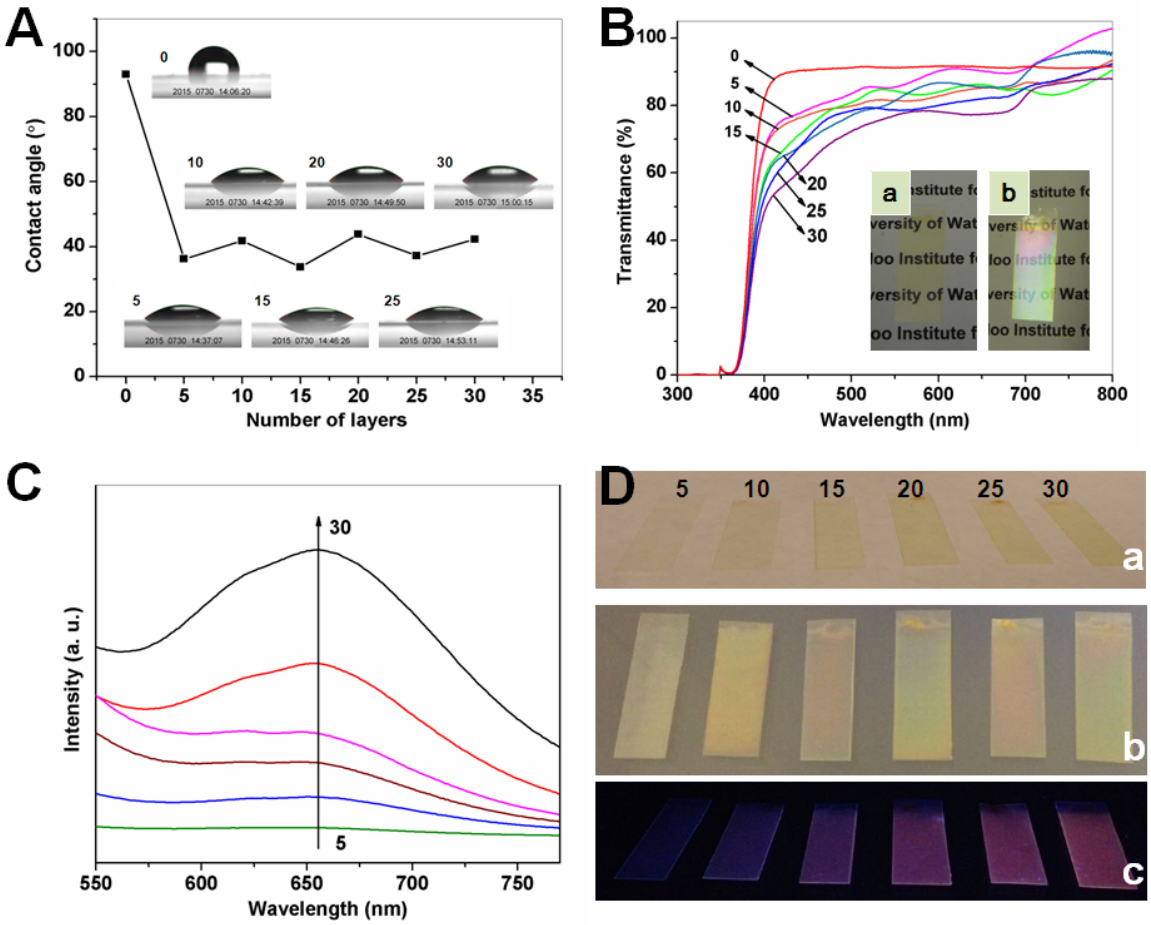

Figure 7.8. (A) Contact angle for PET films coated with (CNC-COOH@CdS/pdsCNC-PEI@CdS)$_n$ (n = 0-30); (B) Transmittance spectra of PET films coated with (CNC-COOH@CdS/pdsCNC-PEI@CdS)$_n$ (n = 0-30); (C) Fluorescence spectra of PET films coated with (CNC-COOH@CdS/pdsCNC-PEI@CdS)$_n$ (n = 5-30) excited at 410 nm; (D) PET films coated with (CNC-COOH@CdS/pdsCNC-PEI@CdS)$_n$ (n = 5-30) under room light (a and b) and under 365 nm UV lamp (c).

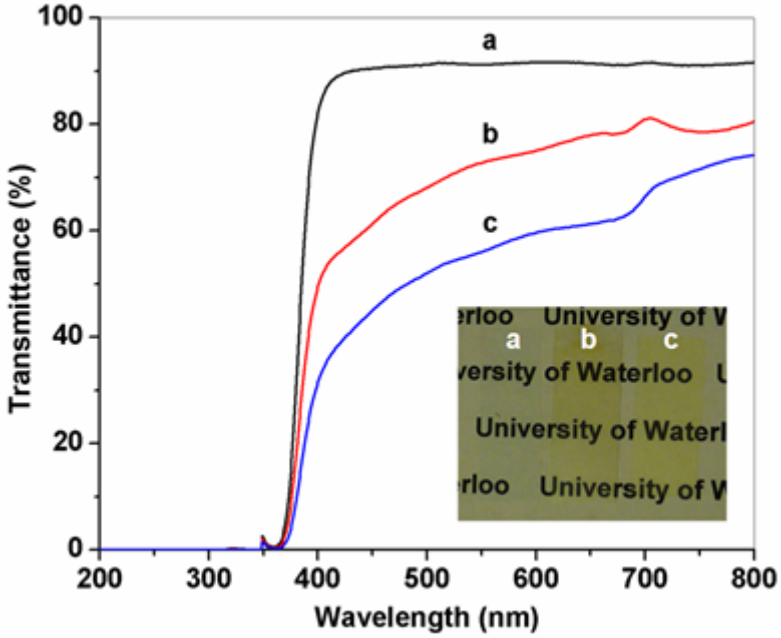

Figure 7.9. Transmittance spectra of raw PET film (a), PET film coated with (CNC-COOH@CdS/pdsCNC-PEI@CdS)$_{30}$ (b), and PET film modified first with (CNC-COOH@CdS/pdsCNC-PEI@CdS)$_{25}$ and then (PSS/pdsCNC-PEI@CdS)$_5$ (c).

7.3.7.4 Structural colours and photoluminescence properties

The emission spectra of CNC/QD modified PET films were obtained to further confirm the layer-by-layer coating process (Figure 7.8C). To emphasize the intensity increase over the number of coating layers, only emission peaks from CNC-COOH@CdS excited at 410 nm were shown in Figure 7.8C. The broad emission peaks centered at 660 nm was from CNC-COOH@CdS and showed a gradual increase over layers. Unlike other systems, the increase is not linear which may be due to energy transfer from pdsCNC-PEI@CdS to CNC-COOH@CdS,[288] as well as light interference (Figure 7.8B). Digital images for these films under different lighting conditions were taken (Figure 7.8D). These films are mostly transparent, with colour changing from colourless to light green under uniform white light (Figure 7.8D a). The green colour is due to the visible absorption from CNC-COOH@CdS. When these films were put on a dark background under non-uniform light and observed at right angles, they show distinct structural colours (Figure 7.8D b). These structural colours can become bright and obvious when the films are aligned perpendicularly to a white-light lamp (Figure 7.8B, inset b), as a much larger amount of incident light can be reflected. In addition,

these films emit strong red light under a 365 nm UV Lamp, with an increase in emission intensity as the number of layers increases (Figure 7.8D c). These digital images intuitively demonstrate the structural colours and photoluminescence properties of the prepared films, which make these films useful in anti-counterfeiting applications.

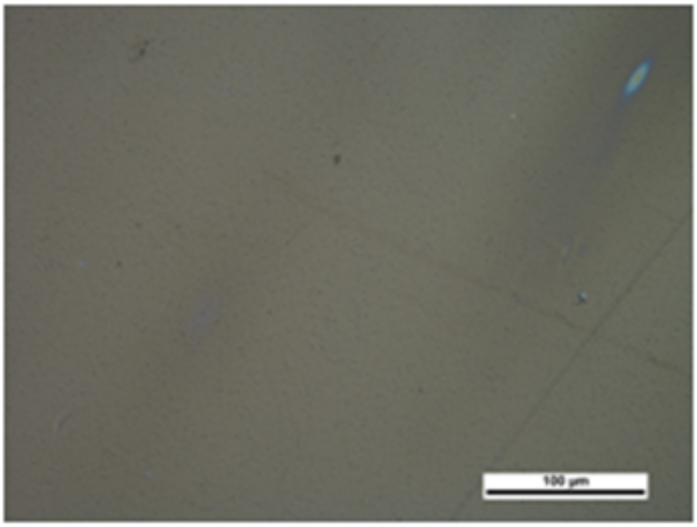

Figure 7.10. Optical microscopy image of PET substrate under polarized microscope with white light source.

Liquid crystal self-assembly of CNCs into a chiral nematic phase with adjustable helical pitch has been extensively studied and applied to form multifunctional thin films for applications in energy storage, sensors and chirality purifiers.[54,53] In previous works, the radial orientation of spin-coated CNC films was also observed. In this work, while no orientation of CNCs were observed from SEM images, it is necessary to study the packing of CNCs during the fabrication process and to confirm the structural colour from thin film interference. Prepared films were investigated with a polarized optical microscope (Nikon, LV-UEPI). During the measurement, light reflected off these films under a white light source was collected. As a control sample, one raw PET substrate without coating was placed under the polarized microscope, and only dark grey colour was observed (Figure 7.10). All films coated with various layers of (CNC-COOH@CdS/pdsCNC-PEI@CdS)$_n$ show distinct colours but no birefringence, as no colour change was observed at different angular positions. The lack of birefringence suggests a lack of CNC orientation during the coating process, which is in agreement with the SEM images. The optical microscope images were taken under plane-polarized light to demonstrate the change of reflected light over different film layers (Figure 7.11). With *n* increasing

from 5 to 30, in intervals of 5 layers, the resulting colours were dark blue, yellow, purple, light blue, purple, and light blue respectively.

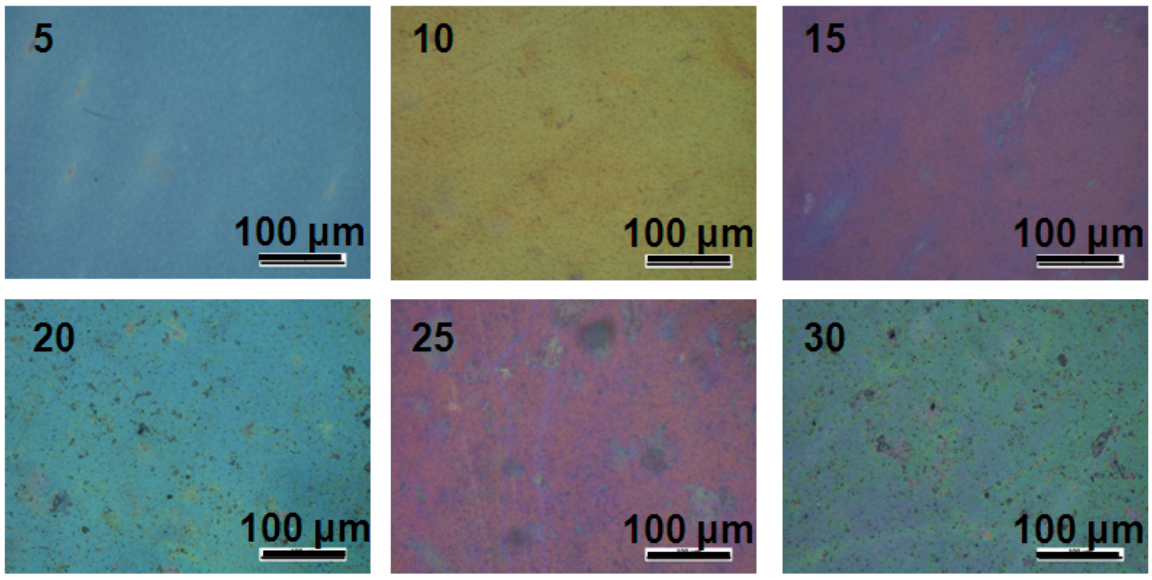

Figure 7.11. Optical microscopy images of CNC/QD coated PET substrates observed under a polarized microscope. The numbers represent the number of layers of CNC-COOH@CdS/pdsCNC-PEI@CdS coated on the PET surfaces.

7.3.7.5 Stability, colour tunability and anti-counterfeiting applications

The stability of $(CNC\text{-}COOH@CdS/pdsCNC\text{-}PEI@CdS)_{30}$ coated PET substrate towards water and ethanol was evaluated by monitoring its photoluminescence spectra. The modified PET substrate was first immersed in water for 3.5 hours and then in ethanol for another 3.5 hours, and its emission spectra over time indicate no obvious decrease of emission intensity, suggesting a highly stable structure (Figure 7.12A). Further, by controlling the concentrations of CNC-COOH@CdS and pdsCNC-PEI@CdS, emssion colours can be tuned. To demonstrate the adjustable peak intensity ratios of CNC-COOH@CdS/pdsCNC-PEI@CdS, emission spectra with two peaks from the two nanobuilding blocks were obtained under an excitation wavelength of 365 nm. Figure 7.12B shows the emission spectra and the digital images of two flexible/bendable modified PET films under a 365 nm UV lamp with red and white emission respectively. Thus, we can combine various structural colours by manipulating film thicknesses, and we can tune emssion colours under UV light by adjusting the concentrations of building blocks during the fabrication process. Finally, we propose a realistic scheme of our products' application for anti-counterfeiting purposes, in this case specifically

for the protection of Canadian currencies (as shown in Figure 7.12C). In this example, pink and gold structural colours from $(CNC\text{-}COOH@CdS/pdsCNC\text{-}PEI@CdS)_{25}$ and $(CNC\text{-}COOH@CdS/pdsCNC\text{-}PEI@CdS)_{10}$ provide a method for colourimetric security, and the embedded QDs offer a secondary security layer with red emission under UV light. We therefore report a simple and low-cost method to fabricate nanothin films for anti-counterfeiting applications.

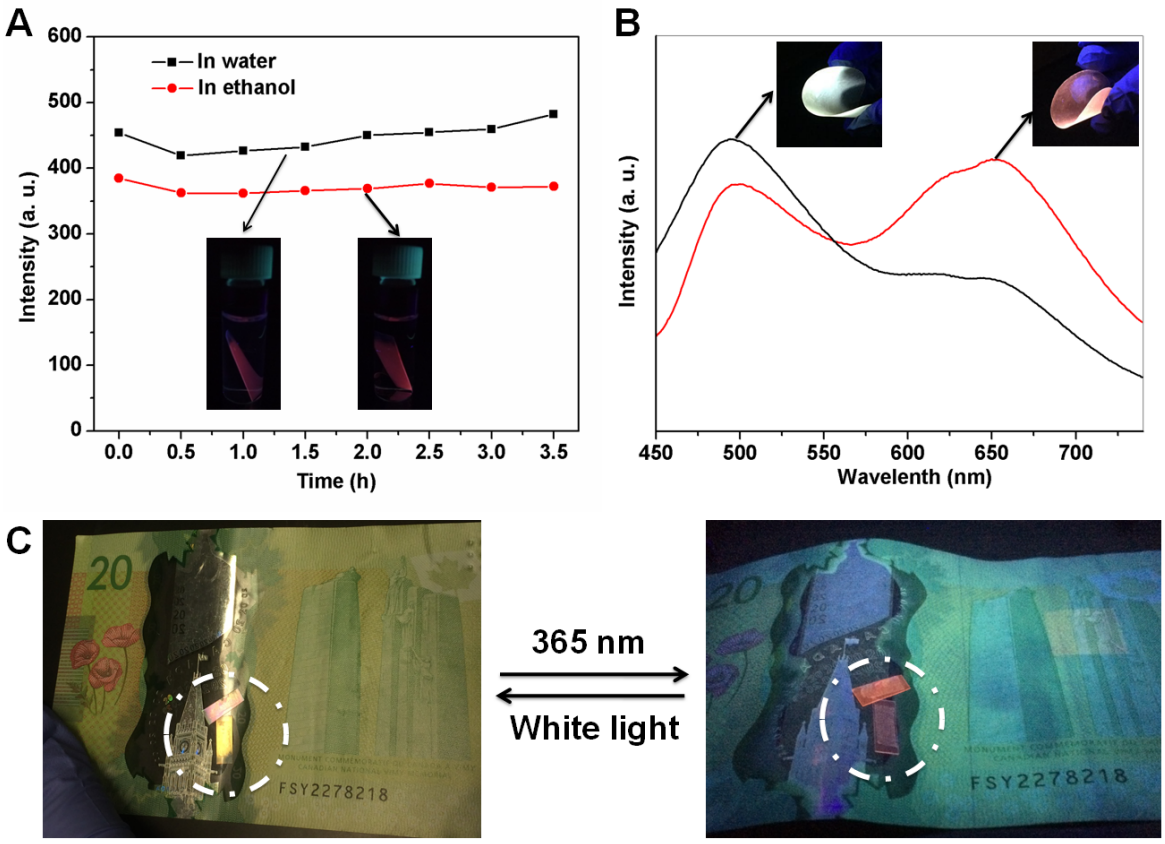

Figure 7.12. (A) Stability test for $(CNC\text{-}COOH@CdS/pdsCNC\text{-}PEI@CdS)_n$ using fluorescence spectra; (B) Emission spectra of $(CNC\text{-}COOH@CdS/pdsCNC\text{-}PEI@CdS)_{30}$ on PET substrates assembled with CdS concentrations 0.4 mM/L (black curve) and 0.8 mM/L (red curve) respectively in pdsCNC-PEI@CdS dispersions; (C) The proposed scheme of anti-counterfeiting protection, in this example for Canadian currencies.

7.4 Conclusion

In summary, robust nanothin films were successfully fabricated onto various substrates using two new QD-modified CNCs. The functionalization of CNCs using CdS QDs were confirmed using TEM,

EDX, XRD, UV-vis spectra and photoluminescence spectra. Unlike other inorganic nanoparticle-modified CNCs, the CNC/QDs prepared showed high stability and good dispersibility with abundant surface charge and narrow size distribution. The controllable LBL coating process was confirmed by SEM and ellipsometry. Modified PET substrates display strong stability agaist water and ethanol, and high transmittance (above 70%) over the entire range of visible light. These films are also hydrophilic with contact angles around 40°. Both tunable structural colours from thin film interference and adjustable emission colours from QDs were observed on modified PET substrates, which may find applications in anti-counterfeiting devices. Finally, the reported modification procedure can be applied to other CNC/functional inorganic nanoparticle systems, greatly expanding the applications of CNC-based nanothin films while simplifying fabrication processes.

Chapter 8

Original contributions and recommendations

8.1 Original contributions to research

Due to the need to resolve the aggregation of CNCs during the functionalization process, the development of novel, simple, reproducible and scalable CNC/inorganic nanoparticle systems with unique properties is extremely desirable. The objective of this thesis largely involved the development of novel functional materials based on CNCs by taking advantage of the inorganic nanoparticles with attractive magnetic, catalytic and optical properties. The goal is to investigate the synergistic roles of CNCs and inorganic nanoparticles for applications in water treatment, catalysis, bioimaging and anti-counterfeiting. This thesis includes the preparation techniques of three types of CNC/inorganic nanoparticle hybrids: (i) CNC/Fe_3O_4; (ii) CNC/Au; (iii) CNC/QDs. Three different methodologies were investigated in the preparation of these CNC/inorganic nanoparticle hybrids, namely physical adsorption, polymer encapsulation, and in-situ deposition. Our products possess superior dispersibility of inorganic nanoparticles on CNC surface, excellent aqueous stability, and enhanced performance in the fields mentioned above. The following sections summarize the main findings of each of the systems:

Development of a CNC/Fe_3O_4 nanohybrid system

The uniform dispersion of Fe_3O_4 through physical adsorption was achieved with the assistance of polymer coatings on CNCs. Poly(diallyldimethylammonium chloride) and polyvinylpyrrolidone not only facilitated the loading of Fe_3O_4, but also assisted the subsequent coating of silica. Silica coating was achieved through the well-developed sol-gel method, which was applied to confine Fe_3O_4 nanoparticles and protect them from oxidation. Uniform loading of Fe_3O_4 nanoparticles on the surface of CNCs, core-shell structure of silica-coated CNC@Fe_3O_4 and the observed controlled thickness of silica coating was confirmed through TEM and FT-IR. In addition, with the inorganic silica coating, the thermal stability of CNCs was enhanced with the onset decomposition temperature increased by 60 °C. Moreover, with the well-developed surface chemistry of silica, primary amine groups were introduced to facilitate the conjugation with MCT-β-CD. This system was effectively applied to remove drugs found in drinking water, where β-CD modified CNC@Fe_3O_4@SiO_2 nanohybrids were separated from purified water using a high gravity magnetic separator. We successfully addressed the aggregation and fast oxidation of Fe_3O_4 nanoparticles by using CNCs as bio-supporting materials and

silica shell as additional protection layer. Our products displayed good adsorption capability towards trace amounts of drugs found in drinking water and easy separation in the presence of magnetic filed.

Development of a CNC/Au nanohybrid system

Poly (amidoamine) (PAMAM) dendrimers with abundant primary and tertiary amine groups were grafted onto the CNC surface via simple carbodiimide-mediated amidation process. These amine groups together with carboxyl groups on oxidized CNC (CNC-COOH) rendered the G6 PAMAM dendrimer-grafted CNC (CNC-PAMAM) with interesting pH-responsive properties. Stable aqueous dispersions of CNC-PAMAM were obtained at pH $\leq$ 4 and pH $\geq$ 10, driven by electrostatic repulsion from positive and negative charge, respectively. However, large aggregates were formed at pH ranging from 5 to 9 due to electrostatic attraction. In addition, the intrinsic fluorescent property of PAMAM was preserved after grafting onto CNC-COOH. Thus, it is also important to investigate the interactions between surfactants (i.e. SDS and CTAB) and CNC-PAMAM under various pH values, which would be beneficial for applications in pharmaceutical and cosmetic industries. Moreover, CNC-PAMAM was employed as support for the Au nanoparticles, playing the roles of nanoreactor and reducing agent. The size of Au nanoparticles was between 2 to 4 nm when $NaBH_4$ was used as the reducing agent, and the Au nanoparticles were confined within the cavities of PAMAM. With abundant amine groups, CNC-PAMAM could also serve as reducing agents for Au nanoparticles, and the effects of pH, CNC-PAMAM concentrations, and temperatures on resulting size of the gold nanoparticles were examined. As a result of improved dispersibility and accessibility of gold nanoparticles, our products displayed superior catalytic properties towards the reduction of 4-nitrophenol to 4-aminophenol with an effective kinetic rate constant of 1.5×10^{-2} s^{-1}. In this work, CNC-PAMAM with pH dependent dispersibility was successfully synthesized, and the dual functionalities of CNC-PAMAM as encapsulators and reducing agents were investigated. Our products showed superior catalytic performance and easy recyclability by adjusting pH.

Development of CNC/QDs for bioimaging applications

CdS@ZnS core-shell quantum dots (QDs) were loaded onto oxidized CNC surface through a one-step in-situ deposition, taking the advantages of the affinity of Cd^{2+} towards carboxylate groups. The reaction conditions of QD to CNC ratio, pH, and ZnS to CdS ratio on colloidal stability and photoluminescence property of CNC/QD nanohybirds were studied. The products synthesized at pH 8 with a CdS to CNC weight ratio of 0.19 and a ZnS/CdS molar ratio of 1.5 possessed excellent

colloidal stability and highest photoluminescence intensity. With CNCs as biosupports, CNC/QD nanohybirds were shown to exhibit low cytotoxicity and high cellular uptake by HeLa cells, as well as strong red-emitting fluorescence. Therefore, the synthesized core-shell QDs on the surface of CNCs could serve as promising bioimaging probes. This work reported the simple synthesis of CNC/CdS@ZnS hybrids in aqueous phase at low temperature (50 °C). Our products showed excellent colloidal stability, high photoluminescence, low cytotoxicity, and good performance in bioimaging applications.

Development of CNC/QDs as nanobuilding blocks for functional thin films for anti-counterfeiting

Two CNC/CdS QD nanohybrids were prepared using different synthetic methods. Negatively charged CNC/CdS QD hybrids were synthesized using the same in-situ nucleation and growth of CdS QDs on carboxylated CNCs. Positively charged CNC/CdS QD hybrids were prepared by first forming a PEI coating on partially desulphated CNCs and then in-situ synthesizing CdS QDs. Both systems were highly stable in aqueous phase and served as excellent nanobuilding blocks for fabricating thin films on various substrates through electrostatic layer-by-layer self-assembly. The films coated on poly(ethylene terephthalate) (PET) substrates exhibited high transparency (above 70%) over the entire range of visible light, and strong hydrophilicity (contact angles around 40°), due to the rigid structure and hydrophilic surface of CNCs. These films were also shown to be flexible and stable against water and ethanol. In addition, these films showed tunable, stable and metallic structure colours from thin-film interference, and photoluminescence from CdS QDs. As such, we reported the first work on using CNC/QD hybrids as building blocks to fabricate thin films on both silicon wafers and PET substrates, and our films could be potentially used in anti-counterfeiting products.

8.2 Recommendations for future studies

Based on the results from the studies conducted in this thesis research, the following recommendations are proposed for future studies. In the present research on CNC/Fe_3O_4 (Chapter 3), the strategy of using polymers in assisting nanoparticle immobilization and silica coating can be applied to other inorganic nanoparticles, such as, noble metal nanoparticles and metal oxides. Multiple types of inorganic nanoparticle through layer-by-layer deposition can be loaded on CNCs using similar procedures, to achieve multifunctional systems. Silica coating can be controllably etched over time under alkaline solutions, which can render these systems with mesopores for

advanced applications as nanoreactors or adsorbents. In addition, the silica shell can be chemically modified with reactive groups (e.g. —SH, —NH_2, —Cl), through which functional groups can be further introduced. Despite the complex procedure, the experimental protocols are simple in terms of operation and are mostly conducted in aqueous phase. Moreover, with silica coating, the thermal stability of CNCs is largely enhanced which can be beneficial for their applications at high temperatures.

In Chapter 4 and 5, we demonstrated the successful grafting of G6 PAMAM on CNCs, and investigated the pH-responsive and fluorescent properties of the hybrid systems, and also studied their use in the encapsulation and synthesis of Au nanoparticles. CNC-PAMAM can also serve as a support for other inorganic nanoparticles with precise size control. Moreover, there is a possibility for incorporating and encapsulating other macromolecules, such as proteins, pharmaceuticals, etc. Furthermore, with pH responsive amine groups, the structure of PAMAM dendrimers changes from an expanded structure at low pH with high accessibility to the cavity to a compact structure at high pH with low permeability. This leads to their applications in pH-triggered encapsulation and release. Taking advantage of CNCs' biocompatibility and PAMAM's pH-triggered structural change, CNC-PAMAM can find promising applications in targeted drug delivery. PAMAM dendrimers from G0 to G10 with different sizes and amounts of functional groups are commercially available. Full generation PAMAM dendrimers possess amine groups at the end of the polymer chains, while half generation of PAMAM dendrimers comprise of carboxyl groups that can be used for further modification. The cavity size of PAMAM dendrimers generally increases from G0 to G10, it would be interesting to investigate the impact of dendrimer generation on the physicochemical properties and the encapsulation properties of CNC-dendrimer systems. Further, with abundant primary amine groups or carboxyl groups, functional groups leading to fluorescence, chelation, photon absorption, or paramagnetic imaging can be further conjugated.

In Chapter 5, oxidized CNCs were applied as biosupports for CdS and CdS@ZnS QDs. High aqueous stability was achieved without the formation of CNC aggregates. The reaction process is simple, reproducible, scalable, and free of organic solvents and surfactants. With the photoluminescence property from QDs, low cytotoxicity and high cellular uptake of CNC/QDs were confirmed. With carboxyl groups on CNC, further functionalization through chemical reactions can be carried out, which would dramatically expand the applications of CNC/QD nanohybrids in targeted drug delivery and sensing.

In Chapter 6, PEI was coated on partially desulphated CNCs for loading CdS QDs. PEI possesses abundant metal affinity groups-amine groups for loading various inorganic nanoparticles. By partially removing sulphate ester groups on CNC, uniform PEI coating was formed on CNC surface with no CNC agglomerates observed. The abundant amine groups served as effective nucleation sites for synthesizing CdS QDs. This positively charged CNC/CdS system and the negatively charged CNC/CdS nanohybrid are reported in Chapter 5, and they serve as perfect counterparts for building thin films using electrostatic layer-by-layer coating process. The films coated onto PET substrates showed metallic colours from thin-film interference as colourimetric security and photoluminescence from CdS QDs as additional authentication. Tunable structural colours and photoluminescence colours were also achieved by varying the concentrations of nanobuilding blocks and the thicknesses of the coating. More importantly, the layer-by-layer method applies to various solutions/colloids (i.e. PDDA, PSS, PAA, PAH, polymer micelles, clay nanoplates, graphene oxides, noble metal nanowires/nanoparticles, fluorescent dyes, etc.), and substrates (quartz glass, silicon, PET films, electrodes, etc.). With these flexibilities, multifunctional thin films based on CNCs or CNC/QDs can be fabricated.

Overall, several strategies have been investigated in developing CNC/inorganic nanoparticles systems with well-controlled dispersion of both CNCs and inorganic nanoparticles. In order to maintain the nanostructure of CNCs, greater efforts need to be carried out to introduce sufficient metal-affinity groups, and electrostatic/steric repulsion among CNCs.

References

(1) Sanchez, C.; Julián, B.; Belleville, P.; Popall, M. Applications of hybrid organic-inorganic nanocomposites. *J. Mater. Chem.* **2005**, *15* (35-36), 3559–3592.

(2) Sanchez, C.;.Belleville, P.; Popall, M.; Nicole, L. Applications of advacned hybrid organic-inorganic nanomaterials: from laboratory to market. *Chem. Soc. Rev.* **2011**, *40*, 696–753.

(3) Darder, M.; Aranda, P.; Ruiz-Hitzky, E. Bionanocomposites: a new concept of ecological, bioinspired, and functional hybrid materials. *Adv. Mater.* **2007**, *19* (10), 1309–1319.

(4) Lin, N.; Huang, J.; Dufresne, A. Preparation, properties and applications of polysaccharide nanocrystals in advanced functional nanomaterials: a review. *Nanoscale* **2012**, *4* (11), 3274–3294.

(5) Abitbol, T.; Palermo, A.; Moran-Mirabal, J. M.; Cranston, E. D. Fluorescent labeling and characterization of cellulose nanocrystals with varying charge contents. *Biomacromolecules* **2013**, *14* (9), 3278–3284.

(6) Li, D.; Kaner, R. B. Shape and aggregation control of nanoparticles: not shaken, not stirred. *J. Am. Chem. Soc.* **2006**, *128* (3), 968–975.

(7) Hoshino, A.; Fujioka, K.; Oku, T.; Suga, M.; Sasaki, Y. F.; Ohta, T.; Yasuhara, M.; Suzuki, K.; Yamamoto, K. Physicochemical properties and cellular toxicity of nanocrystal quantum dots depend on their surface modification. *Nano Lett.* **2004**, *4* (11), 2163–2169.

(8) Wang, Y.; Hu, R.; Lin, G.; Roy, I.; Yong, K.-T. Functionalized quantum dots for biosensing and bioimaging and concerns on toxicity. *ACS Appl. Mater. Interfaces* **2013**, *5* (8), 2786–2799.

(9) Guo, G.; Liu, W.; Liang, J.; He, Z.; Xu, H.; Yang, X. Probing the cytotoxicity of CdSe quantum dots with surface modification. *Mater. Lett.* **2007**, *61* (8-9), 1641–1644.

(10) Hardman, R. A toxicologic review of quantum dots: toxicity depends on physicochemical and environmental factors. *Environ. Health Perspect.* **2006**, *114* (2),

165–172.

(11) Henriksson, M.; Henriksson, G.; Berglund, L. A.; Lindström, T. An environmentally friendly method for enzyme-assisted preparation of microfibrillated cellulose (MFC) nanofibers. *Eur. Polym. J.* **2007**, *43* (8), 3434–3441.

(12) Saito, T.; Kimura, S.; Nishiyama, Y.; Isogai, A. Cellulose nanofibers prepared by TEMPO-mediated oxidation of native cellulose. *Biomacromolecules* **2007**, *8* (8), 2485–2491.

(13) Bondeson, D.; Mathew, A.; Oksman, K. Optimization of the isolation of nanocrystals from microcrystalline cellulose by acid hydrolysis. *Cellulose* **2006**, *13* (2), 171–180.

(14) Yu, H.; Qin, Z.; Liang, B.; Liu, N.; Zhou, Z.; Chen, L. Facile extraction of thermally stable cellulose nanocrystals with a high yield of 93% through hydrochloric acid hydrolysis under hydrothermal conditions. *J. Mater. Chem. A* **2013**, *1*, 3938–3944.

(15) Beck-Candanedo, S.; Roman, M.; Gray, D. G. Effect of reaction conditions on the properties and behavior of wood cellulose nanocrystal suspensions. *Biomacromolecules* **2005**, *6* (2), 1048–1054.

(16) Espinosa, S. C.; Kuhnt, T.; Foster, E. J.; Weder, C. Isolation of thermally stable cellulose nanocrystals by phosphoric acid hydrolysis. *Biomacromolecules* **2013**, *14*, 1–27.

(17) Sadeghifar, H.; Filpponen, I.; Clarke, S. P.; Brougham, D. F.; Argyropoulos, D. S. Production of cellulose nanocrystals using hydrobromic acid and click reactions on their surface. *J. Mater. Sci.* **2011**, *46* (22), 7344–7355.

(18) Man, Z.; Muhammad, N.; Sarwono, A.; Bustam, M. A.; Kumar, M. V.; Rafiq, S. Preparation of cellulose nanocrystals using an ionic liquid. *J. Polym. Environ.* **2011**, *19* (3), 726–731.

(19) Lam, E.; Male, K. B.; Chong, J. H.; Leung, A. C. W.; Luong, J. H. T. Applications of functionalized and nanoparticle-modified nanocrystalline cellulose. *Trends Biotechnol.* **2012**, *30* (5), 283–290.

(20) Shopsowitz, K. E.; Qi, H.; Hamad, W. Y.; Maclachlan, M. J. Free-standing mesoporous silica films with tunable chiral nematic structures. *Nature* **2010**, *468*

(7322), 422–425.

(21) Isogai, T.; Saito, T.; Isogai, A. TEMPO electromediated oxidation of some polysaccharides including regenerated cellulose fiber. *Biomacromolecules* **2010**, *11* (6), 1593–1599.

(22) Saito, T.; Isogai, A. TEMPO-mediated oxidation of native cellulose. The effect of oxidation conditions on chemical and crystal structures of the water-insoluble fractions. *Biomacromolecules* **2004**, *5* (5), 1983–1989.

(23) Isogai, A.; Saito, T.; Fukuzumi, H. TEMPO-oxidized cellulose nanofibers. *Nanoscale* **2011**, *3* (1), 71–85.

(24) Uth, C.; Zielonka, S.; Horner, S.; Rasche, N.; Plog, A.; Orelma, H.; Avrutina, O.; Zhang, K.; Kolmar, H. A chemoenzymatic approach to protein immobilization onto crystalline cellulose nanoscaffolds. *Angew. Chemie - Int. Ed.* **2014**, *53* (46), 12618–12623.

(25) Arola, S.; Tammelin, T.; Tullila, A.; Linder, M. B. Immobilization − stabilization of proteins on nanofibrillated cellulose derivatives and their bioactive film formation. *Biomacromolecules* **2012**, *13*, 594–603.

(26) Jiang, F.; Esker, A. R.; Roman, M. Acid-catalyzed and solvolytic desulfation of H_2SO_4-hydrolyzed cellulose nanocrystals. *Langmuir* **2010**, *26* (23), 17919–17925.

(27) Cao, X.; Dong, H.; Li, C. M. New nanocomposite materials reinforced with flax cellulose nanocrystals in waterborne polyurethane. *Biomacromolecules* **2007**, *8*, 899–904.

(28) Cao, X.; Habibi, Y.; Lucia, L. A. One-pot polymerization , surface grafting , and processing of waterborne polyurethane-cellulose nanocrystal nanocomposites. *J. Mater. Chem.* **2009**, *19*, 7137–7145.

(29) Samir, M. A. S. A.; Alloin, F.; Sanchez, J.; Dufresne, A. Cellulose nanocrystals reinforced poly (oxyethylene). *Polymer.* **2004**, *45*, 4149–4157.

(30) Samir, M. A. S. A.; Alloin, F.; Gorecki, W.; Sanchez, J.; Dufresne, A. Nanocomposite polymer electrolytes based on poly (oxyethylene) and cellulose nanocrystals. *J. Phys. Chem. B* **2004**, *108*, 10845–10852.

(31) Peresin, M. S.; Habibi, Y.; Zoppe, J. O.; Pawlak, J. J.; Rojas, O. J. Nanofiber composites of polyvinyl alcohol and cellulose nanocrystals : manufacture and characterization. *Biomacromolecules* **2010**, *11*, 674–681.

(32) Fortunati, E.; Armentano, I.; Zhou, Q.; Iannoni, A.; Saino, E.; Visai, L.; Berglund, L. A. Multifunctional bionanocomposite films of poly (lactic acid), cellulose nanocrystals and silver nanoparticles. *Carbohydr. Polym.* **2012**, *87* (2), 1596–1605.

(33) Liu, H.; Liu, D.; Yao, F.; Wu, Q. Bioresource technology fabrication and properties of transparent polymethylmethacrylate/cellulose nanocrystals composites. *Bioresour. Technol.* **2010**, *101* (14), 5685–5692.

(34) Podsiadlo, P.; Choi, S. Y.; Shim, B.; Lee, J.; Cuddihy, M.; Kotov, N. A. Molecularly engineered nanocomposites: Layer-by-layer assembly of cellulose nanocrystals. *Biomacromolecules* **2005**, *6* (6), 2914–2918.

(35) Cranston, E. D.; Gray, D. G. Formation of cellulose-based electrostatic layer-by-layer films in a magnetic field. *Sci. Technol. Adv. Mater.* **2006**, *7*, 319–321.

(36) Cranston, E. D.; Gray, D. G. Morphological and optical characterization of polyelectrolyte multilayers incorporating nanocrystalline cellulose. *Biomacromolecules* **2006**, *7* (9), 2522–2530.

(37) De Mesquita, J. P.; Donnici, C. L.; Pereira, F. V. Biobased nanocomposites from layer-by-layer assembly of cellulose nanowhiskers with chitosan. *Biomacromolecules* **2010**, *11*, 473–480.

(38) Li, F.; Biagioni, P.; Finazzi, M.; Tavazzi, S.; Piergiovanni, L. Tunable green oxygen barrier through layer-by-layer self-assembly of chitosan and cellulose nanocrystals. *Carbohydr. Polym.* **2013**, *92* (2), 2128–2134.

(39) Podsiadlo, P.; Sui, L.; Elkasabi, Y.; Burgardt, P.; Lee, J.; Miryala, A.; Kusumaatmaja, W.; Carman, M. R.; Shtein, M.; Kieffer, J.; et al. Layer-by-layer assembled films of cellulose nanowires with antireflective properties. *Langmuir* **2007**, *23* (20), 7901–7906.

(40) Qi, Z. D.; Saito, T.; Fan, Y.; Isogai, A. Multifunctional coating films by layer-by-layer deposition of cellulose and chitin nanofibrils. *Biomacromolecules* **2012**, *13* (2), 553–

558.

(41) de Mesquita, J. P.; Patrício, P. S.; Donnici, C. L.; Petri, D. F. S.; de Oliveira, L. C. A.; Pereira, F. V. Hybrid layer-by-layer assembly based on animal and vegetable structural materials: multilayered films of collagen and cellulose nanowhiskers. *Soft Matter* **2011**, *7* (9), 4405–4413.

(42) Cerclier, C.; Guyomard-lack, A.; Moreau, C.; Cousin, F.; Beury, N.; Bonnin, E.; Jean, B.; Cathala, B. Coloured semi-reflective thin films for biomass-hydrolyzing enzyme detection. *Adv. Mater.* **2011**, *23*, 3791–3795.

(43) Hanif, Z.; Ahmed, F. R.; Shin, S. W.; Kim, Y. K.; Um, S. H. Size- and dose-dependent toxicity of cellulose nanocrystals (CNC) on human fibroblasts and colon adenocarcinoma. *Colloids Surf. B Biointerfaces* **2014**, *119*, 162–165.

(44) Catalan, J.; Ilves, M.; Jarventaus, H.; Hannukainen, Kati-Susanna Kontturi, E.; Vanhala, E.; Alenius, H.; Savolainen, K. M.; Norppa, H. Genotoxic and immunotoxic effects of cellulose nanocrystals in vitro. *Environ. Mol. Mutagen.* **2015**, *56*, 171–182.

(45) Lacerda, L.; Herrero, M. a.; Venner, K.; Bianco, A.; Prato, M.; Kostarelos, K. Carbon-nanotube shape and individualization critical for renal excretion. *Small* **2008**, *4* (8), 1130–1132.

(46) Geng, Y.; Dalhaimer, P.; Cai, S.; Tsai, R.; Tewari, M.; Minko, T.; Discher, D. E. Shape effects of filaments versus spherical particles in flow and drug delivery. *Nat. Nanotechnol.* **2007**, *2* (4), 249–255.

(47) Simone, E. a; Dziubla, T. D.; Muzykantov, V. R. Polymeric carriers: role of geometry in drug delivery. *Expert Opin. Drug Deliv.* **2008**, *5* (12), 1283–1300.

(48) Mahmoud, K. a; Mena, J. a; Male, K. B.; Hrapovic, S.; Kamen, A.; Luong, J. H. T. Effect of surface charge on the cellular uptake and cytotoxicity of fluorescent labeled cellulose nanocrystals. *ACS Appl. Mater. Interfaces* **2010**, *2* (10), 2924–2932.

(49) Dong, S.; Cho, H. J.; Lee, Y. W.; Roman, M. Synthesis and cellular uptake of folic acid-conjugated cellulose nanocrystals for cancer targeting. *Biomacromolecules* **2014**, *15*, 1560–1567.

(50) Jackson, J. K.; Letchford, K.; Wasserman, B. Z.; Ye, L.; Burt, H. M. The use of

nanocrystalline cellulose for the binding and controlled release of drugs. *Int. J. Nanomedicine* **2011**, *6*, 321–330.

(51) Akhlaghi, S. P.; Berry, R. C.; Tam, K. C. Surface modification of cellulose nanocrystal with chitosan oligosaccharide for drug delivery applications. *Cellulose* **2013**, *20* (4), 1747–1764.

(52) Shopsowitz, K. E.; Stahl, A.; Hamad, W. Y.; Maclachlan, M. J. Hard templating of nanocrystalline titanium dioxide with chiral nematic ordering. *Angew. Chemie - Int. Ed.* **2012**, *51*, 6886–6890.

(53) Shopsowitz, K. E.; Hamad, W. Y.; MacLachlan, M. J. Chiral nematic mesoporous carbon derived from nanocrystalline cellulose. *Angew. Chemie - Int. Ed.* **2011**, *50* (46), 10991–10995.

(54) Lagerwall, J. P. F.; Schütz, C.; Salajkova, M.; Noh, J.; Hyun Park, J.; Scalia, G.; Bergström, L. Cellulose nanocrystal-based materials: from liquid crystal self-assembly and glass formation to multifunctional thin films. *NPG Asia Mater.* **2014**, *6* (1), e80.

(55) Tsuji, S.; Kawaguchi, H.; V, K. U.; June, R. V; Final, I.; September, F. Thermosensitive Pickering emulsion stabilized by poly (N-isopropylacrylamide)-carrying particles. *Langmuir* **2008**, *24*, 3300–3305.

(56) Kalashnikova, I.; Cathala, B.; Capron, I. New Pickering emulsions stabilized by bacterial cellulose nanocrystals. *Langmuir* **2011**, *27*, 7471–7479.

(57) Kalashnikova, I.; Bizot, H.; Bertoncini, P.; Capron, I. Cellulosic nanorods of various aspect ratios for oil in water Pickering emulsions. *Soft Matter* **2013**, *9*, 952–959.

(58) Tang, J.; Fu, M.; Lee, X.; Zhang, W.; Zhao, B.; Berry, R. M.; Tam, K. C. Dual responsive Pickering emulsion stabilized by poly[2-(dimethylamino)ethyl methacrylate] grafted cellulose nanocrystals. *Biomacromolecules* **2014**, *15*, 3052–3060.

(59) Hu, Z.; Marway, H. S.; Kasem, H.; Pelton, R.; Cranston, E. D. Dried and redispersible cellulose nanocrystal Pickering emulsions. *ACS Macro Lett.* **2016**, *5*, 185–189.

(60) Batmaz, R.; Mohammed, N.; Berry, R. M.; Tam, K. C. Cellulose nanocrystals as promising adsorbents for the removal of cationic dyes. *Cellulose* **2014**, *21*, 1655–

1665.

(61) Karim, Z.; Mathew, A. P.; Grahn, M.; Mouzon, J.; Oksman, K. Nanoporous membranes with cellulose nanocrystals as functional entity in chitosan : Removal of dyes from water. *Carbohydr. Polym.* **2014**, *112*, 668–676.

(62) Mohammed, N.; Grishkewich, N.; Ambrose, H.; Berry, R. M.; Chiu, K. Continuous flow adsorption of methylene blue by cellulose nanocrystal-alginate hydrogel beads in fixed bed columns. *Carbohydr. Polym.* **2016**, *136*, 1194–1202.

(63) Lu, A.; Salabas, E. L.; Schüth, F. Magnetic nanoparticles: synthesis, protection, functionalization, and application. *Angew. Chemie - Int. Ed.* **2007**, *46*, 1222–1244.

(64) Jain, P. K.; Huang, X.; El-sayed, I. H.; El-sayed, M. A. Noble metals on the nanoscale: optical and photothermal properties and some applications in imaging, sensing, biology, and medicine. *Acc. Chem. Res.* **2008**, *41* (12), 7–9.

(65) Crabtree, R. H. The plasmon band in noble metal nanoparticles : an introduction to theory and applications. *New J. Chem.* **2006**, *30*, 1121–1132.

(66) Resch-Genger, U.; Grabolle, M.; Cavaliere-Jaricot, S.; Nitschke, R.; Nann, T. Quantum dots versus organic dyes as fluorescent labels. *Nat. Methods* **2008**, *5* (9), 763–775.

(67) Shen, J.; Zhu, Y.; Yang, X.; Li, C. Graphene quantum dots: emergent nanolights for bioimaging, sensors, catalysis and photovoltaic devices. *Chem. Commun.* **2012**, *48*, 3686–3699.

(68) Eustis, S.; El-sayed, M. A.; Kasha, M. Why gold nanoparticles are more precious than pretty gold : Noble metal surface plasmon resonance and its enhancement of the radiative and nonradiative properties of nanocrystals of different shapes. *Chem. Soc. Rev.* **2006**, *35*, 209–217.

(69) Cushing, B. L.; Kolesnichenko, V. L.; Connor, C. J. O. Recent advances in the liquid-phase syntheses of inorganic nanoparticles. *Chem. Rev.* **2004**, *104*, 3893–3946.

(70) Bramley, A. S.; Hounslow, M. J.; Ryall, R. L. Aggregation during precipitation from solution: A method for extracting rates from experimental data. *J. Colloid Interface Sci.* **1996**, *183*, 155–165.

(71) Sharma, V. K.; Yngard, R. A.; Lin, Y. Silver nanoparticles : Green synthesis and their antimicrobial activities. *Adv. Colloid Interface Sci.* **2009**, *145* (1-2), 83–96.

(72) Raveendran, P.; Wallen, S. L. A simple and "green" method for the synthesis of Au, Ag, and Au–Ag alloy nanoparticles. *Green Chem.* **2006**, *8*, 34–38.

(73) Pereira, C.; Pereira, A. M.; Fernandes, C.; Rocha, M.; Mendes, R.; Guedes, A.; Tavares, P. B.; Grene, J.; Arau, P.; Freire, C. Superparamagnetic MFe_2O_4 (M = Fe, Co, Mn) nanoparticles: Tuning the particle size and magnetic properties through a novel one-step coprecipitation route. *Chem. Mater.* **2012**, *24*, 1496–1504.

(74) Liu, Z. L.; Liu, Y. J.; Yao, K. L.; Ding, Z. H.; Tao, J.; Wang, X. Synthesis and magnetic properties of Fe_3O_4 nanoparticles. *J. Mater. Synth. Process.* **2002**, *10* (2), 83–87.

(75) Kumar, A.; Gupta, M. Synthesis and surface engineering of iron oxide nanoparticles for biomedical applications. *Biomaterials* **2005**, *26*, 3995–4021.

(76) Trindade, T.; O'Brien, P. A single source approach to the synthesis of CdSe nanocrystallites. *Adv. Mater.* **1996**, *8* (2), 161–163.

(77) Kim, S.; Lim, Y. T.; Soltesz, E. G.; Grand, A. M. De; Lee, J.; Nakayama, A.; Parker, J. A.; Mihaljevic, T.; Laurence, R. G.; Dor, D. M.; et al. Near-infrared fluorescent type II quantum dots for sentinel lymph node mapping. *Nat. Biotechnol.* **2004**, *22* (1), 93–97.

(78) Vossmeyer, T.; Katsikas, L.; Gienig, M.; Popovic, I. G.; Diesner, K.; Chemseddine, A.; Eychmiiller, A.; Weller, H. CdS nanoclusters: Synthesis , characterization, size dependent oscillator strength, temperature shift of the excitonic transition energy, and reversible absorbance shift. *J. Phys. Chem.* **1994**, *98*, 7665–7673.

(79) Rogach, A. L.; Franzl, T.; Klar, T. A.; Feldmann, J.; Gaponik, N.; Lesnyak, V.; Shavel, A.; Eychmu, A.; Rakovich, Y. P.; Donegan, J. F. Aqueous synthesis of thiol-capped CdTe nanocrystals : state-of-the-art. *J. Phys. Chem. C* **2007**, *111*, 14628–14637.

(80) Rogach, A. L.; Kornowski, A.; Gao, M.; Eychmu, A. Synthesis and characterization of a size series of extremely small thiol-stabilized CdSe nanocrystals. *J. Phys. Chem. B*

1999, *103*, 3065–3069.

(81) Rogach, B. A.; Kershaw, S.; Burt, M.; Harrison, M.; Kornowski, A.; Eychmüller, A.; Weller, H. Colloidally prepared HgTe nanocrystals with strong room-temperature infrared luminescence. *Adv. Mater.* **1999**, *11* (7), 552–555.

(82) Shavel, A.; Gaponik, N.; Eychmu, A. Efficient UV-blue photoluminescing thiol-stabilized water-soluble alloyed ZnSe(S) nanocrystals. *J. Phys. Chem. B* **2004**, *108*, 5905–5908.

(83) Laaksonen, T.; Ahonen, P.; Johans, C.; Kontturi, K. Stability and electrostatics of mercaptoundecanoic acid-capped gold nanoparticles with varying counterion size. *ChemPhysChem* **2006**, *7*, 2143–2149.

(84) Sperling, R. A.; Parak, W. J. Surface modification, functionalization and bioconjugation of colloidal inorganic nanoparticles. *Phil. Trans. R. Soc. A* **2010**, *368*, 1333–1383.

(85) He, J.; Kunitake, T.; Nakao, A. Facile in situ synthesis of noble metal nanoparticles in porous cellulose fibers. *Chem. Mater.* **2003**, *15*, 4401–4406.

(86) Yu, X.; Tong, S.; Ge, M.; Wu, L.; Zuo, J.; Cao, C.; Song, W. Adsorption of heavy metal ions from aqueous solution by carboxylated cellulose nanocrystals. *J. Environ. Sci.* **2013**, *25* (5), 933–943.

(87) Liu, H.; Song, J.; Shang, S.; Song, Z.; Wang, D. Cellulose nanocrystal/silver nanoparticle composites as bifunctional nanofillers within waterborne polyurethane. *ACS Appl. Mater. Interfaces* **2012**, *4*, 2413–2419.

(88) Kelly, J. A.; Giese, M.; Shopsowitz, K. E.; Hamad, W. Y.; Maclachlan, M. J. The development of chiral nematic mesoporous materials. *Acc. Chem. Res.* **2014**, *47*, 1088–1096.

(89) Cirtiu, C. M.; Dunlop-Brière, A. F.; Moores, A. Cellulose nanocrystallites as an efficient support for nanoparticles of palladium: application for catalytic hydrogenation and Heck coupling under mild conditions. *Green Chem.* **2011**, *13* (2), 288–291.

(90) Daniel, M.-C.; Astruc, D. Gold nanoparticles: assembly, supramolecular chemistry,

quantum-size-related properties, and applications toward biology, catalysis, and nanotechnology. *Chem. Rev.* **2004**, *104* (1), 293–346.

(91) Muszynski, R.; Seger, B.; Kamat, P. V. Decorating graphene sheets with gold nanoparticles. *J. Phys. Chem. C* **2008**, *112*, 5263–5266.

(92) Jiang, K.; Eitan, A.; Schadler, L. S.; Ajayan, P. M.; Siegel, R. W.; Reyes-reyes, M.; Terrones, H.; Terrones, M. Selective attachment of gold nanoparticles to nitrogen-doped carbon nanotubes. *Nano Lett.* **2003**, *3*, 275–277.

(93) Zanella, R.; Giorgio, S.; Henry, C. R.; Louis, C.; Curie, M.; Cedex, P.; Cnrs, C.; Luminy, C. De. Alternative methods for the preparation of gold nanoparticles supported on TiO_2. *J. Phys. Chem. B* **2002**, *106*, 7634–7642.

(94) Pol, V. G.; Gedanken, A. Deposition of gold nanoparticles on silica spheres : A sonochemical approach. *Chem. Mater.* **2003**, *15*, 1111–1118.

(95) Pinto, R. J. B.; Marques, P. A. A. P.; Martins, M. A.; Neto, C. P.; Trindade, T. Electrostatic assembly and growth of gold nanoparticles in cellulosic fibres. *J. Colloid Interface Sci.* **2007**, *312*, 506–512.

(96) Koga, H.; Tokunaga, E.; Hidaka, M.; Umemura, Y.; Saito, T. Topochemical synthesis and catalysis of metal nanoparticles exposed on crystalline cellulose nanofibers. *Chem. Commun.* **2010**, *46*, 8567–8569.

(97) Zhang, T.; Wang, W.; Zhang, D.; Zhang, X.; Ma, Y.; Zhou, Y.; Qi, L. Biotemplated synthesis of gold nanoparticle-bacteria cellulose nanofiber nanocomposites and their application in biosensing. *Adv. Funct. Mater.* **2010**, *20* (7), 1152–1160.

(98) Leung, A. C. W.; Hrapovic, S.; Lam, E.; Liu, Y.; Male, K. B.; Mahmoud, K. A.; Luong, J. H. T. Characteristics and properties of carboxylated cellulose nanocrystals prepared from a novel one-step procedure. *Small* **2011**, *7*, 302–305.

(99) Lam, E.; Hrapovic, S.; Majid, E.; Chong, J. H.; Luong, J. H. T. Catalysis using gold nanoparticles decorated on nanocrystalline cellulose. *Nanoscale* **2012**, *4* (3), 997–1002.

(100) Shin, Y.; Bae, I. T.; Arey, B. W.; Exarhos, G. J. Facile stabilization of gold-silver alloy nanoparticles on cellulose nanocrystal. *J. Phys. Chem. C* **2008**, *112* (13), 4844–

4848.

(101) Mahmoud, K. A.; Male, K. B.; Hrapovic, S.; Luong, J. H. T. Cellulose nanocrystal/gold nanoparticle composite as a matrix for enzyme immobilization. *ACS Appl. Mater. Interfaces* **2009**, *1* (7), 1383–1386.

(102) Maneerung, T.; Tokura, S.; Rujiravanit, R. Impregnation of silver nanoparticles into bacterial cellulose for antimicrobial wound dressing. *Carbohydr. Polym.* **2008**, *72*, 43–51.

(103) Ifuku, S.; Tsuji, M.; Morimoto, M.; Saimoto, H. Synthesis of silver nanoparticles templated by TEMPO-mediated oxidized bacterial cellulose nanofibers. *Biomacromolecules* **2009**, *10*, 2714–2717.

(104) Liu, H.; Wang, D.; Song, Z.; Á, N. Á. A. Preparation of silver nanoparticles on cellulose nanocrystals and the application in electrochemical detection of DNA hybridization. *Cellulose* **2011**, *18*, 67–74.

(105) Liu, H.; Wang, D.; Shang, S.; Song, Z. Synthesis and characterization of Ag–Pd alloy nanoparticles/carboxylated cellulose nanocrystals nanocomposites. *Carbohydr. Polym.* **2011**, *83* (1), 38–43.

(106) Drogat, N.; Granet, R.; Sol, V.; Memmi, A.; Saad, N.; Klein Koerkamp, C.; Bressollier, P.; Krausz, P. Antimicrobial silver nanoparticles generated on cellulose nanocrystals. *J. Nanoparticle Res.* **2011**, *13* (4), 1557–1562.

(107) Xiong, R.; Lu, C.; Zhang, W.; Zhou, Z.; Zhang, X. Facile synthesis of tunable silver nanostructures for antibacterial application using cellulose nanocrystals. *Carbohydr. Polym.* **2013**, *95* (1), 214–219.

(108) Johnson, L.; Thielemans, W.; Walsh, D. A. Synthesis of carbon-supported Pt nanoparticle electrocatalysts using nanocrystalline cellulose as reducing agent. *Green Chem.* **2011**, *13* (7), 1686–1693.

(109) Benaissi, K.; Johnson, L.; Walsh, D. A.; Thielemans, W. Synthesis of platinum nanoparticles using cellulosic reducing agents. *Green Chem.* **2010**, *12*, 220–222.

(110) Cirtiu, C. M.; Dunlop-bri, A. F.; Moores, A. Cellulose nanocrystallites as an efficient support for nanoparticles of palladium : application for catalytic hydrogenation and

Heck coupling under mild conditions. *Green Chem.* **2011**, *13*, 288–291.

(111) Shin, Y.; Blackwood, J. M.; Bae, I.; Arey, B. W.; Exarhos, G. J. Synthesis and stabilization of selenium nanoparticles on cellulose nanocrystal. *Mater. Lett.* **2007**, *61*, 4297–4300.

(112) Olsson, R. T.; Samir, M. A. S. A.; Salazar-Alvarez, G.; Belova, L.; Strom, V.; Berglund, L. A.; Ikkala, O.; Nogues, J.; Gedde, U. W. Making flexible magnetic aerogels and stiff magnetic nanopaper using cellulose nanofibrils as templates. *Nat. Nanotechnol.* **2010**, *5*, 584–588.

(113) Sureshkumar, M.; Siswanto, D. Y.; Lee, C. Magnetic antimicrobial nanocomposite based on bacterial cellulose and silver nanoparticles. *J. Mater. Chem.* **2010**, *20*, 6948–6955.

(114) Mahmoud, K. A.; Lam, E.; Hrapovic, S.; Luong, J. H. T. Preparation of well-dispersed gold/magnetite nanoparticles embedded on cellulose nanocrystals for efficient immobilization of papain enzyme. *ACS Appl. Mater. Interfaces* **2013**, *5*, 4978–4985.

(115) Shin, Y.; Bae, I.; Arey, B. W.; Exarhos, G. J. Simple preparation and stabilization of nickel nanocrystals on cellulose nanocrystal. *Mater. Lett.* **2007**, *61*, 3215–3217.

(116) Ke, D.; Liu, S.; Dai, K.; Zhou, J.; Zhang, L.; Peng, T. CdS/regenerated cellulose nanocomposite films for highly efficient photocatalytic H2 production under visible light irradiation. *J. Phys. Chem. C* **2009**, *113*, 16021–16026.

(117) Li, X.; Chen, S.; Hu, W.; Shi, S.; Shen, W.; Zhang, X.; Wang, H. In situ synthesis of CdS nanoparticles on bacterial cellulose nanofibers. *Carbohydr. Polym.* **2009**, *76* (4), 509–512.

(118) Pe, J.; Liz-marza, L. M. Recent progress on silica coating of nanoparticles and related nanomaterials. *Adv. Mater.* **2010**, *22*, 1182–1195.

(119) Wen, J.; Wilkes, G. L. Organic/inorganic hybrid network materials by the sol-gel approach. *Chem. Mater.* **1996**, *8*, 1667–1681.

(120) West, J. O. N. K. The sol-gel process. *Chem. Rev.* **1990**, *90*, 33–72.

(121) Deng, Y.; Wang, C.; Hu, J.; Yang, W.; Fu, S. Investigation of formation of silica-coated magnetite nanoparticles via sol–gel approach. *Colloids Surfaces A*

Physicochem. Eng. Asp. **2005**, *262*, 87–93.

(122) Yin, Y.; Lu, Y.; Sun, Y.; Xia, Y. Silver nanowires can be directly coated with amorphous silica to generate well-controlled coaxial nanocables of silver/silica. *Nano Lett.* **2002**, *2*, 427–430.

(123) Torza, S.; Mason, S. G. Three-phase interactions in shear and electrical fields. *J. Colloid Interface Sci.* **1970**, *33*, 67–83.

(124) Graf, C.; Vossen, D. L. J.; Imhof, A.; Blaaderen, A. Van. A general method to coat colloidal particles with silica. *Langmuir* **2003**, *19*, 6693–6700.

(125) Gerion, D.; Pinaud, F.; Williams, S. C.; Parak, W. J.; Zanchet, D.; Weiss, S.; Alivisatos, A. P. Synthesis and properties of biocompatible water-soluble silica-coated CdSe/ZnS semiconductor quantum dots. *J. Phys. Chem. B* **2001**, *105* (37), 8861–8871.

(126) Shriver-lake, L. C.; Calvert, J. M.; Ligle, S. Use of thiol-terminal silanes and heterobifunctional crosslinkers for immobilization of antibodies on silica surfaces. *Anal. Biochem.* **1989**, *178*, 408–413.

(127) Selvan, S. T.; Tan, T. T.; Ying, J. Y. Robust, non-cytotoxic, silica-coated CdSe quantum dots with efficient photoluminescence. *Adv. Mater.* **2005**, *17*, 1620–1625.

(128) Zhelev, Z.; Ohba, H.; Bakalova, R. Single quantum dot-micelles coated with silica shell as potentially non-cytotoxic fluorescent cell tracers. *J. Am. Chem. Soc.* **2006**, *128*, 6324–6325.

(129) Zhang, X. F.; Mansouri, S.; Clime, L.; Ly, H. Q.; Yahia, L. H.; Veres, T. Fe_3O_4–silica core–shell nanoporous particles for high-capacity pH-triggered drug delivery. *J. Mater. Chem.* **2012**, *22*, 14450–14457.

(130) Joo, S. H.; Park, J. Y.; Tsung, C.; Yamada, Y.; Yang, P.; Somorjai, G. A. Thermally stable Pt/mesoporous silica core–shell nanocatalysts for high-temperature reactions. *Nat. Mater.* **2008**, *8*, 126–131.

(131) Chen, Z.; Cui, Z.; Niu, F.; Song, W. Pd nanoparticles in silica hollow spheres with mesoporous walls: a nanoreactor with extremely high activity. *Chem. Commun.* **2010**, *46*, 6524–6526.

(132) Ogoshi, T.; Harada, A. Chemical sensors based on cyclodextrin derivatives. *Sensors*

2008, *8*, 4961–4982.

(133) Valle, E. M. M. Del. Cyclodextrins and their uses: a review. *Process Biochem.* **2004**, *39*, 1033–1046.

(134) Szejtli, J. Introduction and general overview of cyclodextrin chemistry. *Chem. Rev.* **1998**, *98*, 1743–1753.

(135) Nagy, Z. M.; Molnár, M.; Fekete-kertész, I.; Molnár-perl, I.; Fenyvesi, É.; Gruiz, K. Removal of emerging micropollutants from water using cyclodextrin. *Sci. Total Environ.* **2014**, *485-486*, 711–719.

(136) Jurecska, L.; Dobosy, P.; Barkács, K.; Fenyvesi, É.; Záray, G. Characterization of cyclodextrin containing nanofilters for removal of pharmaceutical residues. *J. Pharm. Biomed. Anal.* **2014**, *98*, 90–93.

(137) Kurapatia, R.; Raichur, A. M. Composite cyclodextrin–calcium carbonate porous microparticles and modified multilayer capsules: novel carriers for encapsulation of hydrophobic drugs. *J. Mater. Chem. B* **2013**, *1*, 3175–3184.

(138) Ghosh, S.; Badruddoza, A. Z. M.; Hidajat, K.; Uddin, M. S. Adsorptive removal of emerging contaminants from water using superparamagnetic Fe_3O_4 nanoparticles bearing aminated β-cyclodextrin. *Biochem. Pharmacol.* **2013**, *1* (3), 122–130.

(139) Boas, U.; Christensen, J. B.; Heegaard, P. M. H. Dendrimers: design, synthesis and chemical properties. *J. Mater. Chem.* **2006**, *16* (38), 3785.

(140) Esfand, R.; Tomalia, D. A.; Arbor, A.; Arbor, A. Poly (amidoamine) (PAMAM) dendrimers: from biomimicry to drug delivery and biomedical applications. *Drug Discov. Today* **2001**, *6* (8), 427–436.

(141) Svenson, S.; Tomalia, D. A. Dendrimers in biomedical applications—reflections on the field. *Adv. Drug Deliv. Rev.* **2012**, *64*, 102–115.

(142) Lee, I.; Athey, B. D.; Wetzel, A. W.; Meixner, W.; Baker, J. R. Structural molecular dynamics studies on polyamidoamine dendrimers for a therapeutic application: effects of pH and generation. *Macromolecules* **2002**, *35* (11), 4510–4520.

(143) Maiti, P. K.; Tahir, C.; Lin, S.; Goddard, W. A. Effect of solvent and pH on the structure of PAMAM dendrimers. *Macromolecules* **2005**, *38*, 979–991.

(144) Welch, P.; Muthukumar, M. Tuning the density profile of dendritic polyelectrolytes. *Macromolecules* **1998**, *31*, 5892–5897.

(145) Larson, C. L.; Tucker, S. A. Intrinsic fluorescence of carboxylate-terminated polyamido amine dendrimers. *Appl. Spectrosc.* **2001**, *55* (6), 679–683.

(146) Wang, D.; Imae, T. Fluorescence emission from dendrimers and its pH dependence. *J. Am. Chem. Soc.* **2004**, *126*, 13204–13205.

(147) Wang, D.; Imae, T.; Miki, M. Fluorescence emission from PAMAM and PPI dendrimers. *J. Colloid Interface Sci.* **2007**, *306*, 222–227.

(148) Chu, C.; Imae, T. Fluorescence investigations of oxygen-doped simple amine compared with fluorescent PAMAM dendrimer. *Macromol. Rapid Commun.* **2009**, *30*, 89–93.

(149) Tsai, Y.; Hu, C.; Chu, C. Intrinsically fluorescent PAMAM dendrimer as gene carrier and nanoprobe for nucleic acids delivery: bioimaging and transfection study. *Biomacromolecules* **2011**, *12*, 4283–4290.

(150) Astruc, D.; Boisselier, E.; Ornelas, C. Dendrimers designed for functions: from physical, photophysical, and supramolecular properties to applications in sensing, catalysis, molecular electronics, photonics, and nanomedicine. *Chem. Rev.* **2010**, *110* (4), 1857–1959.

(151) Crooks, R. M.; Zhao, M.; Sun, L.; Chechik, V.; Yeung, L. K. Dendrimer-encapsulated metal nanoparticles: synthesis, characterization, and applications to catalysis. *Acc. Chem. Res.* **2001**, *34* (3), 181–190.

(152) Kim, Y.; Oh, S.; Crooks, R. M. Preparation and characterization of 1-2 nm dendrimer-encapsulated gold nanoparticles having very narrow size distributions. *Chem. Mater.* **2004**, *16*, 167–172.

(153) Gröhn, F.; Bauer, B. J.; Akpalu, Y. a.; Jackson, C. L.; Amis, E. J. Dendrimer templates for the formation of gold nanoclusters. *Macromolecules* **2000**, *33*, 6042–6050.

(154) Zhao, M.; Sun, L.; Crooks, R. M. Preparation of Cu nanoclusters within dendrimer templates. *J. Am. Chem. Soc.* **1998**, *120*, 4877–4878.

(155) Esumi, K.; Isono, R.; Yoshimura, T. Preparation of PAMAM- and PPI- metal (silver,

platinum, and palladium) nanocomposites and their catalytic activities for reduction of 4-nitrophenol. *Langmuir* **2004**, *20*, 237–243.

(156) Lemon, B. I.; Crooks, R. M. Preparation and characterization of dendrimer-encapsulated CdS semiconductor quantum dots. *J. Am. Chem. Soc.* **2000**, *122*, 12886–12887.

(157) Nigam, S.; Chandra, S.; Newgreen, D.; Bahadur, D.; Chen, Q. Poly (ethylene glycol) modified PAMAM-Fe_3O_4-doxorubicin triads with potential for improved therapeutic efficacy: generation-dependent increased drug loading and retention at neutral pH and increased release at acid pH. *Langmuir* **2014**, *30*, 1004–1011.

(158) Sirés, I.; Brillas, E. Remediation of water pollution caused by pharmaceutical residues based on electrochemical separation and degradation technologies: A review. *Environ. Int.* **2012**, *40* (1), 212–229.

(159) Fatta-Kassinos, D.; Meric, S.; Nikolaou, A. Pharmaceutical residues in environmental waters and wastewater: current state of knowledge and future research. *Anal. Bioanal. Chem.* **2011**, *399* (1), 251–275.

(160) Joakim Larsson, D. G.; Fick, J. Transparency throughout the production chain—a way to reduce pollution from the manufacturing of pharmaceuticals? *Regul. Toxicol. Pharmacol.* **2009**, *53* (3), 161–163.

(161) Sirés, I.; Brillas, E. Remediation of water pollution caused by pharmaceutical residues based on electrochemical separation and degradation technologies: A review. *Environ. Int.* **2012**, *40*, 212–229.

(162) Blöcher, C. Elimination of micropollutants and hazardous substances at the source in the chemical and pharmaceutical industry. *Water Sci. Technol.* **2007**, *56* (12), 119–123.

(163) Ai, L.; Huang, H.; Chen, Z.; Wei, X.; Jiang, J. Activated carbon/$CoFe_2O_4$ composites: Facile synthesis, magnetic performance and their potential application for the removal of malachite green from water. *Chem. Eng. J.* **2010**, *156* (2), 243–249.

(164) Lee, H.; Lee, E.; Kim, D. K.; Jang, N. K.; Jeong, Y. Y.; Jon, S. Antibiofouling polymer-coated superparamagnetic iron oxide nanoparticles as potential magnetic

resonance contrast agents for in vivo cancer imaging. *J. Am. Chem. Soc.* **2006**, *128*, 7383–7389.

(165) Hayashi, K.; Moriya, M.; Sakamoto, W.; Yogo, T. Chemoselective synthesis of folic acid-functionalized magnetite nanoparticles via click chemistry for magnetic hyperthermia. *Chem. Mater.* **2009**, *21*, 1318–1325.

(166) Cheng, K.; Peng, S.; Xu, C.; Sun, S. Porous hollow Fe_3O_4 nanoparticles for targeted delivery and controlled release of cisplatin. *J. Am. Chem. Soc.* **2009**, *131*, 10637–10644.

(167) Nanoparticles, B. A. O.; Bao, J.; Chen, W.; Liu, T.; Zhu, Y.; Jin, P.; Wang, L.; Liu, J.; Wei, Y.; Li, Y. Bifunctional Au-Fe_3O_4 nanoparticles for protein separation. *ACS Nano* **2007**, *1* (4), 293–298.

(168) He, Y. P.; Wang, S. Q.; Li, C. R.; Miao, Y. M.; Wu, Z. Y.; Zou, B. S. Synthesis and characterization of functionalized silica-coated Fe_3O_4 superparamagnetic nanocrystals for biological applications. *J. Phys. D Appl. Phys.* **2005**, *38*, 1342–1350.

(169) Santra, S.; Tapec, R.; Theodoropoulou, N.; Dobson, J.; Hebard, A.; Tan, W. Synthesis and characterization of silica-coated iron oxide nanoparticles in microemulsion: the effect of nonionic surfactants. *Langmuir* **2001**, *17*, 2900–2906.

(170) Gass, J.; Poddar, P.; Almand, J.; Srinath, S.; Srikanth, H. Superparamagnetic polymer nanocomposites with uniform Fe_3O_4 nanoparticle dispersions. *Adv. Funct. Mater.* **2006**, *16*, 71–75.

(171) Habibi, Y. Key advances in the chemical modification of nanocelluloses. *Chem. Soc. Rev.* **2014**, *43*, 1519–1542.

(172) Habibi, Y.; Lucia, L. A.; Rojas, O. J. Cellulose nanocrystals: chemistry, self-assembly, and applications. *Chem. Rev.* **2010**, *110*, 3479–3500.

(173) Peng, B. L.; Dhar, N.; Liu, H. L.; Tam, K. C. Chemistry and applications of nanocrystalline cellulose and its derivatives: a nanotechnology perspective. *Can. J. Chem. Eng.* **2011**, *89*, 1191–1206.

(174) Siqueira, G.; Bras, J.; Dufresne, A. Cellulosic bionanocomposites: a review of preparation, properties and applications. *Polymers.* **2010**, *2*, 728–765.

(175) Lam, E.; Hrapovic, S.; Majid, E.; Chong, J. H.; Luong, J. H. T. Catalysis using gold nanoparticles decorated on nanocrystalline cellulose. *Nanoscale* **2012**, *4* (3), 997–1002.

(176) Rezayat, M.; Blundell, R. K.; Camp, J. E.; Walsh, D. A.; Thielemans, W. Green one-step synthesis of catalytically active palladium nanoparticles supported on cellulose nanocrystals. *ACS Sustain. Chem. Eng.* **2014**, *2* (5), 1241–1250.

(177) Silva, R.; Al-sharab, J.; Asefa, T. Edge-plane-rich nitrogen-doped carbon nanoneedles and efficient metal-free electrocatalysts. *Angew. Chemie - Int. Ed.* **2012**, *51*, 7171–7175.

(178) Okamatsu, A.; Motoyama, K.; Onodera, R.; Higashi, T.; Koshigoe, T.; Shimada, Y.; Hattori, K.; Takeuchi, T.; Arima, H. Folate-appended β‐cyclodextrin as a promising tumor targeting carrier for antitumor drugs in vitro and in vivo. *Bioconjug. Chem.* **2013**, *24*, 724–733.

(179) Astray, G.; Mejuto, J. C. A review on the use of cyclodextrins in foods. *Food Hydrocoll.* **2009**, *23*, 1631–1640.

(180) Hu, J.; Shao, D.; Chen, C.; Sheng, G.; Li, J.; Wang, X.; Nagatsu, M. Plasma-induced grafting of cyclodextrin onto multiwall carbon nanotube/iron oxides for adsorbent application. *J. Phys. Chem. B* **2010**, *114*, 6779–6785.

(181) Kang, Y. S.; Risbud, S.; Rabolt, J. F.; Stroeve, P. Synthesis and characterization of nanometer-size Fe_3O_4 and γ-Fe_2O_3 particles. *Chem. Mater.* **1996**, *8*, 2209–2211.

(182) Song, W.; Li, H.; Liu, H.; Wu, Z.; Qiang, W.; Xu, D. Fabrication of streptavidin functionalized silver nanoparticle decorated graphene and its application in disposable electrochemical sensor for immunoglobulin E. *Electrochem. commun.* **2013**, *31*, 16–19.

(183) Hou, Y.; Li, T.; Huang, H.; Quan, H.; Miao, X.; Yang, M. Electrochemical immunosensor for the detection of tumor necrosis factor a based on hydrogel prepared from ferrocene modified amino acid. *Sensors Actuators B. Chem.* **2013**, *182*, 605–609.

(184) Liu, J.; Xu, H.; Shen, L.; Chen, R.; Yu, Z. Synthesis of monochlorotriazinyl-*β*-cyclodextrin as a novel textile auxiliary. *Adv. Mater. Res.* **2012**, *441*, 431–435.

(185) Reuscher, H.; Hirsenkorn, R. Beta W7 MCT - new ways in surface modification. *J. Incl. Phenom. Mol. Recognit. Chem.* **1996**, *25*, 191–196.

(186) Wong, Y. J.; Zhu, L.; Teo, W. S.; Tan, Y. W.; Yang, Y.; Wang, C.; Chen, H. Revisiting the Stober method: inhomogeneity in silica shells. *J. Am. Chem. Soc.* **2011**, *133*, 11422–11425.

(187) Al-oweini, R.; El-rassy, H. Synthesis and characterization by FTIR spectroscopy of silica aerogels prepared using several $Si(OR)_4$ and $R''Si(OR')_3$ precursors. *J. Mol. Struct.* **2009**, *919* (1-3), 140–145.

(188) Andhariya, N.; Chudasama, B.; Mehta, R. V; Upadhyay, R. V. Nanoengineering of methylene blue loaded silica encapsulated magnetite nanospheres and nanocapsules for photodynamic therapy. *J. Nanoparticle Res.* **2011**, *13*, 3619–3631.

(189) Shin, S.; Jang, J. Thiol containing polymer encapsulated magnetic nanoparticles as reusable and efficiently separable adsorbent for heavy metal ions. *Chem. Commun.* **2007**, 4230–4232.

(190) Yang, H.; Zhuang, Y.; Hu, H.; Du, X.; Zhang, C.; Shi, X.; Wu, H.; Yang, S. Silica-coated manganese oxide nanoparticles as a platform for targeted magnetic resonance and fluorescence imaging of cancer cells. *Adv. Funct. Mater.* **2010**, *20*, 1733–1741.

(191) Bifeo, P.; Valant, M.; Axelsson, A.; Alford, N. Peculiarities of a solid-state synthesis of multiferroic polycrystalline $BiFeO_3$. *Chem. Mater.* **2007**, *19*, 5431–5436.

(192) Mittal, A.; Katahira, R.; Himmel, M. E.; Johnson, D. K. Effects of alkaline or liquid-ammonia treatment on crystalline cellulose : changes in crystalline structure and effects on enzymatic digestibility. *Biotechnol. Biofuels* **2011**, *4*, 1–16.

(193) Wang, R.; Baran, G.; Wunder, S. L. Packing and thermal stability of polyoctadecylsiloxane compared with octadecylsilane monolayers. *Langmuir* **2000**, *16*, 6298–6305.

(194) Hribernik, S.; Sfiligoj, M.; Stana, K.; Bele, M.; Jamnik, J.; Gaberscek, M. Flame retardant activity of SiO_2-coated regenerated cellulose fibres. *Polym. Degrad. Stab.* **2007**, *92*, 1957–1965.

(195) Wang, Z.; Wang, Y.; Luo, G. A selective voltammetric method for uric acid detection

at *β*-cyclodextrin modified electrode incorporating carbon nanotubes. *Analyst* **2002**, *127*, 1353–1358.

(196) Huq, R.; Mercier, L. Incorporation of cyclodextrin into mesostructured silica. *Chem. Mater.* **2001**, *13*, 4512–4519.

(197) Grigoriu, A.; Racu, C.; Diaconescu, R. M.; Grigoriu, A. Modeling of the simultaneous process of wet spinning-grafting of bast fibers using artificial neural networks. *Text. Res. J.* **2012**, *82*, 324–335.

(198) Hebeish, A.; Aly, A. A.; El-shafei, A. M.; Zaghloul, S. Innovative starch derivatives as textile auxiliaries for application in sizing, finishing and flocculation. *Starch* **2008**, *60*, 97–109.

(199) Kim, J.; Bruggen, B. Van Der. The use of nanoparticles in polymeric and ceramic membrane structures : Review of manufacturing procedures and performance improvement for water treatment. *Environ. Pollut.* **2010**, *158* (7), 2335–2349.

(200) Liu, Y.; Bryantsev, V. S.; Diallo, M. S.; Goddard III, W. A. PAMAM dendrimers undergo pH responsive conformational changes without swelling. *J. Am. Chem. Soc.* **2009**, *131*, 2798–2799.

(201) Venditto, V. J.; Regino, C. A. S.; Brechbiel, M. W. PAMAM dendrimer based macromolecules as improved contrast agents. *Mol. Pharm.* **2005**, *2*, 302–311.

(202) Lee, W. I.; Bae, Y.; Bard, A. J. Strong blue photoluminescence and ECL from OH-terminated PAMAM dendrimers in the absence of gold nanoparticles. *J. Am. Chem. Soc.* **2004**, *126*, 8358–8359.

(203) Zhang, B.; Chen, Q.; Tang, H.; Xie, Q.; Ma, M.; Tan, L.; Zhang, Y.; Yao, S. Characterization of and biomolecule immobilization on the biocompatible multi-walled carbon nanotubes generated by functionalization with polyamidoamine dendrimers. *Colloids Surf. B Biointerfaces* **2010**, *80*, 18–25.

(204) Wang, S. H.; Shi, X.; Antwerp, M. Van; Cao, Z.; Swanson, S. D.; Bi, X.; Baker, J. R. Dendrimer-functionalized iron oxide nanoparticles for specific targeting and imaging of cancer cells. *Adv. Funct. Mater.* **2007**, *17*, 3043–3050.

(205) Tao, X.; Yang, Y.; Liu, S.; Zheng, Y.; Fu, J.; Chen, J. Poly(amidoamine) dendrimer-

grafted porous hollow silica nanoparticles for enhanced intracellular photodynamic therapy. *Acta Biomater.* **2013**, *9*, 6431–6438.

(206) Lang, H.; May, R. A.; Iversen, B. L.; Chandler, B. D. Dendrimer-encapsulated nanoparticle precursors to supported platinum catalysts. *J. Am. Chem. Soc.* **2003**, *125*, 14832–14836.

(207) Kim, Y.; Kim, J. Modification of indium tin oxide with dendrimer-encapsulated nanoparticles to provide enhanced stable electrochemiluminescence of $Ru(bpy)_3^{2+}$/tripropylamine while preserving optical transparency of indium tin oxide for sensitive electrochemiluminescence-ba. *Anal. Chem.* **2014**, *86*, 1654–1660.

(208) Kan, K. H. M.; Li, J.; Wijesekera, K.; Cranston, E. D. Polymer-grafted cellulose nanocrystals as pH-responsive reversible flocculants. *Biomacromolecules* **2013**, *14*, 3130–3139.

(209) Way, A. E.; Hsu, L.; Shanmuganathan, K.; Weder, C.; Rowan, S. J. pH-responsive cellulose nanocrystal gels and nanocomposites. *ACS Macro Lett.* **2012**, *1*, 1001–1006.

(210) Dong, S.; Roman, M. Fluorescently labeled cellulose nanocrystals for bioimaging applications. *J. Am. Chem. Soc.* **2007**, *129* (45), 13810–13811.

(211) Nielsen, L. J.; Eyley, S.; Thielemans, W.; Aylott, J. W. Dual fluorescent labelling of cellulose nanocrystals for pH sensing. *Chem. Commun.* **2010**, *46* (47), 8929–8931.

(212) Sehgal, D.; Vijay, I. K. A method for the high efficiency of water-soluble carbodiimide-mediated amidation, *Anal. biochem.*1994, 87–91.

(213) Green, R. J.; Hopkinson, I.; Jones, R. A. L. Unfolding and intermolecular association in globular proteins adsorbed at interfaces. *Langmuir* **1999**, *15*, 5102–5110.

(214) Perez, S.; Montanari, S.; Vignon, M. R. TEMPO-mediated oxidation of cellulose III. *Biomacromolecules* **2003**, *4*, 1417–1425.

(215) Jasmine, M. J.; Kavitha, M.; Ã, E. P. Effect of solvent-controlled aggregation on the intrinsic emission properties of PAMAM dendrimers. *J. Lumin.* **2009**, *129*, 506–513.

(216) Jasmine, M. J.; Prasad, E. Fractal growth of PAMAM dendrimer aggregates and its impact on the intrinsic emission properties. *J. Phys. Chem. B* **2010**, *114*, 7735–7742.

(217) Saha, K.; Agasti, S. S.; Kim, C.; Li, X.; Rotello, V. M. Gold nanoparticles in chemical

and biological sensing. *Chem. Rev.* **2012**, *112* (5), 2739–2779.

(218) Stratakis, M.; Garcia, H. Catalysis by supported gold nanoparticles: beyond aerobic oxidative processes. *Chem. Rev.* **2012**, *112* (8), 4469–4506.

(219) Shi, Z.; Tang, J.; Chen, L.; Yan, C.; Tanvir, S.; Anderson, W. a.; Berry, R. M.; Tam, K. C. Enhanced colloidal stability and antibacterial performance of silver nanoparticles/cellulose nanocrystal hybrids. *J. Mater. Chem. B* **2015**, *3* (4), 603–611.

(220) Dong, F.; Guo, W.; Park, S.-K.; Ha, C.-S. Controlled synthesis of novel cyanopropyl polysilsesquioxane hollow spheres loaded with highly dispersed Au nanoparticles for catalytic applications. *Chem. Commun.* **2012**, *48* (8), 1108–1110.

(221) Wu, X.; Lu, C.; Zhou, Z.; Yuan, G.; Xiong, R.; Zhang, X. Green synthesis and formation mechanism of cellulose nanocrystal-supported gold nanoparticles with enhanced catalytic performance. *Environ. Sci. Nano* **2014**, *1* (1), 71–79.

(222) Hayakawa, K.; Yoshimura, T.; Esumi, K. Preparation of gold-dendrimer nanocomposites by laser irradiation and their catalytic reduction of 4-nitrophenol. *Langmuir* **2003**, *19*, 5517–5521.

(223) Crooks, R. M.; Zhao, M. Dendrimer-encapsulated Pt nanoparticles: synthesis, characterization, and applications to catalysis. *Adv. Mater.* **1999**, *11* (3), 217–220.

(224) Jiang, Y.; Gao, Q. Heterogeneous hydrogenation catalyses over recyclable Pd(0) nanoparticle catalysts stabilized by PAMAM-SBA-15 organic-inorganic hybrid composites. *J. Am. Chem. Soc.* **2006**, *128*, 716–717.

(225) Rahim, E. H.; Kamounah, F. S.; Frederiksen, J.; Christensen, J. B. Heck reactions catalyzed by PAMAM-dendrimer encapsulated Pd(0) nanoparticles. *Nano Lett.* **2001**, *1* (9), 499–501.

(226) Ren, N.; Dong, A.; Cai, W.; Zhang, Y.; Yang, W. Mesoporous microcapsules with noble metal or noble metal oxide shells and their application in electrocatalysis. *J. Mater. Chem.* **2004**, *14*, 3548–3552.

(227) Esumi, K.; Suzuki, A.; Aihara, N.; Usui, K. Preparation of gold colloids with UV irradiation using dendrimers as stabilizer. *Langmuir* **1998**, *14*, 3157–3159.

(228) Genco, T.; Zemljič, L. F.; Bračič, M.; Stana-Kleinschek, K.; Heinze, T.

Characterization of viscose fibers modified with 6-deoxy-6-amino cellulose sulfate. *Cellulose* **2012**, *19* (6), 2057–2067.

(229) Tao, L.; Chen, G.; Mantovani, G.; York, S.; Haddleton, D. M. Modification of multi-wall carbon nanotube surfaces with poly(amidoamine) dendrons: Synthesis and metal templating. *Chem. Commun.* **2006**, 4949–4951.

(230) Link, S.; El-sayed, M. A. Spectral properties and relaxation dynamics of surface plasmon electronic oscillations in gold and silver nanodots and nanorods. *J. Phys. Chem. B* **1999**, *103*, 8410–8426.

(231) Panigrahi, S.; Basu, S.; Praharaj, S.; Pande, S.; Jana, S.; Pal, A.; Ghosh, S. K.; Pal, T. Synthesis and size-selective catalysis by supported gold nanoparticles: study on heterogeneous and homogeneous catalytic process. *J. Phys. Chem. C* **2007**, *111*, 4596–4605.

(232) Li, J.; Liu, C.; Liu, Y. Au/graphene hydrogel: synthesis, characterization and its use for catalytic reduction of 4-nitrophenol. *J. Mater. Chem.* **2012**, *22* (17), 8426.

(233) Deka, S.; Quarta, A.; Lupo, M. G.; Falqui, A.; Boninelli, S.; Giannini, C.; Morello, G.; Giorgi, M. De; Lanzani, G.; Spinella, C.; et al. CdSe/CdS/ZnS double shell nanorods with high photoluminescence efficiency and their exploitation as biolabeling probes. *J. Am. Chem. Soc.* **2009**, *131*, 2948–2958.

(234) Kim, M. R.; Kang, Y.; Jang, D. Synthesis and characterization of highly luminescent CdS@ZnS core-shell nanorods. *J. Phys. Chem. C* **2007**, *111* (50), 18507–18511.

(235) Loukanov, A. R.; Dushkin, C. D.; Papazova, K. I.; Kirov, A. V.; Abrashev, M. V.; Adachi, E. Photoluminescence depending on the ZnS shell thickness of CdS/ZnS core-shell semiconductor nanoparticles. *Colloids Surf. A Physicochem. Eng. Asp.* **2004**, *245* (1-3), 9–14.

(236) Lewinski, N.; Colvin, V.; Drezek, R. Cytotoxicity of nanoparticles. *Small* **2008**, *4* (1), 26–49.

(237) Chen, M. L.; He, Y. J.; Chen, X. W.; Wang, J. H. Quantum dots conjugated with Fe_3O_4-filled carbon nanotubes for cancer-targeted imaging and magnetically guided drug delivery. *Langmuir* **2012**, *28* (47), 16469–16476.

(238) Sathe, T. R.; Agrawal, A.; Nie, S. Mesoporous silica beads embedded with semiconductor quantum dots and iron oxide nanocrystals: Dual-function microcarriers for optical encoding and magnetic separation. *Anal. Chem.* **2006**, *78* (16), 5627–5632.

(239) Azouz, K. Ben; Ramires, E. C.; Van Den Fonteyne, W.; El Kissi, N.; Dufresne, A. Simple method for the melt extrusion of a cellulose nanocrystal reinforced hydrophobic polymer. *ACS Macro Lett.* **2012**, *1*, 236–240.

(240) Cheung, C. C. Y.; Giese, M.; Kelly, J. a.; Hamad, W. Y.; Maclachlan, M. J. Iridescent chiral nematic cellulose nanocrystal/polymer composites assembled in organic solvents. *ACS Macro Lett.* **2013**, *2*, 1016–1020.

(241) Liu, B.; Campo, E. M.; Bossing, T. Drosophila embryos as model to assess cellular and developmental toxicity of multi-walled carbon nanotubes (MWCNT) in living organisms. *PLoS One* **2014**, *9* (2), e88681.

(242) Czaja, W. K.; Young, D. J.; Kawecki, M.; Brown, R. M. The future prospects of microbial cellulose in biomedical applications. *Biomacromolecules* **2007**, *8* (1), 1–12.

(243) Wang, X. F.; Zhou, Y.; Xu, J. J.; Chen, H. Y. Signal-on electrochemiluminescence biosensors based on CdS-carbon nanotube nanocomposite for the sensitive detection of choline and acetylcholine. *Adv. Funct. Mater.* **2009**, *19*, 1444–1450.

(244) Wang, F.; Liu, B.; Ip, A. C. F.; Liu, J. Orthogonal adsorption onto nano-graphene oxide using different intermolecular forces for multiplexed delivery. *Adv. Mater.* **2013**, *25*, 4087–4092.

(245) Koneswaran, M.; Narayanaswamy, R. Mercaptoacetic acid capped CdS quantum dots as fluorescence single shot probe for mercury(II). *Sensors Actuators, B Chem.* **2009**, *139*, 91–96.

(246) Raubach, C. W.; De Santana, Y. V. B.; Ferrer, M. M.; Longo, V. M.; Varela, J. a.; Avansi, W.; Buzolin, P. G. C.; Sambrano, J. R.; Longo, E. Strutural and optical approach of CdS@ZnS core-shell system. *Chem. Phys. Lett.* **2012**, *536*, 96–99.

(247) Dabbousi, B. O.; Dabbousi, B. O.; Rodriguez-Viejo, J.; Rodriguez-Viejo, J.; Mikulec, F. V.; Mikulec, F. V.; Heine, J. R.; Heine, J. R.; Mattoussi, H.; Mattoussi, H.; et al. (CdSe)ZnS core-shell quantum dots: Synthesis and characterization of a series of

highly luminescent nanocrystallites. *J. Phys. Chem. B* **1997**, *101* (97), 9463–9475.

(248) Gaspar, D.; Fernandes, S. N.; de Oliveira, A. G.; Fernandes, J. G.; Grey, P.; Pontes, R. V; Pereira, L.; Martins, R.; Godinho, M. H.; Fortunato, E. Nanocrystalline cellulose applied simultaneously as the gate dielectric and the substrate in flexible field effect transistors. *Nanotechnology* **2014**, *25*, 094008.

(249) Li, H.; Shih, W. Y.; Shih, W.-H. Synthesis and characterization of aqueous carboxyl-capped CdS quantum dots for bioapplications. *Ind. Eng. Chem. Res.* **2007**, *46* (7), 2013–2019.

(250) Kar, A.; Datta, A.; Patra, A. Fabrication and optical properties of core/shell CdS/$LaPO_4$:Eu nanorods. *J. Mater. Chem.* **2010**, *20* (5), 916–922.

(251) Wang, W.; Germanenko, I.; El-shall, M. S. Room-temperature synthesis and characterization of nanocrystalline CdS, ZnS, and $Cd_xZn_{1-x}S$. *Chem. Mater.* **2002**, *14* (7), 3028–3033.

(252) Xie, R.; Kolb, U.; Li, J.; Basché, T.; Mews, A. Synthesis and characterization of highly luminescent CdSe-core CdS/$Zn_{0.5}Cd_{0.5}S$/ZnS multishell nanocrystals. *J. Am. Chem. Soc.* **2005**, *127* (20), 7480–7488.

(253) Gu, Z.; Zou, L.; Fang, Z.; Zhu, W.; Zhong, X. One-pot synthesis of highly luminescent CdTe/CdS core/shell nanocrystals in aqueous phase. *Nanotechnology* **2008**, *19* (13), 135604.

(254) Chen, N.; He, Y.; Su, Y.; Li, X.; Huang, Q.; Wang, H.; Zhang, X.; Tai, R.; Fan, C. The cytotoxicity of cadmium-based quantum dots. *Biomaterials* **2012**, *33* (5), 1238–1244.

(255) Song, M.; Bi, H.; Wang, L.; Yu, L. Perylene diimide-based organic fluorescent nanorods for live cell imaging. *Bioelectron. Bioinforma. (ISBB), 2011 Int. Symp. on. IEEE* **2011**.

(256) Durr, N. J.; Larson, T.; Smith, D. K.; Korgel, B. a; Sokolov, K.; Ben-Yakar, a. Two-photon luminescence imaging of cancer cells using molecularly targeted gold nanorods. *Nano Lett.* **2007**, *7* (4), 941–945.

(257) Mullard, A. The anticounterfeiter's technological tool kit. *Nat. Med.* **2010**, *16* (4), 361.

(258) Yoon, B.; Lee, J.; Park, I. S.; Jeon, S.; Lee, J.; Kim, J.-M. Recent functional material

based approaches to prevent and detect counterfeiting. *J. Mater. Chem. C* **2013**, *1* (13), 2388–2403.

(259) Mackey, T. K.; Liang, B. A. The global counterfeit drug trade: patient safety and public health risks. *J. Pharm. Sci.* **2011**, *100* (11), 4571–4579.

(260) Royal Canadian Mounted Police. Currency Counterfeiting Statistics.

(261) Martino, R.; Malet-Martino, M.; Gilard, V.; Balayssac, S. Counterfeit drugs: Analytical techniques for their identification. *Anal. Bioanal. Chem.* **2010**, *398* (1), 77–92.

(262) Li, L. Technology designed to combat fakes in the global supply chain. *Bus. Horiz.* **2013**, *56* (2), 167–177.

(263) Cui, Y.; Phang, I. Y.; Lee, Y. H.; Lee, M. R.; Zhang, Q.; Ling, X. Y. Multiplex plasmonic anti-counterfeiting security labels based on surface-enhanced Raman scattering. *Chem. Commun.* **2015**, *51*, 5363–5366.

(264) Kim, H.; Ge, J.; Kim, J.; Choi, S.; Lee, H.; Lee, H.; Park, W.; Yin, Y.; Kwon, S. Structural colour printing using a magnetically tunable and lithographically fixable photonic crystal. *Nat. Photonics* **2009**, *3* (9), 534–540.

(265) Zhao, Y.; Xie, Z.; Gu, H.; Zhu, C.; Gu, Z. Bio-inspired variable structural color materials. *Chem. Soc. Rev.* **2012**, *41* (8), 3297–3317.

(266) Hu, H.; Chen, Q.-W.; Tang, J.; Hu, X.-Y.; Zhou, X.-H. Photonic anti-counterfeiting using structural colors derived from magnetic-responsive photonic crystals with double photonic bandgap heterostructures. *J. Mater. Chem.* **2012**, *22* (22), 11048–11053.

(267) Mermut, O.; Barrett, C. J. Stable sensor layers self-assembled onto surfaces using azobenzene-containing polyelectrolytes. *Analyst* **2001**, *126* (11), 1861–1865.

(268) Li, Z.; Wang, J.; Liu, X.; Liu, S.; Ou, J.; Yang, S. Electrostatic layer-by-layer self-assembly multilayer films based on graphene and manganese dioxide sheets as novel electrode materials for supercapacitors. *J. Mater. Chem.* **2011**, *21* (10), 3397–3403.

(269) Dou, Y.; Pan, T.; Xu, S.; Yan, H.; Han, J.; Wei, M.; Evans, D. G.; Duan, X. Transparent, ultrahigh-gas-barrier films with a brick-mortar-sand structure. *Angew.*

Chemie Int. Ed. **2015**, *54* (33), 9673–9678.

(270) Xiao, F.-X.; Miao, J.; Liu, B. Layer-by-layer self-assembly of CdS quantum dots/graphene nanosheets hybrid films for photoelectrochemical and photocatalytic applications. *J. Am. Chem. Soc.* **2014**, *136* (4), 1559–1569.

(271) Han, S.; Bae, H. J.; Kim, J.; Shin, S.; Choi, S.; Lee, S. H.; Kwon, S.; Park, W. Lithographically encoded polymer microtaggant using high-capacity and error-correctable QR code for anti-counterfeiting of drugs. *Adv. Mater.* **2012**, *24*, 5924–5929.

(272) Hendrick, E.; Frey, M.; Herz, E.; Wiesner, U. Cellulose acetate fibers with fluorescing nanoparticles for anti-counterfeiting and pH-sensing applications. *J. Eng. Fiber. Fabr.* **2010**, *5* (1), 21–30.

(273) You, M.; Lin, M.; Wang, S.; Wang, X.; Zhang, G.; Hong, Y.; Dong, Y.; Jin, G.; Xu, F. Three-dimensional quick response code based on inkjet printing of upconversion fluorescent. *Nanoscale* **2016**.

(274) You, M.; Zhong, J.; Hong, Y.; Duan, Z.; Lin, M.; Xu, F. Inkjet printing of upconversion nanoparticles for anti-counterfeit applications. *Nanoscale* **2015**, *7*, 4423–4431.

(275) Meruga, J. M.; Cross, W. M.; May, P. S.; Luu, Q.; Crawford, G. A.; Kellar, J. J. Security printing of covert quick response codes using upconverting nanoparticle inks. *Nanotechnology* **2012**, *23*, 395201.

(276) Sun, L. W.; Shi, H. Q.; Li, W. N.; Xiao, H. M.; Fu, S. Y.; Cao, X. Z.; Li, Z. X. Lanthanum-doped ZnO quantum dots with greatly enhanced fluorescent quantum yield. *J. Mater. Chem.* **2012**, *22*, 8221–8227.

(277) Shi, H. Q.; Li, W. N.; Sun, L. W.; Liu, Y.; Xiao, H. M.; Fu, S. Y. Synthesis of silane surface modified ZnO quantum dots with ultrastable , strong and tunable luminescence. *Chem. Commun.* **2011**, *47*, 11921–11923.

(278) Zhou, Y.; Ji, Q.; Masuda, M.; Kamiya, S.; Shimizu, T. Helical arrays of CdS nanoparticles tracing on a functionalized chiral template of glycolipid nanotubes. *Chem. Mater.* **2006**, *18*, 403–406.

(279) Rayevska, O. E.; Grodzyuk, G. Y.; Dzhagan, V. M.; Stroyuk, O. L.; Kuchmiy, S. Y.; Plyusnin, V. F.; Grivin, V. P.; Valakh, M. Y. Synthesis and characterization of white-emitting CdS quantum dots stabilized with polyethylenimine. *J. Phys. Chem. C* **2010**, *114*, 22478–22486.

(280) Yu, W. W.; Qu, L.; Guo, W.; Peng, X. Experimental determination of the extinction coefficient of CdTe, CdSe, and CdS nanocrystals. *Chem. Mater.* **2003**, *15*, 2854–2860.

(281) Roman, M.; Winter, W. T. Effect of sulfate groups from sulfuric acid hydrolysis on the thermal degradation behavior of bacterial cellulose. *Biomacromolecules* **2004**, *5* (5), 1671–1677.

(282) Höök, F.; Kasemo, B.; Nylander, T.; Fant, C.; Sott, K.; Elwing, H. Variations in coupled water, viscoelastic properties, and film thickness of a Mefp-1 protein film during adsorption and cross-linking: A quartz crystal microbalance with dissipation monitoring, ellipsometry, and surface plasmon resonance study. *Anal. Chem.* **2001**, *73* (24), 5796–5804.

(283) Kleimann, J.; Lecoultre, G.; Papastavrou, G.; Jeanneret, S.; Galletto, P.; Koper, G. J. M.; Borkovec, M. Deposition of nanosized latex particles onto silica and cellulose surfaces studied by optical reflectometry. *J. Colloid Interface Sci.* **2006**, *303* (2), 460–471.

(284) Cranston, E. D.; Gray, D. G. Birefringence in spin-coated films containing cellulose nanocrystals. *Colloids Surfaces A Physicochem. Eng. Asp.* **2008**, *325* (1-2), 44–51.

(285) Zhang, L.; Li, Y.; Sun, J.; Shen, J. Mechanically stable antireflection and antifogging coatings fabricated by the layer-by-layer deposition process and postcalcination. *Langmuir* **2008**, *24* (19), 10851–10857.

(286) Aulin, C.; Johansson, E.; Wågberg, L.; Lindström, T. Self-organized films from cellulose I nanofibrils using the layer-by-layer technique. *Biomacromolecules* **2010**, *11* (4), 872–882.

(287) Lu, G.; Hupp, J. T. Metal-organic frameworks as sensors: A ZIF-8 based fabry-pérot device as a selective sensor for chemical vapors and gases. *J. Am. Chem. Soc.* **2010**, *132* (23), 7832–7833.

(288) Liang, R.; Xu, S.; Yan, D.; Shi, W.; Tian, R.; Yan, H.; Wei, M.; Evans, D. G.; Duan, X. CdTe quantum dots/layered double hydroxide ultrathin films with multicolor light emission via layer-by-layer assembly. *Adv. Funct. Mater.* **2012**, *22*, 4940–4948.